



**HAL**  
open science

# Contribution to the multi-physical analysis of the risk of recriticality of corium during severe accident in a PWR reactor

Paul Boulard

► **To cite this version:**

Paul Boulard. Contribution to the multi-physical analysis of the risk of recriticality of corium during severe accident in a PWR reactor. Nuclear Theory [nucl-th]. Université Paris-Saclay, 2020. English. NNT : 2020UPASP054 . tel-03250446

**HAL Id: tel-03250446**

**<https://theses.hal.science/tel-03250446>**

Submitted on 4 Jun 2021

**HAL** is a multi-disciplinary open access archive for the deposit and dissemination of scientific research documents, whether they are published or not. The documents may come from teaching and research institutions in France or abroad, or from public or private research centers.

L'archive ouverte pluridisciplinaire **HAL**, est destinée au dépôt et à la diffusion de documents scientifiques de niveau recherche, publiés ou non, émanant des établissements d'enseignement et de recherche français ou étrangers, des laboratoires publics ou privés.

Contribution to the multi-physical  
analysis of the risk of recriticality of  
corium during severe accident in a  
PWR reactor

Thèse de doctorat de l'université Paris-Saclay

École doctorale n° 576, PHENIICS  
Spécialité de doctorat: Energie nucléaire  
Unité de recherche : Université Paris-Saclay, CEA,  
Département de Modélisation des Systèmes et Structures, 91191, Gif-sur-Yvette,  
France.  
Référent Faculté des sciences d'Orsay

Thèse présentée et soutenue à Saclay, le 13/11/2020, par

**Paul BOULARD**

**Composition du Jury**

<b>Gilles BAN</b> Professeur, Université de Caen	Rapporteur & Examineur
<b>Sevostian BECHTA</b> Professeur, KTH	Rapporteur & Examineur
<b>Mikhaïl BUCK</b> Ingénieur, IKE	Examineur
<b>Pierre DESESQUELLES</b> Professeur, Paris-Saclay	Examineur et président du jury
<b>Elsa MERLE</b> Professeur, Université de Grenoble	Examinatrice

<b>Jean-Marc MARTINEZ</b> Ingénieur R&D, CEA	Directeur de thèse
<b>Andrea ZOIA</b> Ingénieur R&D, CEA	Co-Directeur de thèse
<b>Jean-Charles JABOULAY</b> Ingénieur R&D, CEA	Encadrant



## **Acknowledgments**

Thank you!



# Contents

Table of contents . . . . .	v
List of figures . . . . .	vi
List of tables . . . . .	a
Introduction . . . . .	1
Context . . . . .	1
Preliminary investigation of published material . . . . .	2
Objectives . . . . .	3
Plan of this work . . . . .	4
Published material . . . . .	5
Bibliography . . . . .	6
A Context and models for critical debris beds . . . . .	7
I Overview of critical debris beds . . . . .	9
I.1 A survey of severe accidents and debris beds . . . . .	10
I.1.1 International nuclear event scale (INES) . . . . .	10
I.1.2 TMI-2 . . . . .	11
I.1.3 Chernobyl . . . . .	13
I.1.4 Fukushima-Daiichi . . . . .	15
I.2 Phenomenology of debris bed formation . . . . .	18
I.2.1 Decay heat . . . . .	18
I.2.2 Melting of the core . . . . .	20
I.2.3 Relocation at the bottom of the pressure vessel . . . . .	20
I.2.4 Fuel Coolant Interaction and steam Explosion . . . . .	21
I.2.5 Molten Core Concrete Interaction . . . . .	23
I.3 Criticality in debris bed . . . . .	25
I.3.1 Fundamentals of criticality . . . . .	25
I.3.2 Neutron physics overview . . . . .	26
I.3.3 Feedback mechanisms . . . . .	27
I.3.4 Neutron kinetics . . . . .	28
I.3.5 Criticality of debris beds . . . . .	29
I.3.6 Experiments concerning criticality of debris beds . . . . .	30
I.4 Cooling debris bed in diphasic conditions . . . . .	32
I.4.1 Challenges related to the cooling of debris beds . . . . .	32
I.4.2 Diphasic flows trough a porous medium . . . . .	32
I.4.3 Dryout heat flux characterization . . . . .	34
I.5 Synthesis . . . . .	36
Bibliography . . . . .	37

II	Models and simulation tools related to critical debris beds	40
II.1	Models and simulation tools for thermal-hydraulics in debris beds	41
II.1.1	Models of flow through porous media	41
II.1.2	Simulation codes for debris bed cooling	44
II.1.3	Thermal model	49
II.2	Models and simulation tools for criticality in debris beds	50
II.2.1	Neutron transport	50
II.2.2	Simulation codes for neutron transport	53
II.2.3	Quasi-static method	54
II.2.4	Generation of random geometries	54
II.3	Statistical learning as a tool to accelerate calculations	56
II.3.1	Overview of surrogate models	56
II.3.2	Linear models	57
II.3.3	Artificial neural networks	58
II.4	Synthesis	61
	Bibliography	61
B	Development of the methodology and applications to generic debris beds	65
III	Simulating debris beds: a preliminary investigation	67
III.1	Assumptions for a generic numerical debris bed	68
III.1.1	Composition and mass	68
III.1.2	Debris size distribution	69
III.1.3	Decay heat	73
III.1.4	Geometry of the debris bed	74
III.2	Numerical modelling	78
III.2.1	Neutronics	78
III.2.2	Thermal-hydraulics	80
III.2.3	Mesh used to simulate the debris bed	80
III.3	Debris size distribution modelling	82
III.3.1	Debris equivalent size in neutronics	82
III.3.2	Debris equivalent temperature	87
III.3.3	Debris equivalent size for steam and water flow	87
III.4	Synthesis	88
	Bibliography	88
IV	Criticality assessment of debris beds	91
IV.1	Criticality assessment methodology	92
IV.1.1	Multi-physics coupling procedure	92
IV.1.2	Determining the thermal-hydraulics conditions	93
IV.2	Training of surrogate models for neutronics	94
IV.2.1	Building of the database	94
IV.2.2	Database filtration	96
IV.2.3	Selection of the surrogate model	96
IV.2.4	Mixture of models	100
IV.3	Assessment of the criticality domain	100
IV.3.1	Reactivity sensibility to decay power and pressure	100
IV.3.2	Assessment of the impact of power density and total mass	101
IV.3.3	Discussion of the observed trends	103
IV.4	Synthesis	104

Bibliography	105
V Deposited energy estimation of a critical event in debris beds	106
V.1 Fully coupled simulation procedure	107
V.1.1 Required precision	107
V.1.2 Strategies to speed-up the neutron transport	108
V.1.3 Adaptative time-step	110
V.1.4 Simulation time	111
V.2 Assessment of power excursion	112
V.2.1 Simulation of critical transients in debris beds while reflooding	112
V.2.2 Discussion on the behaviour of the simulated systems	116
V.2.3 Investigation of "ad hoc" cases to identify a reliable maximum source term	118
V.3 Synthesis	124
Bibliography	125
VI Preliminary assessment of the consequences of a critical event in a generic debris bed	126
VI.1 Qualitative assessment based on debris temperature	127
VI.2 A first attempt of mechanical consequences evaluation	129
VI.2.1 Model and assumptions	129
VI.2.2 Description of the simulated transient	131
VI.2.3 Assessment of the mechanical impulsion	134
VI.2.4 Sensitivity calculations	135
VI.3 Synthesis	136
Bibliography	137
Conclusions	138
Preliminary investigations and state of art	138
Discussion of the methodology development	138
Summary	143
Perspectives	144
Bibliography	145
A Nomenclature and back-propagation example	147
A.1 Nomenclature	147
A.1.1 Thermal-hydraulics nomenclature	147
A.1.2 Thermal diffusion nomenclature	148
A.1.3 Neutron transport nomenclature	148
A.2 Example of back propagation computation	150
B Résumé détaillé en français	151
B.1 Introduction	151
B.2 État de l'art concernant la criticité des lits de débris	151
B.3 Modèles et codes de simulation	152
B.4 Simulation de lits de débris : une étude préliminaire	152
B.5 Évaluation de la criticité des lits de débris	153
B.6 Estimation de l'énergie déposée lors d'un événement critique dans un lit de débris	153
B.7 Évaluation préliminaire des conséquences d'un événement critique dans un lit de débris	154
B.8 Conclusions	154
Références	155

# List of Figures

I.1	Diagram of the INES scale, taken from [1]. . . . .	11
I.2	TMI-2 final state, taken from [6]. . . . .	12
I.3	Chernobyl reactor post-accident state after the construction of the first shelter building, taken from [2]. . . . .	15
I.4	Locations of crucial structures and components and indication of flooding level at the Fukushima Daiichi nuclear power plant, taken from [17]. . . . .	16
I.5	Contemplated configurations for the corium state in the Fukushima Daiichi unit 1, 2, and 3, based on [17]. . . . .	17
I.6	Picture of the solidified molten core taken in early 2019 in the unit 2 pressure vessel, taken from [19]. . . . .	18
I.7	Modelling of the decay heat in nuclear reactor. . . . .	19
I.8	Schematics of the degradation of the core in the pressure vessel which can lead to fuel debris bed formation. . . . .	20
I.9	Melting and reactions threshold temperatures of core material, taken from [6]. . . . .	21
I.10	Hydrodynamics instabilities creating fragmentation, taken from [24]. . . . .	21
I.11	Diagram of the progress of the steam explosion [25]. . . . .	22
I.12	Phenomena during propagation phase of the steam explosion, taken from [24]. . . . .	23
I.13	Schematic of the M3b test of molten corium concrete interaction, taken from [26]. . . . .	24
I.14	Scheme of corium concrete interaction with water ingress and melt eruption mechanisms, taken from [6] . . . . .	24
I.15	Chain reaction. . . . .	25
I.16	Neutron energy spectrum in a thermal reactor. . . . .	27
I.17	Impact of the moderation ratio on reactivity and void effect. . . . .	28
I.18	Doppler broadening of one resonance at different temperatures, taken from [28]. . . . .	29
I.19	STACY pattern in the testing section: blue dots are the testing rods, taken from [30]. . . . .	30
I.20	STACY critical assembly, taken from [30]. . . . .	31
I.21	$k_{eff}$ of each core as a function of effective water height, taken from [30]. . . . .	31
I.22	Debris bed created in the pressure vessel (left) and in the vessel pit (right). . . . .	33
I.23	Channel creation in top flooding of debris bed, taken from [38]. . . . .	34
I.24	Top-flooding of a cylindrical debris bed (top) and multi-dimensional flooding of a conical bed (bottom), taken from [33]. . . . .	35
I.25	dryout heat flux of debris bed depending on the pressure and its shape in COOLOCE experiments, taken from [33]. . . . .	36
II.1	Example of porous medium with material chunks (in black). . . . .	42
II.2	Counter flows into a heated debris bed, the water is depicted in blue, the steam in white and the debris in red. . . . .	43
II.3	Validation of MC3D capabilities to model interfacial friction against TUTU cold experiments [18]. . . . .	47

II.4	PEARL debris bed with quartz bypass and locations of the thermocouple on the right [21]. . . . .	48
II.5	Validation of MC3D capabilities against PEARL experiment [18]. . . . .	49
II.6	Example of two-phase geometries generated with Poisson generator (left) and Voronoi generator (right). . . . .	55
II.7	Diagram of an artificial neuron [47]. . . . .	59
II.8	Shallow artificial neural network made of 4 neurons (in the hidden layer), with 3 inputs and 2 outputs [47]. . . . .	59
III.1	FARO experiments results [4]. . . . .	70
III.2	DAVINCI experimental set-up [10]. . . . .	74
III.3	Measurements of the debris distribution in single phase and diphasic conditions [10].	75
III.4	Geometry of the test case. . . . .	76
III.7	Porosity in debris beds in function of the volumetric power using the code MC3D.	76
III.5	Initial state of the debris bed (water presence on the left and bed porosity on the right) using the code MC3D. . . . .	77
III.6	State after 180 s (water presence on the left and bed porosity on the right) using the code MC3D. . . . .	77
III.8	Example of face-centered-cubic lattice modelled in TRIPOLI-4 <sup>®</sup> . . . . .	78
III.9	Example of Poisson disordered geometry modelled in TRIPOLI-4 <sup>®</sup> [13]. . . . .	79
III.10	Neutron transport calculation procedure with Apollo-2 . . . . .	80
III.11	MC3D mesh, the axial symmetry is on the left and the debris bed is at the bottom. . . . .	81
III.12	Apollo-2 mesh (cylindrical shape) of the debris bed, the axial symmetry is on the left. . . . .	81
III.13	Coupling mesh (cylindrical shape), the axial symmetry is on the left. . . . .	82
III.14	Comparison of experimental debris size and simulated debris. . . . .	83
III.15	Comparison of the $k_{\infty}$ obtained with random geometries similar to experimental size distribution and mono-sized spheres in FCC lattice. . . . .	84
III.16	Comparison of the $k_{\infty}$ obtained with random geometries to experimental size distribution and mono-sized spheres in FCC lattice. . . . .	85
IV.1	Criticality assessment procedure scheme. . . . .	92
IV.2	MC3D simulation of debris bed cooling with constant power. Insertion of liquid water (at the top boundary on the right) to keep a liquid water layer above the debris bed (water velocity visualized by coloured arrows, the cell colours representing the liquid water presence). . . . .	94
IV.4	Scheme of the data dimensions . . . . .	95
IV.3	Scheme of the pre-calculation sequences to build the database . . . . .	95
IV.5	Representation of the database filtration, the validation database is on the right and the training database is on the left. . . . .	96
IV.6	Prediction of the reactivity by polynomial regression of degree 1 against the expected reactivity on the validation dataset. . . . .	97
IV.7	Prediction of the reactivity by polynomial regression of degree 2 against the expected reactivity on the validation dataset. . . . .	98
IV.8	Analysis of the number of neurons required to increase the accuracy of the ANN. The performance are not improved when the number of neurons goes beyond 32.	99
IV.9	Prediction of the reactivity by ANN regression against the expected reactivity on the validation dataset. . . . .	99
IV.10	Oscillations of the reactivity during the debris bed cooling with 60 t of debris and a power density of 0.45 MW/m <sup>3</sup> . . . . .	102

IV.11 Oscillations of the reactivity during the debris bed cooling with <b>80 t</b> of debris and a power density of <b>0.45 MW/m<sup>3</sup></b> .	103
V.1 Scheme of the coupling requirements for transient simulations.	107
V.2 Scheme of the coupling calculations on one time-step.	109
V.3 Example of ANN correction after Apollo-2 calculation.	110
V.4 Example of time step adaptation during a transient, the orange line is the time step and the blue line is the reactivity.	111
V.5 Reflooding at 0.1 MPa of a 75 t debris bed.	113
V.6 Reflooding at 0.2 MPa of a 75 t debris bed.	113
V.7 Reflooding at 0.3 MPa of a 75 t debris bed.	114
V.8 Reflooding at 0.4 MPa of a 75 t debris bed.	115
V.9 Reflooding at 0.1 MPa of a 65 t debris bed.	115
V.10 Reflooding at 0.1 and 0.4 MPa of a 75 t debris bed from <b>140 to 300 s</b> .	117
V.11 Reflooding at 0.1 and 0.4 MPa of a 75 t debris bed, normalized from <b>140 to 300 s</b> .	117
V.12 Sample of the reflooding at <b>0.4 MPa</b> of a 75 t debris bed, the time ranges from <b>170 s to 190 s</b> .	118
V.13 Schematic of the artificial quick reflooding.	118
V.14 Large visualisation of the void fraction, reactivity and maximum debris temperature during the artificial reflooding of the <b>80 t</b> case.	120
V.15 Focus on the prompt transient of the void fraction, reactivity and maximum debris temperature during the artificial reflooding of the <b>80 t</b> case.	120
V.16 Focus on the prompt transient of the void fraction, reactivity and maximum debris temperature during the artificial reflooding of the <b>100 t</b> case.	121
V.17 State of the debris bed before the power peak (the vertical line indicates the time in the graphic).	122
V.18 State of the debris bed after the power peak (the vertical line indicates the time on the graphic).	123
V.19 Map of the density of deposited energy during the most powerful artificial reflooding transient.	124
VI.1 Initial temperature field inserted for MC3D. This is the source term, the debris temperature difference with water temperature will generate rapidly a steam bubble.	128
VI.2 Heat transfer regime in boiling conditions depending on the wall temperature [3].	128
VI.3 Scheme of the geometry modelled in MC3D.	130
VI.4 Scheme of the entire geometry at the initial time (liquid water in blue).	130
VI.5 Scheme of the geometry at the initial time (liquid water in blue), orange disks indicate where the pressures are recorded.	131
VI.6 Evolution of the debris presence and the liquid water. There is an axial symmetry in the centre, the debris fraction is on the left and the liquid water fraction is on the right.	132
VI.7 Evolution of the debris presence and the liquid water. Axial symmetry in the centre, the debris fraction is on the left and the liquid water fraction is on the right.	132
VI.8 Evolution of the debris presence and the liquid water. Axial symmetry in the centre, the debris fraction is on the left and the liquid water fraction is on the right.	133
VI.9 Final state of the debris presence and the liquid water. Axial symmetry in the centre, the debris fraction is on the left and the liquid water fraction is on the right.	133
VI.10 Recorded pressure during the simulation.	134

VI.11	Pressures and impulsions at the pressure peak. . . . .	135
VI.12	Preliminary requirement to model critical debris bed. . . . .	139
VI.13	Procedure to build the database and train the ANN. . . . .	141
VI.14	The procedure to estimate the risk of criticality and the potential mechanical consequences. . . . .	144
A.1	Small artificial neural network to do an example of backpropagation. . . . .	150

## List of Tables

II.1	Models of relative permeability and passability. . . . .	44
III.1	Fuel debris composition. . . . .	69
III.2	Experiments conditions and debris data [3] [4]. . . . .	70
III.3	FARO L debris size distribution. . . . .	71
III.4	Debris size distribution measured in DEFOR-A [8]. . . . .	72
III.5	Debris size distribution [3]. . . . .	73
III.6	$k_{\infty}$ comparison of Apollo-2 and TRIPOLI-4 <sup>®</sup> on face-centre-cubic cells. . . . .	79
III.7	Simplification to model debris beds in neutronics [6] . . . . .	86
III.8	Reactivity impact of averaged $T_{eff}$ . . . . .	87
III.9	Summary of the tactics applied on each physic to represent the debris size distribution. . . . .	88
IV.1	Maximum reactivity recorded during simulations [5]. . . . .	101
IV.2	Maximum reactivity recorded during simulations (the green cells show the lowest reactivity value and the orange cells show the highest reactivity at a set power density). . . . .	103
V.1	Strategy to accelerate transient simulations. . . . .	110
V.2	Example of simulation time on one transient lasting 1150 s . . . . .	112
V.3	Physical values of interest recorded during simulations. . . . .	119
VI.1	Maximum impulsions recorded corresponding to modified configurations. . . . .	136





# Introduction

As of today, there are 442 nuclear reactors for energy production [1]. This fleet demands the highest standards for the nuclear power plant safety. Accidents have unfortunately happened in the past, highlighting the existence of interwoven phenomena and consequences. Severe nuclear accidents, like those occurred at Three-Miles-Island (TMI), Chernobyl or Fukushima, had a tremendous impact [2] [3]. Although a severe accident is a major issue by itself, many complex physical phenomena, such as hydrogen explosion or steam explosion, could worsen the state of the nuclear power plant: in this work we will focus on the criticality risk and its consequences. A re-criticality excursion occurs if the neutron chain reaction is sustained by physical conditions without any control, following an initiating accident. Fissions will create radioactive nuclides and will therefore be an immediate source of irradiation [4]. A re-criticality accident may create further issues: indeed the neutron population might suddenly rise and the produced heat might even induce structural damage. However, re-criticality excursions require very specific physical conditions [4]. This potential event must be thoroughly investigated by using models and numerical simulations in order to evaluate its consequences, impact on the nuclear system. In this respect, knowledge based on severe accidents occurred in the past provides invaluable information that can help in selecting and tuning the models. The aim of this thesis is to attempt to assess the re-criticality risk and its consequences during a severe accident, with special emphasis on multi-physics aspects in non-stationary conditions, namely via the coupling between neutron kinetics and thermal-hydraulics.

## Context

When the tsunami generated by the Tohoku earthquake flooded the nuclear power plant of Fukushima Daiichi in March 2011 [5], it flooded also the diesel generators supplying electrical energy to the power plant to maintain the cores cooling. Although the chain reaction in the core was stopped, the fuel from the radioactive nuclides produced heat power, so pumps injecting water were used to ensure the cooling of the core. At Fukushima Daiichi the loss of core cooling was eventually responsible for the melting of the cores [5]. The molten core formed a hot and aggressive lava, so-called “corium” (whose temperature was higher than  $2800\text{ K}$ ), mainly made of  $UO_2$  and  $ZrO_2$  and structural material as iron, and generating heat because of the decay heat and oxidation phenomena [2]. As long as the melted core is not cooled, it can progress through the reactor building thanks to gravity, digging its way by interacting with different materials (vessel, concrete). One possible mitigation process is the injection of water to stop the corium progression. The contact between water and the hot molten material can lead to a fragmentation process, partial/or total corium solidification and the formation of a corium *debris bed* [2]. Such configuration can be considered as a porous medium, which in the presence of water without boric acid might increase the risk of re-criticality.

The accident at Fukushima Daiichi power plant has drawn renewed interest about the

risk of re-criticality when a core debris bed is created during a severe accident. When the core is melted or degraded from its initial shape (fuel rods in zirconium alloy), detailed investigations are required to prevent the possibility of re-criticality during the progression of the severe accident and later at mid/long term corium stabilization. However, many physical parameters affect the estimation of re-criticality risk. Debris bed configurations also considerably depend on scenarios and reactor design [2].

In the case of re-criticality, a power surge might possibly lead to a large amount of nuclear heating. The fission products created during the power transient will increase the radioactivity of the area and the released fission energy may bring mechanical loading on structures. These unforeseen consequences would worsen the state of the nuclear facility.

The re-criticality risk will in principle persist up until to dismantlement operations, depending mainly on the following parameters : geometry modification, neutron moderator insertion and/or neutron absorber disappearance, and thermal-hydraulics conditions for corium cooling. For these reasons, it is necessary to assess the risk of re-criticality during and after a severe accident in a nuclear reactor. In this thesis we will propose a methodology to quantify the amount of energy release and estimate its mechanical outcome.

## Preliminary survey of published material

We begin our analysis by providing a brief overview of the existing literature concerning the simulation and analysis of severe accidents. We consider first the issues related to neutron transport and multiplication, and then thermal-hydraulics models in debris beds.

The paper [6] deals with neutron transport and multiplication in debris bed, with special emphasis on the effect of the debris size distribution. Experiments of debris creation have shown that the debris are distributed in size. The simulation of neutron transport by explicitly taking into account the size distribution of the debris requires complex modelling. These simulations are time-consuming and can be done only with Monte-Carlo codes. The use of a spherical equivalent debris in face-centre-cubic lattice might simplify the analysis. The homogenisation of the debris bed model into a mixture was assessed, but led to serious under-estimation of the  $k_{eff}$ . Numerical investigations have revealed that using the same equivalent debris size is not always adequate, depending on the porosity of the debris bed.

The paper [7] discusses the impact of random geometries on the criticality of fuel assemblies. A random geometry generator was used to model the fragmentation of fuel assemblies. Two fuel compositions were investigated, UO<sub>2</sub> and MOX. The neutron multiplication factor and the kinetics parameters were carefully studied as a function of the fragmentation (typical debris size) of the random geometries. Three different methods to model geometries were considered, showing a difference in results despite using the same average (linear) debris size. Although the geometry investigated in this paper is too simplified (infinite 3D fuel assembly) to conclude about nuclear reactor cores, it was shown that the fragmentation may increase the neutron multiplication factor. The modelling of random geometries is required to accurately compute the criticality of debris beds, and the tools developed in this paper will prove to be useful for the thesis work.

The document [4] discusses of the simulation of criticality in debris beds. The methodology presented in this paper consists in a reactivity assessment done in a debris bed, followed by a kinetics calculation and a thermal diffusion calculation. To estimate the reactivity, multiple feedback effects are taken into account, including the moderator effect, and the Doppler ef-

fect. The feedback coefficients are pre-calculated thanks to a Monte-Carlo code. The kinetic simulation gives the nuclear power evolution as a function of time and the thermal-diffusion calculation gives the fuel debris temperature. The water radiolysis is also taken into account. A modelling of the dose generated by the fission products in the case of criticality is implemented. The dose to the workers and the public can be thus assessed. The scenario is an uncontrolled reflooding of the debris bed, with the boron insertion occurring with a given delay. The parameters are randomly selected, and a set of 1000 simulations was performed with varying parameters. The maximum worker dose reached 128 mSv. Only 0.2% of the simulations have shown worker doses or public doses higher than the safety criteria. The simulations were done on very coarse spatial meshes. Moreover, the power profile was not updated during the transient, which can introduce significant discrepancies on the reactivity assessment. Also, the reflooding of the debris bed was not calculated with a thermal-hydraulics code, thus the behaviour of water in the debris bed after a power peak could be unreliable.

The issue of criticality during the Fukushima Daiichi accident in 2011 was investigated in the paper [8]. The isotopic composition is pre-calculated by doing Monte-Carlo calculations. The core was modelled with the code MELCOR [9] (devoted to severe accidents simulation), and the evolution of the core during its meltdown was thus simulated. The obtained geometry and the composition was then used in the Monte-Carlo simulations. The injection of non-borated water (as obtained by diluting the borated water) leads to a better moderation ratio in the flooded part of the core. The main contributor to recriticality was shown to be the reflooding of the core and the melting of the control blades. The simulations suggest that the reflooding of at least 37.1 cm of a vertical part of intact fuel without control blades might lead to criticality. This simulation was done in severe accident conditions, but the nuclear power was not modelled in the case of criticality. The generation of nuclear power may have induced the vaporisation of water, leading to a decreases of reactivity.

Paper [10] discusses the capabilities of the code MC3D to model the water/steam flow and heating into debris beds. The porous medium modelling demands devoted simulation tools as the flow behaviour is highly peculiar in such media. The cooling of debris bed is complex: the heat generates steam within the debris, and in the case of top reflooding this steam will flow in counter-flow against the liquid water. Previously developed friction models (Ergun [11], Schulenberg [12]) were implemented in the code MC3D. The PEARL experiments [13] that concern two-phases flow in debris bed were simulated, and the steam generation results show a good agreements with the measurements. The top reflooding of a hot debris beds experiment was also simulated, illustrating the capabilities of MC3D to model diphasic flows in debris beds.

## Objectives

The objective of this thesis is to develop a general methodology coupling thermal-hydraulics and neutron transport in debris beds to assess the risk of re-criticality and the fission energy release during and after a severe nuclear accident. A first objective of this work is to identify the key-parameters of corium debris and cooling configurations useful for re-criticality assessment and the range of variation of these key parameters. Fuel debris bed are porous media, thus water and steam flow depend on different physical quantities such as the porosity or the permeability of the debris bed [14]. To extract heat from debris bed, the coolant may reach a diphasic state (liquid/gas) because of the difficulty of cooling the medium. The pres-

ence or absence of liquid water would strongly influence the re-criticality in the fuel debris bed [4] That is why properly describing the thermal-hydraulics into the fuel debris bed is also a crucial objective. In certain conditions the fuel debris bed may become critical, and in this case additional physics models are needed to simulate the evolution of nuclear power. Power transients are simulated using numerical tools coupling neutronics and thermal-hydraulics with a balance of time/precision tilting in the direction of precision. The reliability of the simulation must be high enough to give accurate estimates for the released energy in the case of re-criticality. For these reasons, special attention has to be given to the domain of validity of the coupled simulations, which is another objective of this work. To fulfil these objectives, the following steps will be taken:

- establish a physical description of corium debris beds in neutronics;
- simulate two-phase thermal-hydraulics in porous media;
- characterize physical parameters necessary for re-criticality assessment;
- develop a methodology to estimate the risk of re-criticality;
- develop a methodology to estimate the released energy ;
- propose a first approach to assess the mechanical loading.

## **Plan of this thesis**

The first chapter will be devoted to the description of the key parameters and physical laws for the ex-vessel debris bed configurations formed in the case of severe accidents and needed for re-criticality modelling. The phenomenology of a severe accident will be explained, then the phenomena appearing in critical debris beds such as neutron interactions with matter and the behaviour of the diphasic flow in debris beds during cooling are presented.

The second chapter will focus on the thermal-hydraulics and neutronics modelling. First, the simulation models to study the cooling of porous media will be described, then the neutronics tools to generate random geometries and to simulate fuel debris bed re-criticality are presented. Finally, surrogate models allowing fast regression, will be described.

The third chapter will describe the test cases, then the methodology to assess the debris bed criticality will be explained together with the solutions which will be selected. Eventually an analysis of the validity domain will be presented, with an investigation of the debris distribution size with simplified models.

The fourth chapter will illustrate the multi-physics model capacity on generic debris bed configurations. Two investigations will be applied on the generic test cases as a benchmark. The first case will show the impact of decay heat generated in the debris bed to assess re-criticality risk. The second case will describe the effect of total mass coupled with decay heat on re-criticality.

The fifth chapter will discuss the neutron transport and thermal-hydraulics coupling tools, taking into account the nuclear power. Its implementation will require some approximations and the whole coupling flow will be carefully presented. The behaviour of the generic test case will be assessed and the source term to estimate the consequences will be obtained.

The last chapter will be devoted to the estimation of the consequences of a power transient. The source term obtained in the previous chapter will be analysed, then a simulation is done to assess the potential mechanical consequences. Finally, the mechanical impulsion will be analysed to conclude about the structure damage that can be foreseen.

## Published material

Part of the material presented in this thesis has been published in the following proceedings of international conferences:

- P. Boulard, J.C. Jaboulay, J.M. Martinez & A. Zoia *Simulation of transients in fuel-water mixtures*, Proceedings of ICAPP, Juan-les-pins, France, May 12-15 (2019).
- P. Boulard, C. Larmier, J.C. Jaboulay, A. Zoia & J.M. Martinez *Neutron Multiplication in Fuel-Water Random Media*, Proceedings of ICNC, Paris, France, September 15-20 (2019).
- P. Boulard, J.C. Jaboulay, J.M. Martinez & A. Zoia *Contribution of thermal-hydraulics simulation to criticality analysis of a debris bed numerical mock-up*, Proceedings of PHYSOR, Cambridge, United Kingdom, 30 March 2 April (2020).

# Bibliography

- [1] IAEA, “PRIS - home,” 2020. <https://pris.iaea.org/pris/>.
- [2] B. R. Sehgal, ed., *Nuclear Safety in Light Water Reactors Severe Accident Phenomenology*. Boston: Academic Press, 2012.
- [3] B. Tarride, *Physique, fonctionnement et sûreté des REP Maîtrise des situations accidentelles du système réacteur*. Génie Atomique, EDP Sciences, 2013.
- [4] R. Kimura and T. Yutaka, “Development of analysis code PORCAS-f for dynamic behavior of re-critical fuel debris,” *ICAPP Proceedings*, 2017.
- [5] *The Fukushima Daiichi Accident*. Non-serial Publications, Vienna: International Atomic Energy Agency, 2015.
- [6] M. F. López, M. Buck, and J. Starflinger, “Neutronic modeling of debris beds for a criticality evaluation,” *Annals of Nuclear Energy*, vol. 130, pp. 164 – 172, 2019.
- [7] C. Larmier, A. Zoia, F. Malvagi, E. Dumonteil, and A. Mazzolo, “Neutron multiplication in random media: Reactivity and kinetics parameters,” *Annals of Nuclear Energy*, vol. 111, pp. 391–406, 2018.
- [8] P. Darnowski, K. Potapczyk, and K. Świrski, “Investigation of the recriticality potential during reflooding phase of fukushima daiichi unit-3 accident,” *Annals of Nuclear Energy*, vol. 99, pp. 495–509, 2017.
- [9] B. J. Merrill, “Recent updates to the melcor 1.8.2 code for iter applications,” 2007.
- [10] B. Raverdy, R. Meignen, L. Piar, S. Picchi, and T. Janin, “Capabilities of mc3d to investigate the coolability of corium debris beds,” *Nuclear Engineering and Design*, vol. 319, pp. 48 – 60, 2017.
- [11] S. Ergun, “Fluid flow through packed columns,” *Chemical Engineering Progress*, vol. 48, pp. 89–97, 1952.
- [12] T. Schulenberg and U. Müller, “An improved model for two-phase flow through beds of coarse particles,” *International Journal of Multiphase Flow*, vol. 13, no. 1, pp. 87–97, 1987.
- [13] N. Chikhi and F. Fichot, “Experimental and theoretical study of large scale debris bed reflood in the pearl facility,” *Nuclear Engineering and Design*, vol. 312, pp. 48 – 58, 2017.
- [14] E. Takasuo, “Coolability of porous core debris beds effects of bed geometry and multidimensional flooding.” PhD thesis’.

## **Part A**

# **Context and models for critical debris beds**





# Chapter I

## Overview of critical debris beds

### Contents

---

<b>I.1</b>	<b>A survey of severe accidents and debris beds</b>	<b>10</b>
I.1.1	International nuclear event scale (INES)	10
I.1.2	TMI-2	11
I.1.3	Chernobyl	13
I.1.4	Fukushima-Daiichi	15
<b>I.2</b>	<b>Phenomenology of debris bed formation</b>	<b>18</b>
I.2.1	Decay heat	18
I.2.2	Melting of the core	20
I.2.3	Relocation at the bottom of the pressure vessel	20
I.2.4	Fuel Coolant Interaction and steam Explosion	21
I.2.5	Molten Core Concrete Interaction	23
<b>I.3</b>	<b>Criticality in debris bed</b>	<b>25</b>
I.3.1	Fundamentals of criticality	25
I.3.2	Neutron physics overview	26
I.3.3	Feedback mechanisms	27
I.3.4	Neutron kinetics	28
I.3.5	Criticality of debris beds	29
I.3.6	Experiments concerning criticality of debris beds	30
<b>I.4</b>	<b>Cooling debris bed in diphasic conditions</b>	<b>32</b>
I.4.1	Challenges related to the cooling of debris beds	32
I.4.2	Diphasic flows through a porous medium	32
I.4.3	Dryout heat flux characterization	34
<b>I.5</b>	<b>Synthesis</b>	<b>36</b>
	<b>Bibliography</b>	<b>37</b>

---

## Introduction

A severe nuclear accident is a sequence of events resulting in damage to a nuclear facility, which can lead to the release of radio-nuclides in the environment and have consequences to the public [1]. The TMI-2, Chernobyl, and Fukushima accidents led to an increased attention on the phenomena occurring in severe accidents and how to properly model these events. Although severe accidents are unlikely events, an important effort was done to deepen the knowledge about all the physical mechanism related to severe accidents [2]. As a part of these efforts, in this document we will focus on uncontrolled criticality events that could occur during and after the accident. A particular attention is paid to debris bed configurations. Assuming a severe accident in progress, the molten core may take the shape of a debris bed. Debris beds are an unusual form of nuclear fuel, resulting from a serious degradation of its original shape and material composition. Debris were observed in the past during severe accidents as well as during controlled experiments [3].

In this chapter, we present an overview of three major severe accidents and discuss the accident sequence and the criticality issues. Then, we present with the phenomena occurring during a severe accident and possibly leading to a debris bed formation. We address the notion of criticality of fission chains, which is required to understand the phenomena sustaining and hindering neutron multiplication in fissile media and the typical time scale of the effects. We finally discuss the thermal-hydraulics effect that might contribute to cool a debris bed generating heat, highlighting the complexity of the coolant flow through the debris.

### I.1 A survey of severe accidents and debris beds

This section is devoted to a short survey of severe accidents that have led to the creation of fuel debris beds and/or to an extensive degradation of the fuel. During such accidents, the status of the core and the consequences have been extremely difficult to address and mitigate.

#### I.1.1 International nuclear event scale (INES)

The international nuclear and radiological event scale (INES) was created in 1990 [1] by the international atomic energy agency (IAEA). This scale was first used to characterize abnormal events in power plants but the scale has been extended to every nuclear facility. The aim of the INES is to inform the general public quickly and in a coherent way on the severity of an accident involving radioactive materials [1].

The events are classified in 7 levels: from the level 1 to 3 the events are characterized as incidents; from 4 to 7 the events are characterized as accidents. The level 0 corresponds to events without impact on the safety of the facilities. The scale is illustrated in the figure I.1. The events are considered according to three aspects: impact on people and the environment, impact on radiological barriers, and impact on in-depth defense.

Criteria are defined for the three kinds of consequences [1] and the country where the event occurs may have a committee of experts who will give a rating of the event in accordance with the criteria established by the IAEA [1].

The scale should be used only for civilian activities and security events as malicious actions or terrorism do not belong to its scope. The events are rated after the consequences that have or may have occurred and the emergency response actions taken do not belong to the criteria for the INES evaluation. Two events were classified as level 7 accident on the INES scale (as of 2020), as detailed in the following sections.

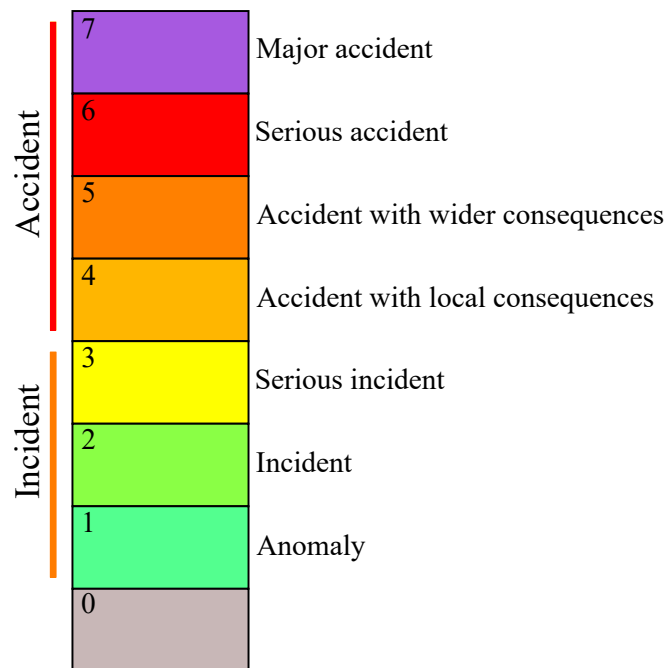


Figure I.1: Diagram of the INES scale, taken from [1].

### I.1.2 TMI-2

The TMI-2 severe accident happened in 1979 at the *"Three-Mile Island"* nuclear power plant located in Pennsylvania in the United States of America [4]. The following description is mainly taken from references [5] and [6]. This accident was classified as an event of level 5 on the INES scale.

#### The accident

TMI-2 was a pressurised water reactor using light water. On 28th March 1979, during normal operation, a minor event happened: the pumps supplying water to the steam generator stopped and an emergency stop was triggered in the core. In order to follow the progress of the severe accident and the actions done by the operators to control the progression, this time is conventionally defined as time 0 *h*. Without supply of water, the steam generators were quickly dried out and this led the primary circuit temperature and the primary pressure to increase. When the primary pressure went up, a discharge valve in the primary pressurizer opened to maintain the proper pressure in the primary circuit. However, the valve was mechanically blocked in the open position and the primary circuit was therefore subject to a steam leak.

The leak in the primary circuit decreased the pressure quickly and triggered the safety injection of water. However, the operators seeing the liquid level increasing in the pressuriser although that the safety injection of water was not needed: they stopped the safety injection and then the primary circuit pumps (vibrations in the pumps were created by the mixture of liquid and steam in the circuit). This action led to the dry-out of the top part of the nuclear core 1 *h* 40 after the beginning of the accident [5]. Yet, the nuclear core must be always cooled even when the power generation is halted. The dry-out of the nuclear core pushed the fuel temperature to reach the melting temperature due to the decay heat and oxidation of the cladding. The fuel rods started to melt at 2 *h* 10 [6] [5] and most of the upper part of the core collapsed. In some parts of the core the melting materials formed a kind of lava,

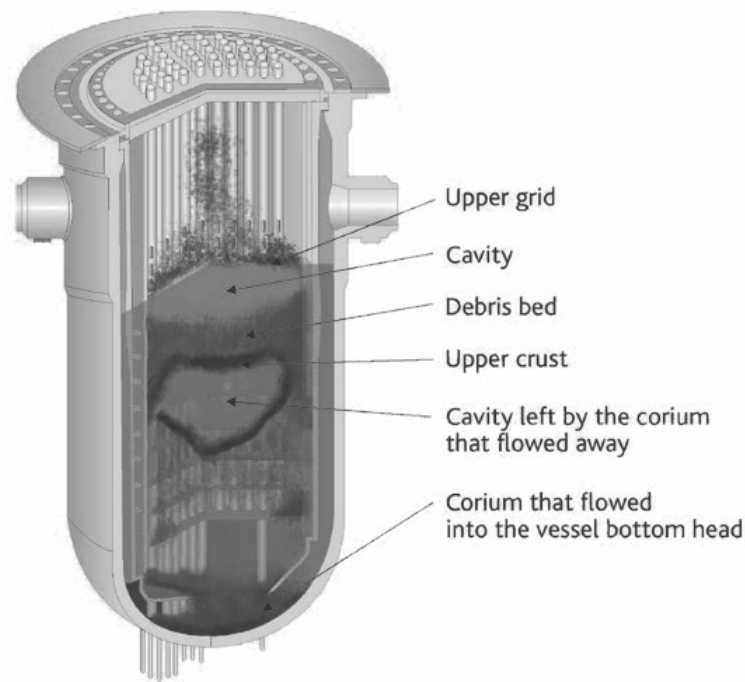


Figure I.2: TMI-2 final state, taken from [6].

the so-called corium, which is a complex and aggressive mixture composed of nuclear fuel and different elements present in the vessel (stainless steel, control rods). The corium finally flowed ( $\approx 20$  t) around the lower part of the core to attain the pressure vessel bottom. When the operators detected the steam leak, they closed a serial valve of the pressuriser and then restarted one of the primary coolant pump at 2 h 50 to stop the progress of the accident. The cold coolant met the hot lava, a violent interaction happened, which fragmented a fraction of the corium and solidified a part of it into a debris bed. This caused a pressure surge in the primary circuit. Eventually, the safety injection system was put back on service and the cooling of the core was recovered.

### Post accident analysis

The decommissioning of the damaged core took years, from 1979 to 1993 [5]. The size of the debris was measured in the range of mm to cm. The examinations at laboratory shown that the debris in the upper-core debris bed were fractured in fuel pellets and oxidized cladding. Moreover the density of an average debris was  $9000 \text{ kg/m}^3$ . Using the obtained density, the porosity was estimated to be equals to 54% [7] [8]. Numerous investigations showed that 80% of the bulk debris was larger than 1 mm. There were two layers in the debris bed, the lower one contained more small particles and at a density of  $5200 \text{ kg/m}^3$ . The top one had a density of  $3600 \text{ kg/m}^3$  [7]. Most of the particles reached 2800 K and a small quantity exceeded 3000 K. The debris bed in the core was homogeneous at a macroscopic scale but heterogeneous at the microscopic scale. Analysis of the debris have highlighted that there had been a significant interaction between the fuel assemblies, grids, and steel structures. Another conclusion was the absence of component Ag-Zr in the debris bed (the Ag component comes from the control rods). The average porosity of the debris samples in the the vessel bottom head was measured to be around  $18\% \pm 11\%$  [9] and the average density was  $8400 \pm 600 \text{ kg/m}^3$ . The criticality of the molten core configuration was assessed to ensure safety during the recovery

and clean-up operations [10]. Estimating the melting of the control rods, the reactor core was maintained in shutdown state with between 3000 and 4000 ppm of boron concentration in the coolant (boron is a strong neutron absorber). During the defueling operation of the core, the minimum boron concentration was increased to 4350 ppm to keep at least 1 percent of margin based on the criticality analyses. No critical events were observed during the TMI-2 defueling and dismantling operations. Moreover, studies in 1993 showed that there was no potential criticality risk during accident and normal conditions at TMI-2 [10].

This was the first known severe accident in a nuclear light-water reactor power plant. The containment building played a fundamental role and thus prevented large radioactive nuclide releases in the atmosphere. Moreover, no critical accident happened during the accident or the dismantling operation thanks to the high boron concentration in the water used during the fuel recovering and clean-up operations.

### I.1.3 Chernobyl

The following description is mainly taken from references [5], [6], and [11]. This accident was classified as an event of level 7 on the INES scale. On 26th April 1986, during a safety test of the reactor 4 of the "*Lenin*" nuclear power plant in Ukraine (100 km north from Kiev) a severe accident was triggered by a shut-down exercise conducted in bad conditions and worsened by an unsafe design of this kind of reactor [6].

#### Overview of the RBMK reactors

This nuclear reactor was a graphite nuclear reactor called RBMK (for "high-power channel-type reactor" in Russian). The reactor nominal power was 3600 MWth. Each core contained approximately 190 t of nuclear fuel with an enrichment of 2 % and fuel rods were cooled by boiling light water. The graphite was present in the core to moderate the neutrons. The RBMK core is over-moderated. Thus, the water has a role of neutron absorber material: if the generation of steam increases, the first effect will be a reactivity insertion (called a positive void effect). However, the Doppler effect is still negative and predominant at high power in normal operation.

#### The accident

During the test of the emergency reactor shut-down and turbine slowing-down power recovery, the operators proceeded to a strong decrease of the reactor power. When the power decreases a neutron poison ( $^{135}\text{Xe}$ ) is no-longer destroyed by the neutron flux, thus its concentration increases, which decreases the reactivity. This presence of neutron poison prevents the power from being raised quickly and safely (operators should wait for the decay of the Xenon). The neutron poison is destroyed by the neutron flux, which means that increasing the power would lead to the destruction of this neutron absorber and so insert positive reactivity.

Because of the Xenon transient, the power decreased too much for the test to be performed as expected. The operators tried then to increase the reactor power immediately by lifting most of the control rods (beyond the safety margin). Eventually, the nuclear power went up, which destroyed the neutron poison. Thus, the increase of power led to insertion of reactivity and thus to a more steep increase of power and the generation steam increased as well. The positive void effect of the core inserted more reactivity and the system became prompt-critical, leading to a power surge. The number of fissions was so high in such a short time that the core exploded (the fuel melted and a steam explosion occurred in the core), blasting the reactor building. The explosion released a great amount of radioactive nuclides

in the environment and the debris of the destroyed core itself were projected towards the atmosphere.

The severe accident was triggered by what is called a "prompt critical power transient", which generated enough heat to create huge mechanical consequences. Simulations performed during the analysis of the accident found a value of deposited energy of 190 GJ in a few seconds and a maximum power of 550 GW [12]: these values are extremely high and consistent with the observed consequences. This event illustrates the potential consequences of a prompt critical accident: it led to the highest evaluated release of radioactive materials in the atmosphere ( $14 \times 10^{18}$  Bq) [13].

### **Post-accident concerns about criticality**

After the accident and during approximately 10 days, helicopters flew over the reactor to drop more than 5000 t [14] of a mixture of lead, sand, dolomite, marble powder, and boron. The goal was to extinguish the fire in the reactor shaft. The boron was needed because graphite and fuel were still present in the severely damaged core. Graphite is a neutron moderator and the geometry was unknown inside the burning and melting core, therefore nothing could ensure that super-criticality would not be reached. This risk justified the drop of boron on the core. It is estimated that 96 % of the fuel (depleted and new) in the reactor remained inside it with an uncertain configuration [11].

In November 1986 the reactor shelter building was completed [14]. This structure, called the "Sarcophagus", played a role of a temporary containment building. However, leaks appeared in the roof and raining water flowed in the building. The criticality risk has been monitored inside the reactor building since the accident. One event of neutron population surge was measured in 1990: the neutron flux remained non-negligible (60 times the usual measurement) for several days. Eventually the scientific surveillance team decided to pour a gadolinium solution in the area where criticality appeared, stopping the reaction. Another neutron burst was detected in 1996 [11]. The fact that both burst stabilized themselves suggests that the system was still sub-critical and that negative feedback reactions occurred in the reaction [15].

The very high doses of radiation prevent easy recognition of the real core status. Studies were conducted to estimate the possibility of criticality accident [11]. It was shown that at least 60 t of fuel containing material in form of solidified corium and core fragments are present in the core shaft. In the lower part of the building, it is assumed that approximately 3000 m<sup>3</sup> of water are present, which brought the question of over-moderation (and thus positive feedback) of the fuel [15].

The Chernobyl accident has emphasized different aspects of criticality accidents (as in the core itself). The dropping of boron during the first phase of the battle to stop the diffusion of radioactive material addressed the criticality risk. In the post-accident phase, criticality may have been reached in the past and it will be an issue for the decommissioning operations in the future.

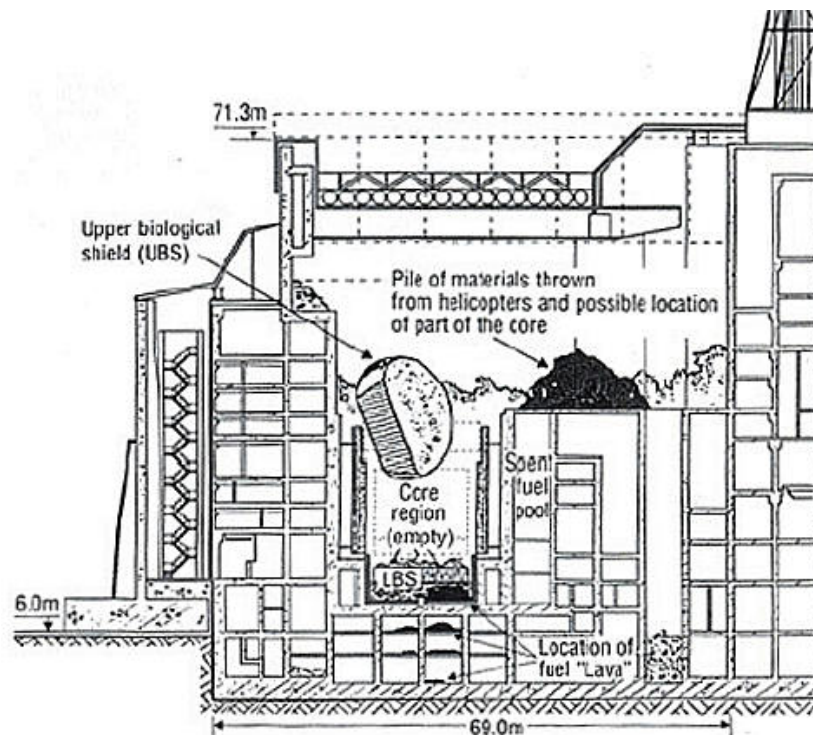


Figure I.3: Chernobyl reactor post-accident state after the construction of the first shelter building, taken from [2].

### I.1.4 Fukushima-Daiichi

The following description is mainly taken from references [16] and [17]. This accident was classified as an event of level 7 on the INES scale. On 11th March 2011 at 14 h 46 the Tohoku-Chihou-Taiheiyo-Oki earthquake occurred (9.0 on the Richter magnitude scale) at 70 km from the Japanese eastern-coast [16]. On the eastern coast (100 km from Sendai city) is situated the nuclear power plant Fukushima-Daiichi. This power plant is composed of 6 nuclear reactor units. All the units are boiling water reactors (BWR).

#### The accident

Immediately after the earthquake detection at the power plant, the control rods (made of boron carbide) were inserted into each active core (unit 1, 2, and 3 were operated in normal conditions at that time) to stop the chain reaction and thus the heat generation. The earthquake wave did not damage the nuclear power plant, which was designed to endure this kind of accelerations.

However, the earth-quake was powerful enough to create a tsunami, which ran in the Pacific ocean. The tsunami wave was the most powerful on the eastern Japanese coast. Here, the waves destroyed most of the weak buildings at low altitude in the hit area. The power plant seawall was not high enough in front of the incoming wave (only 5 m compared to 10 – 15 m of the reported wave at the site) and thus the nuclear power plant of Fukushima Daiichi was also flooded by the tsunami [16] [6].

The power-lines of the power plant were destroyed and the only on-site energy source were Diesel generators located in the basement of the power plant building as described in figure I.4. When the basements were totally flooded by the tsunami, the power plant lost its last energy source and thus the cooling system of the cores. A nuclear reactor core must be



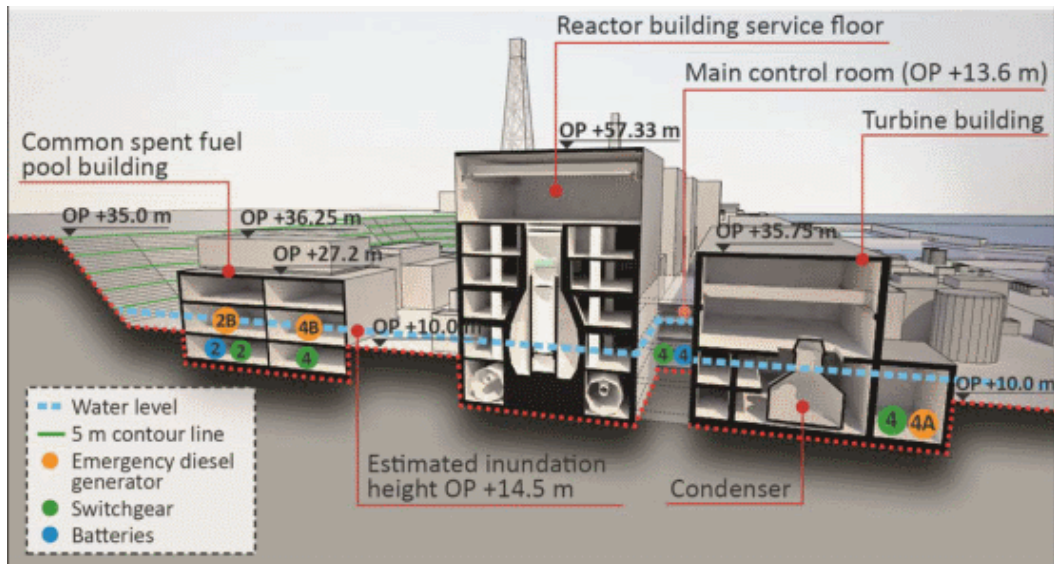


Figure I.4: Locations of crucial structures and components and indication of flooding level at the Fukushima Daiichi nuclear power plant, taken from [17].

cooled even if no chain reactions occurs because of the heat generated by radioactive fission products. Three nuclear cores underwent meltdown in the power plant: the events which led to the meltdown for each nuclear core are not described and only a general explanation is given here. Extensive details can be found in the IAEA report [17].

When the tsunami wave hit the power plant, several reactors lost their cooling system. Without cooling, the pressure started to increase in the pressure vessel as the water started to boil. The upper part of core was dried out, which means that the melting of fuel materials would start soon. The oxidation of the cladding, which is an exothermic reaction activated by high temperature, started to create hydrogen gas in the pressure vessel. The high hydrogen concentration brought favourable conditions to have an hydrogen explosion in the reactor building. The corium was relocated on the bottom of the pressure vessel. The relocation of the molten fuel occurred differently in the three units. Indeed, the melting-down of the fuel and the cooling with water had started at different times for each unit. In every case, the contact of the injected cold water with the hot molten material led to violent interactions and the solidification of the molten fuel lead to a partial fragmentation. All cores (molten or severely degraded) were cooled 72 *h* after the beginning of the accident.

The summary of the progress in each nuclear reactor is the following: in unit 1, the core melted, flowed on the pressure vessel floor, pierced the pressure vessel and then started to erode the concrete basement until cooling water was injected; in unit 2 the core melted, flowed on the pressure vessel and started to melt it but cooling water was injected soon enough to prevent the flow of the entire molten fuel on the concrete beneath; in unit 3 the core melted, flowed on the pressure vessel and finally cooling water was injected, halting the progress of the accident.

This accident illustrates that fuel debris bed can be created during severe accidents. During the severe accident progress it might be hard for the operators to know and to evaluate the exact state of the damaged reactor. Mitigation actions can be engaged, such as injecting sea water to prevent the failure of the containment, which could create favourable conditions to have criticality in the fuel debris created during the accident. The radioactive releases have been estimated to be one tenth of the Chernobyl releases [17].



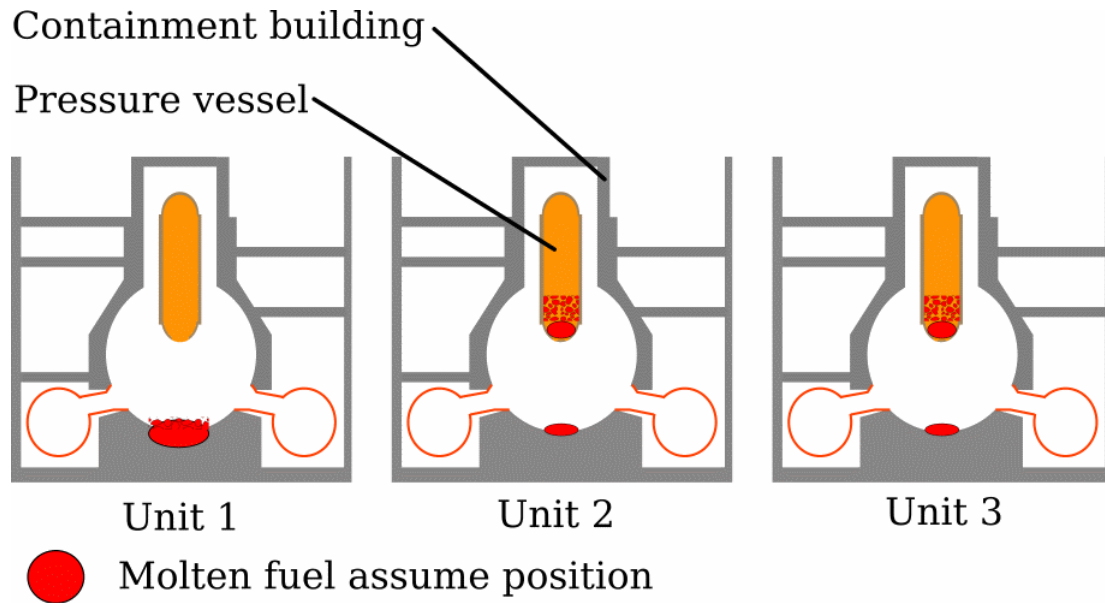


Figure I.5: Contemplated configurations for the corium state in the Fukushima Daiichi unit 1, 2, and 3, based on [17].

### Post-accident concerns about criticality

No critical accidents were detected during the progress of the accident: recent publications [18] explained that fission products concentration is monitored to detect critical events. If a critical event was detected, borated water (boron is a strong neutron absorber) would be injected. The state of the molten core is not precisely known. The fuel debris bed shape and location have not been established with precision. Robots were sent in the most dangerous areas to assess the state of the molten core. The picture in figure I.6 was taken by one of these robots in the pressure vessel of the unit 2 below the normal height of the control rods housing [19]. The investigations made thanks to radiation-resistant robots showed that a debris bed was formed over the pressure vessel bottom, which might be 40 – 50 cm thick [19]. Works were done to estimate the potential consequences of reflooding the fuel debris bed and reaching favourable conditions for criticality [18]. These works have shown that the probability of having serious consequences is limited (only 0.2% of chance to exceed the emergency dose > 100 mSv and the most powerful pulse would be 17 MW). The critical accident is now carefully studied, because a critical accident would stop decommissioning operations and have radiological consequences on the workers and the public.



Figure I.6: Picture of the solidified molten core taken in early 2019 in the unit 2 pressure vessel, taken from [19].

## I.2 Phenomenology of debris bed formation

Fuel debris beds can be created when a part of the nuclear reactor is degraded. This degradation of the core starts when the core is dried out. The progress of the accidents will directly affect the formation of the debris bed. Indeed, in the scenario of debris beds generation the main factor is the time when the cooling water is injected. In this section the phenomenology leading to the creation of fuel debris beds is briefly described, with reference to the configurations and conditions that would be typically met in a PWR, starting from an operating condition corresponding to full power.

### I.2.1 Decay heat

When a fission occurs, neutrons are emitted and the nucleus is split into fission products. Many fission products are unstable and thus will be subject to a radioactive decay (most are  $\beta^-$  decays). The fission fragments are located inside the fuel rods. Thus, after the shutdown of the reactor, alpha, beta- and gamma radiation is emitted by fission products: during the transport of these rays through the fuel, their kinetic energy is converted into heat, called decay heat. This heat is non-negligible and requires by design to cool the core after the shutdown (1 h after shutdown the heat generated is still larger than 1 % of the nominal core power [20]). If an accident occurs in the power plant, the chain reaction is immediately stopped after the insertion of neutron absorber rods. However, the decay heat will be generated for a long period of time. As seen in I.1, the difficulty to manage the decay heat can lead to severe accident conditions with melting of the nuclear fuel. As the decay heat is generated by radioactive decay, it will decrease with time (determined by the half-life of the fission products) and it depends on the quantity of fission products in the core at the shutdown.

To properly model the decay heat a correct knowledge of the nuclides involved is required. As the fission products vary in a broad range and depend on the fuel composition and power history (known as the burn-up of the nuclear fuel), most models created in the past are based on empirical observations. Two models are mentioned in the following.

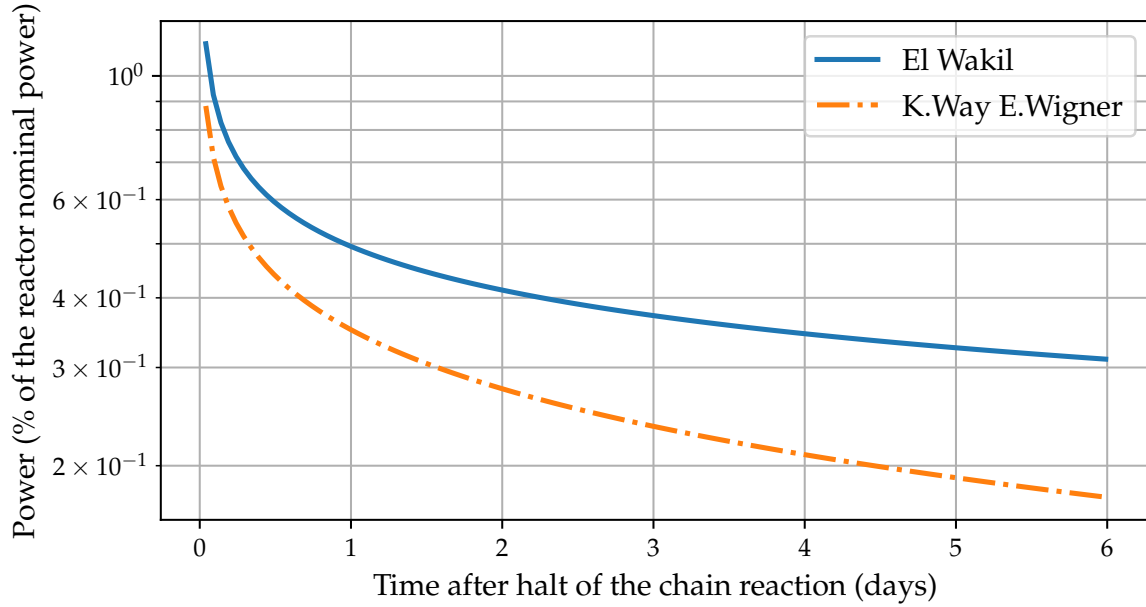


Figure I.7: Modelling of the decay heat in nuclear reactor.

$$P_{decay} = 5.9 \times 10^{-3} \times P_0 [t^{-0.2} - (t + T)^{-0.2}] \quad (I.1)$$

The first one was proposed by K. Way and E. Wigner in 1948 [21]. This formula is written in equation I.1. The  $P_0$  is the nominal power in Watt,  $t$  is the time after shutdown and the  $T$  is the irradiation time of the fuel. This equation is considered to correctly yield the order of magnitude of decay heat [21].

$$P_{decay} = 0.095 \times P_0 \times t^{-0.26} \quad (I.2)$$

The second one is described in equation I.2. This equation was proposed by El Wakil in 1971 [20] and has shown good agreement applied in the range of times longer than 200 s after shutdown. In this equation  $P_0$  is the nominal power of the reactor and  $t$  is the time expressed in seconds. The fraction of nominal power of the reactor generated by decay heat predicted by the two proposed laws is illustrated in the figure I.7 (the irradiation time was taken to 90 days).

The El-Wakil equation is the one used in severe accidents studies [22] and so it was selected to be used in the thesis. These equations give rough orders of magnitude of the expected decay heat. In order to obtain more precise estimates, numerical simulations should be done with the proper compositions and reactor inventories, for instance by using: the depletion module PEPIN2 in the Darwin code [23].

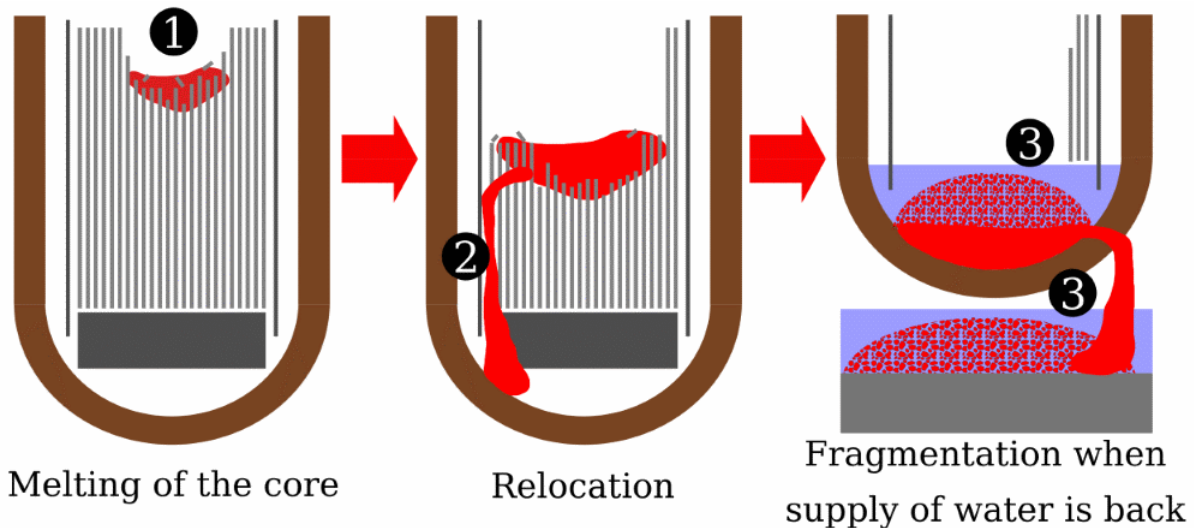


Figure I.8: Schematics of the degradation of the core in the pressure vessel which can lead to fuel debris bed formation.

### I.2.2 Melting of the core

Without cooling, the reactor core temperature will rise, which leads to the boiling of the coolant. The over-pressure in the primary circuit will trigger its depressurisation. When the fuel rods are dried out, their inner temperature will rise dramatically. As long as no cold water is injected in the dried out core, the temperature will increase.

The zirconium cladding of the fuel rods will start to balloon and burst at 1000 K [24]. The control rods (made of Ag-In-Cd) are the first materials to start melting at a temperature of 1100 K. At approximately 1300 K the cladding made of zirconium alloy may start to be oxidized releasing hydrogen and generating more heat. At 2300 – 2500 K the cladding that has not failed mechanically may lose its integrity. Around 3100 K the uranium oxide starts to melt. The figure I.9 summarizes these phenomena. If nothing is done at this stage, the upper part of the core (the first one to be dried out) will collapse, as illustrated in figure I.8, and the melting will continue. It is possible that, before the whole core is melted, a part of the liquid molten fuel will be relocated on the bottom of the pressure vessel (as happened at TMI-2 [24]). This corresponds to the phase 2 in the scheme of figure I.8.

### I.2.3 Relocation at the bottom of the pressure vessel

The molten pool of fuel and structural material is at very high temperature and could corrode the pressure vessel wall and/or melt it. If the supply of water is set on-line at this stage, the molten pool would be flooded with relatively colder water, which may stop the progress of the severe accident. However, the interaction between cold water and hot molten fuel might bring other issues that are explained in the next sub-section. If the water is still not injected in the core, the severe accident will continue its progress and the whole core would melt.

In some configurations, a metallic layer upon the molten pool may appear (by diffusion of different materials in the molten pool) [24]. This metallic layer could create a "focusing effect", where a high flux of heat would penetrate the pressure vessel wall thanks to the high thermal conductivity of the metallic material and dig a hole. Even without the focusing effect, the molten fuel may break the pressure vessel, just taking more time to erode it. In the case of pressure vessel failure, the molten fuel would flow outside the pressure vessel into the pit.

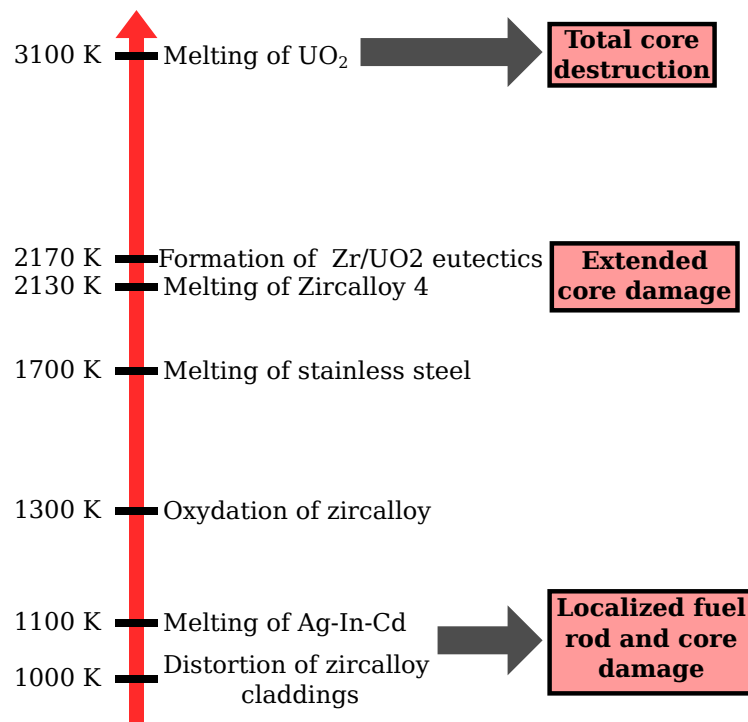


Figure I.9: Melting and reactions threshold temperatures of core material, taken from [6].

#### I.2.4 Fuel Coolant Interaction and steam Explosion

If the hot molten core material (at a temperature higher than 2800K) meets cold water, violent interactions may happen. Indeed, the molten material will be quenched and fragmented into small particles into the cold coolant. If a number of conditions are fulfilled, then the results of this transfer of heat to water would be the quick vaporization of water. Fuel - coolant interaction (FCI) is divided into four stages: premixing, triggering, propagation, expansion (explosion) [6]. As a matter of fact, the whole mixing process can escalate to a steam explosion or go just through non-violent melt quenching.

First the molten corium would penetrate the water and break into a film boiling regime. This creates a mixture of fuel, coolant and steam, which is called the premixing phase. During this phase the size of the corium debris is generally centimeter (coarse mixing) as described in figure I.10. The presence of a steam film between the corium and the water decreases the heat transfer.

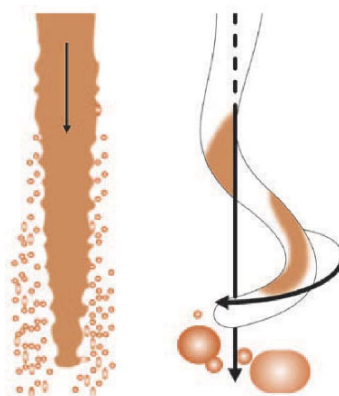


Figure I.10: Hydrodynamics instabilities creating fragmentation, taken from [24].

After a certain mass of molten material has penetrated the coolant, a trigger may initiate the next phase. This trigger may be the contact between the corium and the vessel pit floor; during experiments the trigger is artificial and comes from small shock-waves. The destabilisation of the steam film would induce a local collapse. The liquid corium is now in contact with liquid water, the heat transfer rate is higher, which induces a fine fragmentation and a rapid pressurization.

The local pressurization will be propagated and will destabilize the steam film around the origin of the trigger. Thus the pressurization would happen in the whole pre-mixing zone, inducing a higher vaporisation and more fragmentation. As the heat transfer between the corium and the coolant is now very high, the steam volume created will become non-negligible. The rapid expansion of the steam may create an overpressure wave. This is the phase of thermal explosion. The phases are illustrated in figure I.11. From the thermodynamic point of view, the FCI can be treated like a chemical detonation: it is called thermal detonation [6].

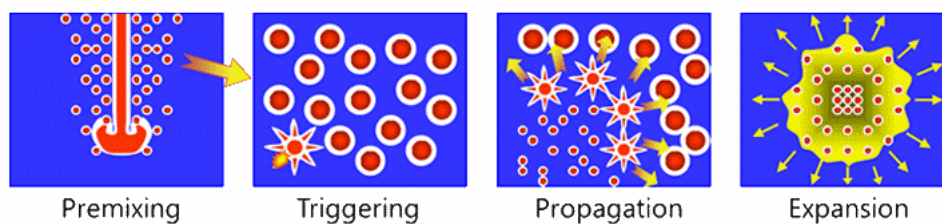


Figure I.11: Diagram of the progress of the steam explosion [25].

With favourable conditions, a steam explosion may be triggered and large amount of the molten core material would be finely fragmented by these phenomena. The two possible locations (out-vessel and in vessel) where the fragmentation would happen are described as phase 3 in the figure I.8. The steam explosion happens when liquid material with temperature difference ( $> 300$  K) creates a high heat exchange rate between the two fluids. The figure I.12 illustrates the chain phenomena which leads to the steam explosion. The corium might be partially or totally fragmented in debris of size lower than 1 cm.



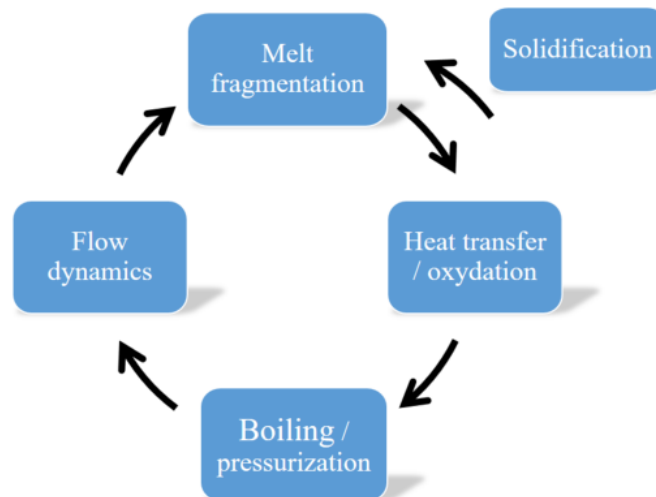


Figure I.12: Phenomena during propagation phase of the steam explosion, taken from [24].

### I.2.5 Molten Core Concrete Interaction

When the molten core is spread in the reactor vessel pit, concrete erosion will start due to the hot temperature (higher than 2000 K) [6]. The decay heat drives the molten core concrete interaction (MCCI). The corium melting temperature is around 2600 K and the degradation of the concrete starts between 1300 K and 1800 K [6]. Thus, the erosion will start as soon as the corium is in contact with the concrete. The ablation velocity has been estimated between 6 cm/h and 13 cm/h using different simulation codes [6]. If the corium is not cooled soon enough, the erosion will lead to the loss of integrity of the reactor containment building. Moreover, during the process of concrete ablation, several gases are emitted: non-condensables and hydrogen [6]. This results in a pressurization of the reactor containment building. Hence, to stop the ablation of the concrete, the decay heat must be extracted.

Among MCCI experiments the MACE experiments [26] brought knowledge about the cooling of corium pool. The MACE experiments considered the cooling of a melted pool during the MCCI by water injection on the top. The aim was to study the phenomena which occur during MCCI and top cooling of a melt pool. Four phenomena were identified to cool the corium in these conditions: the bulk cooling, water ingression, melt eruption and crust breach [26]. The repetition of crust breach during the water cooling might create small debris upon the molten pool [6] as described in figure I.14. Moreover, the melt eruption can lead to the creation of loose debris by entrainment mechanism of melt [26]. The figure I.13 shows the configuration obtained after the experiments *M3b*: two solidified crusts can be identified and some loose debris were recovered around the melt eruption. However, the amount of debris created represents a small fraction of the total melt mass as it was measured to be 16 % [26].

The MCCI is another phenomenon that may contribute to create debris beds in the case of water flooding. As the concrete ablation is a slow mechanism the generation of debris is slower with MCCI than FCI. MCCI and FCI debris will lead to significant differences in the composition and the shape of the debris.

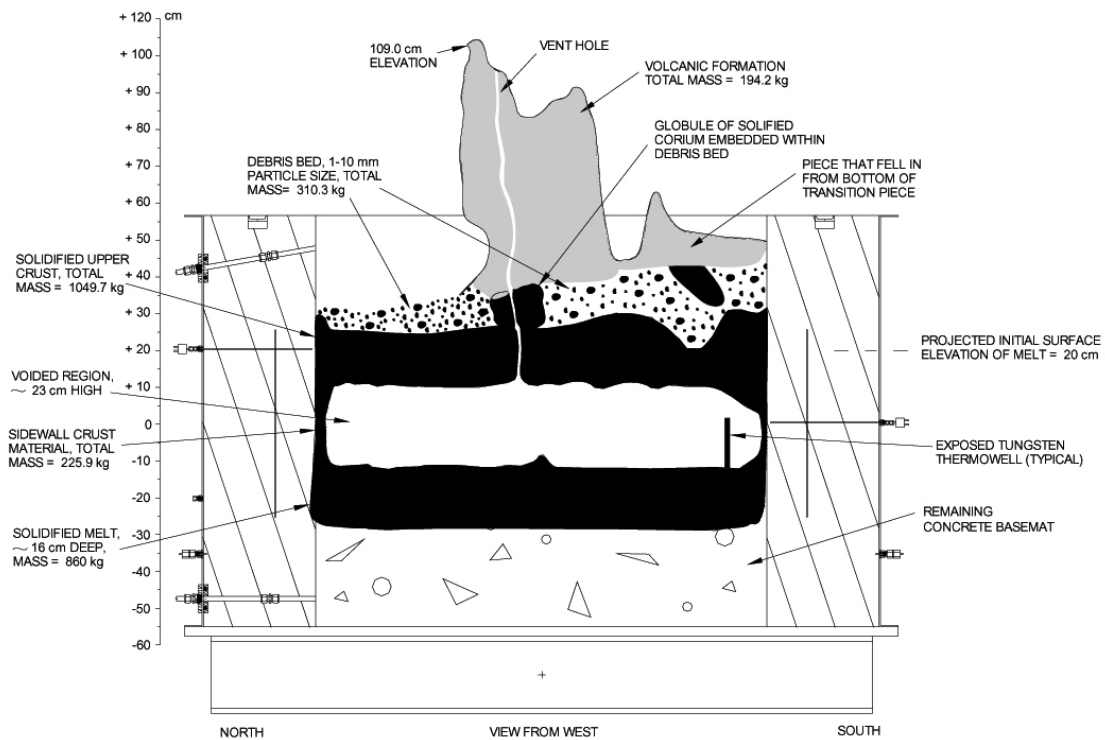


Figure I.13: Schematic of the *M3b* test of molten corium concrete interaction, taken from [26].

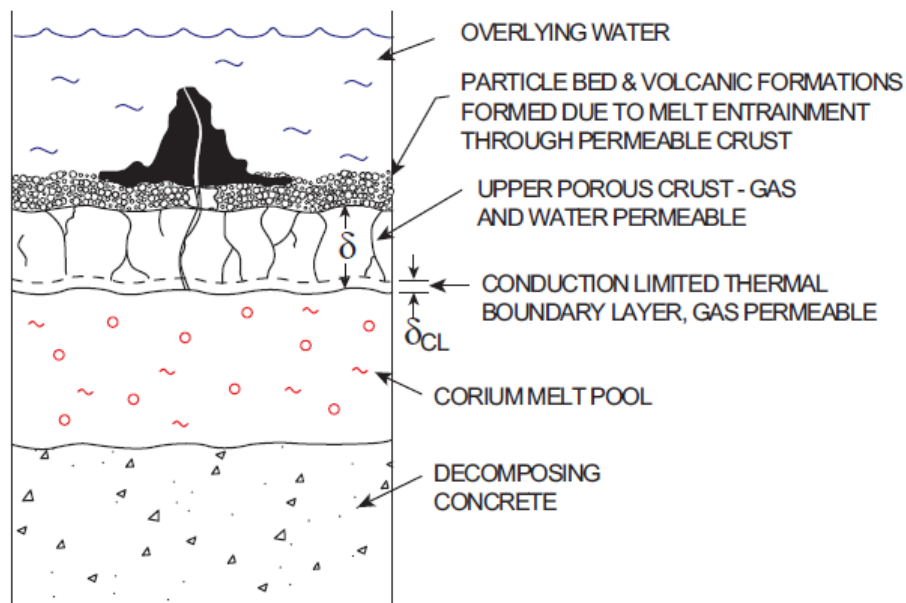


Figure I.14: Scheme of corium concrete interaction with water ingress and melt eruption mechanisms, taken from [6]



### I.3 Criticality in debris bed

Criticality is a branch of neutron physics aimed at investigating and quantifying the behaviour of neutron multiplication in fissile materials, with special emphasis on fission chains [27]. This section summarizes the physical conditions to reach the critical state, and describes the phenomena possibly leading to a super-critical system to the sub-critical and how a critical accident would progress.

#### I.3.1 Fundamentals of criticality

In a fissile system, neutrons induce fissions, which set free new neutrons, which in turn can induce new fissions, and so on; this is the chain reaction mechanism, where energy is released at each fission [21]. Figure I.15 shows the evolution of the chain reaction. Other concurrent phenomena can make neutrons disappear from the multiplying medium: leakage from the boundaries of the system, and sterile captures on absorbing nuclei. The criticality state is reached when the neutron population is stable, which means that the loss of neutrons is compensated by the creation of neutrons by fission. In a critical system the neutron population does not evolve with respect to time, which expresses the fact that a balance between the rate at which neutrons are produced and the rate at which they disappear is reached [28]. The power generated by the chain reaction is proportional to the neutron population (as more neutrons imply more fissions).

$$k_{eff} = \frac{\text{Production from fission}}{\text{Disappearance (Absorption + Leakage)}} \quad (\text{I.3})$$

$$\rho = \frac{k_{eff} - 1}{k_{eff}} \quad (\text{I.4})$$

To characterize the system, the *effective multiplication factor* (written  $k_{eff}$ ) is used as defined in equation I.3. When  $k_{eff} = 1$  the system is critical and the number of neutrons is stable; when  $k_{eff} < 1$  the system is sub-critical and the neutron population is decreasing; when  $k_{eff} > 1$  the system is super-critical the number of neutron is increasing. The key value to characterize the system criticality is the *reactivity*, written  $\rho$  defined in equation I.4. The usual way to express the reactivity is by using the pcm:  $1 \text{ pcm} = 10^{-5}$ . In the following the reactivity will be used instead of the effective multiplication factor as reactivity is more convenient in the forthcoming formulation of the kinetic equations I.5 and I.6. Another useful scalar quantity is the neutron flux, which is related to the neutron density  $n$  and the neutron velocity  $v$ , as in  $\phi = n \times v$  [29].

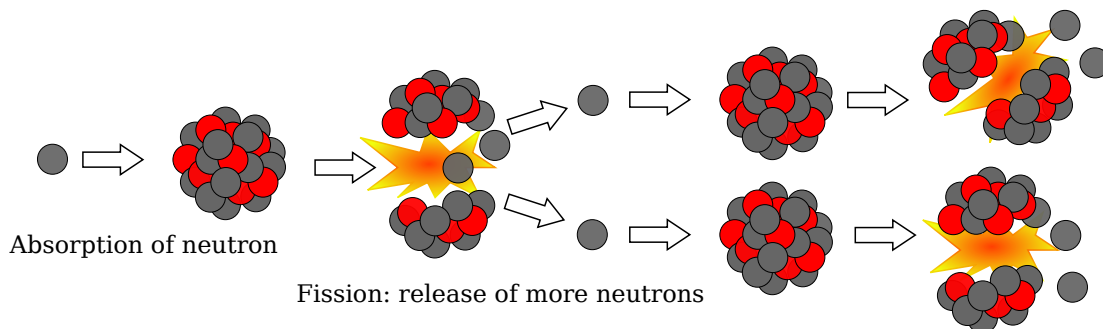


Figure I.15: Chain reaction.

### I.3.2 Neutron physics overview

The  $k_{eff}$  can be also seen as the ratio between the number of neutrons of the  $n - th$  generation and the number of neutrons of the  $(n - 1) - th$  generation [21]. Upon collision, a neutron interacts with a nuclide composing the material; many interactions exist: fission, (n,gamma) (capture with emission one or several photons), elastic or inelastic scattering, and so on. The probability of interaction of the particles with a selected nuclide, is proportional to the cross section noted  $\sigma$ . Cross sections carry the units of barns which corresponds to  $10^{-24}$  cm<sup>2</sup>. This value depends on the particle, the energy of the particle, the nuclide, (temperature) of the nuclide and the reaction.

The interactions can be separated in two classes; the absorptions (including sterile capture and fission) and the diffusions. The absorption results in the termination of the neutron history, the particle disappearing into the collided nuclide. Diffusions give rise to an exchange of energy and momentum between the neutron and the nuclide: after the collision, the neutron is still travelling but with a different energy and direction. Upon fission, the collided nuclide becomes unstable and splits into several smaller fragments (called the fission fragments), setting free a random number of neutrons. Neutrons produced by fissions are called prompt neutrons because they are emitted immediately after the fission [21]. These neutrons are emitted at high energy ( $E_{average} = 2.0$  MeV). Traditionally, the energy range of interest for nuclear reactors has been partitioned into a "thermal" range (for  $E < 0.625$  eV), an "intermediate" range ( $0.625$  eV  $< E < 1$  KeV) and a "fast" range (for  $E > 1$  keV).

A nuclide whose fission cross section is higher than its sterile capture cross section in the thermal energy range is called fissile. The nuclide <sup>235</sup>U is fissile, whereas the most abundant (99.3%) uranium isotope <sup>238</sup>U is not. Therefore, enrichment of the fuel in <sup>235</sup>U is needed in light-water reactors to sustain chain reactions [21].

A nuclide whose scattering cross section is higher than its capture cross section is called moderator; indeed, this kind of nuclides can slow down (moderate) the neutrons by exchanging energy and momentum and thus bringing the neutron from fast energies ( $> 1$  KeV) to a thermal energies ( $< 0.625$  eV), where the neutron can thus more efficiently contribute to the fission chains by inducing fission with much higher probability [21]. Figure 1.16 illustrates the neutron energy distribution in a thermal reactor; two peaks can be remarked, the first one around  $10^{-7}$  MeV is due to neutrons at thermal equilibrium with the nuclides of the medium following a Maxwellian distribution, and the second one is due to fast neutrons following the fission energy distribution (around 2 MeV). In between the peaks, the shape of the energy distribution is due to the slowing-down of neutrons from the fission energy to the thermal equilibrium.

The thermal nuclear reactor in normal conditions are designed to have a proper ratio of moderator volume on fuel volume to enable chain reactions with low enriched uranium (LEU) and enable negative feedback coefficients as described in the next section. However, this ratio could be reached in very deteriorated situations and specific configurations as it is shown in the thesis.

In thermal reactors the neutrons need to be brought to the thermal energy and light water plays the role of moderator. Without the presence of light water between fissile materials, the neutron spectrum would not be suitable to have enough fissions and thus the chain reaction may be not maintained.

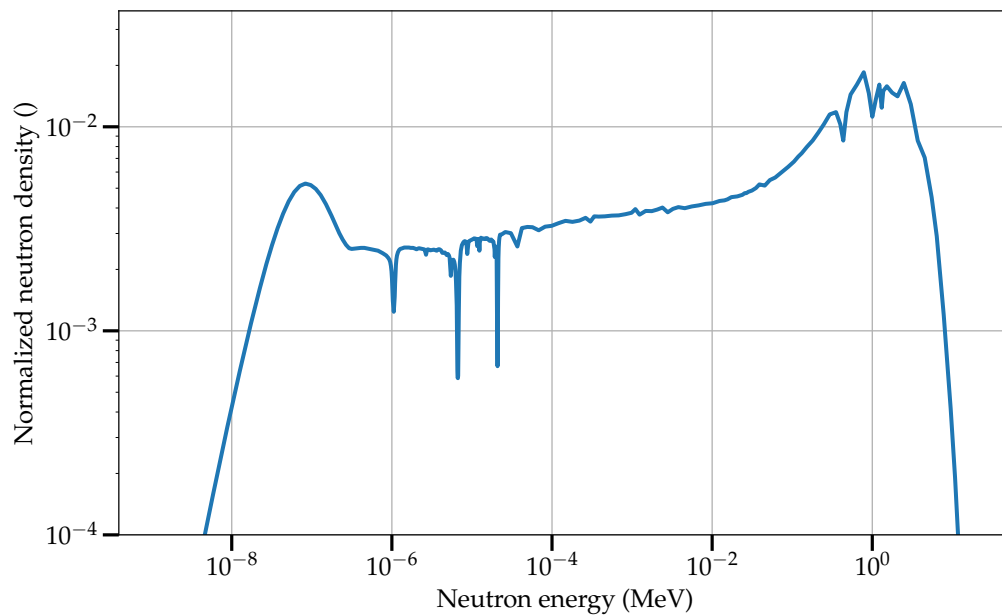


Figure I.16: Neutron energy spectrum in a thermal reactor.

### I.3.3 Feedback mechanisms

In a nuclear system, physics-induced effects should by design stabilize the neutron population and so help to decrease the reactivity when the operating conditions are not safe (for example temperature increase or loss of coolant).

#### Moderator density effect (or void effect)

A first feedback mechanism is the moderator effect, which is expected to bring negative reactivity to the system when the moderator density decreases (for example if the water heats up or boils) [21]. When the moderator density decreases, the neutron slowing-down is less efficient and so the reactivity decreases, since a smaller number of neutrons is capable of reaching the thermal energies and induce fissions. This feedback exists by design in light water reactors: indeed, the quantity of moderator in between fuel cells is chosen in such a way that if the density decreases the moderation of neutron will not be enough to sustain the chain reaction. This feedback is also called void effect because the decrease of density can be seen as an insertion of void in the moderator volume. Figure I.17 depicts the trends of moderation ratio. The optimum of moderation corresponds to the value of ratio of moderation where the maximum reactivity can be reached. By design the moderation ratio is below the optimum to ensure a negative void effect.

If the designed moderation ratio were higher, a positive effect would appear; the decrease of density would first decrease the neutrons capture, increasing the reactivity. The moderator feedback would occur after a few seconds during power excursion: this delay stems from the time to transfer the heat from the fuel (where the fission occurs) to the moderator (which is the coolant in light-water reactors).

#### Moderator temperature effect

A second feedback mechanism is the moderator temperature effect: when the moderator temperature increases, the thermal energy of the moderator nuclides increases and the en-

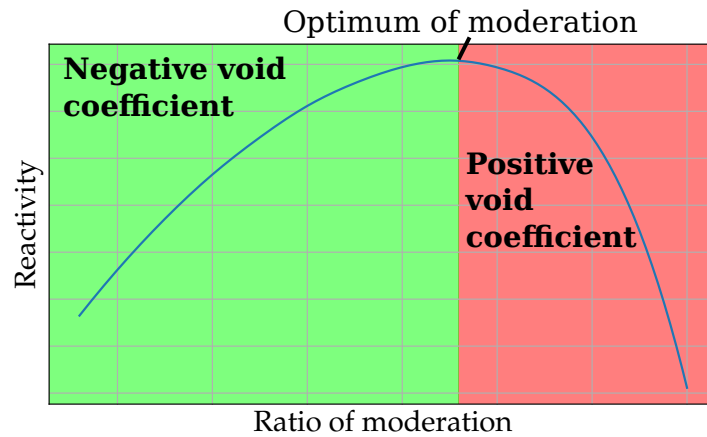


Figure I.17: Impact of the moderation ratio on reactivity and void effect.

ergy of the moderated neutrons will increase as well [21]. This small displacement of the thermal peak in the energy spectrum leads to a decrease of the fission cross section with respect to the capture cross section, and the reactivity of the system will therefore decrease.

### Doppler effect

A third feedback mechanism is the Doppler effect. If the temperature in the fuel increases (because the cooling is slowed or absent or the number of fissions increases) the cross-sections of nuclides (the  $^{238}\text{U}$  which composes > 96% of the low enrichment fuel in reactor is the main nuclide bringing this effect [27]) would be enlarged close to resonances, as illustrated in figure I.18. The enlargements of resonances will increase the neutron absorption ratio of the  $^{238}\text{U}$  and negative reactivity will therefore be inserted in the system (as long as the fuel is made of low enrichment uranium). A peculiar feature of the Doppler feedback is that its effects have an almost immediate (microseconds) action on the system reactivity, since the Doppler mechanism is localized in the fuel, which is the source of new fissions.

These feedback mechanisms help to operate safely a critical system generating power, since they all contribute to the self-stabilization of the system. For example, an increase of power would heat the fuel and the coolant water, which will insert negative reactivity and thus decreases the power. The moderator density effect is the strongest feedback in light water reactors, but in the case of fast transients the Doppler feedback would occur first [28].

### I.3.4 Neutron kinetics

Knowing whether a system is super-critical or sub-critical is not enough to determine how fast the neutron population is increasing or decreasing. In a light-water reactor, the prompt neutrons created from fission typically leave the fuel, try to escape the capture by  $U^{238}$ , then interact with moderator nuclides and are finally captured in the fuel and induce another fission. The average time between the neutron emission and the following fission is called the generation time, noted  $\Lambda$ . This time constant is close to  $2.5 \times 10^{-5}$  s in nuclear reactors using light water as moderator for example [21]. This time parameter depends on the fuel composition, moderator composition and moderator ratio.

Upon fission, the fission products are not exactly the same for each event. Some fission products (named delayed neutron precursors) will decay to lower energy states by emitting

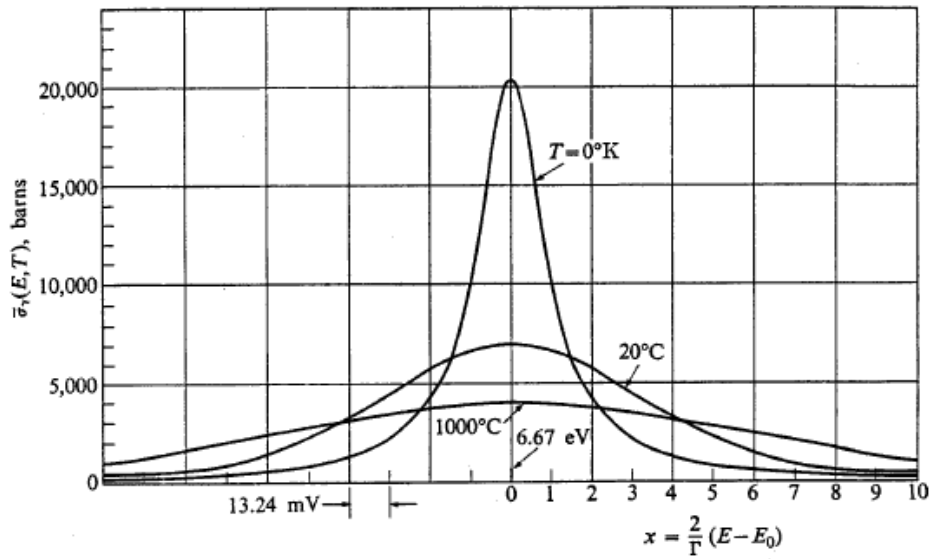


Figure I.18: Doppler broadening of one resonance at different temperatures, taken from [28].

neutrons after some time. The neutron balance within the nuclear reactor will thus benefit from these extra neutrons as their time of creation is large enough to considerably slow down the typical time evolution of the the reactor reactivity. The precursors are typically grouped into 6 or 8 "families", for which the decay times are approximately similar. The decay rate (events per second) of precursors of family  $i$  is noted  $\lambda_i$ . The sum of the precursors ratios is named  $\beta_{eff} = \sum_i \beta_i$ . The neutron kinetics is governed by the coupled equations:

$$\frac{\partial n}{\partial t} = \frac{\rho - \beta_{eff}}{\Lambda} n + \sum_{i=1}^8 \lambda_i c_i + S \quad (I.5)$$

$$\frac{\partial c_i}{\partial t} = \frac{\beta_i}{\Lambda} n - \lambda_i c_i \quad (I.6)$$

where  $n$  is the neutron population,  $\Lambda$  is the neutron generation time,  $c_i$  are the precursors  $i$  concentration and the  $\beta_i$  is the effective fraction of delayed neutron precursors produced at each fission event.  $S$  is the neutron source per unit of time inside the system.

Three regimes can be remarked:

- When  $\rho < 0$ , the system is sub-critical: the neutron population and thus the precursors concentrations will asymptotically decrease with respect to time;
- When  $\beta_{eff} > \rho > 0$ , the system is delayed-super-critical, the neutron population is increasing at a time scale which is basically governed by the precursors;
- When  $\rho > \beta_{eff}$  the system is prompt-super-critical, the neutron population will evolve with a time scale that is increasingly closer to that of the mean generation time, much faster than the typical time scale of the precursors.

Nuclear reactors are operated in the region where  $\rho \ll \beta$  for positive power excursions, so that the reactivity evolution is slow and the reactor control is much easier.

### I.3.5 Criticality of debris beds

Regarding criticality, the debris have a geometry close to the intact nuclear fuel pellets: indeed the size of the debris ( $< 1$  cm) is smaller or equal to the fuel pellet height and diameter

( $\approx 1$  cm). This may help to reach criticality. However, as the fissile material in corium comes from low-enriched uranium fuel, a moderator is required to have criticality. As explained in I.3.3, an optimal ratio of moderation exists. In intact fuel, the target value is obtained by design. In the case of debris bed, the porosity of the debris bed might drive the criticality, when the void between debris is filled by a moderator. The moderator will be the water supplied to cool the corium. The assumptions to have a critical debris bed are :

- Same typical size as intact fuel pellets;
- Presence of liquid water with low boron concentration;
- Value of porosity high enough.

If all these conditions are met, the debris bed might be critical in an infinite medium, i.e. without any neutrons leakage. The corium mass is finite, so that in practice more conditions must be added: the total mass and the geometry must ensure that the neutron leakage is small enough.

### I.3.6 Experiments concerning criticality of debris beds

A debris bed can be described by a porous disordered material. It may be characterized by a debris size distribution, debris composition and a porosity. Thus, after the accident at the Fukushima power plant, it was planned by JAEA (Japan Atomic Energy Agency) to conduct experiments to address the behaviour of the molten-core-concrete-interaction debris bed from the standpoint of neutron transport and multiplication. This experiment would be done in STACY (STatic experimental Critical facilityY), which is a small research reactor. As of early 2020, the system STACY is under planning for modification [30]. However, pre-calculations were done to estimate the potential results of the characterization of fuel debris [30].

STACY is an experimental core devoted to critical analysis. It is planned to be used in two different configurations to study fuel debris criticality: over-moderated and under-moderated. The criticality would be assessed as a function of the water height in the system. Three parameters should be studied: the  $^{235}\text{U}$  enrichment (on 3, 4, 5 wt%), the concrete volume fraction (in the range 0, 20, 40, 60, 80%) and the porosity (in the range 0, 20, 40, 60, 80%). The test section is surrounded by fuel rods with 5wt% enrichment, as illustrated in figure I.20. Special patterns in the testing volume of the core were selected, as shown in figure I.19.

Monte Carlo simulations using MCNP [31] were done with the JENDL-4.0 library [32]. The figure I.21 shows the relation between the  $k_{eff}$  and the water height, revealing that criticality is possible ( $k_{eff} > 1$ ). The impact of the concrete in the composition is strong in the under-moderated configuration. By contrast, the effect is relatively low in the over-moderated configuration. In the under-moderated configuration with the pattern 5a, the  $^{235}\text{U}$  enrichment

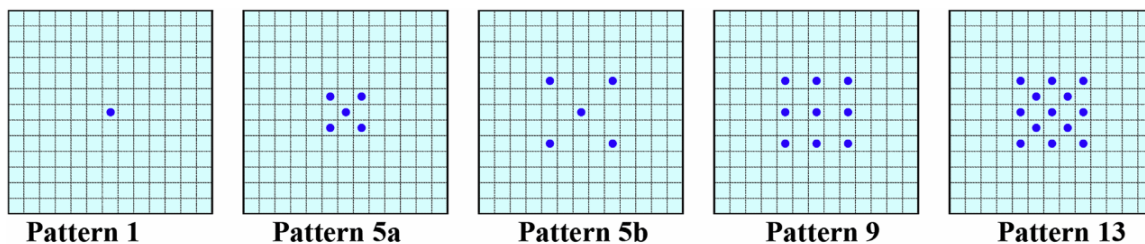


Figure I.19: STACY pattern in the testing section: blue dots are the testing rods, taken from [30].



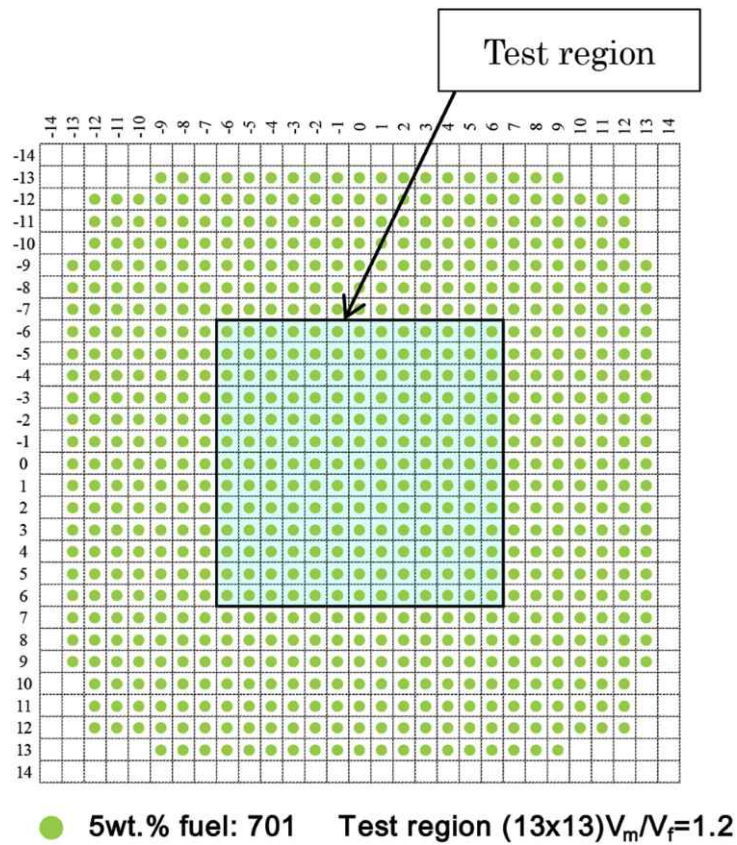


Figure I.20: STACY critical assembly, taken from [30].

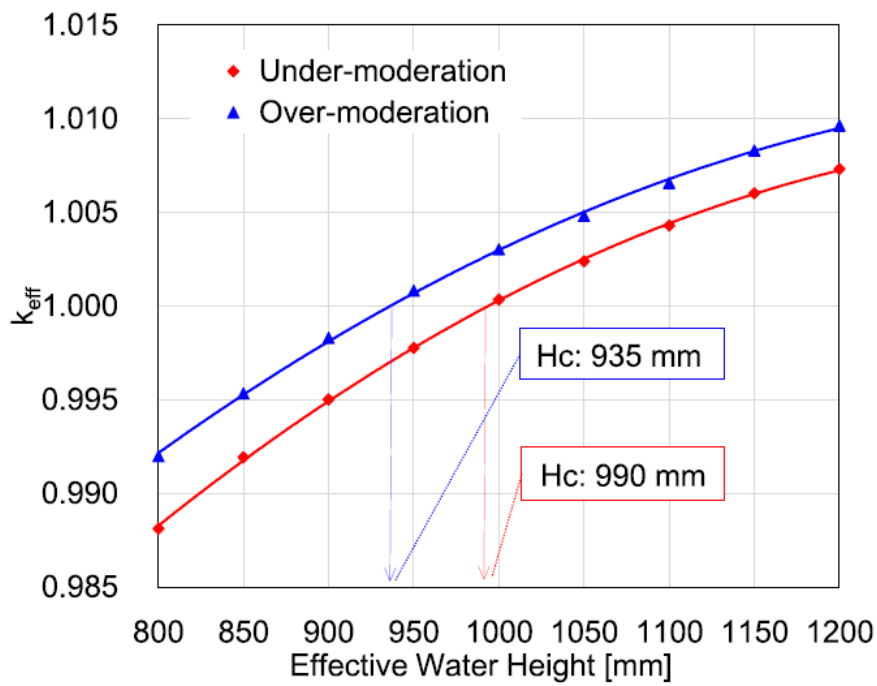


Figure I.21:  $k_{eff}$  of each core as a function of effective water height, taken from [30].

at 4 wt%, the increase of porosity brought a high reactivity increase ( $> 30 \text{ cent}$ ). In the over-moderated configuration with the pattern 5a, the  $^{235}\text{U}$  enrichment at 4 wt%, the increase of porosity led to the same effect but a little less reactivity increase ( $> 20 \text{ cent}$ ). The over-moderated configuration was not enough moderated: thus, a new configuration with more moderation was created. Future studies on neutron absorber materials are planned.

These preliminary calculations show that debris made of molten-core-concrete-interaction fragments maybe close to criticality, therefore calling for more investigations to expand the knowledge about the return to criticality in debris beds.

## I.4 Cooling debris bed in diphasic conditions

In the case of a hypothetical severe accident scenario, a part of the available corium inventory may create a debris bed in the vessel pit. Depending on debris bed temperature, porosity and water flooding, two-phase flows (water-steam) or single flow (water or steam) may be encountered. The liquid water presence drives the reactivity of debris bed and under the unfavourable conditions (of porosity, debris size and moderator ratio) criticality concerns may appear. Therefore, water density spatial distribution in the debris bed must be known to estimate the criticality risk.

### I.4.1 Challenges related to the cooling of debris beds

After the interaction of the molten material with water, a part of the corium is solidified as "cake" (large chunk without porosity [3]) and another part is solidified as debris. The debris bed is mainly made of fuel, thus generating heat. In order to cool the debris bed, water should find a way between the debris to reach the bottom of the fuel debris bed. An example of a debris bed configuration considered after core degradation is shown in figure 1.22. The high decay heat rate causes the water to vaporize and the resulting steam to escape from the top of the bed. The liquid water available above the bed then fills the pores under the action of gravity and capillary forces. There are two possible scenarios:

- If the internal pressure drop is not too large and the liquid ingress is sufficient to establish a permanent boiling regime, then the entire bed is at saturation temperature.
- On the other hand, if the decay power is large, the strong steam production prevents the water from reflooding the void between the debris. The liquid vaporizes before the entire bed is flooded, and the high steam production hinders the gravitational liquid flow.

The pressure drop depends on the characteristics of the debris bed and of the steam flow, as the steam takes up volume that is in return not available to let the water flow. In this respect, a key quantity is the dryout flux [33]. It corresponds to the maximum heat flux that can be extracted from the debris bed. If the heat generated within the debris bed exceeds the dryout heat flux, the debris bed will be dried out and eventually leading to the melting of the debris : the melting debris will erode the material where the debris bed lies [34]. Cooling a fuel debris bed during a severe accident is not trivial and experiments were performed to expand the knowledge on this subject [35].

### I.4.2 Diphasic flows through a porous medium

Debris bed is a special material: the voids between the debris are big enough to let fluid flow through it and the material is disordered enough to not considered each debris separately.



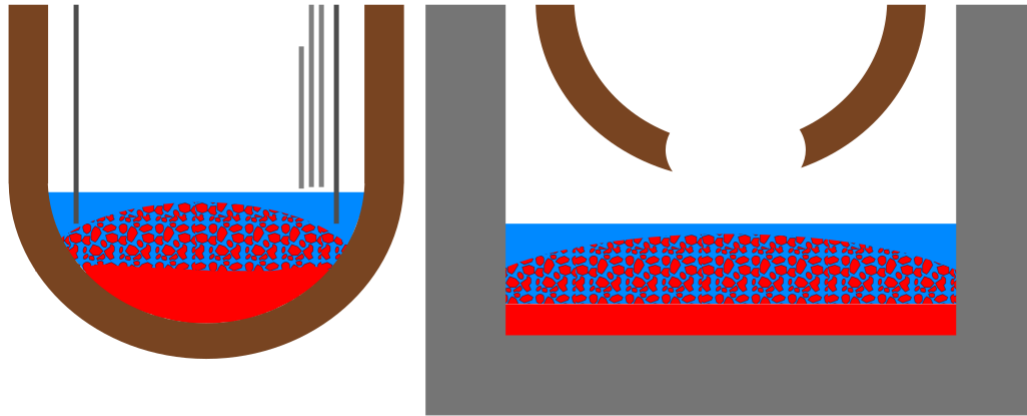


Figure I.22: Debris bed created in the pressure vessel (left) and in the vessel pit (right).

Thus debris beds are usually modelled as porous media [36]. Porous media are characterized by porosity and permeability [36]. These physical parameters help to represent the pressure drop created by the tortuosity within the porous medium. The behaviour of a fluid in porous media was initially investigated by Darcy [36].

When two immiscible fluids are flowing through a porous medium, interactions between them lead to a complexification of the physical phenomenon. The physical value of passability should be introduced to help the modelling of flows with higher Reynolds number (usually seen with diphasic flows) [37]. In diphasic flows, the two fluids will be in competition with each other for the same pores. This behaviour is represented thanks to the relative passability and relative permeability, which depend on the volume ratio of the fluid 1 and the fluid 2 in the volume [38]. Thus, the passability and the permeability of each fluid depends on the presence of the other fluid. Moreover, there are interfacial drags between the two fluids. In the case of top flooding by water, the phenomena of counter-current flow limitations can appear due to interfacial instabilities [38]. The limitation of water flow shows that the maximum heat flux extracted from the debris bed is reached.

Another issue in diphasic conditions within debris bed is the entrainment effect on debris. Indeed, in the case of a water/steam cooling of the debris bed, the debris may be dragged away by the steam. This is the fluidification of debris bed, which can happen if the debris are small enough and the steam flow is strong enough. It was shown that the fluidification of the debris can enhance the cooling capabilities of the debris bed by creating channels [38] as illustrated in figure I.23. However this mechanism might occur only in the case of high velocity and turbulent flows.

Simple flooding models were developed to calculate the maximum heat flux that can be transferred from the debris bed to the coolant, by imposing the equilibrium between the momentum, energy and mass of water and steam flows inside the debris bed. The limitation of those approaches is the dimension taken into account, since most of its approaches are typically based on zero-dimensional models giving the maximum heat flux. The Lipinski model is able to assess the 1 dimension steam ratio [38] following vertical axis in a top flooding scenario. However none of these simple models take into account 2 dimensions cross-flow in debris bed. Neglecting cross flow means that the models can be representative only if the heat generated in the debris bed is homogeneously distributed.

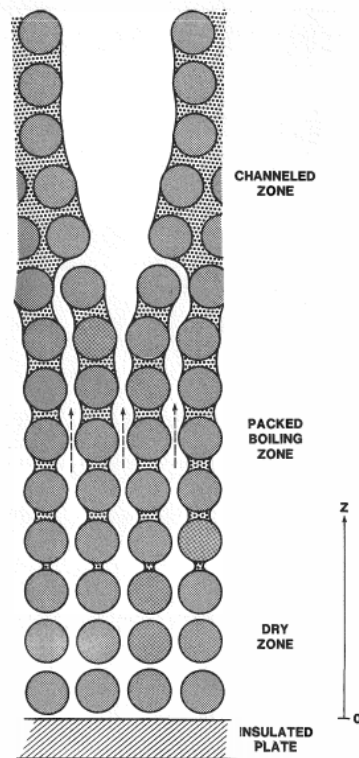


Figure I.23: Channel creation in top flooding of debris bed, taken from [38].

### I.4.3 Dryout heat flux characterization

The dryout heat flux is the maximum heat flux that can be transferred from the debris bed to the coolant: if the heat generated within the debris bed is higher than the dryout heat flux the debris bed will be dried up. The dryout heat flux is expressed as a heat flux through a surface, hence the units are  $W/m^2$ . A debris bed is characterized by geometrical parameters (height, diameter) by the geometrical and physico-chemical features of the debris: size distribution, debris shape and material. Porosity, permeability, passability and bed configuration (homogeneous, stratified) are also essential parameters. Empirical laws were obtained from the several experiments performed on the cooling of debris beds. An increase in the dryout heat flux is observed as the debris diameter ( $d$ ) increases [39]. For sub-millimetre particles, the evolution of the dryout heat flux follows a  $d^2$ -type law, whereas for debris with a diameter greater than 1 – 2 mm, the dryout heat flux seems to increase as  $d^{1/2}$ . At 1 bar and in the case of water, the dryout flux varies from 500  $kW/m^2$  to 2  $MW/m^2$  for particles whose diameter varies from 1 to 10 mm. Pressure tests show an increase in the dryout heat flux with pressure up to around 50 – 60 bars and a decrease beyond 60 – 70 bars [39]. This behaviour can be attributed to significant changes in the physical properties of the water over this pressure variation range: the increase of the density of the steam or the decrease of the density of the liquid phase. Also the decrease in the latent heat of vaporisation helps to explain the observed behaviour. It can be seen that up to a pressure  $P$  around 20 – 30 bars the dryout heat flux varies as  $P^{1/2}$ . In the case of a stratified configurations, the presence of a bed of fine particles above a bed of coarse particles can significantly reduce the dryout heat flux of the coarse particle bed.

The shape of the debris beds also impacts significantly the dryout heat flux. Figure I.24 illustrates two geometries: cylindrical with top-flooding and conical with multi-dimensional flooding. In the cylindrical debris bed, the only surface where the water can flow is the top

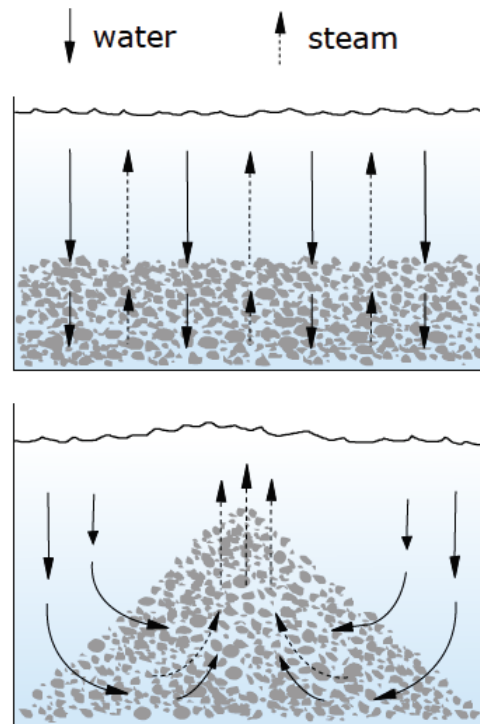


Figure I.24: Top-flooding of a cylindrical debris bed (top) and multi-dimensional flooding of a conical bed (bottom), taken from [33].

of the debris bed. In the conical debris bed, the water can penetrate the debris bed from the sides: for the same volume we have then a larger surface of exchange. Moreover, in the conical debris bed, the steam flows and the water flows are not going in opposite direction, so that each phase will create a lower drag force than in the cylindrical debris bed. However, the height of a conical debris bed is higher than a cylindrical debris bed, and the steam created in the lower part of the conical debris bed will prevent the water from cooling the higher part of the debris bed, leading to a dryout heat flux lower than a cylindrical debris bed for an equivalent volume and surface spreads.

Simulations and experiments [35] show a 47% to 51% lower dryout heat flux considering a conical debris bed compared to a cylindrical debris bed with the same volume and diameter [33]. Yet, the multidimensional coolability of a conical debris bed leads to an increase of 48–73% [33] of the dryout heat flux of conical debris bed compared to a cylindrical debris bed of the same height. The COOLOCE experimental measurement of dryout heat flux illustrated in figure I.25 shows the impact of debris bed shape and of pressure on the dryout heat flux [33].

The reflooding of a heated debris bed is a complex phenomenon, the two phases interact strongly with each other and the properties of the porous medium make experiments and models extremely difficult. Previous studies has nonetheless reached some conclusions on the behaviour of the debris bed regarding pressure, debris size and geometries. We will use this large experimental database to create models and to implement them in the codes detailed in section II.1.1.

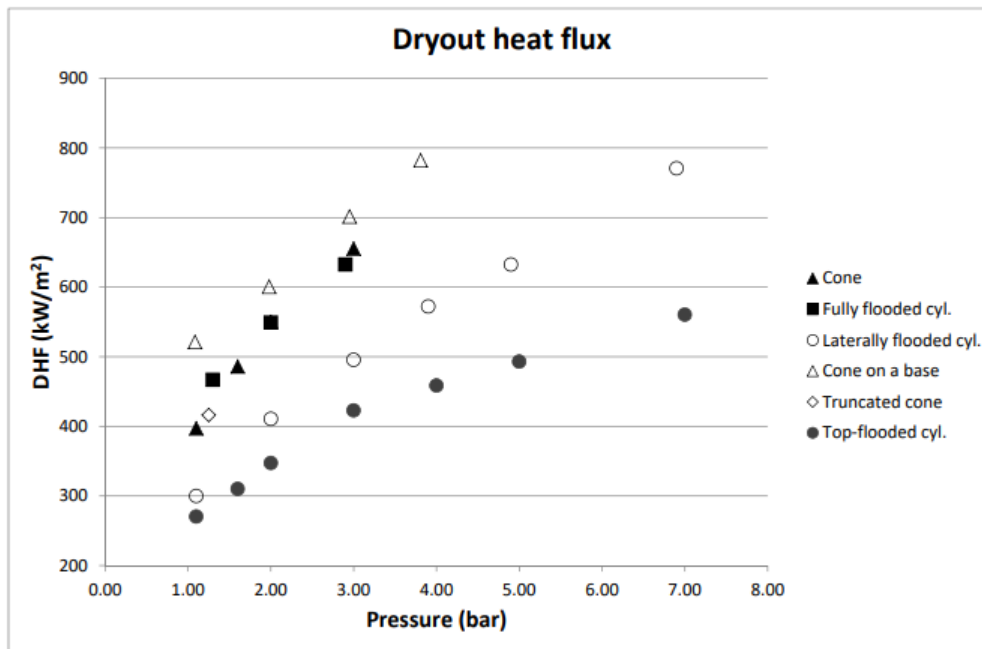


Figure I.25: dryout heat flux of debris bed depending on the pressure and its shape in COOLOCE experiments, taken from [33].

## I.5 Synthesis

Three historical severe accidents (rated 5 or higher on the INES scale) were briefly recalled. These events triggered a large effort to improve the knowledge related to severe accidents and to study the criticality risk in such abnormal situations. The phenomenology of a severe accident was explained, in particular the creation of debris bed from corium. In this case, the core has reached a very degraded state and the molten core has flowed out of the pressure vessel. When the debris bed is flooded by cooling water, the issue of criticality must be addressed. Moreover, in the past severe accidents the past, the criticality was already a concern [10] [14], which was addressed thanks to boron injection at TMI-2 [40] and with mitigation actions at Chernobyl when criticality was detected [11]. Significant resources are deployed in Japan to analyse the criticality issues at the Fukushima nuclear facility and to ensure that the dismantling, recovery, and clean-up operations will not create a criticality risk [18].

Studies done for the severe accident conditions met at Fukushima showed that debris bed can be super-critical [41] when reflooded. However, thermal-hydraulics feedbacks were not addressed. Debris beds have a disordered geometry, which may be complex to model for neutron transport. Efforts were done to model this kind of materials [42] with simple methods (with only one debris size). Recent investigations have also considered the use of stochastic geometries in order to take into account the random dispersion of debris beds [43] [44], improving the reliability of the neutronics analyses. It was shown that critical accidents may have mechanical or radiological consequences [18] hence the study of criticality is especially required. However, although the thermal-hydraulics of the debris bed has an impact on criticality, the complex flows within hot debris bed was not taken into account so far [18] [41]. The criticality analyses of debris bed should take into account the decay heat effect on the coolant flows and therefore demands exploring the multi-physics aspects. The consequences

of these extreme events will be evaluated if the criticality risk is possible.

## Bibliography

- [1] *INES: The International Nuclear and Radiological Event Scale User's Manual*. Non-serial Publications, Vienna: International Atomic Energy Agency, 2013.
- [2] U.S. Nuclear Regulatory Commission, "Report on the Accident at the Chernobyl Nuclear Power Station," 1987.
- [3] D. Magallon and I. Huhtiniemi, "Corium melt quenching tests at low pressure and sub-cooled water in FARO," *Nuclear Engineering and Design*, vol. 204, no. 1, pp. 369–376, 2001.
- [4] J. G. Kemeny, *The president's commission on The accident at three mile island*. Pergamon Press, 1980.
- [5] B. Tarride, *Physique, fonctionnement et sûreté des REP Maîtrise des situations accidentelles du système réacteur*. Génie Atomique, EDP Sciences, 2013.
- [6] B. R. Sehgal, ed., *Nuclear Safety in Light Water Reactors Severe Accident Phenomenology*. Boston: Academic Press, 2012.
- [7] P. Piluso, "Private communication." May 2020.
- [8] P. Kuan, "Tmi-2 upper-core particle bed thermal behavior," tech. rep., EG&G Idaho, Inc, August 1987. <https://tmi2kml.inl.gov/Documents/9b-Data-Accident/EGG-TMI-7757>,
- [9] K. L. Thomsen, *Review of the TMI-2 accident evaluation and vessel investigation projects*. No. 1004 in Risø-R, Risø National Laboratory, Mar 1998. OCLC: 245704187.
- [10] "Three Mile Island Accident of 1979 Knowledge Management Digest Recovery and Cleanup," tech. rep., USNRC, 2016.
- [11] V. M. Pavlovych, "Nuclear Fuel in the Destroyed 4th Unit of Chernobyl NPP," *Recent Research Activities about the Chernobyl NPP Accident in Belarus, Ukraine and Russia*, 2002.
- [12] C. D. Fletcher, R. Chambers, M. A. Bolander, and R. J. Dallman, "Simulation of the Chernobyl accident," *Nuclear engineering and design*, vol. 105, no. 2, pp. 157–172, 1988.
- [13] "Environmental consequences of the Chernobyl accident and their remediation: twenty years of experience: report of the Chernobyl Forum Expert Group 'Environment'," 2006. OCLC: 255788636.
- [14] R. Stone, "Chernobyl: The Explosions That Shook the World," *Science*, vol. 272, no. 5260, pp. 352–354, 1996.
- [15] C. D. Bowman, "Eliminating the possibility at Chernobyl 4 of recriticality with positive feedback," 1996.
- [16] TEPCO, "Fukushima nuclear accidents investigation report and schedule," 2012.

- [17] *The Fukushima Daiichi Accident*. Non-serial Publications, Vienna: International Atomic Energy Agency, 2015.
- [18] R. Kimura and T. Yutaka, "Development of analysis code PORCAS-f for dynamic behavior of re-critical fuel debris," *ICAPP Proceedings*, 2017.
- [19] TEPCO and M. S., "Current status and recent investigation result of Fukushima Daiichi," 2019.
- [20] M. M. El-Wakil, *Nuclear heat transport*. International Textbook Co., 1971.
- [21] P. Reuss, *Précis de neutronique*. Génie Atomique, EDP Sciences, 2003.
- [22] H. Na, H. J. Lee, S. Kwon, S. J. Kim, and J. Kim, "One-dimensional coolability and concrete ablation analysis of volumetrically heat-generating debris bed," *Annals of Nuclear Energy*, vol. 106, pp. 256–270, 2017.
- [23] A. Tsilanizara, C. M. Diop, B. Nimal, M. Detoc, L. Lunéville, M. Chiron, T. D. Huynh, I. Brésard, M. Eid, J. C. Klein, B. Roque, P. Marimbeau, C. Garzenne, J. M. Parize, and C. Vergne, "Darwin: An evolution code system for a large range of applications," *Journal of Nuclear Science and Technology*, vol. 37, no. sup1, pp. 845–849, 2000.
- [24] D. Jacquemain, *Nuclear power reactor core melt accident*. Science and technology series, EDP Sciences, 2015.
- [25] "Postech lab." <http://phome.postech.ac.kr/user/indexSub.action?codyMenuSeq=2588121&siteId=twophaseflow&menuUIType=sub>, 2020.
- [26] F. Mitchell, K. Dennis, and A. Robert, "Corium coolability under ex-vessel accident conditions for lwrs," *Nuclear Engineering and Technology*, vol. 41, no. 5, pp. 575–602, 2009. cited By 26.
- [27] G. I. Bell and S. Glasstone, *Nuclear Reactor Theory*. Van Nostrand Reinhold Company, 1970.
- [28] J. R. Lamarsh and A. J. Baratta, *Introduction to Nuclear Engineering*. Prentice Hall, 2001.
- [29] L. Duderstadt, J.J. ; Hamilton, *Nuclear Reactor Analysis*. John Wiley and Sons Ltd. New York, 1976.
- [30] S. Gunji, K. Tonoike, K. Izawa, and H. Sono, "Study of experimental core configuration of the modified STACY for measurement of criticality characteristics of fuel debris," *Progress in Nuclear Energy*, vol. 101, pp. 321–328, 2017.
- [31] X-5 Monte Carlo Team, "MCNP a general monte carlo n-particle transport code, version 5," 2003.
- [32] K. Shibata, O. Iwamoto, T. Nakagawa, N. Iwamoto, A. Ichihara, S. Kuneida, S. Chiba, K. Furutaka, N. Otuka, T. Ohsawa, T. Murata, H. Matsunobu, A. Zukeran, S. Kamada, and J. Ichi Katakura, "Jendl-4.0: A new library for nuclear science and engineering," *Journal of Nuclear Science and Technology*, vol. 48, no. 1, pp. 1–30, 2011.
- [33] E. Takasuo, "Coolability of porous core debris beds effects of bed geometry and multidimensional flooding." PhD thesis'.

- [34] H. Na, H. J. Lee, S. Kwon, S. J. Kim, and J. Kim, "One-dimensional coolability and concrete ablation analysis of volumetrically heat-generating debris bed," *Annals of Nuclear Energy*, vol. 106, pp. 256–270, 2017.
- [35] E. Takasuo, "An experimental study of the coolability of debris beds with geometry variations," *Annals of Nuclear Energy*, vol. 92, pp. 251–261, 2016.
- [36] A. E. Scheidegger, *The physics of flow through porous media*. University of Toronto Press, 1957.
- [37] S. Ergun, "Fluid flow through packed columns," *Chemical Engineering Progress*, vol. 48, pp. 89–97, 1952.
- [38] R. J. Lipinski, "A particle-bed dryout model with upward and downward boiling," *Transport American Nuclear Society; (United States)*, vol. 35, Jan 1980.
- [39] E. Decossin, "Ebullition et assechement dans un lit de particules avec production interne de chaleur : premières expériences et simulations numériques en situation multi-dimensionnelle," 2000. Thèse de doctorat dirigée par Bories, Serge Mécanique des fluides Toulouse, INPT 2000.
- [40] R. Westfall, J. West, G. Whitesides, and J. T. Thomas, "Criticality analyses of disrupted core models of Three Mile Island unit 2," tech. rep., ORNL, december 1979.
- [41] P. Darnowski, K. Potapczyk, and K. Świrski, "Investigation of the recriticality potential during reflooding phase of Fukushima Daiichi unit-3 accident," *Annals of Nuclear Energy*, vol. 99, pp. 495–509, 2017.
- [42] M. F. López, M. Buck, and J. Starflinger, "Neutronic modeling of debris beds for a criticality evaluation," *Annals of Nuclear Energy*, vol. 130, pp. 164 – 172, 2019.
- [43] C. Larmier, *Stochastic particle transport in disordered media : beyond the Boltzmann equation*. PhD thesis, (Paris Saclay), 2018.
- [44] C. Larmier, A. Zoia, F. Malvagi, E. Dumonteil, and A. Mazzolo, "Neutron multiplication in random media: Reactivity and kinetics parameters," *Annals of Nuclear Energy*, vol. 111, pp. 391–406, 2018.

# Chapter II

## Models and simulation tools related to critical debris beds

### Contents

---

<b>II.1 Models and simulation tools for thermal-hydraulics in debris beds . . . . .</b>	<b>41</b>
II.1.1 Models of flow through porous media . . . . .	41
II.1.2 Simulation codes for debris bed cooling . . . . .	44
II.1.3 Thermal model . . . . .	49
<b>II.2 Models and simulation tools for criticality in debris beds . . . . .</b>	<b>50</b>
II.2.1 Neutron transport . . . . .	50
II.2.2 Simulation codes for neutron transport . . . . .	53
II.2.3 Quasi-static method . . . . .	54
II.2.4 Generation of random geometries . . . . .	54
<b>II.3 Statistical learning as a tool to accelerate calculations . . . . .</b>	<b>56</b>
II.3.1 Overview of surrogate models . . . . .	56
II.3.2 Linear models . . . . .	57
II.3.3 Artificial neural networks . . . . .	58
<b>II.4 Synthesis . . . . .</b>	<b>61</b>
<b>Bibliography . . . . .</b>	<b>61</b>

---



## Introduction

Appropriate neutron transport and thermal-hydraulics models of a debris bed require specific simulation tools. Since the TMI-2 accident, significant efforts have been made to improve knowledge and models that addressing debris bed behaviour. This field has met a renewed interest after the Fukushima accident, which has led to an intensification of the research activities on how to properly model porous media [1]. Indeed, porous media are assumed to be the prototype description of debris beds. In this chapter the models and the simulations tools for the description of porous media will be presented, with special emphasis on neutron transport and thermal-hydraulics. We will first illustrate the literature work previously done to simulate diphasic flows through porous media. Then, we will present the models used in the neutronics fields and a particular attention will be paid to the modelling of disordered media. Finally we will consider the potential for statistical learning methods to accelerate the coupled simulation of neutron transport and thermal-hydraulics feedbacks.

## II.1 Models and simulation tools for thermal-hydraulics in debris beds

During the TMI-2 and the Fukushima nuclear accidents, a part of the corium took the shape of debris beds, with water (liquid and vapour) streaming and flowing through the components of the corium. Corium displays features that are strikingly different from the usual nuclear fuel in composition or shape [2] [2]. The debris have disordered random shapes and have been traditionally modelled as porous media. The cooling of the corium, is required to halt the severe accident. In particular, the dry-out heat flux plays a prominent role in the dynamics of the severe accidents. As the water flows through the debris bed, steam may be created due to the large heat generated within the debris. Hence, the modelling of the debris beds cooling will required the utilisation of complex diphasic models.

### II.1.1 Models of flow through porous media

#### Mono-phasic flow: the Darcy Law

The issue of fluid flows in porous media has been investigated for a long time [3], [4]. Porous media where are characterized by the presence of void between solid materials. They can be also assimilated to a solid body that contains pores [5]. The locations of the pores can have with a regular structure (as in a lattice), or be randomly dispersed (as in disordered media). Debris beds typically belong to the latter category [5]. The pores in the system may be interconnected. If enough pores are connected, the flow through interstitial pores is allowed and there will be percolation in the media [5]. An important feature of porous media is the porosity, written  $\epsilon$ , and defined in equation II.1:

$$\epsilon = \frac{\text{Void volume in the medium}}{\text{Total volume in the medium}}. \quad (\text{II.1})$$

The permeability of a porous medium corresponds to its ability to allow a fluid (liquid or gas) to pass through it under the effect of a pressure gradient. It depends on the distinct features of the debris, such as shape and size; an example of cross section of a porous medium made of particles is illustrated in figure II.1.

The reference law to described fluid flowing through porous media is the Darcy law [5]:

$$-\frac{k}{\mu_i} (\vec{\nabla}P - \rho_i \vec{g}) = \vec{v}_i. \quad (\text{II.2})$$

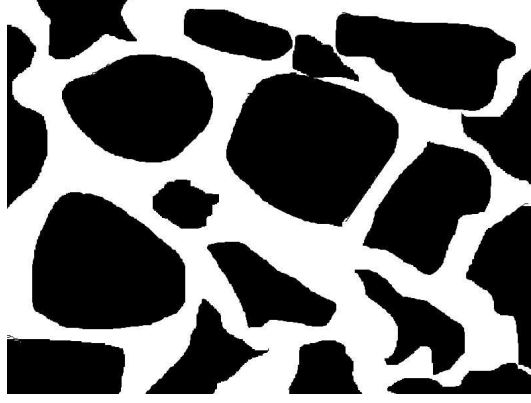


Figure II.1: Example of porous medium with material chunks (in black).

Darcy law expresses the flow rate of an incompressible fluid streaming through a porous medium. The flow is determined by the hydraulic conductivity or the coefficient of permeability of the substrate and by the pressure gradient of the fluid. The law is described in equation II.2 for a phase  $i$  where  $P$  is the pressure,  $k$  is the permeability of the medium,  $\mu$  the dynamic viscosity,  $\rho_i$  the fluid density,  $\vec{g}$  is the gravity acceleration and  $\vec{v}_i$  the fluid  $i$  velocity. This law is valid for mono-phasic, incompressible and steady state flow in an isotropic porous medium. It includes a viscosity term  $\mu_i \vec{v}_i$ . The Darcy law is usually appropriate for low Reynolds number ( $Re < 1$ ) [5]. For high velocity flows, deviations can be observed [5]. These discrepancies come from the inertia effect, which is not taken into account in Darcy law. The permeability  $k$  in single-phase flow in a debris bed can be estimated in accordance with the *Carman – Kozeny* relation [6] which reads:

$$k = \frac{d^2 \epsilon^3}{c_k (1 - \epsilon)^2} \quad (\text{II.3})$$

with the variable  $d$  the average debris size express in meters, and the dimensionless constant  $c_k$ . The permeability can be seen as the flow conductance of the medium. The dimensionless constant  $c_k$  is an empirical value varying between 150 and 181, depending on the choice made by the authors [5].

### Diphasic flow

Ergün [4] has proposed a model to estimate the loss of pressure of a porous medium made of dispersed particles with higher Reynolds numbers (recall that the Darcy law is valid for  $Re < 1$ ) and introduced the notion of passability defined in:

$$\eta = \frac{d \epsilon^3}{c_\eta (1 - \epsilon)} \quad (\text{II.4})$$

with the dimensionless constant  $c_\eta = 1.75$ . He also proposed a form of friction factor  $f_v$  representing the ratio of the pressure drop made by the viscous energy [4].

In the context of severe accidents, the flooding of debris beds will typically generate steam in the medium: thus, the model of the flooding demands to take into account diphasic flows in the debris bed. In the domain of debris bed cooling, the effects of the counter-flow stemming from the steam should be addressed and the two-phase frictional pressure gradient can be described by a modified form of the Ergün equation, namely:

$$-\frac{dP}{dz} - \rho_i g = \frac{\mu_i}{k} v_{si} + \frac{\rho_i}{\eta} v_{si}^2 \quad (\text{II.5})$$

with  $\mu_i$  the dynamic viscosity,  $\rho_i$  the density of the fluid,  $v_{si}$  the superficial velocity of fluid  $i$ . The term  $v_{si}^2$  helps to represent the inertia effects occurring in high velocity flow [4]. The first term in the right of the equation II.5 is the viscous energy loss and the second term is the kinetic energy loss. It is assumed that the flows are oriented in the vertical direction  $\vec{z}$ , the components in other directions are considered as negligible here. A representation of the flooding conditions is illustrated in figure II.2.

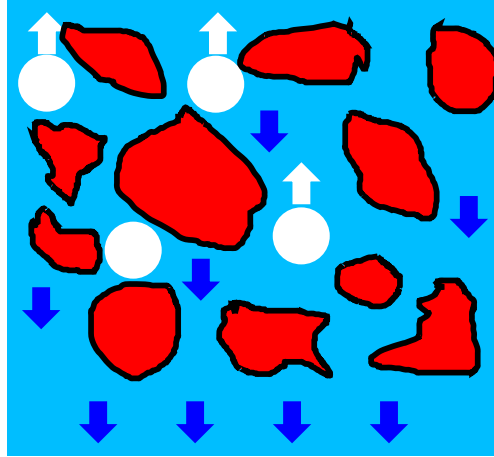


Figure II.2: Counter flows into a heated debris bed, the water is depicted in blue, the steam in white and the debris in red.

### Flooding model

Re-flooding a heated debris bed can be considered as a special case of hydrodynamics in porous media. In the literature, the top flooding is the situation that has motivated most of the research efforts [3], [7]. For such configuration, one would try to determine how the liquid water will penetrate the medium (by the top) and eventually reach the bottom by interacting with steam counter-flow. Most models [3] [8] consider flows along the vertical direction  $z$  oriented towards the top, which implies the minus sign in front of the buoyant term  $\rho g$  in equation II.5. We will introduce the following notation:  $\alpha$  is the steam volume ratio (also called void ratio),  $s$  is the liquid volume ratio ( $s = 1 - \alpha$ ), the superficial velocity  $v_{si} = V_i \alpha_i$ , where  $V_i$  is the phase velocity and  $\alpha_i$  the volume ratio of the phase  $i$  and the liquid and gaseous phase are expressed as  $l$  and  $g$ . Lipinski added some terms to model the interaction between liquid and gas flow in porous media [3]. Indeed, in the presence of another phase, the phase  $i$  would have to make its way through the porous medium and the other phase as well (both are seen as obstacles). The equations taking into account the relative permeability and the relative passability are given by :

$$\begin{aligned} -\frac{dP_l}{dz} - \rho_l g &= \frac{\mu_l}{k k_{rl}} v_{sl} + \frac{\rho_l}{\eta \eta_{rl}} |v_{sl}| v_{sl} \\ -\frac{dP_g}{dz} - \rho_l g &= \frac{\mu_g}{k k_{rg}} v_{sg} + \frac{\rho_g}{\eta \eta_{rg}} |v_{sg}| v_{sg} \end{aligned} \quad (\text{II.6})$$

with  $\frac{dP_i}{dz}$  the component of the pressure gradient of the phase  $i$ ,  $k_{ri}$  and  $\eta_{ri}$  respectively the relative permeability and the passability if the phase  $i$ . The notion of relative permeability  $k_{rl}$ ,  $k_{rg}$  and relative passability  $\eta_{rl}$ ,  $\eta_{rg}$  were introduced to represent the difficulty met by the phase  $i$  to make its way through the other phase [3].

	$k_{rg}$	$\eta_{rg}$	$k_{rl}$	$\eta_{rl}$
Lipinski (1981) [3]	$\alpha^3$	$\alpha^3$	$s^3$	$s^3$
Reed (1982) [8]	$\alpha^3$	$\alpha^5$	$s^3$	$s^5$
Hu and Theofanous (1991) [9]	$\alpha^3$	$\alpha^6$	$s^3$	$s^6$

Table II.1: Models of relative permeability and passability.

The functional forms for the relative passability and relative permeability were developed by Reed, Lipinski and Hu and Theofanous [8] [3] [9] and are provided in the table II.1. The Lipinski model was developed in particular for diphasic flow in partially fluidified debris bed [3]. Reed has developed a model for the permeability and the relative passability in porous media. The capillary forces can be optionally included in the equation II.6. Generally speaking, the capillary forces are negligible for deep debris beds (higher than 100 times the particle size) [8].

For a thorough description of the flooding of porous media, the modelling of interfacial drag is needed. It was first proposed by Schulenberg and Müller [10] as defined in :

$$\begin{aligned} -\frac{dP_l}{dz} + \rho_l g &= \frac{\mu_l}{k k_{rl}} v_{sl} + \frac{\rho_l}{\eta \eta_{rl}} |v_{sl}| v_{sl} - \frac{F_i}{s} \\ -\frac{dP_g}{dz} + \rho_g g &= \frac{\mu_g}{k k_{rg}} v_{sg} + \frac{\rho_g}{\eta \eta_{rg}} |v_{sg}| v_{sg} + \frac{F_i}{\alpha} \end{aligned} \quad (\text{II.7})$$

with the model of interfacial friction noted  $F_i$ , which is described in:

$$F_i = 350 s_l s_g \frac{\rho_l k}{\eta \sigma} (\rho_l - \rho_g) g \left( \frac{v_g}{s_g} - \frac{v_l}{s_l} \right)^2. \quad (\text{II.8})$$

Improvements were suggested by Tung and Dhir and Schmidt: to model the interfacial friction forces as a function of the regime flows [11] [12]: three diphasic flow regimes have been inserted in the modelling: the bubbly flow, the slug flow and the annular flow [13]. In order to properly compute the cooling of debris beds (depending on the beds properties [12]), such flow regimes must be accurately taken into account.

Debris bed cooling has been carefully investigated since the TMI-2 accident. In parallel to the development of models, intense experimental activities have been also carried out, in order to validate the various equations and empirical laws. Most of these experiments have been conducted for debris with porosities close to those of TMI (29% to 54 % [14] [2]).

## II.1.2 Simulation codes for debris bed cooling

The models described above (such as the Lipinski model) give good results on the maximum extractable heat flux of the debris bed in one-dimensional configuration. However, the effects related to spatial heterogeneity (e.g. lateral flows) cannot be represented with these simplified models. The simulations of large fuel debris demand at least two-dimensional or three-dimensional simulations. In the same way, equations devoted to flooding models developed in the past can be easily solved by numerical methods, but higher spatial dimensions would require highly sophisticated numerical codes. In the following we will present a non-exhaustive list of simulation codes capable of simulating debris bed cooling in diphasic conditions. Some of them (like DECOSIM [15]) are devoted to debris bed cooling calculations, while others (such as MC3D [16]) are specialized to fuel-water interactions, with permeability and passability models.

## COCOMO

COCOMO (CORium COolability MOdel 3-D) [17] is developed by IKE (Institut für Kernenergetik und Energiesysteme) at Stuttgart in Germany. It is the coupling of two codes: the JEMI code and the MEWA code [17]. JEMI calculates the fragmentation of the corium jet in water, by solving the equations of motion and heat to obtain the properties of the debris bed, such as the size of the grains. The MEWA code solves the heat, momentum and energy conservation equations to obtain the temperature, density and velocity of the coolant.

## DECOSIM

The DECOSIM code [15] is a multiphase thermal-hydraulic code. It is developed at KTH (Kungliga Tekniska Högskolan) in Stockholm, Sweden. It is devoted to the study of the cooling of porous media. Turbulence models have been integrated to calculate the flows in the pool above the debris bed. It has been validated on the COOLOCE experiment in comparison with the COCOMO code [15].

## MC3D

The MC3D code is a multiphase 3-D thermo-hydraulics code that is able to predict the behaviour of fuel coolant interaction (FCI) [16]. It has many models of thermal-hydraulics exchange, including porous media out of equilibrium [18]. Moreover, corium fragmentation and steam explosion can be taken into account.

In MC3D, debris are considered as an incompressible phase, which enables the code to compute debris fluidification. The Eulerian description is used to model the behaviour of water, steam and solid phase (debris). As a consequence, the code relies on the assumption of three continuity equations, three momentum equations and three internal energy equations. It is possible for each field to exchange momentum and energy with the other fields and the solid phase cannot exchange mass with the two other fields. To solve these equations, the pressure is considered to be uniform within each cell [16]. The equations of continuity, momentum and energy are solved by a semi-implicit method. 3D-Cartesian mesh or axisymmetric mesh can be used. The time-step usually depends on the evaporation rate. The code considers 3 phases: the liquid phase, the gas phase and the solid phase. The variables are the gas pressure, the volume fraction of each phase ( $\alpha_{liquid}$ ,  $\alpha_{gas}$ ,  $\alpha_{solid}$ ), the fraction of incondensable gas and the temperature within the cell (with the assumption of thermal equilibrium within the cell). There are 3 equations for each phase: the continuity equation, the momentum equation and the energy balance equation. The assumption is done that the debris of porous medium are static, which means there is not exchange of momentum between the solid phase and the other phases.

The continuity equations read:

$$\begin{aligned} -\frac{\partial \alpha_l \rho_l}{\partial t} + \nabla \alpha_l \rho_l \vec{V}_l &= -G_{lv} \\ -\frac{\partial \alpha_g \rho_g}{\partial t} + \nabla \alpha_g \rho_g \vec{V}_g &= +G_{lv} \\ -\frac{\partial \alpha_s \rho_s}{\partial t} &= 0 \end{aligned} \quad (II.9)$$

with  $G_{lv}$  the mass of phase exchange between the phase  $l$  and the phase  $g$  (where incondensable gas is not taken into account) and with the generalized mass continuity equation:

$$\frac{\partial}{\partial t} \alpha_g \rho_g x_g + \nabla \alpha_g \rho_g x_g \vec{V}_g = 0. \quad (II.10)$$

Then, the momentum equations are:

$$\begin{aligned} -\frac{\partial}{\partial t} \alpha_l \rho_l \vec{V}_l + \nabla(\alpha_l \rho_l \vec{V}_l \vec{V}_l) &= -\alpha_l \nabla P_l + \alpha_l \rho_l \vec{g} - G_{lv} \vec{V}_l - \frac{\alpha_l^2 \mu_l}{k k_l} \vec{V}_l - \frac{\alpha_l^3 \rho_l}{\eta \eta_l} |\vec{V}_l| \vec{V}_l \\ -\frac{\partial}{\partial t} \alpha_g \rho_g \vec{V}_g + \nabla(\alpha_g \rho_g \vec{V}_g \vec{V}_g) &= -\alpha_g \nabla P_g + \alpha_g \rho_g \vec{g} + G_{lv} \vec{V}_g - \frac{\alpha_g^2 \mu_g}{k k_g} \vec{V}_g - \frac{\alpha_g^3 \rho_g}{\eta \eta_g} |\vec{V}_g| \vec{V}_g. \end{aligned} \quad (\text{II.11})$$

The energy balance equations are :

$$\begin{aligned} -\frac{\partial}{\partial t} (\alpha_l \rho_l e_l + \alpha_g \rho_g e_g + \alpha_s \rho_s e_s) + \nabla(\alpha_l \rho_l e_l \vec{V}_l + \alpha_g \rho_g e_g \vec{V}_g) &= \\ -P_l \left( \frac{\partial \alpha_l}{\partial t} + \nabla \alpha_l \vec{V}_l \right) - P_g \left( \frac{\partial \alpha_g}{\partial t} + \nabla \alpha_g \vec{V}_l + \nabla(\lambda \nabla T) + Q \right). \end{aligned} \quad (\text{II.12})$$

with the temperature equilibrium assumption in porous media (where  $\lambda$  is the heat conductivity of the porous medium and  $Q$  the volumetric power generated in the porous media). The constraints to have volume continuity are :

$$\begin{aligned} \epsilon &= \alpha_L + \alpha_G = 1 - \alpha_S \\ \alpha_L + \alpha_G + \alpha_S &= 1. \end{aligned} \quad (\text{II.13})$$

The closure relations are the equations giving the thermodynamic properties (density  $\rho$  and internal energy  $e$ ) as a function of pressure and temperature:

$$\rho_i = \rho_i(P, T) \quad e_i = e_i(P, T). \quad (\text{II.14})$$

It was validated against relevant experiments described hereafter.

The code MC3D was previously compared to experiments such as the TUTU experiments [18] and PEARL. The TUTU experiments were conducted at the Brookhaven national laboratory in USA in 1984 [19]. The interfacial drags govern the two-phase flows in porous medium, therefore it is important to model them properly in order to compute the flows in heated debris beds. One of the main objectives of the TUTU experiment was to measure the interfacial drag for two-phase flows in porous media [19]. So the debris bed was not always heated, as heat generation is not necessary to have two-phase conditions. Indeed, the injection of air bubbles is good enough to model the interaction of gas and water in porous media. The system was made of a cylindrical debris bed of stainless steel. Pressure was measured in the system in order to obtain the pressure gradient created by the debris in different regimes of two-phase flows. The figure II.3 illustrates the results of the validation of the code on this experiment. The simulation code showed good agreement on the two tested debris sizes.

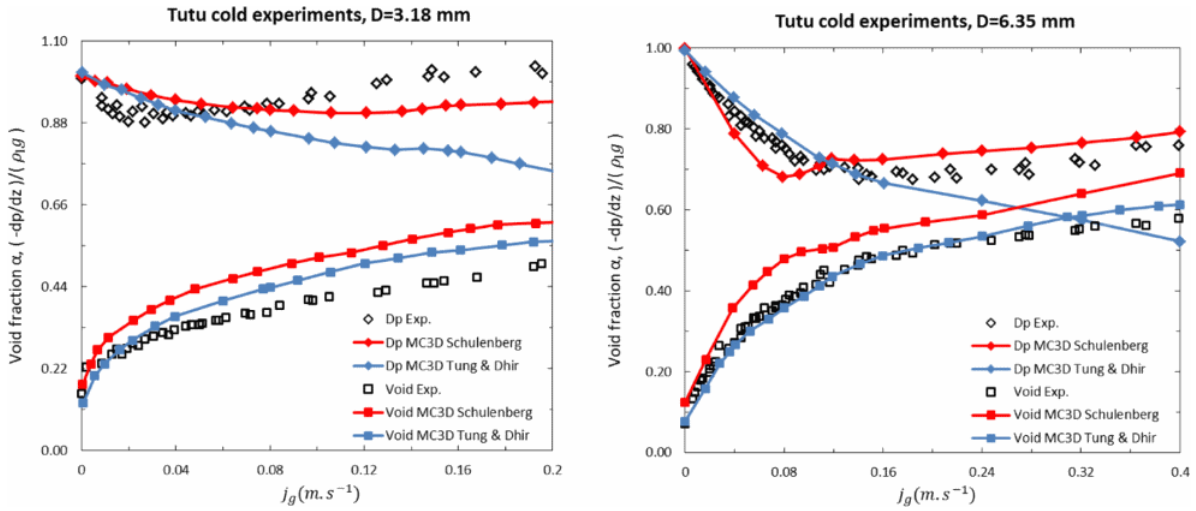


Figure II.3: Validation of MC3D capabilities to model interfacial friction against TUTU cold experiments [18].

The Ginsberg experiment [20] (which corresponds to the top re-flooding of a superheated debris bed) and the PEARL experiments highlight also the potential contribution of MC3D to the accurate description of water flows in debris beds. Indeed, Ginsberg and PEARL are complex experiments where transients of cooling the debris bed were realized. The PEARL experimental tests were performed at Cadarache in 2017 [21]. The main objective of the PEARL tests was to study the transient cooling of a heated debris bed surrounded by a by-pass [21]. The cooling water injected from below encounters debris at very high temperature and thus a mixture of liquid water and steam goes up into the porous medium. The quench front corresponds to the location where the water remains in a liquid state. The progression of front quench at low pressure is a very complex phenomenon. The velocity of progression of the quench front is the criterion that should be validated with models. The system was working at different pressures from  $1.0 \times 10^5$  to  $5.0 \times 10^5$  Pa. Multiple effects were studied, such as the prediction of debris cooling rate, front propagation, steam production and pressure difference across the bed during the quenching following water injection. Analysis of the quench front was more specifically studied. The experimental configuration consists of a cylindrical debris bed with stainless steel balls with a diameter of 4 mm. The debris bed is surrounded by a torus-shape debris bed made of quartz balls with diameter of 8 mm as described in figure II.4. This quartz debris bed was used as a by-pass. Indeed, only the debris bed made of steel balls was heated by induction during the experiments.



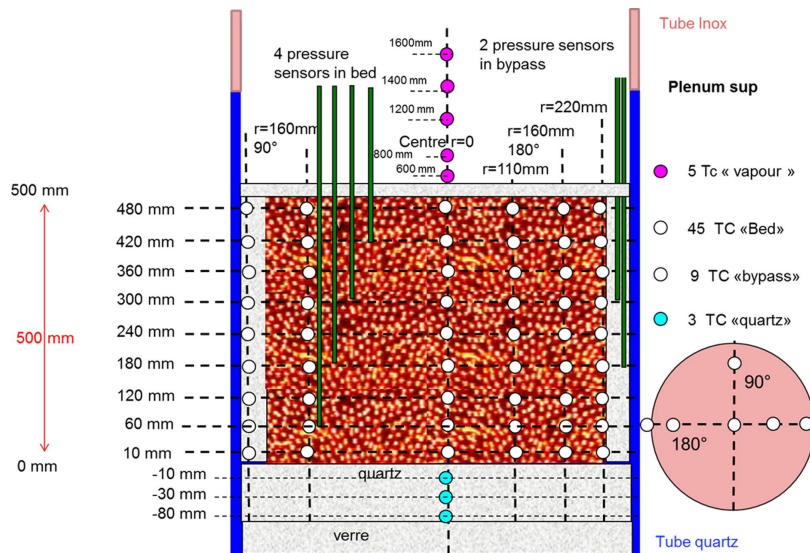


Figure II.4: PEARL debris bed with quartz bypass and locations of the thermocouple on the right [21].

The figure II.5 illustrates the results of the simulation against the experiments *PA\_1*, *PA\_2*, and *PA\_3*. Generally speaking, the quench front predictions showed a very good agreement despite the complex conditions [18].

The validation of MC3D shows that the code is able to model the interfacial friction properly and to predict the flooding of hot debris bed with good agreement. Regarding these validation results, this code seems to be quite suitable to simulate complex transients in heated debris beds. However, in most experiments, the void fraction was not measured, therefore MC3D was not validated on the computation of void fraction, a key data for neutron transport. Another important feature of MC3D is the capability of computing violent interactions between hot material and water. Indeed, MC3D was developed and validated to simulate steam explosions [22], thus this code can be also used to assess the mechanical consequences of power transients, which we will be examined in chapter VI.



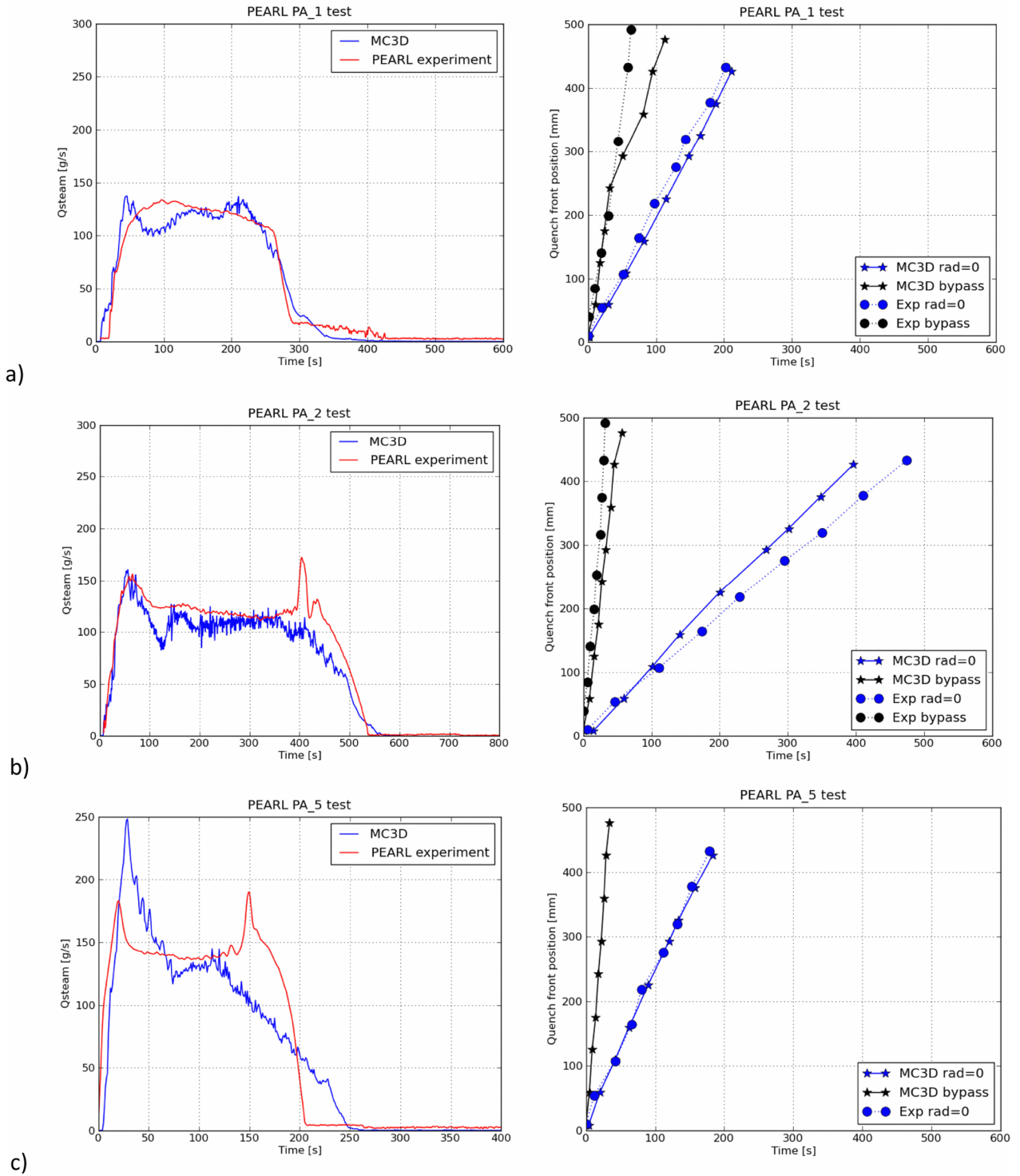


Figure II.5: Validation of MC3D capabilities against PEARL experiment [18].

### II.1.3 Thermal model

The heat transfer in the debris bed can be decomposed in two domains: the diffusion of heat inside the debris and the heat transfer from the debris to the coolant fluid. The diffusion of heat is governed by the Fourier law:

$$F_{heat}^{\vec{v}} = -\lambda \vec{\nabla} T \quad (II.15)$$

with  $\lambda$  the thermal conductivity,  $F_{heat}$  is the heat flux and  $\vec{\nabla}T$  the temperature gradient. The heat diffusion law is obtained:

$$\frac{\partial T}{\partial t} - \frac{\lambda}{\rho C_p} \nabla^2 T = \frac{S}{\rho C_p} \quad (\text{II.16})$$

by doing a thermal energy balance inside a region heated by the volumetric source  $S$ , with the specific calorific capabilities  $C_p$  and a density of  $\rho$  and assuming that the thermal conductivity is constant with respect to the temperature. The heat transfer between the debris surface and the coolant fluid occurs thanks to free convection. The evaluation of the heat coefficient in free convection conditions demands the use of dimensionless numbers as the Rayleigh number and the Prandtl number [13] respectively defined as:

$$Ra_D = \frac{g\beta(T_s - T_\infty)D^3}{\nu\gamma} \quad (\text{II.17})$$

$$Pr = \frac{\mu}{\gamma}. \quad (\text{II.18})$$

The Rayleigh number represents the ratio of the buoyant convection on the diffusion convection of heat in the fluid [13],  $\beta$  is the dilatation coefficient of the fluid,  $T_s$  is the surface temperature of the solid,  $T_\infty$  the fluid temperature and  $D$  is the typical size of the solid (for a sphere, the diameter is used). The Prandtl number depends only of the fluid characteristics: it represents the ratio of the convection capacity over the diffusion capacity of heat in the fluid, where  $\mu$  is the dynamic viscosity and  $\gamma$  is the thermal diffusion coefficient of the fluid [13]. The Nusselt number in equation II.19 describes the heat exchange capacity between a flow and the solid material:

$$Nu_D = \frac{hD}{k} \quad (\text{II.19})$$

$h$  is the heat exchange coefficient,  $D$  is the typical size of the solid and  $k$  is the thermal conductivity of the fluid. The Nusselt number is the ratio of the convection over the diffusion of heat between the solid material and the fluid [13]. The Nusselt of a sphere in the case of free convection [13] is :

$$Nu_{sphere} = 2 + \frac{0.589Ra_D^{1/4}}{[1 + (0.469/Pr)^{9/16}]^{4/9}}. \quad (\text{II.20})$$

## II.2 Models and simulation tools for criticality in debris beds

Criticality in fuel debris beds may occur when suitable conditions (porosity, presence of liquid water) are fulfilled. To evaluate the reactivity of the system, we need to properly model neutron transport. For this purpose, in the following we will present some relevant simplified methods and sophisticated simulation codes. Fuel debris beds are often characterized by disordered geometries, so specific tools are needed to generate suitable random geometries for neutron transport.

### II.2.1 Neutron transport

#### The Boltzmann equation

In order to compute the neutron density throughout the system, and thus deduce the associated reactivity, one must solve the problem of neutron transport [23] [24]. Neutrons created by fission will travel through and interact with matter. Such interactions, in the form of

neutron-nuclei collisions, will determine the neutron energy and direction, which in turn, will affect the probability of interaction with matter.

The phase-space coordinates of the neutron density are listed here:

- Spatial location:  $\vec{r} = [x, y, z]$ ;
- Velocity: norm  $v$  and angular direction  $\vec{\Omega}$  (energy  $E$  can be used as  $E = \frac{1}{2}mv^2$  instead of  $v$ );
- Time:  $t$ .

The neutron density in phase space is defined as the average number of neutrons in  $d^3r$  around a point  $r$ , of velocity between  $v$  and  $v + dv$ , of direction in solid angle  $d\vec{\Omega}$  around  $\Omega$  :  $n(\vec{r}, v, \vec{\Omega}, t)d^3rdvd\Omega$ . The neutron flux is defined as  $\phi(\vec{r}, v, \vec{\Omega}, t) = v \times n(\vec{r}, v, \vec{\Omega}, t)$  [23].

The neutron current  $\vec{J}$  corresponds to the average number of neutrons going through a unit surface  $dA$  (with the vector  $\vec{p}$  normal to the surface  $A$ ) per unit time integrated over all directions:  $\vec{J}(\vec{r}, E, t) = \int_{4\pi} \vec{p}n(\vec{r}, v, t)d\Omega$  [24].

The Boltzmann equation is obtained by introducing a balance of neutron population into the volume  $dV$ . The terms appearing in the balance are:

- Neutrons produced by fission and sources :

$$+ d^3rdvd^2\vec{\Omega}dt\chi(v) \int_0^{+\infty} dv' \frac{1}{4\pi} \int_{4\pi} d^2\vec{\Omega}' v \Sigma_f(\vec{r}, v') \phi(\vec{r}, v', \vec{\Omega}', t) \quad (\text{II.21})$$

$$+ S(\vec{r}, v, \vec{\Omega}, t)d^3rdvd^2\Omega dt. \quad (\text{II.22})$$

- Arrival of neutrons in the volume  $dV$  by diffusion in

$$+ d^3rdvd^2\vec{\Omega}dt \int_{4\pi} d^2\vec{\Omega} \int_0^{+\infty} dv' [\Sigma_s(\vec{r}, v' \rightarrow v, \vec{\Omega}' \rightarrow \vec{\Omega}, t) \phi(\vec{r}, v', \vec{\Omega}', t)]. \quad (\text{II.23})$$

with  $\Sigma_s$  the cross section of diffusion from  $v', \vec{\Omega}'$  to  $v, \vec{\Omega}$ .

- Disappearance of neutrons by collision in:

$$- \Sigma_t(\vec{r}, v, \vec{\Omega}, t) \phi(\vec{r}, v, \vec{\Omega}, t) d^3rdvd^2\Omega dt \quad (\text{II.24})$$

with the total cross section  $\Sigma_t = \Sigma_a + \Sigma_s$ .

- Disappearance of neutrons by transport in :

$$- \text{div}[J(\vec{r}, v, \vec{\Omega}, t)] d^3rdvd^2\Omega dt = -\text{div}[\vec{\Omega}\phi(\vec{r}, v, \vec{\Omega}, t)] d^3rdvd^2\Omega dt. \quad (\text{II.25})$$

thanks to neutrons leakage (by using the divergence theorem).

The variation of neutrons in the volume  $d^3V = d^3r$  is written as :

$$[n(\vec{r}, v, \vec{\Omega}, t + dt) - n(\vec{r}, v, \vec{\Omega}, t)] d^3rdvd^2\Omega = \frac{\partial n(\vec{r}, v, \vec{\Omega}, t)}{\partial t} dt d^3rdvd^2\Omega \quad (\text{II.26})$$

Here, no distinction between the origin of neutrons (prompt or delayed) is made. All neutrons are assumed to be generated promptly from fission. Eventually the first form of the

Boltzmann equation is obtained for neutron transport in a volume  $d^3r$ , called the integral-differential form:

$$\begin{aligned} \frac{\partial n(\vec{r}, v, \vec{\Omega}, t)}{\partial t} dt d^3r dv d^2\Omega = & d^3r dv d^2\Omega dt \chi(v) \int_0^{+\infty} dv' \frac{1}{4\pi} \int_{4\pi} d^2\Omega' v \Sigma_f(\vec{r}, v') \phi(\vec{r}, v', \vec{\Omega}', t) \\ & + d^3r dv d^2\Omega dt \int_{4\pi} d^2\Omega \int_0^{+\infty} dv' [\Sigma_s(\vec{r}, v' \rightarrow v, \vec{\Omega}' \rightarrow \vec{\Omega}, t) \phi(\vec{r}, v', \vec{\Omega}', t)] \\ & + S(\vec{r}, v, \vec{\Omega}, t) d^3r dv d^2\Omega dt \\ & - \Sigma_t(\vec{r}, v, \vec{\Omega}, t) \phi(\vec{r}, v, \vec{\Omega}, t) \\ & - \text{div}[J(\vec{r}, v, \vec{\Omega}, t)] d^3r dv d^2\Omega dt \end{aligned} \quad (\text{II.27})$$

We introduce the net disappearance operator  $L$ :

$$L\phi(\vec{r}, v, \vec{\Omega}) = +\Sigma_t(\vec{r}, v, \vec{\Omega}) \phi(\vec{r}, v, \vec{\Omega}) + \Omega \cdot \nabla \phi(\vec{r}, v, \vec{\Omega}) - \int_{4\pi} d^2\vec{\Omega}' \int_0^{+\infty} dv' \Sigma_s(\vec{r}, v' \rightarrow v, \vec{\Omega}' \rightarrow \vec{\Omega}) \phi(\vec{r}, v', \vec{\Omega}') \quad (\text{II.28})$$

and the fission operator  $F$ :

$$F\phi(\vec{r}, v, \vec{\Omega}) = \chi(v) \int_0^{+\infty} dv' \frac{1}{4\pi} \int_{4\pi} d^2\vec{\Omega}' v \Sigma_f(\vec{r}, v') \phi(\vec{r}, v', \vec{\Omega}'). \quad (\text{II.29})$$

The stationary Boltzmann equation takes now the form:

$$L\phi(\vec{r}, v, \vec{\Omega}) = F\phi(\vec{r}, v, \vec{\Omega}) + S(\vec{r}, v, \vec{\Omega}). \quad (\text{II.30})$$

The stationary Boltzmann operator is defined  $B = F - L$ . An eigenvalue formulation of the Boltzmann equation can be now introduced by rescaling the average fission yield  $\nu$  by a factor  $k$ :  $\nu \rightarrow \nu/k$ . This corresponds to asking whether there exists a value of  $k > 0$  such that the system is critical, in the absence of an external source  $S$ .

$$L\phi_k(\vec{r}, v, \vec{\Omega}) = \frac{F}{k} \phi_k(\vec{r}, v, \vec{\Omega}). \quad (\text{II.31})$$

where  $k$  are the eigenvalues and  $\phi_k$  the associated eigenfunctions. In particular, the fundamental eigenvalue  $k_0$  represents the multiplication factor ( $k_0 = k_{eff}$ ) and the fundamental mode  $\phi_{k_0}$  represents the asymptotic distribution of the neutron population in the core [24].

### Solving the Boltzmann equation

In order to compute the neutron population density in a system, we must solve the neutron transport equation. The methods can be classified in two categories:

- Deterministic methods: the Boltzmann equation is solved thanks to discretization of the phase space and introduction of some approximations, such as the use of energy groups or using a consistent geometry mesh. The results can be obtained quickly once the phase space has been discretized, by using efficient methods of linear algebra [24].

- Monte Carlo (stochastic) methods: in this case the neutrons are simulated individually from birth to death. No physical approximations are required but the statistical convergence time can be computationally expensive. This is traditionally assumed as the reference method [25].

More details about the codes and the solution methods will be given in [II.2.2](#).

## II.2.2 Simulation codes for neutron transport

The codes described below are commonly used at CEA to assess the criticality risk of a debris bed.

### Deterministic code: Apollo-2

The Apollo-2 code [26] is a deterministic transport code. It is written in ESOP which is an extension of the Fortran 77 language proposed in the 1980s at CEA. Apollo-2 is the reference lattice code for CEA, EDF and Framatome. During a criticality calculation, the code solves the eigenvalue formulation of the Boltzmann transport equations. The implemented methods of resolution are: the method of characteristic (MOC) and the Pij method [26]. In the Sn method, which is a MOC method, angular variables are discretized by discrete ordinates and weighted quadrature sets. Then the transport equation is solved on each direction of the discrete ordinates. When the number of discrete angles is increased, the solution of the Sn method converges to the exact solution [27].

Porous media can be represented in Apollo-2 using an internal model. Indeed, the code includes a calculation method for the reactivity of granular media named the double heterogeneity model [28]. It allows modelling media containing a random distribution of grains in a matrix. It was initially developed to evaluate the impact of  $PuO_2$  grains in a  $UO_2$  matrix for MOX modelling. This method allows also the modelling Tristructural-isotropic (TRISO) fuel. For the applications considered in this thesis, the grains can be used to represent molten core spheres and the matrix can be used to represent water. The input parameters of this model are the size of the grains (radius of the spheres) and the filling rate of the matrix by the grains (the volume of the grains divided by the total volume). The number of different grains in the matrix is arbitrary. However, adding more than 5 different sizes of grains would make the calculation time consuming.

### Stochastic code: TRIPOLI-4<sup>®</sup>

TRIPOLI-4<sup>®</sup> is the reference Monte Carlo code developed at CEA since the 1990s [25] used by the CEA and EDF. It can be used for both eigenvalue and fixed-source calculations. Neutrons are simulated in the usual energy range ( $10^{-5}$  eV to 20 MeV). The simulated particles are simulated with continuous-energy nuclear data representation and the libraries required for the calculations (scattering, absorption, scattering cross sections, fission spectra, etc.) are given in ENDF format files [29]. Interpolation models are implemented to obtain the effective cross-sections between the temperature values at which the nuclear data were evaluated. A large number of particles is simulated and the average behaviour of the transported particles approaches the neutrons density when the number of simulated particles is sufficiently large [25]. This code can yield the fission rates and the neutron flux in the geometry. The IFP (Iterated Fission Probability) method is used [30] to obtain the kinetics parameters of the simulated system.

### II.2.3 Quasi-static method

To simulate power transients, different strategies can be applied. The neutron transport equation should be solved taking into account the time-evolution of the physical conditions.

The quasi-static method [31] is often used to solve space and time dependent neutron transport problem by introducing some suitable approximations in order to reduce the computational cost. It corresponds to the factorization of the amplitude and the shape of the neutron flux (as the nuclear power distribution is proportional to the neutron flux):

$$\Phi(\vec{r}, \vec{\Omega}, E, t) = \Phi(\vec{r}, \vec{\Omega}, E) \times n(t) \quad (\text{II.32})$$

with  $\Phi$  is the neutron flux and  $n$  is the amplitude of the neutron flux in the system. The shape factor  $\Phi(\vec{r}, \vec{\Omega}, E)$  is obtained by solving the stationary form of the Boltzmann equation (defined in II.31). The evolution of the magnitude is solved using the neutron kinetics equation as defined in I.3.4. Each time, a static calculation is done followed by a magnitude correction computed with the point kinetics equation. Therefore the amplitude is time-dependent and the shape might be not updated or with a lower frequency than the amplitude. This method leads to computational time gain during transient simulations.

An improved quasi-static method (IQS) has been also proposed, which consists in doing point kinetics calculations on small-time scales and shape calculations (neutron transport calculation) on long-time scales [32].

The quasi-static method may be specially efficient to simulate prompt power transients. When this event occurs in a very short-time window ( $\approx 20$  ms [33]) the only physical quantity that changes significantly during this interval is the fuel temperature. Since fuel and the moderator position/density do not sensibly change during the power transient, the update of the shape can be performed quite seldom during this kind of transients. Therefore, the quasi-static method is relevant for power excursions and as such will make the multi-physics simulations faster than a full-scale Monte-Carlo or deterministic calculations.

### II.2.4 Generation of random geometries

#### Neutron transport in random geometries

Disordered media with multi-scale heterogeneities must be taken into account in many criticality applications. In this context, the propagation of particles in these structures is often characterized and modelled using linear transport theory in random media [34]. There are two methods for this purpose: a reference method and an approximate method.

#### The reference method

So-called reference results can be obtained by generating a large number of random geometries describing the medium through which the particles are transported. For each geometrical realization, the Boltzmann equation is solved, (for example using the Monte-Carlo transport code TRIPOLI-4<sup>®</sup>), and, the quantities of interest, such as the particle flux, are calculated. Finally, the statistical averages of the observables are determined over all the realizations. This strategy, which is in principle exact, requires a numerical tool for modelling stochastic geometries and generates an extremely high calculation time [35]. In the literature, there are different classes of random geometries suitable for transport-related applications, such as stochastic inclusions [36], in which objects are placed in a domain according to a given probability law, or random tessellations [37], [38], in which a domain is partitioned into polyhedra by sampling hyperplanes according to a given law. The CEA has recently developed a software for the generation of different geometry models, in  $d=1, 2$  and  $3$  [39] [35].

## Random tessellations

Poisson geometries represent an important example of random tessellations [37], [38]: a number of hyperplanes are sampled according to a Poisson law whose intensity depends on the dimension  $d$  and a parameter corresponding to the density of the tessellation. Then, each hyperplane is randomly drawn in order to ensure the spatial homogeneity of the tessellation, and its intersections with the polyhedra making up the tessellation are calculated. An arbitrary line will eventually be cut by the polyhedra into exponentially distributed segments (chords). The mean length of the chords characterizes the scale of the geometric disorder (to be compared with the typical size of the particle displacements in the modelled medium) and is inversely proportional to the density of the tessellation. Voronoi tessellations [37], [38] are also very common. Points (germs) of a homogeneous Poisson process in the domain to be partitioned are randomly drawn. For each germ, Voronoi cells are then constructed, defined as the regions of the points in space that are closer to the germ under consideration than to any other germ [35].

Effects of anisotropy and spatial heterogeneity can possibly be taken into account [40] [41]. Once the tessellations have been generated, the so-called colouring procedure is carried out, in which each polyhedron is assigned a material composition, such as water or fuel, respecting the volume proportions. Colouring potentially induces preferential paths for the particles, which can be studied using percolation theory [42]. An example of Voronoi, Poisson and box geometries is illustrated in the figure II.6.

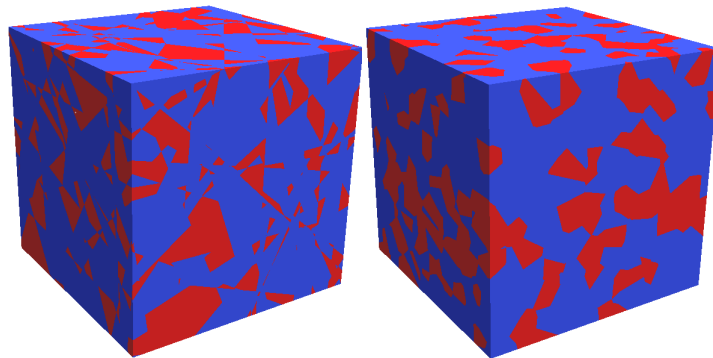


Figure II.6: Example of two-phase geometries generated with Poisson generator (left) and Voronoi generator (right).

## The approximate models

A complementary approach consists in taking into account the disorder without explicitly modelling the geometry, based on homogenization theory: effective but approximated Boltzmann equations can be obtained, such as the Levermore-Pomraning model [34], for each material of the stochastic mixture, with coupling terms condensing the effects of the chord distribution. There is also an equivalent stochastic model that can be solved by Monte-Carlo simulation (Chord Length Sampling algorithm [43]). These methods are much less costly in terms of computation time, but their scope of validity must be established using reference solutions [44]. Moreover, they only provide access to the mean of the quantities of interest and not to their statistical distribution.

## II.3 Statistical learning as a tool to accelerate calculations

The neutronics and thermal-hydraulics calculations can be time-consuming. In the case of transient simulations, several calculations must be done to capture the behaviour of the system. The total simulation time of a transient can thus become prohibitive [35]. Therefore, in order to accelerate the computation, surrogate models can be conveniently used to estimate the physical quantities of interest in the cases where an extreme accuracy is not required. These simpler models can generally quickly compute the outputs [45]. One interesting property of surrogate models is the capability of generalization: it means that such models would be able to predict values in a phase space which was not entirely explored during the training. The drawback is usually a lower accuracy. In this section, we will present two kinds of surrogate models which can be useful to speed up the simulation of critical debris beds.

### II.3.1 Overview of surrogate models

In the field of numerical simulation, a simulation code can be typically represented as  $y = f(x)$ , where  $x \in \mathbb{R}^p$  are the inputs and  $y \in \mathbb{R}$  the output. Here only one output  $y$  is taken, but multi-dimensional generalizations are possible. Thus, the assumption is done that there is a function that maps  $\mathbb{R}^p$  into  $\mathbb{R}$ . Building a surrogate-model of  $f(x)$  consists in using a parametric function  $h(x, \beta)$  where the parameters  $\beta$  will be adjusted to fit as accurately as possible the function  $f(x)$  over a given domain [45]. Usually, the adjustment of the parameters is done by minimising a loss function, which is obtained by the average of the quadratic difference between  $f(x)$  and  $h(x, \beta)$ . This average is calculated thanks to the statistical distribution of the inputs  $x$ , denoted by  $p(x)$  [45]. The *functional risk* is defined as the expected value of the loss function:

$$\beta_{adjusted} = \arg \min_{\beta} \int (f(x) - h(x, \beta))^2 p(x) dx. \quad (\text{II.33})$$

Generally the *functional risk* to minimize can not be calculated as the statistical distribution of  $f(x)$  can not be calculated. However, the *functional risk* can be approached by the *empirical risk* calculated thanks to a set of examples  $B = \{(x_i, y_i = f(x^i))_{1, \dots, n}\}$  where  $x_i$  are obtained from the statistical function  $p(x)$ .

$$\widehat{\beta}_B = \arg \min_{\beta} \frac{1}{n} \sum_{i=1}^n (f(x^{(i)}) - h(x^{(i)}, \beta))^2. \quad (\text{II.34})$$

This approach raises the problem of *over-fitting* [45]. Indeed, the solution obtained by minimising the empirical risk can be sensibly different from the solution obtained by minimising the functional risk:

$$\int (f(x) - h(x, \beta))^2 p(x) dx \neq \frac{1}{n} \sum_{i=1}^n (f(x^{(i)}) - h(x^{(i)}, \beta))^2. \quad (\text{II.35})$$

The risk of over-fitting depends on the computation capabilities of the family of the functions  $h(x, \beta)$ . However, several solutions exist to control the risk of over-fitting. One such method is the regularisation method, which consists in adding to the loss function a penalising term defined on  $h(x, \beta)$  [45]. Another regularisation method, named *ridge regression*, consists in adding to the loss function a term proportional to the euclidean norm of the parameters [45]. In the machine learning field, in addition to the penalising methods, statistical methods are used to estimate the functional risk. This risk, named generalisation error, is based on the tactic of *cross validation*. By applying this method, the database  $B$  must be



decomposed in two datasets. The first is the learning dataset  $B_{learning}$ , which will be used to train the model and obtain the optimal parameter values [45]. The second is the test dataset  $B_{test}$  used to evaluate the model. This yields:

$$\mathcal{B} = \mathcal{B}_{learning} \oplus \mathcal{B}_{test} \quad (i.e. : \mathcal{B} = \mathcal{B}_{learning} \cup \mathcal{B}_{test}, \quad \mathcal{B}_{learning} \cap \mathcal{B}_{test} = \emptyset) \quad (\text{II.36})$$

The adaptation of the parameters of the model  $h(x, \beta)$  is done on the learning dataset and the estimation of the *functional risk* is done thanks to the *empirical risk* calculated on the test database. This process can be done on several pairs of sets  $B_{learning}, B_{test}$ . The method of  $K$  - *cross validation* is obtained by partitioning the database in  $K$  sub-sets  $B = \oplus_{k=1}^K B^k$  [45]. For each value of  $k = 1, 2, \dots, K$ , the model  $h(x, \beta)$  is trained using all the datasets but the  $B^k$ . Thus, for a value of  $k = 1, 2, \dots, K$ , the generalisation error is estimated by the test error and the value of the loss function is evaluated on the set  $B^k$ . The generalization error is therefore estimated by means of the empirical error of the  $K$  test errors. This method presents the benefits of controlling the presence of *outliers* by analysing the  $K$  statistical distributions of the test errors.

In addition to the optimization method to calculate the best fitting parameters  $\beta$ , the choice of the functions families  $h(x, \beta)$  determines the quality of the surrogate model and its generalisation capabilities. In the next subsections, we will discuss, two such families, namely, the linear models and the artificial neural networks.

### II.3.2 Linear models

The linear models [45] are defined by a linear combination of a family of functions  $h_j(x)$ ,  $j = 0, 1, \dots, p$  called regressors, parametrized by the coefficients  $\beta_j$ ,  $j = 1, \dots, p$ :

$$h(x, \beta) = \sum_{j=0}^p \beta_j * h(x_j) \quad (\text{II.37})$$

The simplest model is a polynomial model of degree 1. If  $x \in \mathbb{R}^d$ , the regressors simply correspond to the components of the vector  $x$ , the first regressor corresponding to the constant part of the model [45].

$$h(x, \beta) = \beta_0 + \sum_{j=0}^d \beta_j x_j, \quad x = (x_1, x_2, \dots, x_d) \quad (\text{II.38})$$

The polynomial approximation of degree  $p$  can also be put in the form of a linear model. To simplify, taking the example with a single dimension  $x \in \mathcal{R}$ , the regressors are then the monomials  $x_i$ ,  $i = 0, 1, \dots, p$ :

Directly solving the best fitting parameters provides a method to obtain the optimized value of the parameter to fit the data with least squares optimization. Least squares estimation method might be used to choose the coefficient values in order to minimize the residual sum of squared errors:

$$LS(\beta) = \sum_{i=1}^N (y_i - f(x_i))^2 \quad (\text{II.39})$$

In equation II.39 we provide the least square function of linear regression applied on one parameter  $\beta$  on a set of  $N$  points such as  $(x_1, y_1, \dots, x_n, y_n)$ .

To obtain the linear regression of  $p$  parameters which minimizes the least squares, we should consider  $H$  the matrix of  $N \times (p + 1)$  with each row made of an inputs vector and  $y$

the  $N$  vector with each row composed of an output vector and  $\beta$  is the parameters vector. Therefore the residual sum of square can be written as:

$$RSS(\beta) = (y - H\beta)^T (y - H\beta). \quad (\text{II.40})$$

By differentiation we obtain:

$$\begin{aligned} \frac{\partial RSS(\beta)}{\partial \beta} &= -2H^T (y - H\beta) \\ \frac{\partial^2 RSS(\beta)}{\partial \beta \partial \beta^T} &= -2H^T H. \end{aligned} \quad (\text{II.41})$$

Assuming that the  $HH^T$  is positive definite, the first derivation is zero:

$$H^T (y - H\beta) = 0. \quad (\text{II.42})$$

which yields the unique solution:

$$\hat{\beta} = (H^T H)^{-1} H^T y. \quad (\text{II.43})$$

Therefore, the parameters of a linear model can be calculated quickly and efficiently. However, when the matrix  $H$  is poorly conditioned, regularisation methods can be used as the *ridge regression* based on the Euclidean penalisation of the parameters  $\beta$  using parameters  $\lambda$  [45]. In this case, the solution in the form of the equation II.44 is obtained:

$$\hat{\beta} = (H^T H + \lambda I_d)^{-1} H^T y. \quad (\text{II.44})$$

Here, the parameter  $\lambda$  can be obtained by cross validation [46]. This method may introduce a bias in the parameter estimation of the model. However, this method limits the error variance and it decreases the dependence to the potential noise on the data  $y$ .

### II.3.3 Artificial neural networks

Another class of surrogate models is provided by artificial neural networks (ANN). This is a model inspired by the architecture of biological neural networks. Artificial neurons are connected to each other to compute the inputs and predict the output values after a training procedure [45].

In this model, one neuron is made of one or several inputs which are multiplied by weights and then computed with an activation function. A representative scheme of one neuron is described in figure II.7: the parameters of the neurons are the weights  $w_{ij}$  the threshold  $\beta_j$ , the  $x_n$  are the inputs and the  $o_j$  is the output of the neuron.

To build the meta-models we used the classical neural networks for this type of problem, based on the MLP model, Multi Layered Perceptron [45]. The structure of this model is defined by a sequence of layers, from the input layer to the output layer. The layers gather neurons connected to the neurons of the previous layer (seen figure II.8). Mathematically, the MLP neural network model is a composition of functions where each function is coded by a layer. Each layer is associated with a matrix of weight  $W$ , the biases  $b$  and a activation function. With these notations we obtain the mathematical form of an MLP with  $S$  the number of layers:

$$\begin{aligned} h(x, \beta) &= h_s \circ h_{s-1} \circ \dots \circ h_1(x) \\ h(z_\alpha)_\alpha &= \phi_\alpha(W_\alpha z_\alpha + b_\alpha), z_0 = x, \alpha = 1, 2, \dots, S \end{aligned} \quad (\text{II.45})$$

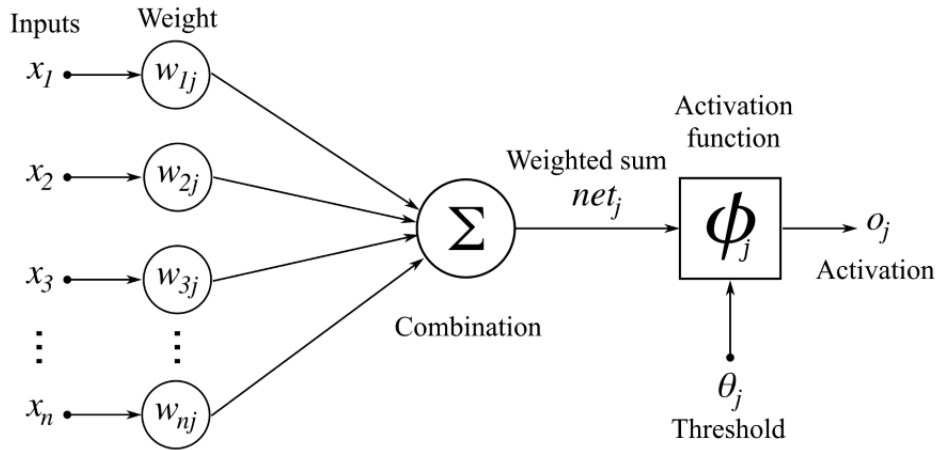


Figure II.7: Diagram of an artificial neuron [47].

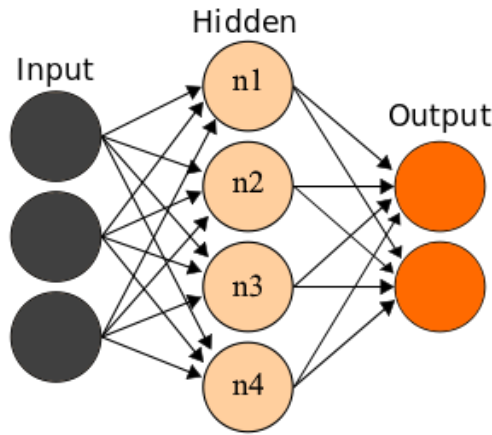


Figure II.8: Shallow artificial neural network made of 4 neurons (in the hidden layer), with 3 inputs and 2 outputs [47].

The only non-linearities are those introduced by the activation functions  $\phi_\alpha$ . The activation functions apply to each of the components of the synaptic potential  $u_\alpha = W_\alpha z_\alpha - 1 + b_\alpha$  [45]. The most commonly used activation functions are the logistic function  $\phi(u)_\alpha = (1 + \exp(-u_\alpha))^{-1}$ , the hyperbolic tangent or the function called ReLU (*Rectified Linear Unit*) defined by  $\phi_\alpha(u) = \max(0, u_\alpha)$ .

The parameters of the neural network  $\beta = (W, b)_{\alpha=[1:S]}$  are calculated by minimizing a loss function. In non-linear regression problems, the loss function is the mean square deviation as defined for linear models by equation II.33. Noting  $B_l$  the examples used for learning the model, the loss function is written as:

$$\mathcal{L}(B_l; \beta) = \frac{1}{B_l} \sum (x^i, y^i \in B_l) (y^i - h(x^i, \beta))^2. \quad (\text{II.46})$$

Given the non-linearity of the loss function with respect to of the coefficients, the calculation of the coefficients is obtained iteratively by a gradient descent [45]. From an initial value of the coefficients, an iterative algorithm is used to minimize the loss function in :

$$\beta(t+1) = \beta(t) - \eta \nabla_{\beta} \mathcal{L}(B_l; \beta(t)). \quad (\text{II.47})$$

This algorithm therefore requires the calculation of the gradients  $\nabla h(x(i), \beta)$  for each example  $x(i)$ . A prominent advantage of neural networks is the relatively efficient computation of these gradients. The calculation of the gradients is based on the gradients back-propagation, calculated from the output layer to the input layer (hence the name given to the algorithm). In other words, the gradients of the output  $y$  are the first to be computed with respect to the parameters of the last layer, then the gradients with respect to the parameters of the second last layer which depend on the first gradients, and so on until the entry layer.

Deep neural networks are a class of artificial neural networks (ANN) having more than one hidden layer of neurons: these artificial neural networks were developed for complex tasks as image recognition or playing real-time strategy games [45].

The computation of the minimisation of the *loss function* by batch is described in the algorithm 1.

---

**Algorithm 1** Learning in batch mode.

---

- 1: Learning database  $B = \{(x^{(i)}, y^{(i)}), i = 1, \dots, n\}$
  - 2:  $\Delta = 0$
  - 3: **for**  $i=1$  to  $n$  **do**
  - 4:   Propagation of the example  $i : x^{(i)} \rightarrow \hat{y}^{(i)} = h(x^{(i)}, \beta)$
  - 5:   Back-propagation : gradients calculation  $\delta^{(i)} = \nabla_{\beta} h(x^{(i)}, \beta)(\hat{y}^{(i)} - y^{(i)})$
  - 6:   Calculation of the gradient  $\Delta = \Delta + \delta^{(i)}$
  - 7: **end for**
  - 8: Modification of the coefficient  $\beta = \beta - \eta \Delta$
  - 9: Test of a stopping criteria (quadratic average error, number of cycle, etc.), else, go back to 2
- 

One interesting feature of the multi-layer ANN is that the gradient  $\nabla_{\beta} h(x^{(i)}, \beta)$  can be obtained very easily by the method of *back propagation* [48] [49].

As every method based on gradient descent, the reached optimum is just local. To avoid the pitfall of local minima, or when the database are very large, the method of *stochastic gradient* can be use [45]. It is described in the algorithm 2. In this case, the parameters adjustment  $\beta$  is done using the error calculated for each example  $x^{(i)}$  :

$$\beta(t+1) = \beta(t) - \eta \nabla_{\beta} h(x^{(i)}, \beta(t))(h(x^{(i)}, \beta(t)) - y^{(i)}). \quad (\text{II.48})$$

---

**Algorithm 2** Learning by stochastic gradient descent.

---

- 1: Random initialisation of the network  $\beta = \beta_0$
  - 2: Random mixing of the learning example  $\mathcal{B} = \{\mathbf{x}^{(i)}, y^{(i)}, i = 1, \dots, n\}$
  - 3: **for**  $i=1$  to  $n$  **do**
  - 4:   Propagation of the example  $i : x^{(i)} \rightarrow \hat{y}^{(i)} = h(x^{(i)}, \beta)$
  - 5:   Back-propagation : calculation of the gradients  $\delta^{(i)} = \nabla_{\beta} h(x^{(i)}, \beta)(\hat{y}^{(i)} - y^{(i)})$
  - 6:   Modification of the parameters  $\beta = \beta - \eta \delta^{(i)}$
  - 7: **end for**
  - 8: Test of a stopping criteria (quadratic average error, number of cycle, etc.), else, go back to 2
- 

In the case where the number of examples is large, the algorithm of the stochastic gradient descent is replaced by the algorithm of gradient *batch* [45]. It is described in the algorithm 3.

The adaption of the parameters is done by considering a small group (a batch) of examples from the database:

---

**Algorithm 3** Learning in mini batch mode.

---

- 1: Learning database  $\mathcal{B} = \{x^{(i)}, y^{(i)}, i = 1, \dots, n\}$
  - 2: Random mixing of the learning example  $\mathcal{B}$
  - 3: Partition of the database  $\mathcal{B} = \oplus_{k=1}^K \mathcal{B}^{(k)}$  of approximatively the same size
  - 4: **for**  $k=1,2,\dots,K$  **do**
  - 5:   Learning in batch mode of the examples in the set of batch  $\mathcal{B}^{(k)}$
  - 6: **end for**
  - 7: Test of stopping criteria (quadratic average error, number of cycle, etc.), else, go back to 2
- 

Surrogate-models can be extremely efficient under certain conditions to estimate the physical quantity of interest. The linear model is usually the first one that must be assessed. However, if the target performances is not met, the use of ANN can be an option to increase the accuracy of the surrogate model.

## II.4 Synthesis

The simulation of neutron transport and thermal-hydraulics in debris beds requires sophisticated models. In the field of thermal-hydraulics, codes as MC3D or COCOMO provide efficient tools to take into account the cooling mechanism of debris beds. The neutronics field needs also a detailed treatment to describe the criticality of debris beds. Available codes solve the neutron transport equation using deterministic methods (as Apollo-2) or Monte Carlo method (as TRIPOLI-4<sup>®</sup>). Models as double-heterogeneity or Poisson tessellations pave the way to the simulation of disordered media. Statistical models have been presented. Transient simulation involve to do several calculations which requires high computing times. The use of surrogate-models may allow us to perform fast estimations of some physical quantities and thus speed up the transient simulation.

# Bibliography

- [1] R. Kimura and T. Yutaka, "Development of analysis code PORCAS-f for dynamic behavior of re-critical fuel debris," *ICAPP Proceedings*, 2017.
- [2] P. Kuan, "Tmi-2 upper-core particle bed thermal behavior," tech. rep., EG&G Idaho, Inc, August 1987. <https://tmi2kml.inl.gov/Documents/9b-Data-Accident/EGG-TMI-7757>,
- [3] R. J. Lipinski, "A particle-bed dryout model with upward and downward boiling," *Transport American Nuclear Society ; (United States)*, vol. 35, Jan 1980.
- [4] S. Ergun, "Fluid flow through packed columns," *Chemical Engineering Progress*, vol. 48, pp. 89–97, 1952.

- [5] A. E. Scheidegger, *The physics of flow through porous media*. University of Toronto Press, 1957.
- [6] P. C. Carman, "The determination of the specific surface area of powder," *I. J. Soc. Chem. Ind.*, vol. 57, 1937.
- [7] E. Takasuo, "An experimental study of the coolability of debris beds with geometry variations," *Annals of Nuclear Energy*, vol. 92, pp. 251–261, 2016.
- [8] A. Reed, *The effect of channeling on the dry-out of heated particulated beds immersed in a liquid pool*. PhD thesis, Massachusetts Institute of Technology, Cambridge, 1982.
- [9] K. Hu and T. Theofanous, "On the measurement and mechanism of dryout in volumetrically heated coarse particle beds," *Int. J. Multiphase Flow*, vol. 17, 1991.
- [10] T. Schulenberg and U. Müller, "An improved model for two-phase flow through beds of coarse particles," *International Journal of Multiphase Flow*, vol. 13, no. 1, pp. 87–97, 1987.
- [11] V. X. Tung and V. K. Dhir, "Quenching of a hot particulate bed by bottom quenching," *Proceedings of ASME-JSME Thermal Engineering Joint Conference*, 1983.
- [12] W. Schmidt, "Interfacial drag of two-phase flow in porous media," *International Journal of Multiphase Flow*, vol. 33, no. 6, pp. 638 – 657, 2007.
- [13] D. P. Incropera, Frank P.; DeWitt, *Fundamentals of Heat and Mass Transfer (5th ed.)*. Wiley India Pvt. Limited, 2002.
- [14] K. L. Thomsen, *Review of the TMI-2 accident evaluation and vessel investigation projects*. No. 1004 in Risø-R, Risø National Laboratory, Mar 1998. OCLC: 245704187.
- [15] S. Yakush, P. Kudinov, and T.-N. Dinh, "Modeling of two-phase natural convection flows in a water pool with a decay-heated debris bed," *Proceedings of ICAPP*, vol. 2, pp. 1141–1150, 2008.
- [16] G. Berthoud and M. Valette, "Development of a multidimensional model for the premixing phase of a fuel-coolant interaction," *Nuclear Engineering and Design*, vol. 149, no. 1, pp. 409 – 418, 1994.
- [17] M. Buck and G. Pohlner, "Ex-vessel debris bed formation and coolability – challenges and chances for severe accident mitigation," *Proceedings of ICAPP*, vol. 2, pp. 1217–1226, 2016.
- [18] B. Raverdy, R. Meignen, L. Piar, S. Picchi, and T. Janin, "Capabilities of mc3d to investigate the coolability of corium debris beds," *Nuclear Engineering and Design*, vol. 319, pp. 48 – 60, 2017.
- [19] N. Tutu, T. Ginsberg, J. Klein, C. Schwarz, and J. Klages, "Debris bed quenching under bottom flood conditions (in-vessel degraded core cooling phenomenology)," *NUREG proceeding*, 1984.
- [20] T. Ginsberg, J. Klein, J. Klages, Y. Sanborn, C. E. Schwarz, J. C. Chen, and L. Wei, "Experimental and analytical investigation of quenching of superheated debris beds under top-reflood conditions. final report," 1986.
- [21] N. Chikhi and F. Fichot, "Experimental and theoretical study of large scale debris bed reflood in the pearl facility," *Nuclear Engineering and Design*, vol. 312, pp. 48 – 58, 2017.

- [22] R. Meignen, S. Picchi, J. Lamome, B. Raverdy, S. C. Escobar, and G. Nicaise, “The challenge of modeling fuel–coolant interaction: Part i – premixing,” *Nuclear Engineering and Design*, vol. 280, pp. 511 – 527, 2014.
- [23] P. Reuss, *Précis de neutronique*. Génie Atomique, EDP Sciences, 2003.
- [24] S. Bell, George I. ; Glasstone, *Nuclear Reactor Theory*. Van Nostrand Reinhold Company, 1970.
- [25] E. Brun, A. Zoia, and al., “Tripoli-4®, cea, edf and areva reference monte carlo code,” *Annals of Nuclear Energy*, vol. 82, pp. 151–160, 2015.
- [26] R. Sanchez, I. Zmijarevic, M. Coste-Delclaux, E. Masiello, S. Santandrea, E. Martinolli, L. Villate, N. Schwartz, and N. Guler, “Apollo2 year 2010,” *Nuclear Engineering and Technology*, vol. 42, no. 5, pp. 474–499, 2010.
- [27] B. G. Carlson and G. I. Bell, “Solution of the transport equation by the sn method,” Oct 1958.
- [28] A. Hébert, “A collision probability analysis of the double-heterogeneity problem,” *Nuclear Science and Engineering*, vol. 115, no. 2, pp. 177–184, 1993.
- [29] M. Chadwick, P. Obložinský, M. Herman, N. Greene, R. McKnight, D. Smith, P. Young, R. MacFarlane, G. Hale, S. Frankle, A. Kahler, T. Kawano, R. Little, D. Madland, P. Moller, R. Mosteller, P. Page, P. Talou, H. Trellue, M. White, W. Wilson, R. Arcilla, C. Dunford, S. Mughabghab, B. Pritychenko, D. Rochman, A. Sonzogni, C. Lubitz, T. Trumbull, J. Weinman, D. Brown, D. Cullen, D. Heinrichs, D. McNabb, H. Derrien, M. Dunn, N. Larson, L. Leal, A. Carlson, R. Block, J. Briggs, E. Cheng, H. Huria, M. Zerkle, K. Kozier, A. Courcelle, V. Pronyaev, and S. van der Marck, “ENDF/b-VII.0: Next generation evaluated nuclear data library for nuclear science and technology,” *Nuclear Data Sheets*, vol. 107, no. 12, pp. 2931–3060, 2006.
- [30] G. Truchet, P. Leconte, A. Santamarina, E. Brun, F. Damian, and A. Zoia, “Computing adjoint-weighted kinetics parameters in tripoli-4® by the iterated fission probability method,” *Annals of Nuclear Energy*, vol. 85, pp. 17–26, 2015.
- [31] A. F. Henry, “The application of reactor kinetics to the analysis of experiments,” *Nuclear Science and Engineering*, vol. 3, no. 1, pp. 52–70, 1958.
- [32] S. Dulla, E. H. Mund, and P. Ravetto, “The quasi-static method revisited,” *Progress in Nuclear Energy*, vol. 50, no. 8, pp. 908 – 920, 2008. In Honour of Prof. Bruno Montagnini.
- [33] J. R. Lamarsh and A. J. Baratta, *Introduction to Nuclear Engineering*. Prentice Hall, 2001.
- [34] G. C. Pomraning, *Linear Kinetic Theory and Particle Transport in Stochastic Mixtures*. WORLD SCIENTIFIC, 1991.
- [35] C. Larmier, *Stochastic particle transport in disordered media : beyond the Boltzmann equation*. PhD thesis, (Paris Saclay), 2018.
- [36] S. Torquato, *Random heterogeneous materials: microstructure and macroscopic properties*. No. 16 in Interdisciplinary applied mathematics, Springer, 2002. OCLC: 248518949.
- [37] R. E. Miles, “Poisson flats in euclidean spaces. part i: A finite number of random uniform flats,” *Advances in Applied Probability*, vol. 1, no. 2, pp. 211–237, 1969.

- [38] J. Mecke, "Santaló, I. a., integral geometry and geometric probability, (encyclopedia of mathematics and its applications) 1. london-amsterdam-don mills-sydney-tokyo, addison-wesley publishing company 1976. xvii, 404 s., \$ 17.50," *ZAMM - Journal of Applied Mathematics and Mechanics / Zeitschrift für Angewandte Mathematik und Mechanik*, vol. 59, no. 6, pp. 286–286, 1979.
- [39] C. Larmier, F.-X. Hugot, F. Malvagi, A. Mazzolo, and A. Zoia, "Benchmark solutions for transport in  $d$ -dimensional markov binary mixtures," *Journal of Quantitative Spectroscopy and Radiative Transfer*, vol. 189, Sep 2016.
- [40] A. Marinosci, C. Larmier, and A. Zoia, "Neutron transport in anisotropic random media," *Annals of Nuclear Energy*, vol. 118, pp. 406–413, 2018.
- [41] C. Larmier, A. Marinosci, and A. Zoia, "Chord length distribution in  $d$ -dimensional anisotropic Markov media," *Journal of Quantitative Spectroscopy and Radiative Transfer*, vol. 224, pp. 403 – 414, 2019.
- [42] C. Larmier, E. Dumonteil, F. Malvagi, A. Mazzolo, and A. Zoia, "Finite-size effects and percolation properties of poisson geometries," *Phys. Rev. E*, vol. 94, p. 012130, Jul 2016.
- [43] G. Zimmerman and M. Adams, "Algorithms for monte carlo particle transport in binary statistical mixtures," *Transactions of the American Nuclear Society*, pp. 287–288, 1991.
- [44] C. Larmier, A. Lam, P. Brantley, F. Malvagi, T. Palmer, and A. Zoia, "Monte carlo chord length sampling for  $d$ -dimensional markov binary mixtures," *Journal of Quantitative Spectroscopy and Radiative Transfer*, vol. 204, pp. 256 – 271, 2018.
- [45] T. Hastie, R. Tibshirani, and J. Friedman, *The elements of statistical Learning*. Springer, 2008.
- [46] G. H. Golub, M. Heath, and G. Wahba, "Generalized Cross-Validation as a Method for Choosing a Good Ridge Parameter," *Technometrics*, vol. 21, no. 2, pp. 215–223, 1979.
- [47] "Artificial neural network," 2020. Page Version ID: 975746760.
- [48] Y. LeCun, L. Bottou, Y. Bengio, and P. Haffner, "Gradient-based learning applied to document recognition," *Proceedings of the IEEE*, vol. 86, no. 11, pp. 2278–2323, 1998.
- [49] D. Rumelhart, G. Hinton, and R. Williams, "Learning representations by back-propagating errors," *Nature*, vol. 323, no. 6088, pp. 533–536, 1986. cited By 10082.



## **Part B**

# **Development of the methodology and applications to generic debris beds**



# Chapter III

## Simulating debris beds: a preliminary investigation

### Contents

---

<b>III.1 Assumptions for a generic numerical debris bed</b> . . . . .	<b>68</b>
III.1.1 Composition and mass . . . . .	68
III.1.2 Debris size distribution . . . . .	69
III.1.3 Decay heat . . . . .	73
III.1.4 Geometry of the debris bed . . . . .	74
<b>III.2 Numerical modelling</b> . . . . .	<b>78</b>
III.2.1 Neutronics . . . . .	78
III.2.2 Thermal-hydraulics . . . . .	80
III.2.3 Mesh used to simulate the debris bed . . . . .	80
<b>III.3 Debris size distribution modelling</b> . . . . .	<b>82</b>
III.3.1 Debris equivalent size in neutronics . . . . .	82
III.3.2 Debris equivalent temperature . . . . .	87
III.3.3 Debris equivalent size for steam and water flow . . . . .	87
<b>III.4 Synthesis</b> . . . . .	<b>88</b>
<b>Bibliography</b> . . . . .	<b>88</b>

---

## Introduction

In this chapter, the tools necessary to build the debris bed simulation are addressed. First, the chapter deals with the assumptions done to establish a generic test case of fuel debris bed. Then the hypotheses and the models employed to build the numerical debris bed mock-up used in this work are discussed. Finally, a focus on the debris size distribution modelling is presented.

### III.1 Assumptions for a generic numerical debris bed

In the following, we will introduce a numerical debris bed for the purpose of investigating the criticality risk and testing the related methodological aspects. Debris beds compositions and geometries are difficult to characterize exactly, and must be thoroughly determined by a careful and extensive analysis of the existing (albeit rare) experimental data and of the physico-chemical phenomena involved in their formation and evolution.

#### III.1.1 Composition and mass

For this work a representative composition of the fuel debris bed was chosen, based on the mass inventories proposed in literature [1]. A one-third fuel management was considered and several fission products were disregarded. Another important hypothesis is that the zirconium component is totally oxidized. This led to the mass ratio of 80 % of fuel (mainly composed of  $UO_2$ ) and 20 % of  $ZrO_2$ . The composition is detailed in the table III.1, and corresponds to a 2,3 %<sup>235</sup>U enrichment. According to the material experiments described in [2] the density of this mixture was set to 8000 kg/m<sup>3</sup>.

The total mass of the fuel debris bed depends on the reactor type and generation. A second generation pressurized water reactor (PWR) was selected for this work with a nominal thermal core power of 3000 MW, and the maximum debris mass inventory was set to 100 t. Regarding the creation of fuel debris bed (as detailed in chapter I) it seems highly improbable that the molten core would entirely turn to a debris bed (the steam explosion leads to the fragmentation of the first melt flow).

Isotope	Concentration (barns.cm <sup>-2</sup> )
<sup>235</sup> U	$3.3453 \times 10^{-4}$
<sup>236</sup> U	$3.1920 \times 10^{-5}$
<sup>238</sup> U	$1.4192 \times 10^{-2}$
<sup>238</sup> Pu	$1.2153 \times 10^{-6}$
<sup>239</sup> Pu	$4.3343 \times 10^{-6}$
<sup>240</sup> Pu	$1.6948 \times 10^{-5}$
<sup>241</sup> Pu	$1.0467 \times 10^{-5}$
<sup>242</sup> Pu	$3.7142 \times 10^{-6}$
<sup>237</sup> Np	$3.1785 \times 10^{-6}$
<sup>241</sup> Am	$1.5704 \times 10^{-6}$
<sup>243</sup> Am	$7.7523 \times 10^{-7}$
<sup>244</sup> Cm	$2.9690 \times 10^{-7}$
<sup>245</sup> Cm	$3.4649 \times 10^{-8}$
Zr nat	$8.4494 \times 10^{-3}$

Table III.1: Fuel debris composition.

### III.1.2 Debris size distribution

The quick cooling of the molten fuel from a liquid state to a solid state is the main mechanism responsible for the creation of the debris bed. Two scenarios can be addressed, the one where the molten fuel flows in cold water [3] and the one where cold water flows onto molten fuel. The fast heat exchange may quench and fragment the molten fuel to form a debris bed. In this respect, many experiments were performed to study all the physical phenomena occurring in the course of the interactions of molten fuel with water. The debris size distribution is of great importance to simulate the debris cooling and criticality. FARO and DEFOR experiments have provided relevant information concerning the debris size distribution selected for this work.

#### FARO experiments

The FARO facility (located in Ispra, Italy) is devoted to the investigation of the interaction between molten fuel and water including the triggering conditions of steam explosion. The description and information of these experiments are provided in [3] and [4].

The prototype molten fuel mixture is produced in a graphite electrode furnace. When the mixture has reached a temperature higher than the liquidus temperature, the pneumatic valves open, releasing the mixture into the thermally insulated vessel (TERMOS vessel). These valves are immediately closed again once the mixture has been completely discharged. The molten fuel interacts with the liquid water before reaching the debris collector at the bottom of the tank. Several experiments have been carried out in this installation and the L experiments are of particular interest for our models (because debris size was measured). Indeed, the aim of these experiments was to observe the impact of different parameters (height before contact with the liquid water, the water temperature, pressure) on the fragmentation of the molten fuel.

The various initial conditions for experiments L-24, L-28, L-29 and L-31 are detailed in table III.2. The main parameters that are varied among the three experiments are the amount of molten fuel cast, the water temperature, and the temperature of the molten fuel. The fuel is super-heated by 190 K for L-31 and 270 K for L-29. Overheating of the molten fuel can have

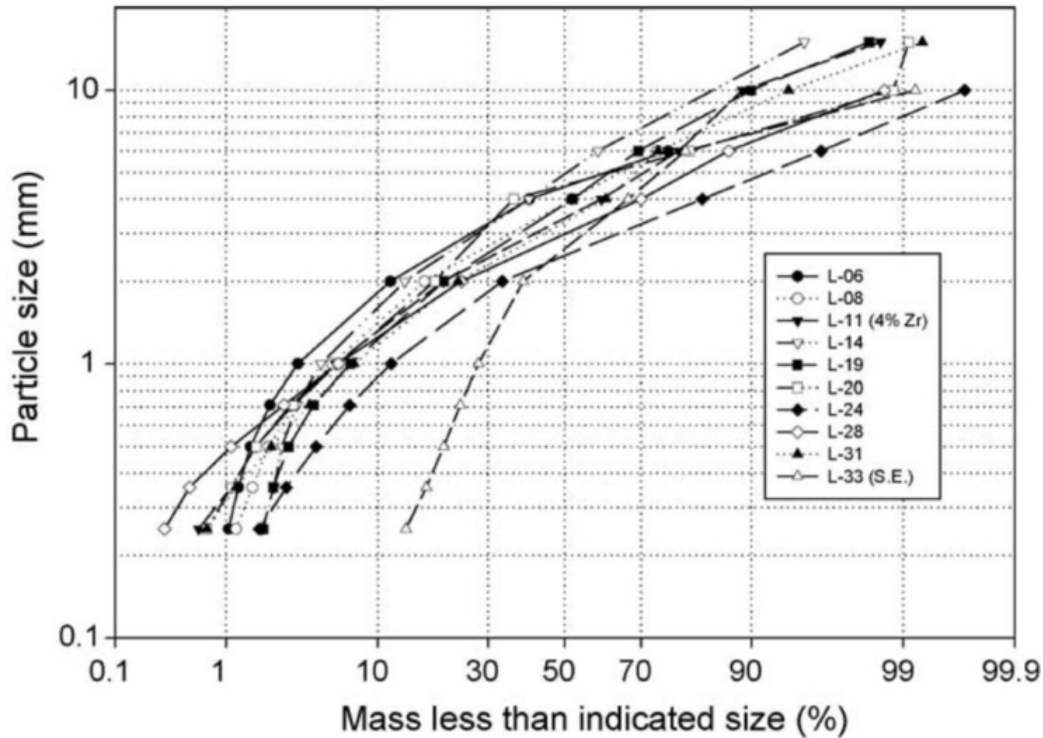


Figure III.1: FARO experiments results [4].

a significant impact on molten fuel fragmentation. The L-28, L-29 and L-31 composition of molten fuel is 80% *wt* of  $UO_2$  and 20% *wt* of  $ZrO_2$  [4]. The L-28 test showed a formation of solidified cake and loose debris, whereas the L-31 test showed a fully fragmented configuration of the molten fuel. The test L-29 did not show any fragmentation.

	L-24	L-28	L-29	L-31
Mass discharged (kg)	177	175	39	92
Temperature of the mixture (K)	3023	3052	3070	2990
Initial pressure (MPa)	0.50	0.51	0.21	0.22
Water deepness (m)	2.02	1.44	1.48	1.45
Water temperature (K)	425	423.7	297	291
Water subcooling (K)	0	2	97	104
Debris formation	Yes	Yes	No	Yes
Hard debris (cake) (%)	16.	48.	100.	0.
Loose debris (%)	84.	52.	0.	100.

Table III.2: Experiments conditions and debris data [3] [4].

The mass distribution of different grain sizes for several FARO experiments can be found in figure III.1. The results of debris sizes are illustrated for 7 trials; for the majority of these trials, 90% by mass of the debris are in the range 1 mm to 10 mm. The table III.3 shows the results of the FARO L-24 and L-28 debris size distribution. The porosity of the debris was not measured during these experiments.

These measurements are highly relevant for the simulations that will be carried out in the following chapters and reveal that the debris beds are not made of single size debris but obey a non-trivial distribution. Therefore, the models to be taken into account by the simulation codes should be able to include the distribution of debris size or at least to mimic its impact

$d_{min}$ (mm)	$d_{max}$ (mm)	L-28 Mass ratio	L-24 Mass ratio
10.0	15.0	0.01	0.01
6.00	10.0	0.12	0.03
4.00	6.00	0.17	0.12
2.00	4.00	0.45	0.49
1.00	2.00	0.16	0.22
0.71	1.00	0.03	0.04
0.50	0.71	0.02	0.03
0.36	0.50	0.02	0.02
0.25	0.36	0.01	0.02
0.	0.25	0.01	0.02

Table III.3: FARO L debris size distribution.

on the calculations.

## DEFOR experiments

The DEFOR (Debris bed Formation) experiments were carried out at KTH (Sweden) to study fuel coolant interaction and more precisely the coolability of the debris bed in relation to its formation [5]. The main objective of the DEFOR experiments was to characterize the debris formed during the fragmentation of a molten fuel simulant material spilled into a water pool. The physical quantities observed were porosity, grain size distribution, and the grain morphology as a function of test conditions such as subcooling of water, the pool depth, and composition of the molten fuel simulant. The experiments of interest for the debris bed type are the E series and the S series [6]. Two simulant materials have been used in the E series [5] and mixtures of four simulants were used in the S series.

The conclusions of the S-series tests are as follows:

- The average measured porosity (from 46% to 70%) is higher than the average porosity used in most of the previous works on debris bed cooling (40% is the commonly used porosity [7]).
- The average porosity of the debris is insensitive to the composition of the fuel simulant material.
- When the water is very sub-cooled, the obtained porosity is higher (62 – 70%) and decreases with decreasing subcooling.
- While porosity was particularly high (57 – 65%) for tests with little or no subcooling, there is a significant fraction of the debris that presents fully or partially encapsulated cavities.
- The lowest measured porosity (46%) is found for the less subcooled water with the highest water temperature, which is consistent with the observation of cake formation.

For Series E, observations and measurements have shown that the porosity affected by the deposition of debris is approximately 60% and small debris can be observed at the periphery of the deposition area, suggesting that such debris were carried along by the flows created during cooling [6]. It was shown that the porosity of the debris is higher than usually assumed (higher than the TMI-2 porosity) in the case where molten fuel would flow in water (which might be the case in ex-vessel phase). During other experiments (series DEFOR-A) [8], the debris size was also measured and the size distribution can be read in the table III.4.

The DEFOR experiments showed that the debris size possibly depends on of the material they are made of. Also, it was shown that the porosity may reach values higher than those

$d_{min}$ (mm)	$d_{max}$ (mm)	Mass ratio
10.0	15.0	0.03
6.00	10.0	0.08
4.00	6.00	0.19
2.00	4.00	0.44
1.00	2.00	0.20
0.71	1.00	0.04
0.50	0.71	0.00
0.36	0.50	0.01
0.25	0.36	0.00
0.	0.25	0.01

Table III.4: Debris size distribution measured in DEFOR-A [8].



measured at TMI-2.

The molten core when fragmented will take the shape of small debris; the size of the debris will depend on the physical conditions when the fragmentation occurs. Several experiments have shown that the size of the debris is usually distributed from millimetres to centimetres.

The main asset of the FARO experiment is that the molten material composition was similar to that of a real molten core. Molten material composition properties such as density and surface tension may impact the phenomena of debris creation [9]. Therefore, it was decided to use the the FARO experimental program to be used as the reference distribution of debris size. In particular in the L-28 experimental configuration is the one where almost equal mass was solidified into debris and hard chunks. The FARO L-28 debris distribution was selected in order to infer values for the numerical simulations that we will carry out in the following chapters, and the corresponding distribution is given in the table III.5.

FARO L-28 debris size distribution		
$d_{min}$ (mm)	$d_{max}$ (mm)	Mass ratio
10.0	15.0	0.01
6.00	10.0	0.12
4.00	6.00	0.17
2.00	4.00	0.45
1.00	2.00	0.16
0.71	1.00	0.03
0.50	0.71	0.02
0.36	0.50	0.02
0.25	0.36	0.01
0.	0.25	0.01

Table III.5: Debris size distribution [3].

The debris size distribution may strongly impact the neutron transport, as briefly described in subsection III.2.1. A particular attention is paid to the utilisation of random geometries in the subsection III.3.1 in view of high fidelity calculations of the neutron transport in debris bed.

### III.1.3 Decay heat

The decay heat during a severe accident is an important physical phenomenon after reactor shutdown. In this work, the multi-physics behaviour of debris bed criticality is taken into account to evaluate criticality risk: the decay heat may affect significantly the state of the water flows into debris beds. The molten fuel is considered as isotropic and homogeneous, so the decay heat is also uniformly distributed. The decay heat density in fuel debris formula is given by:

$$q(t) = \frac{P_{tot}(t)}{\frac{m_{molten\ core}}{density_{molten\ core}}}. \quad (III.1)$$

The power density  $q(t)$  is expressed in volumetric power, the decay power  $P_{tot}$  comes from the El-Wakil equation I.2 (defined in chapter I) using the following notations:  $m_{molten\ core}$  is the total mass of the molten core and  $density_{molten\ core}$  is the density of the debris. For the

simulations, the total mass of the molten core is set at 100 t. The debris density will be set at  $8000 \text{ kg/m}^3$ .

### III.1.4 Geometry of the debris bed

The shape of the debris bed will impact its coolability (as described in chapter I) and thus the criticality. It is thus essential to have a proper estimation of the debris bed shape. In particular, the experiment carried out at the DAVINCI facility [10] (located in South Korea) was aimed at investigating the shape of the debris beds during the fragmentation and the sedimentation phase. Then, a study was performed with the MC3D code [11] to investigate the effect of fluidification on the debris bed porosity distribution.

#### DAVINCI experiment

The description of the experiment comes from the reference [10]. The debris were simulated using cylinders with a diameter and height of 2 mm and with a density of  $8000 \text{ kg/m}^3$ . An air bubble injection system on the debris recovery plate simulates the appearance of steam. A 3D camera scans the area to memorize the shape and size of the debris bed. The device is illustrated in figure III.2.

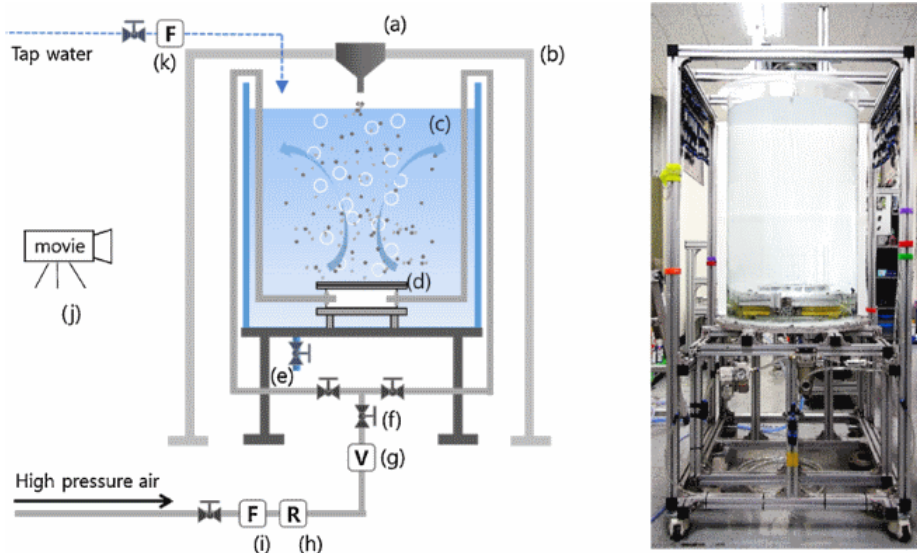


Figure III.2: DAVINCI experimental set-up [10].

The underwater grain deposition experiment shows that the debris bed takes on a conical shape. Nevertheless, during their fall into the water, the molten core fragments are still much warmer than the water. They are cooled by two-phase convective (boiling in a film regime at the beginning) and radiative exchanges. Thus, a column of steam bubbles appears above the area where the debris are deposited. The cooling of the debris during its two-phase fall will then have an impact on the distribution of the debris at the bottom of the cell well.

In figure III.3, the time plots range from  $t_1$  to  $t_5$  corresponding to the range from 10 to 50 s. The graph represents the bed shape in the single-phase case and the graph below represents the two-phase case. The results show that the rise of air bubbles during the fall of the debris will level the formed debris bed illustrated in figure III.3. The debris bed will become conical with an angle of repose of  $8 - 10^\circ$  instead of  $45^\circ$ . Thus, the debris bed is flatter when diphasic conditions are applied. The radius of the cone containing 75 % of the debris bed mass increases by 71 %. These findings show that the debris bed formed during the quenching and

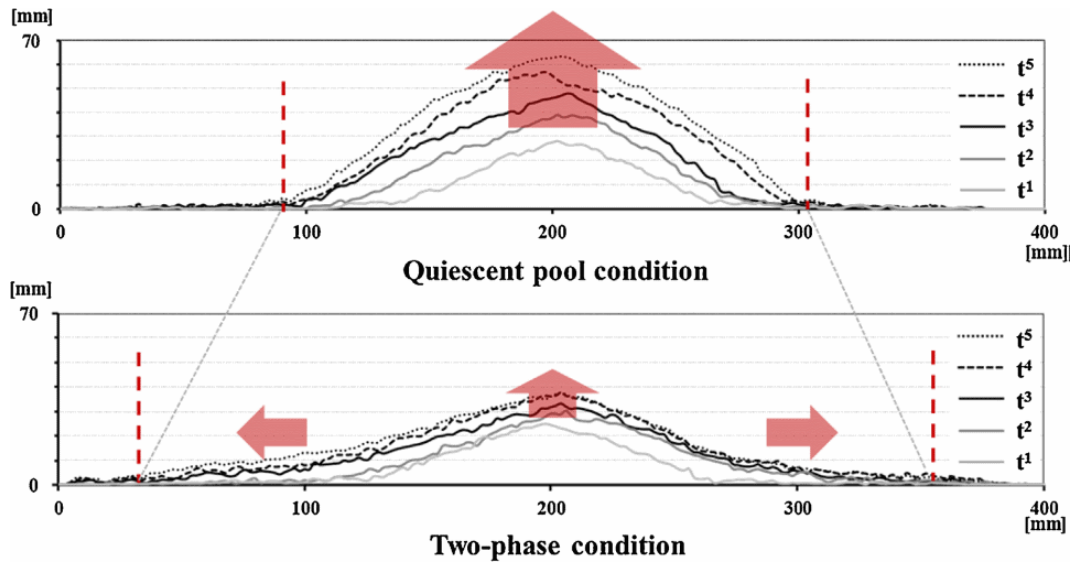


Figure III.3: Measurements of the debris distribution in single phase and diphasic conditions [10].

fragmentation of the molten fuel depends on the inlet temperature and on the decay power of the debris in the liquid water. In addition, a model using energy flows was developed to obtain the radius and angle of the cone [10]. This experiment shows that a molten core debris bed might take a shape closer to a plane cylinder than a cone, which is an important information to model a large fuel debris bed.

### Geometry selected for this work

The molten core debris bed geometry will have an impact on the neutron transport features (the neutron leakage is the main property that would be affected by the geometry). The cooling of the debris bed is also geometry-dependent. As a reminder, experiment [12] has shown that to cool debris bed (in top-flooding configurations) the dryout heat flux is higher for cylindrical geometry than conical geometry.

The DAVINCI experience [10] brought a major conclusion about the geometry, indeed the debris bed created during severe accidents might not take a perfect conical geometry (with a slope angle of  $45^\circ$ ). Actually, the experiment has shown that the geometry is still conical but rather flat. A model proposed by the same team [10] thanks to the experimental data was applied on a mass of 110 t: the radius containing 75 % of the mass may varies between 1.73 to 3.00 m. As the reactor vessel pit radius equals 3.02 m in the studied case, we can assume that a fraction of the debris would be accumulated against the reactor pit walls, thus the geometrical shape of the debris bed will be a flat cone.

In view of these considerations, a cylindrical debris bed will be considered for the numerical model proposed in this thesis. This debris bed fills entirely the surface available on the reactor vessel pit floor. The geometry is described in the figure III.4, where the cylindrical debris bed lies on the reactor vessel pit floor and is surrounded by concrete wall, the cooling water coming from above.

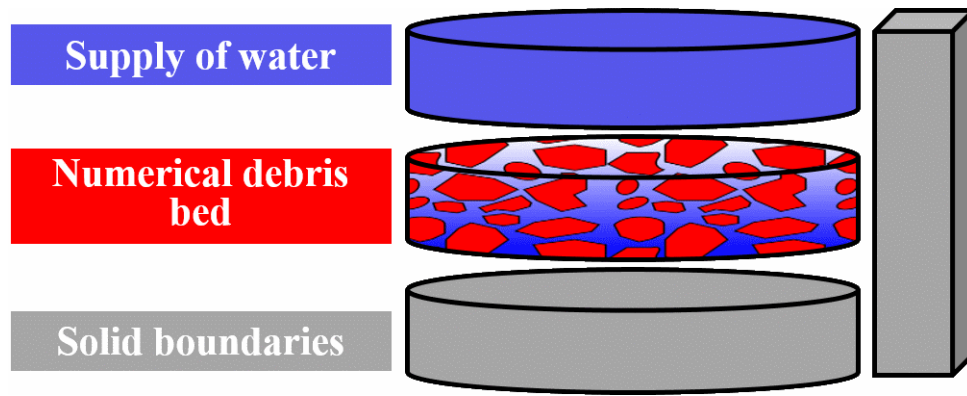


Figure III.4: Geometry of the test case.

### Porosity distribution

The code MC3D [11] is able to compute the movement of the gaseous, liquid and solid phases. This enables the calculations of porosity distribution. However, the development of a simulation following moving debris goes beyond the initial scope of this work. A static porosity distribution was determined using MC3D calculations of debris movement with different decay power.

The debris will be more compact in the lower area of the bed due to the mass of the upper debris pressing and compacting the debris below. The pre-calculations that we have performed by using MC3D (with volumetric power set to  $1.0 \text{ MW/m}^3$ ) and considering debris movement have shown that the porosity profiles have most of the time the same shape, unlike the water density profiles. The initial state of the debris bed is shown in figure III.5. The simulations are designed to attain a stable state at long time; this corresponds to a debris bed with a low porosity at the bottom and higher porosity at the top, as shown in figure III.6. The porosity is axially averaged on 3 levels; the value of the porosity set is equal to 0.334 at the bottom, 0.409 in the middle and 0.489 at the top of the debris bed model.

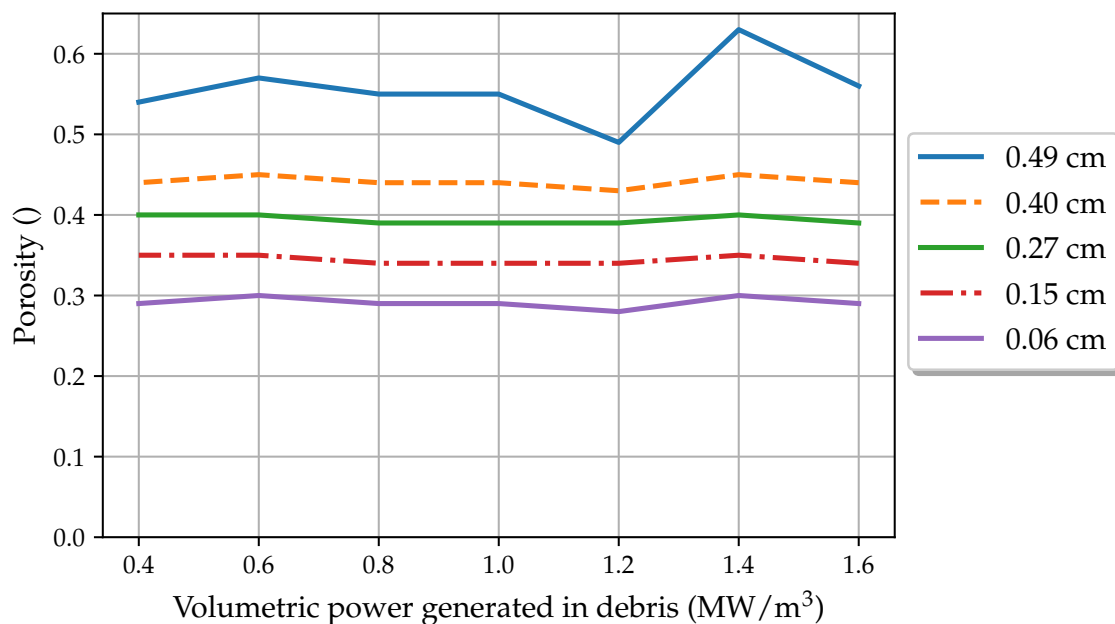


Figure III.7: Porosity in debris beds in function of the volumetric power using the code MC3D.

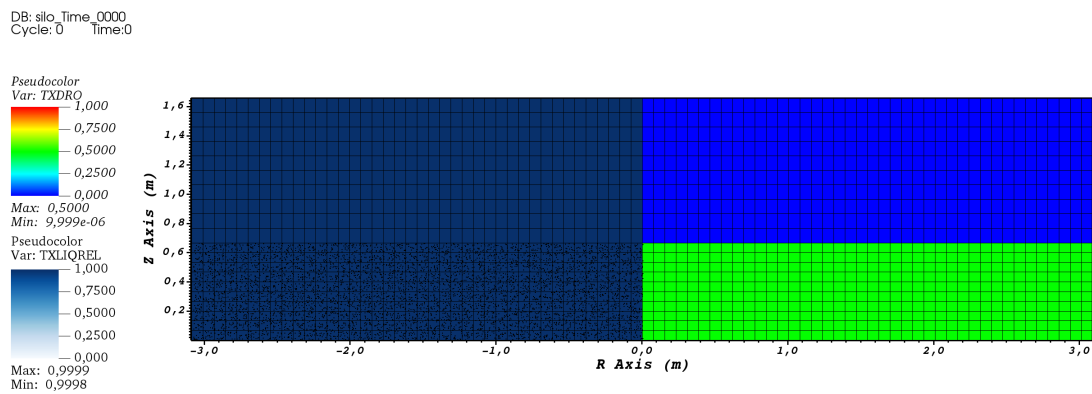


Figure III.5: Initial state of the debris bed (water presence on the left and bed porosity on the right) using the code MC3D.

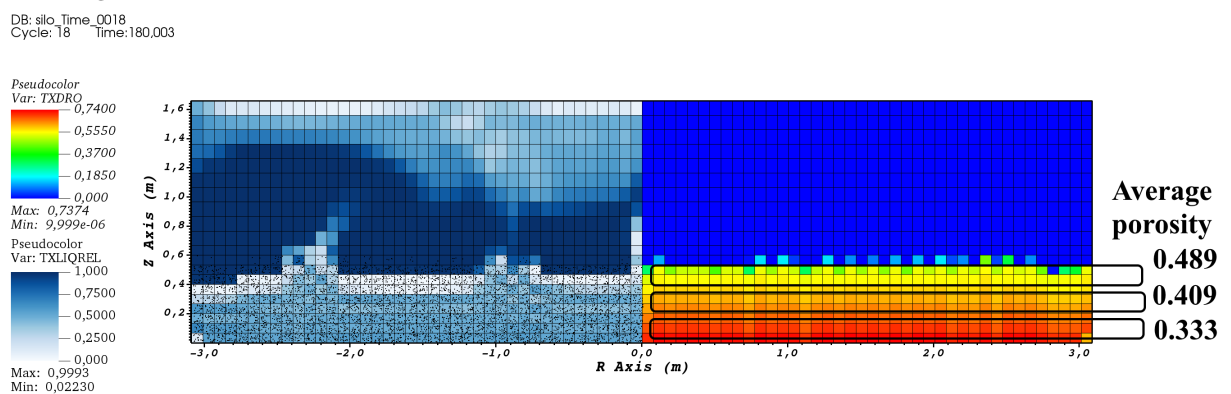


Figure III.6: State after 180 s (water presence on the left and bed porosity on the right) using the code MC3D.

The fluidification of the debris beds can create a continuous movement of the debris at the top of the debris beds. This phenomenon can occur if the heat generation within the debris creates a significant steam flow. Indeed, if the steam flow is strong enough, the debris entrainment would appear when the drag force created by the steam on the debris is stronger than the debris gravitational force.

Figure III.7 shows that the debris fluidification might occur only when the power density exceeds the value of  $1.2 \text{ MW/m}^3$ . Until this value is reached, the porosity in the debris bed is relatively stable. Hence, the porosity profile will be kept static in simulations (unless otherwise specified).

## III.2 Numerical modelling

The shape and the mean physical and chemical features of the model geometry for the debris bed were established. This model will be considered in the numerical simulations presented in the following chapters. Now we will address the main simulation tools to take into account neutron transport and thermal-hydraulics feedbacks in the debris beds.

### III.2.1 Neutronics

Regarding neutron transport, TRIPOLI-4<sup>®</sup> and Apollo-2 codes were considered. The Monte-carlo code TRIPOLI-4<sup>®</sup> code was mainly used to model particle transport within the debris bed with the maximum fidelity and thus assess the accuracy of the simplified Apollo-2 deterministic code.

One of the simplest way to model a debris bed in TRIPOLI-4<sup>®</sup> is to distribute an inclusion (e.g. a sphere) in a regular cubic lattice with spacings corresponding to the desired porosity and debris diameter. This geometry is easily defined by the user (the face-centered-cubic lattice is illustrated in figure III.8), but might not present the same neutronics properties as a real disordered medium. Thus, in order to properly describe the geometry of a debris bed it is necessary to model random objects placed into a background matrix. This approach is more realistic than the case of regular lattices of ideal spherical inclusions. For this purpose, special stochastic geometry generators have been developed for TRIPOLI-4<sup>®</sup> [13]. These modules allow the generation of random tessellations according to different laws such as Poisson or Voronoi: a Poisson random geometry example is shown in figure III.9. This generation of random geometries can be done from very compact media to highly porous media.

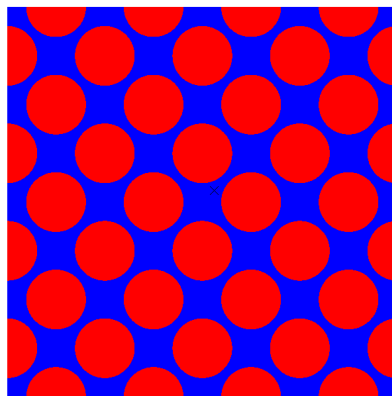


Figure III.8: Example of face-centered-cubic lattice modelled in TRIPOLI-4<sup>®</sup>.



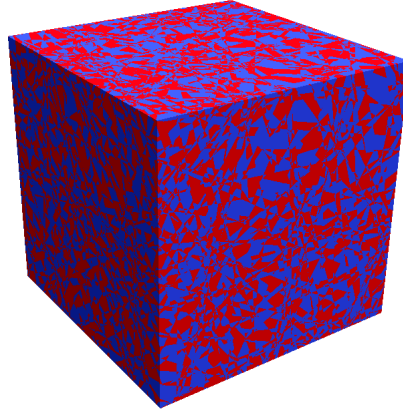


Figure III.9: Example of Poisson disordered geometry modelled in TRIPOLI-4<sup>®</sup> [13].

However, simulating neutron transport in random geometries requires taking averages over a large number of possible configurations, which can be extremely time consuming [13]. That is why the deterministic code Apollo-2 is considered, which uses an approximation (double heterogeneity [14]) to model disordered media that is fast regarding calculation time. When the reactivity of the whole debris beds is needed, approximated calculations show a good balance between simulation time and accuracy. Indeed, exact disordered media simulations with TRIPOLI-4<sup>®</sup> in beds configuration take more time than calculations with only mono-sized spheres in lattice. One should note that simulation of the whole debris bed with Monte Carlo involves an extremely high computational cost. Moreover, table III.6 shows significant computing time gains using Apollo-2 instead of TRIPOLI-4<sup>®</sup> without significant fidelity loss.

Porosity	Debris diameter (cm)	Apollo-2	TRIPOLI-4 <sup>®</sup>	Apollo-2 calculation time (s)	TRIPOLI-4 <sup>®</sup> calculation time (s)
0.5	1.00	1.33506	1.33364 ( $\sigma = 3.9 \times 10^{-4}$ )	1.09	11737
0.5	2.00	1.34379	1.34178 ( $\sigma = 3.9 \times 10^{-4}$ )	1.07	9451
0.6	1.00	1.28878	1.28848 ( $\sigma = 4.1 \times 10^{-4}$ )	0.97	12131
0.6	2.00	1.29131	1.29056 ( $\sigma = 3.8 \times 10^{-4}$ )	1.01	9248

Table III.6:  $k_{\infty}$  comparison of Apollo-2 and TRIPOLI-4<sup>®</sup> on face-centre-cubic cells.

The Apollo-2 calculation procedure is adapted to fit to the specific requirements of this work. First the double heterogeneity model is used to create a mixture with equivalent cross sections as in a solid sphere of debris in a water cell. The radius of the sphere should correspond to the equivalent diameter taken to model the debris distribution for neutron transport. This first step is done using collision probabilities with Pij matrix at 99 energy groups in a 2 dimensional (x,y) space mesh. Then, the cross sections are condensed on an energy grid with 20 groups. Following this condensation, the cross sections are inserted into a 2 dimensional (R,Z) geometry which corresponds to the **real** geometry of the system. A neutron transport calculation is done using the Sn method with an order equal to 8 and with an axial symmetry and reflections applied to the boundaries: neutrons escaping the fissile zone are reflected by water (60 cm) in the upper part and by concrete in the bottom and side part (1 m) leakage is thus weak.

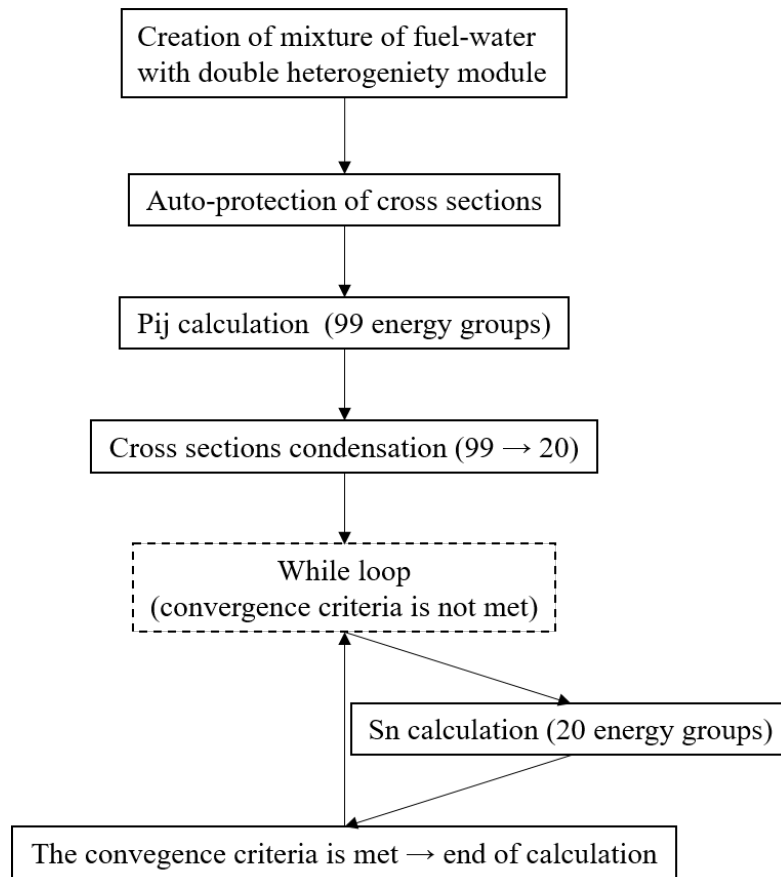


Figure III.10: Neutron transport calculation procedure with Apollo-2

The geometry is relatively large (3 m of radius in the fissile volume), which induces a non-negligible computation cost and numerical instabilities. To decrease the computation time an acceleration scheme (Chebyshev [15]) is used. However, the use of a convergence acceleration method on a large geometry can increase the risk of numerical instabilities. In order to overcome the possible divergence of the calculation one can "cut" the calculation by stopping the acceleration briefly then resuming it. This tactic completely removes the observed instabilities. The calculation procedure is illustrated in figure III.10. Concerning the very long simulation times, the utilisation of pre-calculated neutron flux (corresponding to fully flooded debris bed) to initialize the flux calculation is of great help, since it will considerably reduce the convergence phase. The calculation time was reduced from 40 min to approximately 4 min.

### III.2.2 Thermal-hydraulics

Different models of interfacial friction are implemented in MC3D. The model chosen in this work should be adapted to the equivalent diameter taken to represent the debris size distribution: for debris of small size (<10 mm if diameter) the Ergun correlation shows better agreement [16].

### III.2.3 Mesh used to simulate the debris bed

A special attention must be paid to the mesh used when simulation codes are coupled. The mesh in thermal-hydraulics, neutronics, and the coupling methodology corresponds to a



cylindrical grid (R,Z) with an axial symmetry. First, the MC3D code was used on a very refined mesh with cells having a linear span of 5 cm at maximum. A numerical investigation shows that the use of a coarser mesh does not introduce additional noticeable errors while accelerating the simulation by 2 – 3 times. This coarse mesh corresponds to a grid of  $30 \times 6$  cells to decompose the debris bed with 6 cells in the axial direction and 30 cells in the radial direction: the mesh is drawn in figure III.11.

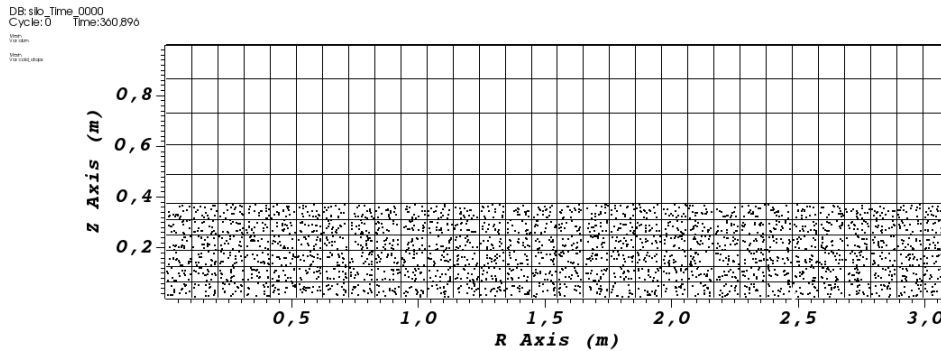


Figure III.11: MC3D mesh, the axial symmetry is on the left and the debris bed is at the bottom.

An equivalent investigation was done on Apollo-2: a more refined mesh near the interface shows some differences with respect to a coarser one, thus the refined mesh was used. The neutronics is driving the transients, so it is crucial to avoid discrepancies. The mesh of the debris corresponds to 100 cells in the radial direction and 60 cells in the axial directions, and is illustrated in figure III.12. A thickness of 1 m of the boundaries is also modelled around the debris bed with a refined mesh near the interface with the *fissile* area.

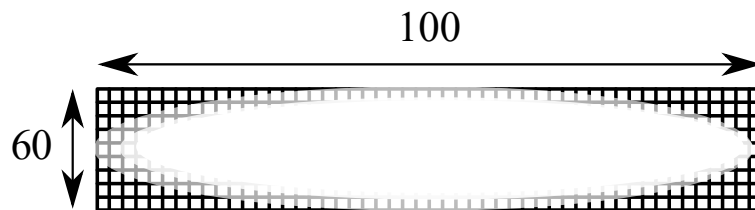


Figure III.12: Apollo-2 mesh (cylindrical shape) of the debris bed, the axial symmetry is on the left.

The mesh used to exchange the information between the codes is named the *coupling mesh* and drawn in figure III.13. This mesh corresponds to the grid where the debris temperature or the void fraction of the cells is computed. To exchange data between codes, the physical values recorded in the neutronics and thermal-hydraulics mesh are averaged to match to the coupling mesh. This mesh is the coarsest mesh used, with 3 axial cells and 10 radial cells. The right balance between accuracy and dataflow was investigated by modelling transient and assessing the discrepancies on the deposited energy. The difference between the selected grid and more refined one ( $6 \times 30$ ) is low enough to justify the use of this grid.

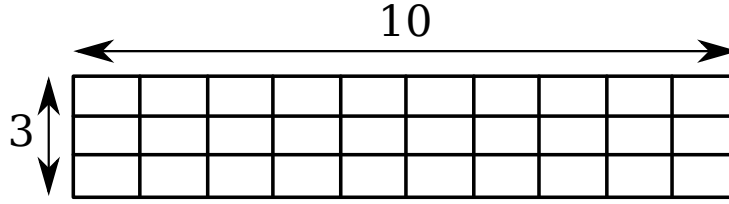


Figure III.13: Coupling mesh (cylindrical shape), the axial symmetry is on the left.

### III.3 Debris size distribution modelling

For our model, the simulations must be done trying to be as representative as possible of the debris size distribution for both neutron transport and thermal-hydraulics. The equivalent debris diameter is established by using the literature [17] and the random geometry generator [13] [18]. Defining an equivalent debris diameter is required to simplify the neutron transport and the thermal-hydraulics calculations and reduce the computational cost.

#### III.3.1 Debris equivalent size in neutronics

In this section an equivalent debris diameter is defined for the neutronics. It is based on the comparison between results obtained using random geometries and mono sized spheres in FCC lattice geometries. Random geometries are relevant to model debris size distribution as those of FARO and DEFOR experiment, and can be generated and studied by Monte-Carlo simulation [13].

The isotropic Poisson tessellation model, is a prototype process of random media [17] [13]. Poisson tessellations represent an idealized mathematical model, whose prominent advantage lies in the fact that they require minimal information content, since the associated correlation function is simply exponential, i.e., characterized by a single parameter (see comments in chapter II). The average correlation length is the only free parameter of the tessellation and physically represents the average chord length of the polyhedral cells, i.e., their typical linear size. For our purpose, we will be in dimension  $d=3$  and the domain to be randomly partitioned by the Poisson tessellation will be a box of side  $L$ .

In order to make the properties of the FCC sphere lattice comparable to those of the Poisson tessellation model, the mean chord length  $\lambda_{sphere}$  for the sphere lattice has been taken equal to the mean chord length  $1/\rho$  of the Poisson tessellation. By using the formulas provided in [17], this yields the constraints:

$$\lambda_{sphere} = \frac{4}{3}r \quad (\text{III.2})$$

$$\rho = \frac{1}{(\lambda_{sphere} \times porosity)} \quad (\text{III.3})$$

The Poisson tessellations are characterized in terms of the tessellation density  $\rho$ , which is defined as the inverse of the average chord length and thus sets the typical size of the random chunks, and the volume ratio of the two phases, namely, fuel and water, which is set by the choice of the material compositions. For most configurations investigated in this work, the size  $L$  of the box was set to have  $L \times \rho = 50$ : this criterion ensures that finite-size effects have a limited impact [17] [13]. For the configurations with very low values of  $\rho$  (below  $2.5 \text{ cm}^{-1}$ ), the size of the box was set to a maximum of 20 cm: in this case, finite-size effects may have a larger impact.

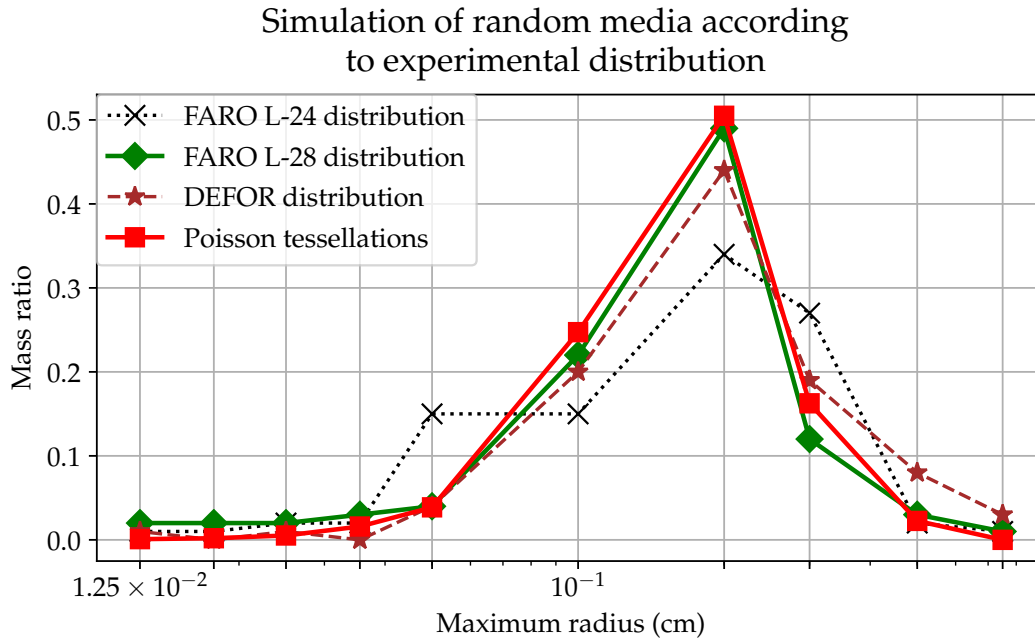


Figure III.14: Comparison of experimental debris size and simulated debris.

The values obtained for a generated random configuration are only representative for the current realization. Therefore, the average over a large number of realizations must be computed in order to assess the mean and the dispersion of the physical quantities of interest.

The fiducial quantity of the investigation is the average infinite multiplication factor  $k_{\infty}$ . In order to compute the ensemble averages of the observables, the number of tessellation realizations that we have sampled for the cases examined in the following varies between 50 and 200. The number of generated geometries was initially set to have a standard error lower than 100 pcm on the  $k_{\infty}$  value. As shown in [19] [13], the dispersion due to the stochastic medium realization might in some cases be much larger than the sought accuracy on the average values: this is why the decision was made for some of the realizations to accept higher standard deviations, as long as they are lower than the variation induced by the stochastic tessellation model with respect to the reference configurations which is a face-centered-cubic lattice (FCC).

The random media generator developed at CEA is endowed with an interface capable of exporting geometry descriptions that are compatible with those of TRIPOLI-4<sup>®</sup>. Particle tracking through the polyhedral cells is accelerated by using a newly developed feature providing a neighbourhood map [13]. The system reactivity stemming from the Poisson tessellation model is then compared to a reference configuration consisting in a FCC lattice of regularly spaced fuel spheres immersed in water.

The cross section library used for the material compositions is JEFF-3.1.1 [20]. The stochastic realizations have reflective boundary conditions on all the faces of the box, which is an attempt at modelling an infinite geometry. The reactivity is thus characterized in terms of the infinite multiplication factor ( $k_{\infty}$ ).

Previous work [18] shows Poisson random geometries are close to debris size distribution in the range of interest. The chord density which gave the best results to model debris size distribution observed in experiment is equal to  $5 \text{ cm}^{-1}$  (see figure III.14): more information about generation of random geometries and comparison is provided in [13] [18]. Poisson random geometries with a size distribution close to the FARO and DEFOR experiments were thus generated and neutronics simulation were done using TRIPOLI-4<sup>®</sup>. The average  $k_{\infty}$  of

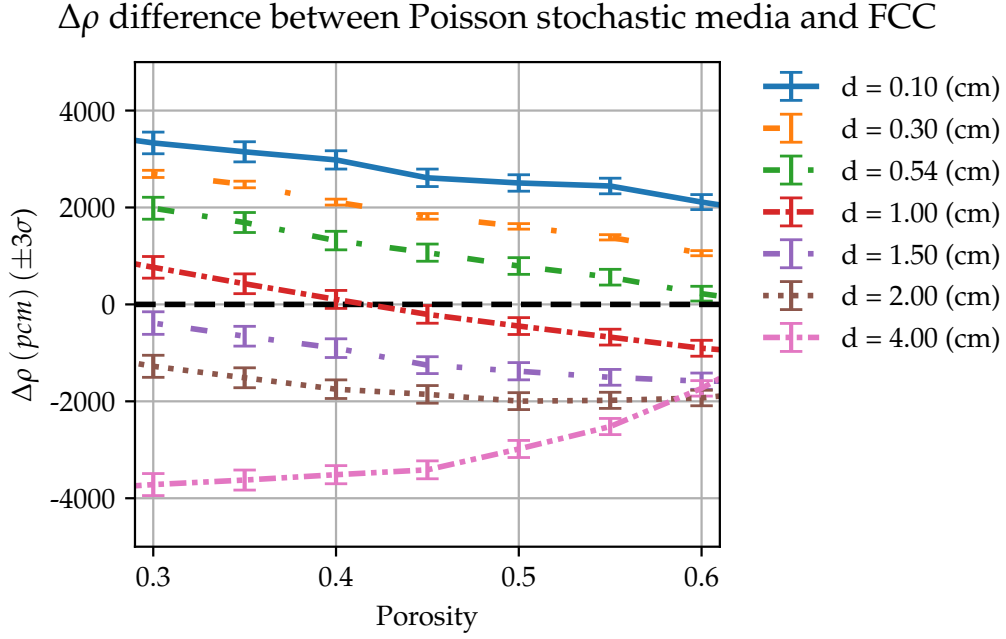


Figure III.15: Comparison of the  $k_\infty$  obtained with random geometries similar to experimental size distribution and mono-sized spheres in FCC lattice.

the Poisson random geometries and the  $k_\infty$  of the FCC lattice with different diameters were compared using equation (III.4). When the value of  $\Delta\rho$  is positive the random geometry is more reactive, reciprocally when the value is negative the FCC geometry is more reactive. The porosity range of interest ranges from 0.31 to 0.60. The results of calculations are shown in figure III.15.

$$\Delta\rho = \left( \frac{1}{\langle k_{FCC} \rangle} - \frac{1}{k_{random}} \right) \times 10^5 \quad (\text{III.4})$$

The figure III.15 shows that the bigger are the FCC debris diameter the lower will be the  $k_\infty$  of the FCC lattice relatively to the Poisson random geometries. However, the compromise is to find the diameter which gives the closest value of  $k_\infty$  to the value of the random geometry while never being less reactive than the random geometries in the chosen porosity range. More calculations between the two best values ( $d = 1.00$  cm and  $d = 1.50$  cm) were done using TRIPOLI-4<sup>®</sup> to find out the best equivalent mono-sized diameter. The results are illustrated on figure III.16.

In the figure III.16 the standard deviation ( $\sigma$ ) is not plotted but reads about 80 pcm. The same trend as in the figure III.15 can be observed. The best equivalent diameter value according to the criteria and taking 1  $\sigma$  of margin is about to 1.32 cm. The surface equivalent diameter is the obtained diameter of one mono-sized debris corresponding to the same area as from the debris size distribution. The volume equivalent diameter is the obtained diameter of one mono-sized debris corresponding to the same volume as from the debris size distribution. For a debris size distribution with volume fraction  $f_i^v$  such as  $\sum_{i=1}^n f_i^v = 1.0$ , the equivalent volume diameter is defined in:

$$d_{eq}^v = \sum_{i=1}^n d_i \times f_i^v \quad (\text{III.5})$$

with  $d_i$  the diameter of the debris fraction,  $f_i^v$  the volume fraction of debris size bins,  $d_{eq}^v$  the equivalent volume diameter. The surface fraction  $f_i^s$  such as  $\sum_{i=1}^n f_i^s = 1.0$  The equivalent

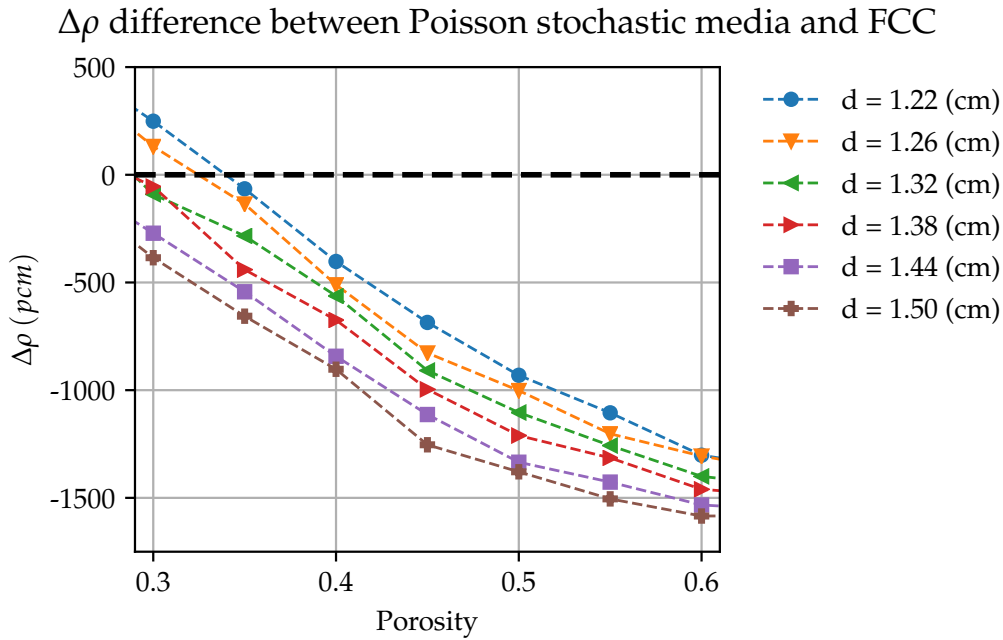


Figure III.16: Comparison of the  $k_\infty$  obtained with random geometries to experimental size distribution and mono-sized spheres in FCC lattice.

surface diameter is defined in:

$$d_{eq}^s = \sum_{i=1}^n d_i \times f_i^s \quad (\text{III.6})$$

with  $f_i^s$  the surface fraction of the debris bin,  $d_{eq}^s$  the equivalent surface diameter. If the surface diameter or the volume diameter would be chosen instead, the obtained equivalent diameter would have been respectively 0.25 cm and 0.45 cm.

An approximation is done on the geometry of the entire debris bed where there are three layers with different porosities: by using the closest diameters of the FCC lattice to the Poisson geometry value at a porosity of 0.333 a positive margin appears on higher porosity as shown in figure III.16, thus the reactivity may be slightly over-estimated. In case of porosity equal to 0.4 a margin of 700 pcm is introduced with the 1.32 cm equivalent diameter: this margin goes up to 1200 pcm at porosity equals to 0.5. The table III.7 summarizes the approximations introduced to accelerate the neutronics calculations. The use of an equivalent diameter allows to use Apollo-2 to model debris bed, leading to large time gains with minimal discrepancies with respect to the reference model.


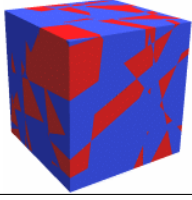
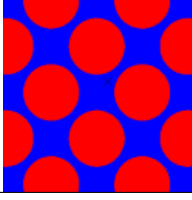
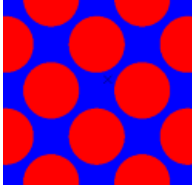
Case	Representation	Distribution	Approximations	Simulation time
Experiment FARO L-28		FARO L-28	None	NA
Poisson random geometries		Close to experiments	Shape	Very long ( $\approx 50 \times 10000$ s)
3D FCC lattice (TRIPOLI-4 <sup>®</sup> )		None, mono-sized spheres	Shape and distribution	Long ( $\approx 10000$ s)
2D double heterogeneity (Apollo-2)		Mono-sized spheres	Shape, distribution and dimension	Very short ( $\approx 1$ s)

Table III.7: Simplification to model debris beds in neutronics [6] .

### III.3.2 Debris equivalent temperature

In order to simplify neutron transport and reduce calculation time, a single temperature is used for the debris. In this subsection an equivalent temperature is defined comparing results between models using a temperature distribution and an average effective temperature. In order to calculate the equivalent temperature ( $T_{equ}$ ) of a debris size distribution, the volume ratio is used to define a weighted average as defined in:

$$T_{equ} = \sum_{i=1}^n T_{eff\ i} \times f_i^v \quad (\text{III.7})$$

with  $f_i^v$  the volume fraction of the debris size bins. A comparison calculation was done with Apollo-2 to estimate the error introduced by applying this method. Indeed, Apollo-2 can simulate debris distribution (however the code is not able to simulate properly and quickly more than 6 different debris sizes). The detail and results are shown in table (III.8). The difference between calculating with the real value and an averaged value amounts about 4 pcm. In view of the large uncertainties of the composition or the shape of the debris bed, this approximation is considered to be good enough for this work.

Moreover, in order to take into account temperature profile inside debris, the fuel temperature used here comes from the effective average (1/3 central temperature + 2/3 boundary temperature) proposed by Rowlands [21]. This effective temperature is required in transient conditions as the temperature may change, so that the temperature profile will not be flat.

diameter (mm)	volume ratio	$T$ (K)	$T_{averaged}$ (K)
15.0	1.	424.57	422.80
10.0	12.	424.29	422.80
6.0	17.	423.82	422.80
4.0	45.	423.46	422.80
2.0	16.	422.27	422.80
1.0	9.	416.20	422.80
Reactivity pcm:		6951.60	6947.81

Table III.8: Reactivity impact of averaged  $T_{eff}$ .

### III.3.3 Debris equivalent size for steam and water flow

Most of the experiments aimed at investigating the coolability of debris were done with beds made of mono-sized spheres or cylinders. However, fuel debris beds might have a size distribution which has an impact on the coolability of the debris bed. Recent work was carried out [16] to validate a method to model particles size distribution which were developed and proposed by [22] and [23]. These works show that, when using mono-sized dispersed spheres to represent a debris size distribution, the equivalent diameter should be chosen as the average surface diameter. However, not enough data about the debris shape were available from the FARO and DEFOR experiments; hence the debris are assumed to be spherical and no shape factor will be used in this work.

Using the surface mean diameter (the maximum diameters of bins was taken as the diameter of calculations) as expressed in III.6 and applied on the FARO L-28 distribution, the obtained equivalent mean diameter is 0.25 cm.



### III.4 Synthesis

In this chapter, we have introduced the assumptions used to build a generic debris bed model, in view of the numerical simulations to be carried out in the next chapters. Then, the numerical aspect for neutron transport and thermal-hydraulics were discussed. Eventually, an equivalent debris diameter was sought to simplify and accelerate the calculations. The generator of Poisson random geometries was used to create a reference model and to compare it to lattice calculations. The thermal-hydraulics equivalent diameter is obtained thanks to the literature. The synthesis of the selected strategies is presented in the table III.9. This preparatory work will be used to build a methodology to analyse the criticality risk of heated debris beds in the following chapter.

Domain	Model to represent debris size distribution	References
Neutronics - $T_{eff}$ Neutronics - calculation	Volume average Mono-sized spheres in FCC lattice	Apollo-2 study Studies on Poisson random geometries
Hydraulics	Mono-sized spheres (average surface diameter)	[16], [22], and [23]

Table III.9: Summary of the tactics applied on each physic to represent the debris size distribution.

## Bibliography

- [1] P. Reuss, *Précis de neutronique*. Génie Atomique, EDP Sciences, 2003.
- [2] C. Journeau, P. Piluso, and K. Frolov, “Corium physical properties for severe accident r and d,” *Proceedings of ICAPP*, 2004.
- [3] D. Magallon and I. Huhtiniemi, “Corium melt quenching tests at low pressure and sub-cooled water in FARO,” *Nuclear Engineering and Design*, vol. 204, no. 1, pp. 369–376, 2001.
- [4] D. Magallon, “Characteristics of corium debris bed generated in large-scale fuel-coolant interaction experiments,” *Nuclear Engineering and Design*, vol. 236, no. 19, pp. 1998–2009, 2006.
- [5] A. Karbojian, W. Ma, P. Kudinov, and T. Dinh, “A scoping study of debris bed formation in the DEFOR test facility,” *Nuclear Engineering and Design*, vol. 239, no. 9, pp. 1653–1659, 2009.
- [6] P. Kudinov, A. Karbojian, W. Ma, and T.-N. Dinh, “The DEFOR-s experimental study of debris formation with corium simulant materials,” *Nuclear Technology*, vol. 170, no. 1, pp. 219–230, 2010.



- [7] E. Takasuo, "An experimental study of the coolability of debris beds with geometry variations," *Annals of Nuclear Energy*, vol. 92, pp. 251–261, 2016.
- [8] P. Kudinov, A. Karbojian, C.-T. Tran, and W. Villanueva, "Agglomeration and size distribution of debris in defor-a experiments with  $\text{Bi}_2\text{O}_3\text{-W}_2\text{O}_3$  corium simulant melt," *Nuclear Engineering and Design*, vol. 263, pp. 284 – 295, 2013.
- [9] R. Meignen, B. Raverdy, M. Buck, G. Pohlner, P. Kudinov, W. Ma, C. Brayer, P. Piluso, S.-W. Hong, M. Leskovar, M. Uršič, G. Albrecht, I. Lindholm, and I. Ivanov, "Status of steam explosion understanding and modelling," *Annals of Nuclear Energy*, vol. 74, pp. 125–133, 2014.
- [10] E. Kim, M. Lee, H. S. Park, K. Moriyama, and J. H. Park, "Development of an ex-vessel corium debris bed with two-phase natural convection in a flooded cavity," *Nuclear Engineering and Design*, vol. 298, pp. 240–254, 2016.
- [11] B. Raverdy, R. Meignen, L. Piar, S. Picchi, and T. Janin, "Capabilities of mc3d to investigate the coolability of corium debris beds," *Nuclear Engineering and Design*, vol. 319, pp. 48 – 60, 2017.
- [12] E. Takasuo, "Coolability of porous core debris beds effects of bed geometry and multidimensional flooding." PhD thesis'.
- [13] C. Larmier, *Stochastic particle transport in disordered media : beyond the Boltzmann equation*. PhD thesis, (Paris Saclay), 2018.
- [14] A. Hébert, "A collision probability analysis of the double-heterogeneity problem," *Nuclear Science and Engineering*, vol. 115, no. 2, pp. 177–184, 1993.
- [15] A. Hébert, "Variational principles and convergence acceleration strategies for the neutron diffusion equation," *Nuclear Science and Engineering*, vol. 91, no. 4, pp. 414–427, 1985.
- [16] J. H. Park, H. S. Park, , and M. Lee, "A new two-phase pressure drop model for porous media in boiling conditions for dryout heat flux prediction," *ERMSAR proceedings*, 2019.
- [17] S. Torquato, *Random heterogeneous materials: microstructure and macroscopic properties*. No. 16 in Interdisciplinary applied mathematics, Springer, 2002. OCLC: 248518949.
- [18] P. Boulard, C. Larmier, J.-C. Jaboulay, A. Zoia, and J.-M. Martinez, "Neutron multiplication in fuel-water random media," *ICNC proceedings*, 2019.
- [19] A. Marinosci, C. Larmier, and A. Zoia, "Neutron transport in anisotropic random media," *Annals of Nuclear Energy*, vol. 118, pp. 406–413, 2018.
- [20] A. Santamarina and OECD Nuclear Energy Agency, *The JEFF-3.1.1 nuclear data library: JEFF report 22 : validation results from JEFF-2.2 to JEFF-3.1.1*. 2009.
- [21] G. Rowlands, "Resonance absorption and non-uniform temperature distributions," *Journal of Nuclear Energy. Parts A/B. Reactor Science and Technology*, vol. 16, no. 4, pp. 235–236, 1962.
- [22] L. Li and W. Ma, "Experimental characterization of the effective particle diameter of a particulate bed packed with multi-diameter spheres," *Nuclear Engineering and Design*, vol. 241, no. 5, pp. 1736–1745, 2011.

- [23] N. Chikhi, O. Coindreau, L. X. Li, W. M. Ma, V. Taivassalo, E. Takasuo, S. Leininger, R. Kulenovic, and E. Laurien, "Evaluation of an effective diameter to study quenching and dry-out of complex debris bed," *Annals of Nuclear Energy*, vol. 74, pp. 24–41, 2014.

# Chapter IV

## Criticality assessment of debris beds

### Contents

---

<b>IV.1</b>	<b>Criticality assessment methodology</b>	<b>92</b>
IV.1.1	Multi-physics coupling procedure	92
IV.1.2	Determining the thermal-hydraulics conditions	93
<b>IV.2</b>	<b>Training of surrogate models for neutronics</b>	<b>94</b>
IV.2.1	Building of the database	94
IV.2.2	Database filtration	96
IV.2.3	Selection of the surrogate model	96
IV.2.4	Mixture of models	100
<b>IV.3</b>	<b>Assessment of the criticality domain</b>	<b>100</b>
IV.3.1	Reactivity sensibility to decay power and pressure	100
IV.3.2	Assessment of the impact of power density and total mass	101
IV.3.3	Discussion of the observed trends	103
<b>IV.4</b>	<b>Synthesis</b>	<b>104</b>
	<b>Bibliography</b>	<b>105</b>

---

## Introduction

This chapter addresses the development of a criticality assessment methodology. First, the construction of the criticality assessment procedure is presented. Then, the selection of the best surrogate model and its training is explained. Next, the surrogate model optimisation is presented. Finally, the procedure is used to study the criticality domain consisting in three variables: pressure, debris bed mass, and power decay generated within the debris. These studies are applied on the generic case defined in chapter III and the results stemming from it are discussed.

### IV.1 Criticality assessment methodology

The proposed criticality assessment is a method developed to explore the domain of pressure, decay power and mass to estimate the maximum possible reactivity value and the associated risk. This criticality assessment is based on two steps: first the assessment of the thermal-hydraulics behaviour and then the assessment of the reactivity related to the accident. In this section we will present the description of the data transfer coupling procedure done between the thermal-hydraulics calculations and the neutronics calculations, followed by the description of the thermal-hydraulics model.

#### IV.1.1 Multi-physics coupling procedure

In order to assess the criticality risk of debris beds including the effects of the generated decay heat, it is required to have a neutronics calculation to obtain the reactivity at the time  $t$  and to perform a thermal-hydraulics calculation to have the thermal-hydraulics state of the debris bed at the time  $t$ . Criticality assessment does not demand the computation of nuclear power, thus a simple data transfer procedure might be sufficient: at each time step the thermal-hydraulics state is transmitted to the neutronics code. For this purpose, a C++ code was developed in order to store the data, print it and transfer it to the codes.

At each time step a thermal-hydraulics calculation is performed followed by an evaluation of the criticality of the new state, and so on as illustrated in figure IV.1. Since there is no nuclear power, the time step of this procedure can be taken as constant and set to capture properly the void fraction variation.

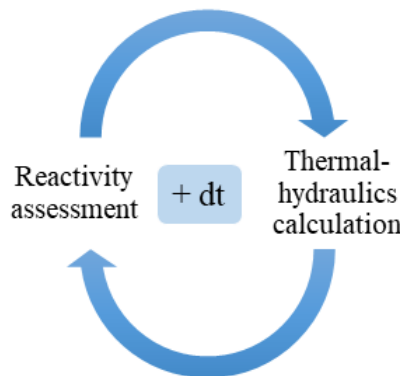


Figure IV.1: Criticality assessment procedure scheme.

This kind of simulation gives us information about the maximum reactivity that can be reached in the physical conditions as defined. The great asset of this method is the small computational cost required to explore the domain consisting in: pressure, debris bed mass, and the decay power (defined in chapter III). When the maximum obtained reactivity is positive, nuclear power might be generated, which would then require a fully coupled simulation in order to estimate the power peak and the deposited energy.

Assuming for the time being that the power density is static and there is no nuclear power, the temperature within the debris will not change. Actually, the debris temperature will stay close to the water boiling temperature, which varies from 373 K to 423 K, depending on the system pressure. The debris temperature difference could insert a reactivity difference of about 250 pcm. The moderator temperature difference could insert a reactivity difference of about 130 pcm. Thus, in view of the stronger effect of the moderator and the goal of the critical assessment, the contribution of Doppler effect was neglected for our purposes.

Concerning the neutronics calculations, the estimation of criticality for the physical system described in section III.1 demands several simulations, each composed of several reactivity assessments. The amount of neutronics calculations is thus non-negligible. The average calculation time with Apollo-2 is around 30 s: for a simulation covering a transient on 600 s with a time step of 0.20 s, the time devoted to neutron transport calculations may exceed 25 h, meaning that total time of the simulation is prohibitive. Therefore, the decision was taken to investigate the possibility of using of surrogate models to speed up the neutronics calculations.

## IV.1.2 Determining the thermal-hydraulics conditions

The thermal-hydraulics calculations with the MC3D code allow determining the inner debris temperature and the coupling, which requires a particular attention to avoid non-physical effects (coming from numerical approximations). The initial temperatures are set near the saturation point at the pressure input, and the porosity profile is static and corresponds to the obtained profile in chapter III. The spatial mesh is a 2-dimensional cylindrical grid. The setting of basic boundaries should be done carefully, as it can create non-physical effects. On the bottom, and the right adiabatic walls boundaries are applied. At the left axial symmetry is applied (as the mesh is cylindrical). The top boundary consists in a pressure condition: when the pressure inside the simulated system is higher than the preset pressure, a volume (gas or steam or liquid water) is extracted. The extracted volume is entirely replaced by the same volume of gas near the saturation temperature.

To avoid numerical problems, the approach we choose is to model the reflooding by keeping a layer of liquid water (around 30 cm) upon the debris bed. The thickness of the layer of liquid water will decrease thanks to the heat generated in the debris bed. To compensate the evaporation of the water, liquid water is injected from the top at the periphery of the mesh. The injected mass rate is carefully adjusted to exactly bring the mass of water that goes to the steam state. On the top boundary, the conditions (apart from water injection) are set to replace the output volume by non-condensable gas. The resulting behaviour is illustrated in figure IV.2.

The initial temperatures are set near to the saturation point at the pressure input. The boundaries of the MC3D calculation consist in a pressure condition at the top of the system and a water insertion close to the solid boundaries. By injecting the same mass of liquid water than expelled steam, it leads to have a stable mass of liquid water during the calculation. This condition allows maintaining the same thermal-hydraulics state (i.e. keeping the same amount of water in the upper layer) in the debris bed during the simulation. As described in chapter I, the diphasic cooling of the debris bed will display oscillations due to the large

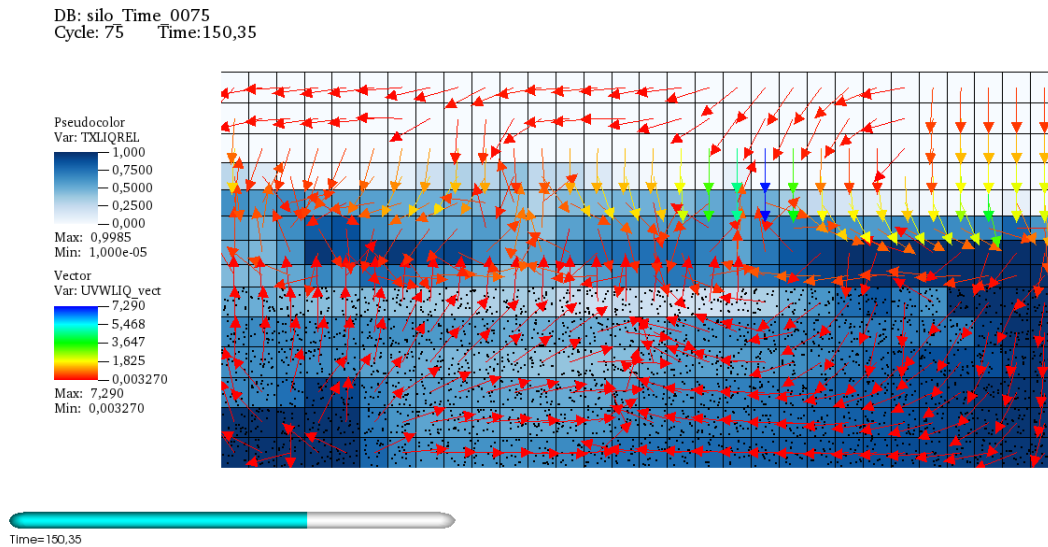


Figure IV.2: MC3D simulation of debris bed cooling with constant power. Insertion of liquid water (at the top boundary on the right) to keep a liquid water layer above the debris bed (water velocity visualized by coloured arrows, the cell colours representing the liquid water presence).

volume of created steam, which expels liquid water upon the debris bed. Hence, the stable state corresponds to a relatively stable heat flux extracted by the boiling of water, although the local void fractions are not stables. The calculation of the thermal-state during 1 s with MC3D and the described spatial mesh takes around 10 s of computational time.

## IV.2 Training of surrogate models for neutronics

This section discusses the selection and training of surrogate models, for the reactivity prediction. The construction of the database, the selection of the best surrogate model, and the optimization of the selected model are presented. To train and select the best surrogate model, the URANIE platform [1] was used.

### IV.2.1 Building of the database

Early investigations have shown that the spatial distribution of the void fraction drives the reactivity in the debris bed [2]. Hence, to accelerate the assessment of the reactivity in the debris bed, a regression model has been developed taking into account the void fraction in the spatial meshes of the debris bed and the total height of the debris bed.

Pre-calculations were required to train the surrogate model. In order to have a large representative database, calculations were done using only the thermal-hydraulics code MC3D. The conditions such as the decay heat and the pressure are set to be time-static in each simulation. The whole domain was randomly covered (a pair of pressure and power density values is randomly selected) and MC3D calculations were done on the parameters generating several void fraction maps over the system geometry. The void fraction maps were then added to the database. Also, some transients were calculated to enlarge the database: the first one is 100% dry debris bed reflooding and the second one is 100% flooded debris bed with high power generation leading to a quick dry up. Another value of interest is the debris bed height, which can be sampled easily as there is only one dimension.

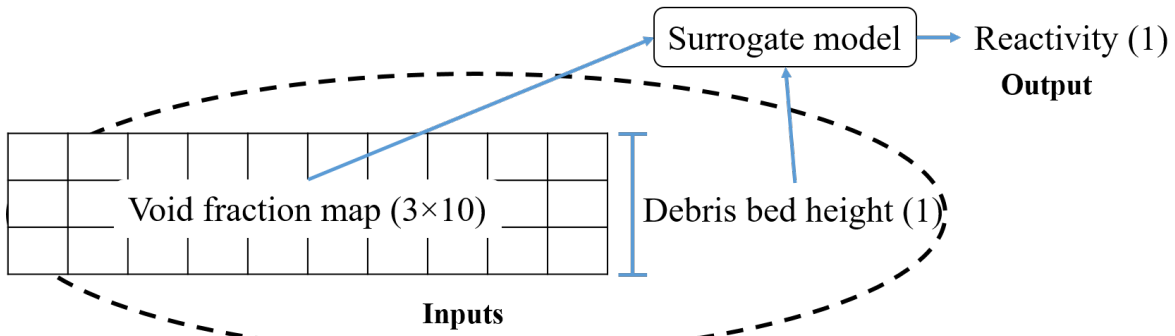


Figure IV.4: Scheme of the data dimensions

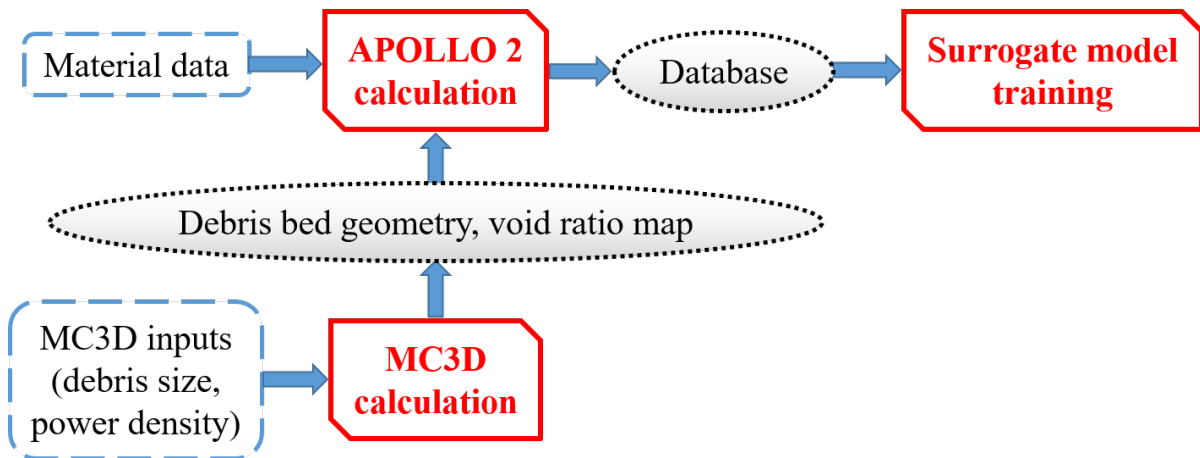


Figure IV.3: Scheme of the pre-calculation sequences to build the database

After the pre-calculations, a database of possible void fraction maps is obtained. For each void fraction map, a debris bed height is selected randomly in the range between 39 cm and 80 cm, which corresponds respectively to 59 t and 110 t of debris. Then, we perform neutronics pre-calculations to obtain the corresponding reactivity. The whole sequence to build the database is illustrated in figure IV.3. The resulting database is made of 7992 points (each point consists in a void fraction map, a debris bed height and a reactivity), the enlargement of the database was arbitrarily stopped when the number of points seemed sufficient, based on previous experiences by trial and error. The inputs are the void fraction map (30 values) and the debris bed height (1 value); the output is the reactivity (1 value). There are thus 32 inputs and 1 output to model. They are illustrated in figure IV.4.

The use of surrogate models would require to have the dataset separated in two pieces, the testing dataset and the learning dataset (usually they represent respectively 20 % and 80 % of the total dataset). When the number dimension of the input is relatively large, it becomes computationally expensive to explore the whole space of the degrees of freedom [3]. In this case it make sense to generate a smaller dataset, which corresponds to the kind of data that the neural network will most likely explore. The inconvenient of this method is that the surrogate model might not be able to predict properly new points if the generated data are not large enough to represent the whole free parameter space. We will discuss a possible remedy to optimize the prediction of surrogate model.

## IV.2.2 Database filtration

In the case of large of inputs, it may be time-expensive to explore the whole space of the degrees of freedom. In order to have a useful database, we propose to create the database with the inputs usually generated during simulations. The asset is that the database might be close to the data which the model will cover. However, no one can say that the data generated by the simulations cover the whole accessible space. Another flaw is that several points might be close to each other (regarding the input values). In this case, a larger database would not improve the accuracy and the generalisation capabilities of the neural network. Actually, the model would become an *expert* where the points are clustered, but might be otherwise suffer from bad precision issues in other portions of the free parameters space.

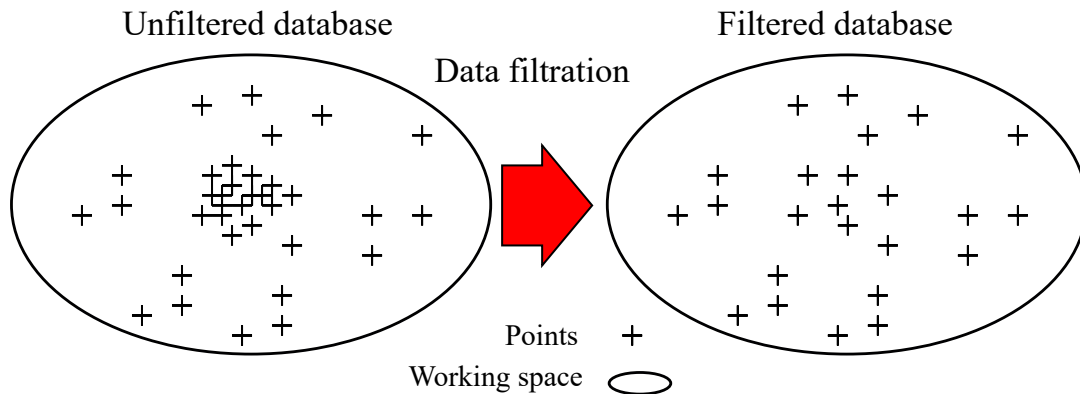


Figure IV.5: Representation of the database filtration, the validation database is on the right and the training database is on the left.

A possible remedy to this flaw is the filtration of the inputs of the database: the Euclidean distance between each points is computed, then all points which are too close to each other are put aside. Here, the Euclidean distance was arbitrarily set to keep only 35 % of the points, based on previous experiences by trial and error. After this operation, the database is separated in two parts: the filtered data, where points are not stacked, and the unfiltered data. The unfiltered data is still made of relevant data that could appear during the use of the surrogate model. Figure IV.5 illustrates the operation done to separate the training and the validation database. The filtered data have a proper points distribution and will be used as the training database. Therefore, the trained surrogate model would be less specialized and its precision would be more relevant. The validation is done on the unfiltered database, meaning that some points were used in training and validation: as the number of points in the training base is lower (2800) than the validation database (7992), the impact of this approximations on the metrics is negligible. The advantage of this method is that without filtering we would have obtained over-represented domains in the inputs space and that the filtering allows to equalize the contribution of each simulation.

## IV.2.3 Selection of the surrogate model

Finally, after building the database, we can train a surrogate model to predict the reactivity of the debris bed. Various models can be trained using existing tools as the URANIE platform [1]; polynomial regression or artificial neural networks for example. The approach consists in building models of increasing complexity when the obtained fidelity is not sufficient. The performance of the model is evaluated on the validation database.

First the performance of a polynomial regression of degree 1 was assessed. The corresponding results are illustrated in figure IV.6. The average absolute error is 2071 pcm, the



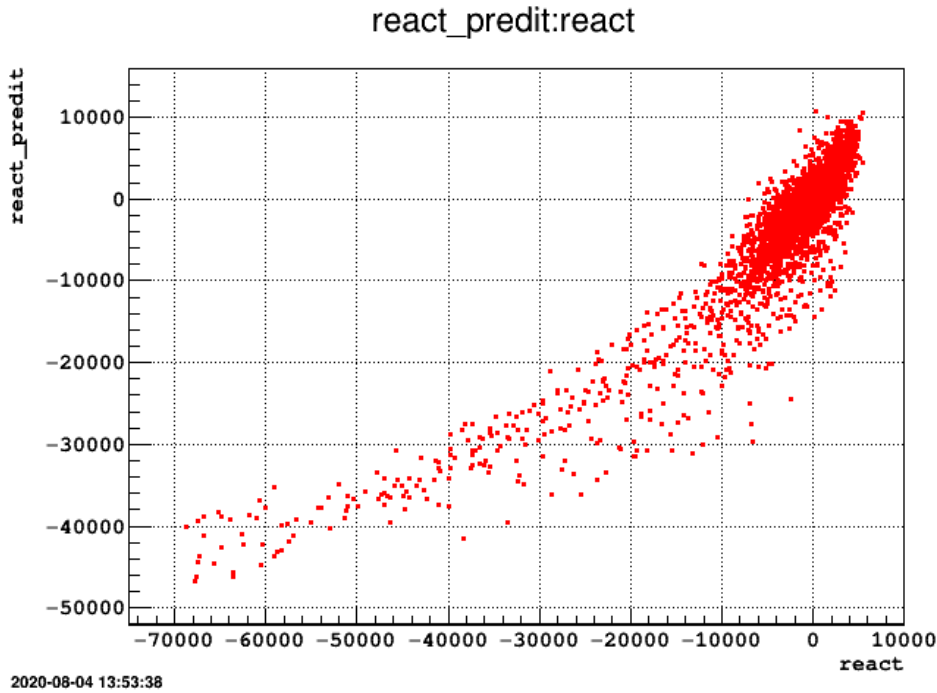


Figure IV.6: Prediction of the *reactivity* by polynomial regression of degree 1 against the expected reactivity on the validation dataset.

standard deviation is 3183 pcm and the maximum error is 22231 pcm. The standard deviation of the errors is higher than the value of the  $\beta_{eff}$  and the maximum error is too high (as the maximum error can be taken as the margin during calculations). These performances are not sufficient enough for our scopes.

The second model assessed is a polynomial regression of degree 2. This offers more possibilities of regression to predict the reactivity. The results of the predicted values against the real values is drawn in figure IV.7. Generally speaking a non-negligible improvement can be remarked between the linear and quadratic regression. The average absolute error is 1011 pcm, the standard deviation is 1500 pcm and the maximum error is 11012 pcm. However, the standard deviation of the errors is still higher than the value of the  $\beta_{eff}$ . Thus, the performances of the quadratic surrogate model are still unsatisfactory. One should note that with 32 inputs the number of parameters for a polynomial regression of degree 3 (5984 parameters) will outnumber the training database points, thus the analysis of the polynomial regression was stopped at 2.

The third class of surrogate models to be assessed is the artificial neural network (ANN) of type multi-layer-perceptron (MLP). A MLP is composed of several layers of neurons, from the input layer to the output layer. Each neuron of a layer is connected to the neurons of the layer before it. An automatic evaluation was build to assess the best number of neurons.

An investigation was done to identify the optimal number of neurons. The performances observed in figure IV.8 show that when the number of neurons increases the performances increase as well. To avoid over-fitting the number of neurons is kept below 36 so as to ensure that the number of model parameters is as low as the number of training sets (around 2800). Moreover, in figure IV.8 we show that the accuracy increase slows down significantly after 32 neurons. The best activation function for the studied case is the hyperbolic tangent, which shows a decrease of the standard deviation of 7 % and the maximum error of 20 %. The results of the predicted values using ANN against the real values are illustrated in figure IV.9. The optimal size of the neural network models is between 26 and 32 neurons with only one

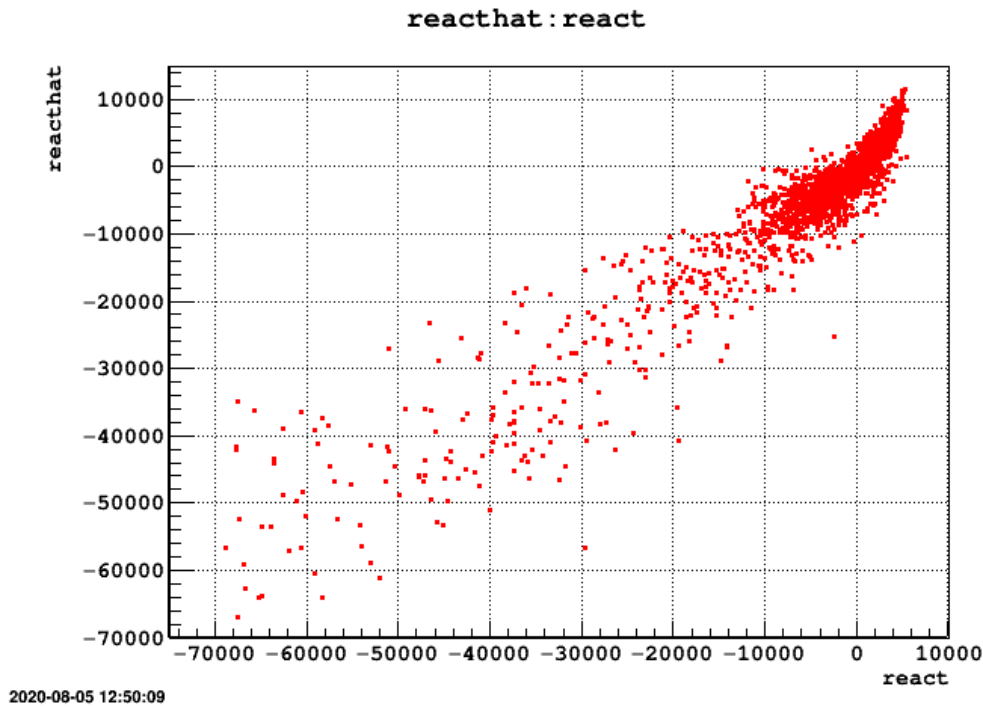


Figure IV.7: Prediction of the *reactivity* by polynomial regression of degree 2 against the expected reactivity on the validation dataset.

hidden layer<sup>1</sup>. The results show that adding more layer do not improve the accuracy of the models.

The average absolute error is 80 pcm, the standard deviation is about 180 pcm and the maximum error is 3200 pcm. With this kind of surrogate models, a significant improvement was observed as compared to the two other surrogate models tested above. The standard deviation of the errors is lower than the value of the  $\beta_{eff}$ . Because accuracy criteria are fulfilled the choice was made to investigate the possibility of improving the prediction capabilities of this surrogate model.

<sup>1</sup>However, one should note that the latest version of URANIE platform is able to compute ANN with more than one hidden layer [1].

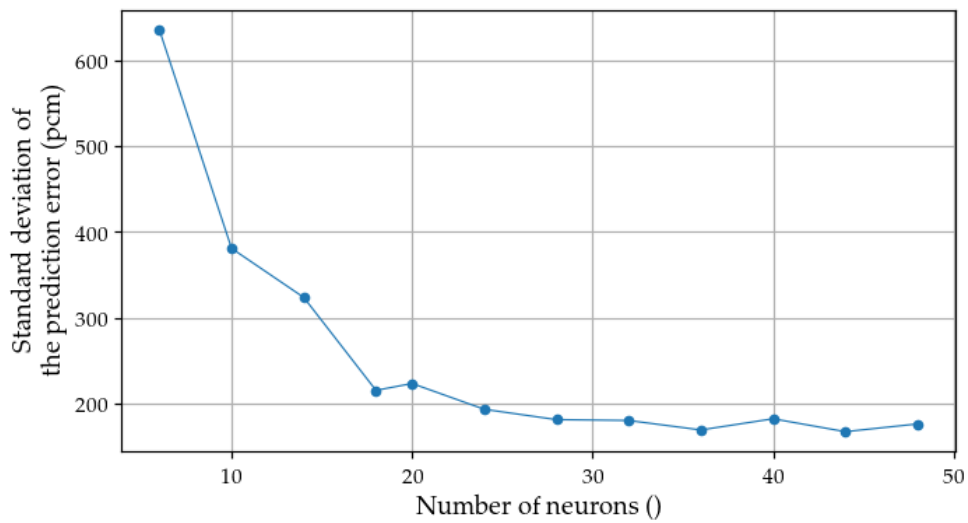


Figure IV.8: Analysis of the number of neurons required to increase the accuracy of the ANN. The performance are not improved when the number of neurons goes beyond 32.

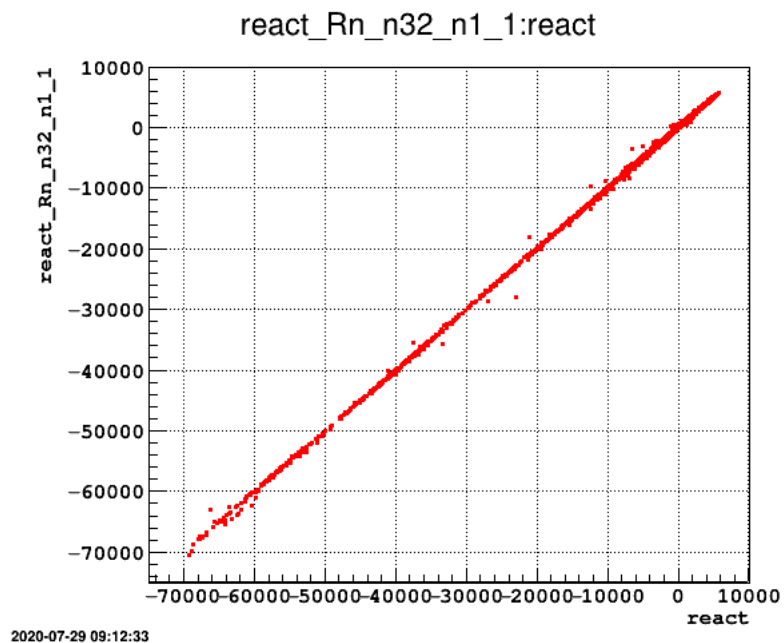


Figure IV.9: Prediction of the *reactivity* by ANN regression against the expected reactivity on the validation dataset.

#### IV.2.4 Mixture of models

When neural networks are not precise enough despite extensive training, the method of model mixtures might improve the statistics of the results [4]. After creating a pool of neural networks, each model is mixed with the others (the mix consists in doing an average of the models outputs). The statistical error is computed only on the validation database, and eventually the best mixture of models is selected. This method might help to improve the overall performance and it is usually more efficient to decrease the maximum error. However, as the error distribution is not following a Gaussian distribution, this method sometimes fails to significantly improve the prediction [3].

A large set of models was trained on the training database. The number of neurons in the hidden layer varies between 26 and 32. In each training sequence, the provided database is randomly cut from 20% of the points which are used as a validation database during the training. The obtained models are stored for a future use, and they should be different from one another. An automatic method was built to estimate the best mixture of models regarding the accuracy of the prediction. The first finding is that the addition of more than 3 models did not bring significant improvements. However, the best mixture of 3 models has shown a decrease of 36 % of the standard error and a decrease of 20 % of the maximum error. Therefore, the best mixture of 3 models was selected to be used in the simulation as a replacement of time-consuming neutron transport calculations with Apollo-2.

### IV.3 Assessment of the criticality domain

The generic case-study presented in chapter III, the associated domain of investigation (in terms of pressure and power density range), and the means of calculation presented in section IV.1 are now used to assess the criticality risk of debris beds.

A preliminary analysis on the combined effects of power density and pressure will be performed. The results and the trends will be described. Then, an investigation about the impact of the power density and the total mass of debris will be presented and analysed.

#### IV.3.1 Reactivity sensibility to decay power and pressure

The decay power and the pressure can have an effect on the thermal-hydraulics behaviour of the debris bed, impacting the reactivity. Liquid water is injected to keep the same amount of liquid water in the system. <sup>2</sup>

---

<sup>2</sup>This preliminary analysis was performed with parameters which differ from the one that are recommended (regarding chapter III). In fact, none equivalent diameters were used, only the pre-calculated porosity profile was used in this study. The debris diameter used in every physical field was equal to 3 mm. These differences impact the reactivity values but the trends must be the same even with equivalent diameter.

Pressure (Pa)	$\Delta\rho$ (pcm)			
	Power density (MW/m <sup>3</sup> )			
	0.60	0.80	1.0	1.2
$10^5$	-12854	-15568	-18815	-21656
$2 \times 10^5$	-10695	-12225	-13770	-15126
$3 \times 10^5$	-9661	-10975	-12295	-12848
$4 \times 10^5$	-9110	-9952	-11250	-12505
$4.5 \times 10^5$	-8344	-9963	-10965	-12029

Table IV.1: Maximum reactivity recorded during simulations [5].

The simulations were performed using the code MC3D and the reactivity was obtained from the surrogate model. The maximum reactivity value ( $-8344$  pcm, with a large margin from zero) is obtained for a power of  $0.6$  MW/m<sup>3</sup> and a pressure of  $4.9 \times 10^5$  Pa. The lowest reactivity values were obtained at the maximum volumetric power for each pressure value. Furthermore, the higher the pressure, the higher becomes the reactivity at the same power level.

This first study shows that the power density generated inside the debris can create enough steam in permanent regime to keep the reactivity of the system below zero [5].

### IV.3.2 Assessment of the impact of power density and total mass

The effect of the power comes from the rate of steam generated within the bed. Indeed, when more steam is created less moderator is present in the debris bed. This lack of moderator will insert negative reactivity. The effect of the pressure comes from the steam density. As the steam is a gas, its density will increase proportionally to the pressure. Thus, at higher pressure, the volume of steam is lower (for the same power density) and more liquid water is present in the debris bed. Reciprocally, at lower pressure, the steam takes a larger volume and the fraction of liquid water is lower.

The choice was made to shift the parametric study from the couple of pressure/power density to total mass/power density. The range of parameters was adapted according to preliminary studies [5]. Thus, the power density was set between  $0.45$  to  $0.65$  MW/m<sup>3</sup> and the total mass from  $40$  to  $80$  t.

For each simulation, the maximum time was set at  $800$  s. The first  $100$  s correspond to the transient where the permanent regime is not yet reached. The injected water rate was set to be equal to the rate of steam created thanks to the total power generated by the power density in the debris. An example of the debris bed behaviour is illustrated in figure IV.10, where the void fractions are averaged by axial layer. The void fraction is higher at the top than at the bottom, and this can be explained by the fact that the steam generated at the bottom goes up, increasing the void fraction in the upper layer. The oscillations of the void fractions come from the power density generated within the debris, which will generate steam. As the pressure is relatively low ( $0.1$  MPa) the steam volume is non-negligible ( $1$  kg of steam has a volume of  $\approx 1$  m<sup>3</sup>) and it expels liquid water from the debris bed. This effect creates drying and reflooding cycles, leading to void fraction oscillations observed in figure IV.10 for example.

The reactivity is strongly correlated to the void fractions, and oscillates by following the opposite behaviour of the void fractions. In figure IV.10, the reactivity values range from  $-13948$  to  $-706$  pcm. The oscillations period is around  $12$  s in this example (this period may come from debris bed properties such as permeability, passability, and the debris bed

thickness). There is no coupling between the neutron transport estimation and the thermal-hydraulics, so that the frequency exclusively depends on the thermal-hydraulics effect.

The usual simulation time was about 10 h, with 96 % coming from the MC3D calculation time. Without the use of ANN, and assuming that the Apollo-2 calculation takes 30 s to estimate the reactivity, 66 h would have been required to evaluate the reactivity on the 8000 points.

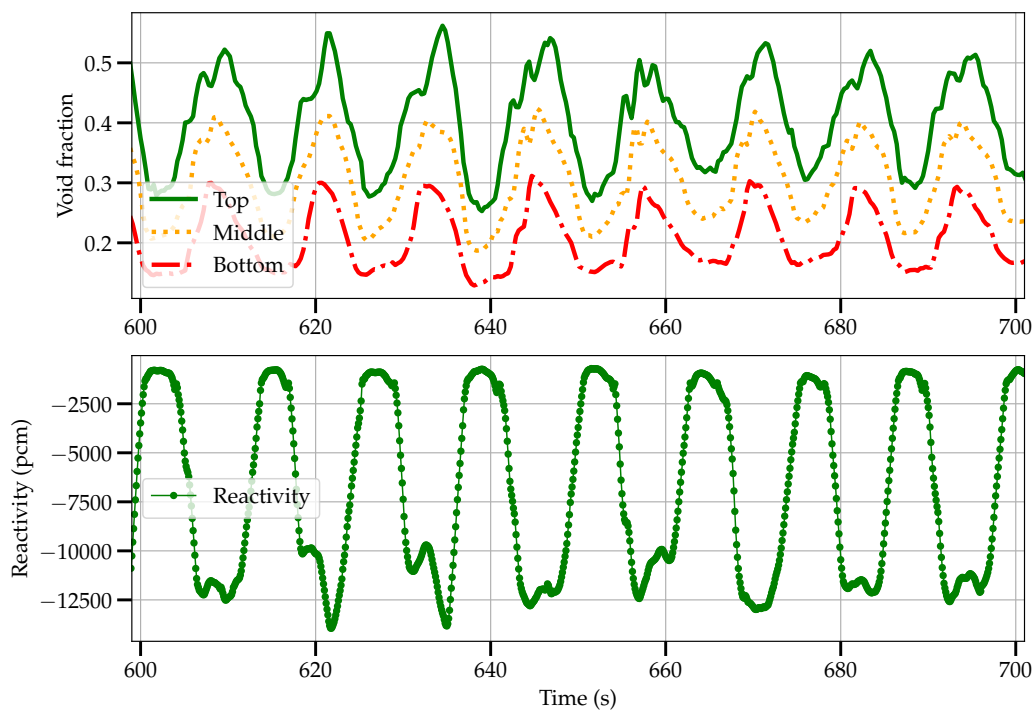


Figure IV.10: Oscillations of the reactivity during the debris bed cooling with 60 t of debris and a power density of  $0.45 \text{ MW/m}^3$ .

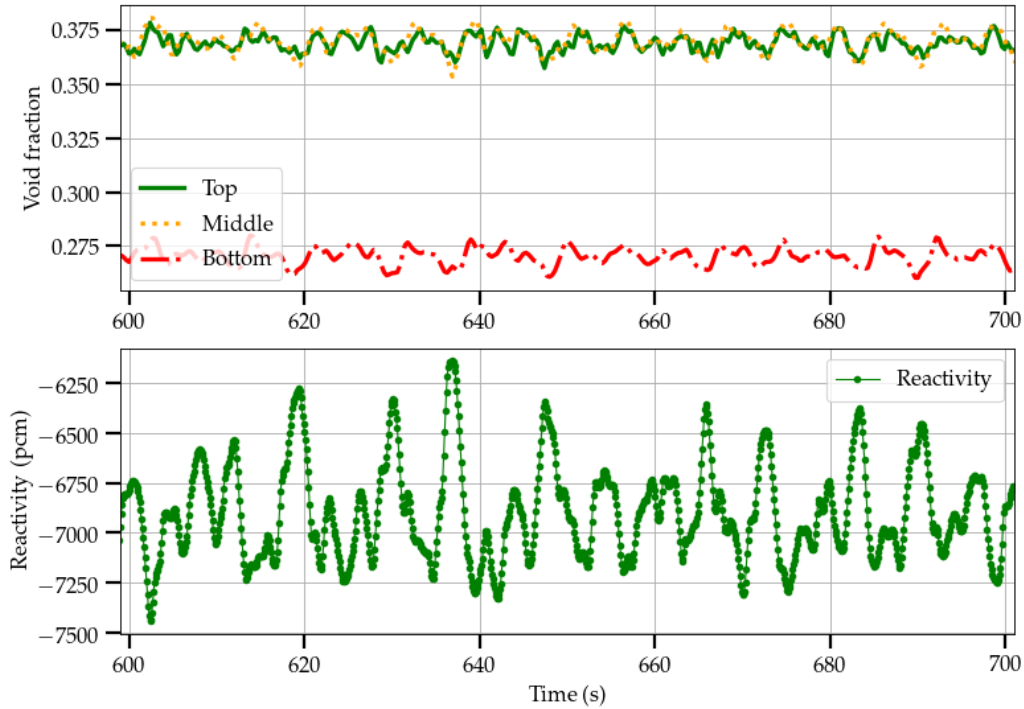


Figure IV.11: Oscillations of the reactivity during the debris bed cooling with 80 t of debris and a power density of  $0.45 \text{ MW/m}^3$ .

In figure IV.10 the reactivity variations correspond to the opposite of the void fraction variations. Moreover, the void fraction is increasing with the height inside the debris bed. In figure IV.11, the debris bed mass was set to 80 t. In this case the reactivity follows the same trends, but the variations of void fraction are weaker than the 60 t case.

Mass of debris ( $t$ )	$\Delta\rho$ (pcm)				
	Power density ( $\text{MW/m}^3$ )				
	0.45	0.50	0.55	0.60	0.65
40	-5920.	-6095	-6123	-6335	-6294
50	-2096.	-2269	-2860	-3943	-8806
60	-612	-1418	-9012	-9988	-10773
70	-6892	-7489	-8852	-10214	-9814
80	-5958	-5066	-6401	-5591	-9428

Table IV.2: Maximum reactivity recorded during simulations (the green cells show the lowest reactivity value and the orange cells show the highest reactivity at a set power density).

### IV.3.3 Discussion of the observed trends

In the calculations presented above, the value of interest is the maximum reactivity seen during the simulation, which is a suitable estimator of the potential risk of a return to criticality of the debris bed. The results of the investigation are summarized in the table IV.2, where the maximum and minimum values of reactivity at a static power density are respectively shown in orange and green.

Two phenomena are here in competition. The effect of the power density helps to generate steam inside the debris bed. Yet, this steam decreases the moderation ratio of the boiling



cells and thus decreases the overall reactivity. Moreover, the steam is created by the total power, which means that the larger the mass, the more steam would be generated, thus decreasing further the reactivity. The effect of mass, helps to decrease the neutron leakage. Hence, the addition of debris mass will increase the reactivity of the system.

In the table IV.2, at  $0.65 \text{ MW/m}^3$  and starting to 60 t the effect of mass is predominant as the reactivity goes up from  $-10773$  to  $-9428$  pcm. However, at  $0.45$  and  $0.50 \text{ MW/m}^3$  it can be clearly seen that the effect of power density is stronger. Indeed, the maximum reactivity is obtained at 60 t despite the higher neutron leakage. In effect, at these power density values, the reactivity decreases when the mass increases, so the power density effect seems to be higher around 60 – 70 t, then the mass effect takes over.

The second investigation illustrated in the table IV.2 shows a significant effect regarding criticality risk. Indeed, it shows that, when taking into account the thermal-hydraulics state of the debris bed, counter-intuitive effects appear: the maximum reactivity recorded was not obtained with the maximum mass of debris. In fact the maximum reactivity is a function of the power density and the mass of debris. The most significant finding is that if the power density prevents the system from becoming supercritical when the mass of debris is high, it is not necessary the case with lower mass of debris (60 t). Indeed, it was observed that the effect of power density is higher than the addition of mass leading to a higher reactivity with less mass (example at 60 t at  $0.45 \text{ MW/m}^3$ ).

Usually, when the total fissile mass increases the reactivity should increase as well. In our example, however, the addition of mass leads to an increase of the total power that must be extracted from the debris beds too cool it. This effect generates more steam in the debris bed and decreases the reactivity.

A parallel can be done with a previous investigation about power density and pressure effect, presented in [5]. Indeed, the lowest value of power density studied in the table IV.2 using the El-Wakil estimation corresponds to approximately 30 days after the reactor shut-down. This significant value highlights that the debris bed can be kept subcritical thanks to the power density generated within the debris during a large period of time in the event of severe accidents. The contribution of thermal-hydraulics was crucial to obtain this result.

## IV.4 Synthesis

We have introduced a methodology to estimate the criticality of debris beds. Special attention was paid to the hydraulics modelling (as the issue of convection loops in the thermal-hydraulics). An artificial neural network was trained and optimized to speed-up the simulations. The results of this speed up are substantial: indeed, without the use of surrogate models the simulation would have been extremely time consuming.

A parameter domain composed of decay power, pressure and mass was explored. Although the preliminary investigation was not performed with an equivalent diameter (published in [5]) it should be noted that the maximum reactivity estimated during simulations decreases when the power density increases and the pressure decreases.

A complementary analysis was done with a debris diameter pertinent for a realistic debris size distribution. This study shows counter-intuitive behaviours, for a constant power density the maximum reactivity was not observed with the higher debris mass. The finding stemming from this second investigation is significant, as it shows that the optimal mass to have criticality strongly depends on the power density: there might exist an optimal mass different from the maximum mass. Finally, the main conclusion of the application of the methodology is that power density prevents the return to criticality.

These investigations have brought important knowledge about criticality of debris beds. Nevertheless, to estimate the potential mechanical consequences in the case of criticality it



is required to have a *source term*. This source term is the energy release by fission within the debris bed in the case of power transient. Therefore, the next steps will be to adapt the methodology in order to compute the energy deposited during the transient, and to implement a kinetics calculation to obtain the nuclear power time-evolution.

## Bibliography

- [1] CEA, “Uranie.” <https://sourceforge.net/projects/uranie/>, Accessed 29 April 2020.
- [2] P. Boulard, J.-C. Jaboulay, A. Zoia, and J.-M. Martinez, “Neutron multiplication in fuel-water random media,” *ICAPP proceedings*, 2019.
- [3] T. Hastie, R. Tibshirani, and J. Friedman, *The elements of statistical Learning*. Springer, 2008.
- [4] L. Breiman, “Bagging predictors,” *Machine Learning*, vol. 24, no. 2, pp. 123–140, 1996.
- [5] P. Boulard, J.-C. Jaboulay, J.-M. Martinez, and A. Zoia, “Contribution of thermal-hydraulics simulation to criticality analysis of a debris bed numerical mock-up,” *PHYSOR proceedings*, 2020.

# Chapter V

## Deposited energy estimation of a critical event in debris beds

### Contents

---

<b>V.1 Fully coupled simulation procedure</b> . . . . .	<b>107</b>
V.1.1 Required precision . . . . .	107
V.1.2 Strategies to speed-up the neutron transport . . . . .	108
V.1.3 Adaptative time-step . . . . .	110
V.1.4 Simulation time . . . . .	111
<b>V.2 Assessment of power excursion</b> . . . . .	<b>112</b>
V.2.1 Simulation of critical transients in debris beds while reflooding . . . . .	112
V.2.2 Discussion on the behaviour of the simulated systems . . . . .	116
V.2.3 Investigation of "ad hoc" cases to identify a reliable maximum source term . . . . .	118
<b>V.3 Synthesis</b> . . . . .	<b>124</b>
<b>Bibliography</b> . . . . .	<b>125</b>

---

## Introduction

In chapter IV three trends were highlighted, namely the dependency of the optimal mass on the power density, the effect of the pressure on the reactivity in diphasic conditions, and the sensitivity of the reactivity to the decay power density. These findings have emphasized some key issues concerning the behaviour of criticality for debris beds. Nevertheless, in order to estimate the potential mechanical consequences in the case of criticality it is required to know precisely where the energy is deposited. Hence, the methodology developed in the chapter IV must be adapted to couple together the neutron transport and the thermal-hydraulics.

This chapter deals with our efforts towards the development of the multi-physics coupling, required to estimate the released fission energy distribution, called here the *source term*. The source term is required to assess the mechanical consequences. First, the coupling procedure and the several strategies to accelerate the simulation are explained. Then, simulations performed with simplified conditions are presented to test the methodology and obtain the source term.

## V.1 Fully coupled simulation procedure

In order to estimate the energy deposited during a power excursion, multiple tools are required:

- a neutron transport calculation to compute the reactivity, the nuclear power shape, and the time evolution of the nuclear power;
- a thermal-hydraulics calculation to simulate the thermal-state (and the presence of water) in the debris bed and the heat diffusion within the debris;

The models required to simulate power transient are illustrated in the figure V.1. We add features to the C++ code developed in chapter IV to simulate the kinetics and transfer the data to the codes (Apollo-2 and M3CD).

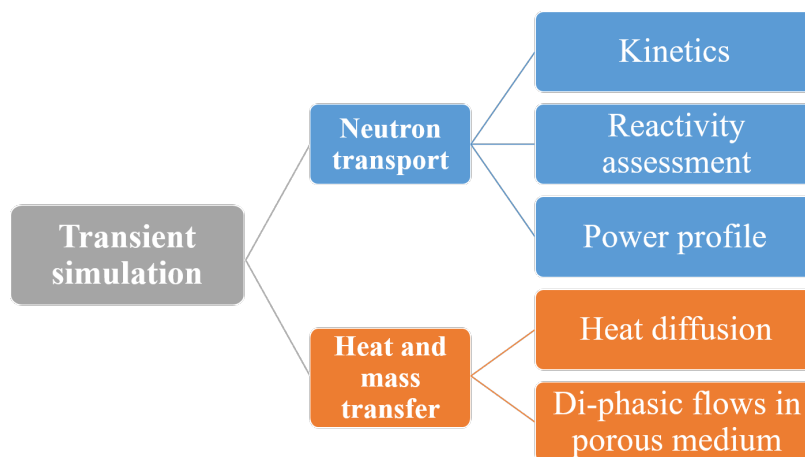


Figure V.1: Scheme of the coupling requirements for transient simulations.

### V.1.1 Required precision

The explicit coupling strategy implies that at each time-step the neutron transport calculation is followed by the thermal-hydraulics calculation. Thus, the thermal-hydraulics state of

the system is properly taken into account. In practice, this strategy depends on the accuracy needed during the simulation.

When  $\rho \geq \beta_{eff}$  the time  $T_d$  to double the neutron population can be expressed as:  $T_d = \frac{\ln(2)\Lambda}{(\rho - \beta_{eff})}$ . This equation yields:  $\ln(T_d) = \ln(\ln(2)\Lambda) - \ln(\rho - \beta_{eff})$  where  $\delta\rho = \rho - \beta_{eff}$  is introduced. Now we can write:  $d\ln(T_d) = \frac{dT_d}{T_d}$  assuming that only  $\delta\rho$  is uncertain, which gives:

$$\frac{\Delta T_d}{T_d} = \frac{|\Delta \delta\rho|}{\delta\rho} \quad (V.1)$$

Applying equation V.1 with  $\delta\rho$  of 10 pcm,  $\beta_{eff}$  equal to 760 pcm,  $\Lambda$  equals to  $2.5 \times 10^{-5}$ , an error of 5 pcm on the  $|\Delta \delta\rho|$  yields a relative error on the doubling time of about 45 %. This error will be propagated to the power and will modified the transient progress; an error that high (50 %) is not adequate to estimate the deposited energy. The reactivity value must be highly reliable when the reactivity comes closer to the  $\beta_{eff}$ , as an error as low as 5 pcm would introduce non-negligible deviations on the power transient.

### V.1.2 Strategies to speed-up the neutron transport

As described in the previous sub-section, an accurate estimation of the reactivity is needed as an input of the kinetics module. The ANN developed in this work does not offer sufficient precision to estimate the reactivity near criticality, so the decision was made to couple the code with the deterministic code Apollo-2. Using Apollo-2, the debris temperatures, the void fraction in each cell and the debris bed height are considered, while the ANN considers only the void fraction in each cell and the debris bed height.

To obtain nuclear power evolution, a module of point kinetics is included. This module was developed in previous work at CEA [1]. The inputs are the new reactivity and the time-step. As the developed method is a quasi-static approach, the kinetics calculation gives the evolution of the integral nuclear power in the debris bed. The spatial distribution of the nuclear power and the reactivity assessment are computed by Apollo-2.

The thermal module calculates the debris temperature profile thanks to a finite-volume numerical scheme that we have developed in this work. The heat which leaves the debris is transmitted to MC3D to simulate the thermal-hydraulics state of the debris bed. The dataset consists of a debris bed where the inputs are the heat generated in the debris and the debris bed height. At each time-step the power density is updated.

At each time-step the thermal-hydraulics state of the debris bed is computed, then the reactivity and the nuclear power distribution is estimated, eventually the new reactivity is used in the kinetics module and the new power and its distribution are obtained, the coupling scheme is illustrated in figure V.2.

An adaptative time step procedure was developed to make this simulation possible: this issue is addressed in the subsection V.1.3. When the time step is decreased to a very low value (lower than 2 ms), the thermal-hydraulics calculation using MC3D is time-consuming without bringing any information (the diffusion time of the heat in the debris is too high). The adopted solution is to skip the MC3D calculations and to activate it only with a time-step of 2 ms. When the MC3D calculations is skipped, an extrapolation of the time evolution of the void fraction is done.

In order to decrease the computing time, the use of ANN offers a way to speed up easily the calculation. As the ANN is not as precise as Apollo-2, a threshold was set on the reactivity to switch from the ANN estimation to the Apollo-2 calculation. The ANN is used to estimate the reactivity when it is far from criticality: more precisely the criterion is defined by a strong negative value of reactivity (lower than  $-5 \beta_{eff}$ ). The threshold value is the the maximum error of the ANN on the validation database. This setting is quite conservative, but, as the

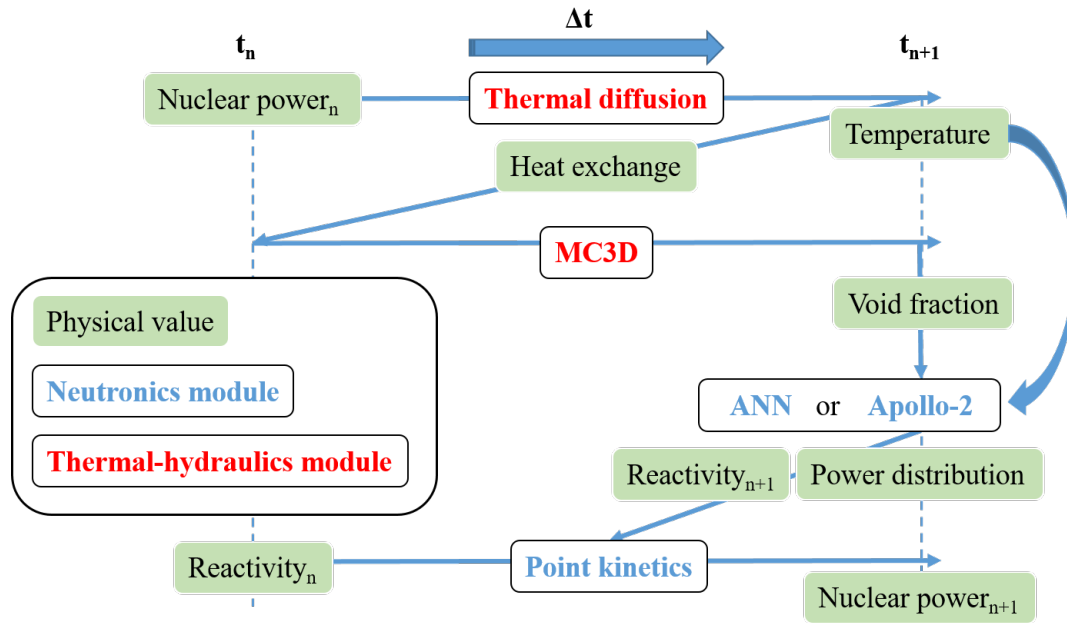


Figure V.2: Scheme of the coupling calculations on one time-step.

coupling code is not able to correct the past estimation knowing the present estimation, it is required to have a sufficiently large error margin.

In this case, instead of doing reactivity assessment with the code Apollo-2, the ANN is used to estimate the reactivity. This enables the procedure to be less time-consuming when high precision is not required. Indeed, when the reactivity is negative, the nuclear power is decreasing quickly and it becomes negligible. This feature accelerates the calculation, since accurate neutron transport calculations will be carried out only when necessary.

In the other hand, the spatial distribution is not updated when the reactivity is assessed with the ANN, which is justified by the fact that the nuclear power is relatively low when the ANN is used. This approximation must have negligible effect on the simulation of transients.

The reactivity that is used to evaluate which model must be used comes from either the Apollo-2 calculation if the last point was obtained with Apollo-2, or from the ANN, corrected by the Apollo-2 calculation. This correction corresponds to the error between last obtained reactivity by Apollo-2 calculation and the ANN calculation. The correction is taken into account and set as a constant if it leads to a higher reactivity value. Otherwise, with a negative correction term, a decay factor (the half life was empirically set to 6 iterations) is applied to the correction to prevent error in the following, this can lead to the trigger of unnecessary Apollo-2 calculations. An example of the correction is illustrated in figure V.3. At 205 s the reactivity is computed using ANN, but a correction is applied on the ANN reactivity giving a lower value. At 209.3 s the Apollo-2 calculation is triggered, the obtained reactivity is lower than the ANN prediction, thus a negative correction is added. It is kept for the following calculations avoiding the triggering of several unnecessary Apollo-2 calculations.

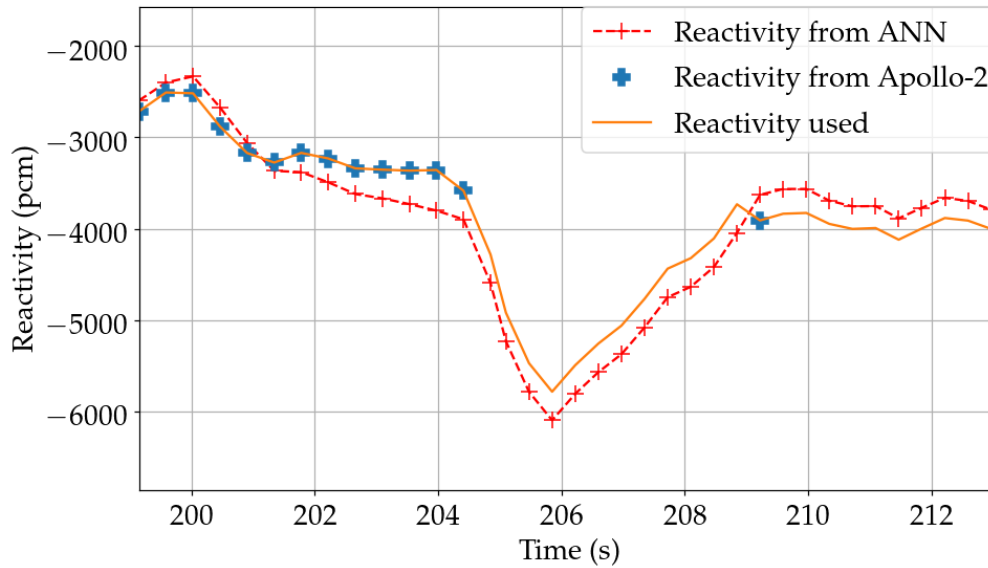


Figure V.3: Example of ANN correction after Apollo-2 calculation.

The two strategies to speed-up the simulation of transient are illustrated in the table V.I.

	Reactivity		
<b>Discipline</b>	$] -\infty; -5 \times \beta_{eff}]$	$[-5 \times \beta_{eff}; 1 \times \beta_{eff}]$	$[1 \times \beta_{eff}; +\infty[$
<b>Thermal-hydraulics</b>	MC3D	MC3D	Extrapolation + MC3D (time step of 2 ms)
<b>Neutronics</b>	ANN	Apollo-2	Apollo-2

Table V.I: Strategy to accelerate transient simulations.

### V.1.3 Adaptive time-step

The precision needed regarding the reactivity is high when the objective is to assess the nuclear energy released by power transients. However, high precision is not required if the system stays sub-critical. The global time-step tells when the information is exchanged between the different models. In order to have accurate simulations the exchange rate for the power density, the void fraction, the debris temperature must be high enough or the physical effects may suffer of numerical delay.

For example, if the power in the nuclear material is not transmitted to the thermal model during a prompt transient, the reactivity feedback created by the Doppler effect will appear too late. In this case, the nuclear power may increase to non-realistic values (introducing a significant over-estimation of the power peak). So, it is crucial to update each physical condition in each model.

On the other hand, an excessive frequency of updates would be time-consuming without bringing a better precision to the simulation. Therefore, the time-step must be adapted to the conditions observed in the simulated system.

The maximum time step is set to 0.5 s and there is no minimal time-step. The time-step is dynamically adapted according to: the reactivity, the reactivity slope, the power, and the power slope. If one criterion is not verified (one slope is stronger than the maximum admitted

slope) the time-step is refined. In the same way, minimal slopes are set depending on the reactivity and if one of this criteria is not respected, the time-step is increased.

Depending on the value of reactivity, a maximum slope is set. For example, the maximum slope decreases from  $5\beta_{eff}/s$  to  $1/20\beta_{eff}s$  if the reactivity goes from  $-20\beta_{eff}$  to  $9/10\beta_{eff}$ . The criteria are based on previous experiences by trial and error.

Time-step is additionally refined if the system is prompt critical with a power criteria to trigger this refinement (indeed, unless the power is high no feedbacks would appear then a refined time-step is unnecessary). For example, the power evolution in prompt critical is kept below 20 % by time-step, in the other cases (sub-critical or delayed critical) the power evolution is kept below 35 - 50% by time-step.

In figure V.4 we illustrate the time step adaptation during a simulated transient. A first time-step refinement can be remarked at 2.2 s triggered by a sudden increase of the reactivity slope. At 3.3 s the reactivity exceeds the  $\beta_{eff}$  triggering a gradual refinement of the time-step. Finally, when the reactivity decreases to negative values at 3.4 s, the time step is enlarged as high precision is no longer required.

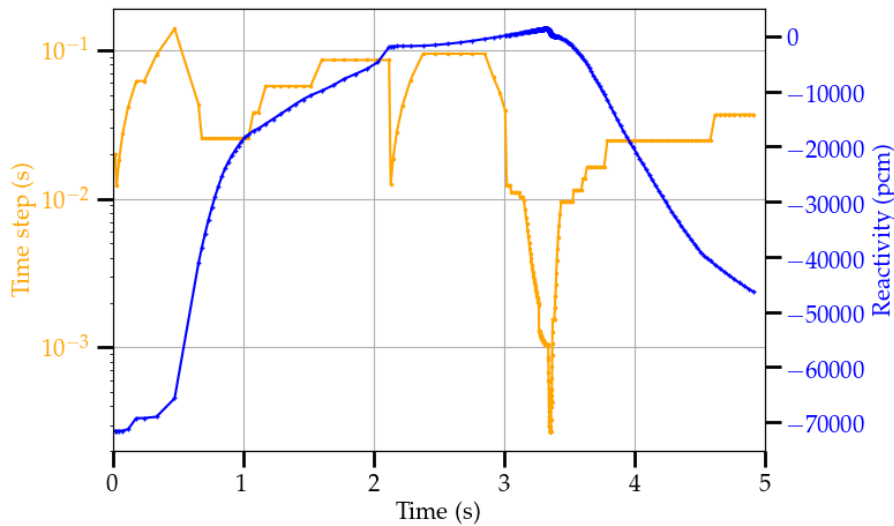


Figure V.4: Example of time step adaptation during a transient, the orange line is the time step and the blue line is the reactivity.

The thermal diffusion, the MC3D code, and the nuclear kinetics have their own internal time-steps adapted to the conditions and the solved model.

#### V.1.4 Simulation time

The simulation time will depend mainly on the quantity of Apollo-2 calculations. The ANN calculations have a negligible time cost, and the MC3D calculations take around 10 min of calculation time to compute 1 min of transient with the spatial mesh described in chapter III. The Apollo-2 static calculations take between 30 s and 300 s depending on whether there was a calculation performed on the previous point (as explained in chapter III, each calculation is initialized with the previous calculation). If the last point was computed by the ANN only, then the initialization of the Apollo-2 calculation will be less efficient as the system state has changed. An example of simulation times is given in the table V.2.

Calculations	Time (s)	Number of calculations	Fraction of computing time (%)	Time simulated (s)
Apollo-2	389 930	5614	92	1150 s
MC3D	33 750	6832	8	
Other (ANN, data exchange)	2 159	NA	$\approx 0$	
Total	425 842	6832	100	

Table V.2: Example of simulation time on one transient lasting 1150 s

## V.2 Assessment of power excursion

The assessment of the power excursion will yield the deposited energy in the debris. This assessment is discussed in this section. In the first subsection we present the behaviour of the critical debris bed when reflooded, followed by a discussion of the behaviour. Finally, an "ad-hoc" simulation is proposed to compute the maximum source term.

### V.2.1 Simulation of critical transients in debris beds while reflooding

#### Transients initialization

As the objective is to estimate the potential maximum *source term*, the physical parameters (such as the power density, the pressure, the liquid water injection rate) are set to favour the return to criticality. Thus, the power density is decreased to a negligible value, the water injection rate is set to an higher rate than the rate needed to cool the debris (inducing reflooding each time the debris bed is dry) and the mass of debris is set in the higher range to decrease the neutron leakage. The pressure was taken in a realistic range between 0.1 and 0.4 MPa. The debris are still static in the system. The simulations start with a half-flooded debris bed, whose reflooding is expected to be the main driver to criticality.

#### Calculations

First, the 75 t generic debris bed results are presented, with the power density set to  $4 \times 10^4 \text{w/m}^3$ . Actually, the pressure range is covered in 4 simulations and a case with a lower debris mass is presented. The effect of pressure would lead to higher reactivity values. The case at 65 t shows a different behaviour as the fissile mass is lower, the maximum reactivity reachable might be lower, although the small volume of water injected in the debris bed might have a stronger impact on reactivity.

The figures V.5 and V.6 show the simulation of a reflooding transient at low pressure. Thus, several prompt critical events are simulated. There are several returns to criticality, moreover they are all prompt critical, inducing the release of a large quantity of energy. Most of the power transients are followed by a long time of negative reactivity due to the expulsion of water from the debris bed by the generated steam. In the simulation shown in V.6 the last power pulse is so powerful that the amount of water expelled leads to a long time of negative reactivity. The same behaviour was recorded in the simulation at 0.1 MPa, only 4 strong power pulse are drawn in V.5 during 300 s.

The simulations performed with a pressure set at 0.3 MPa show a complex behaviour: there are still the trends of strong power pulses leading to the drying of the debris bed followed by a return to criticality, but here multiple weaker power pulses were recorded between the strong power pulses. The number of the weaker power pulses between the strong power



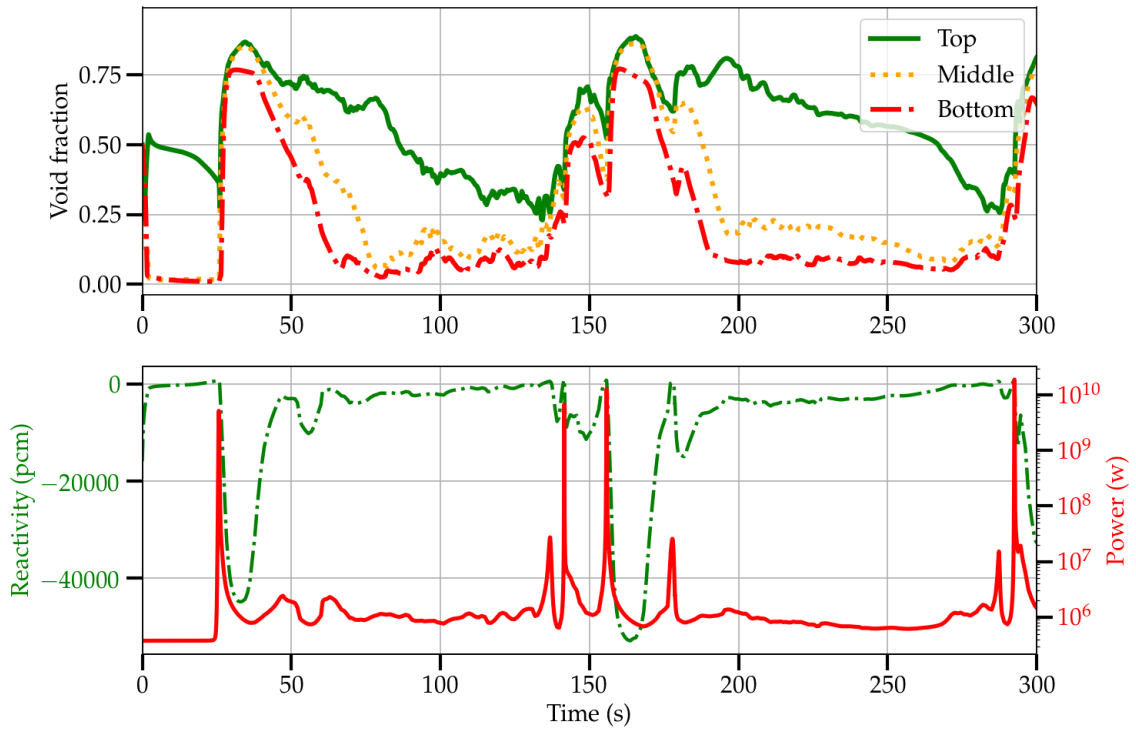


Figure V.5: Reflooding at 0.1 MPa of a 75 t debris bed.

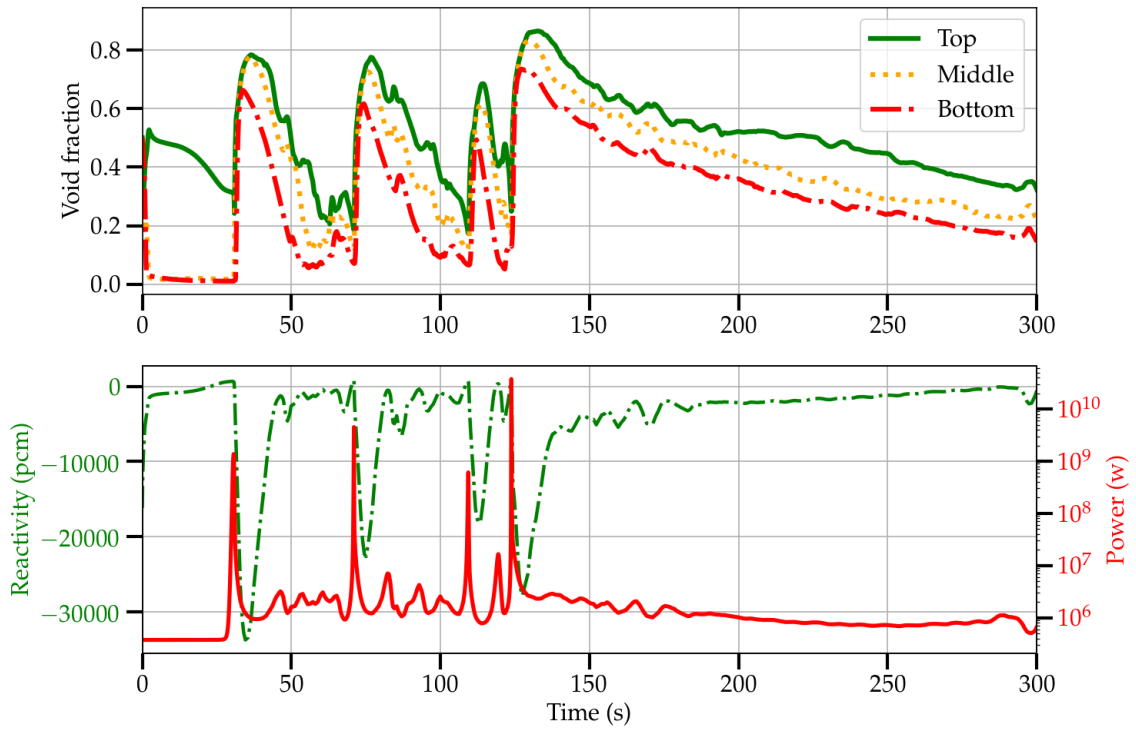


Figure V.6: Reflooding at 0.2 MPa of a 75 t debris bed.

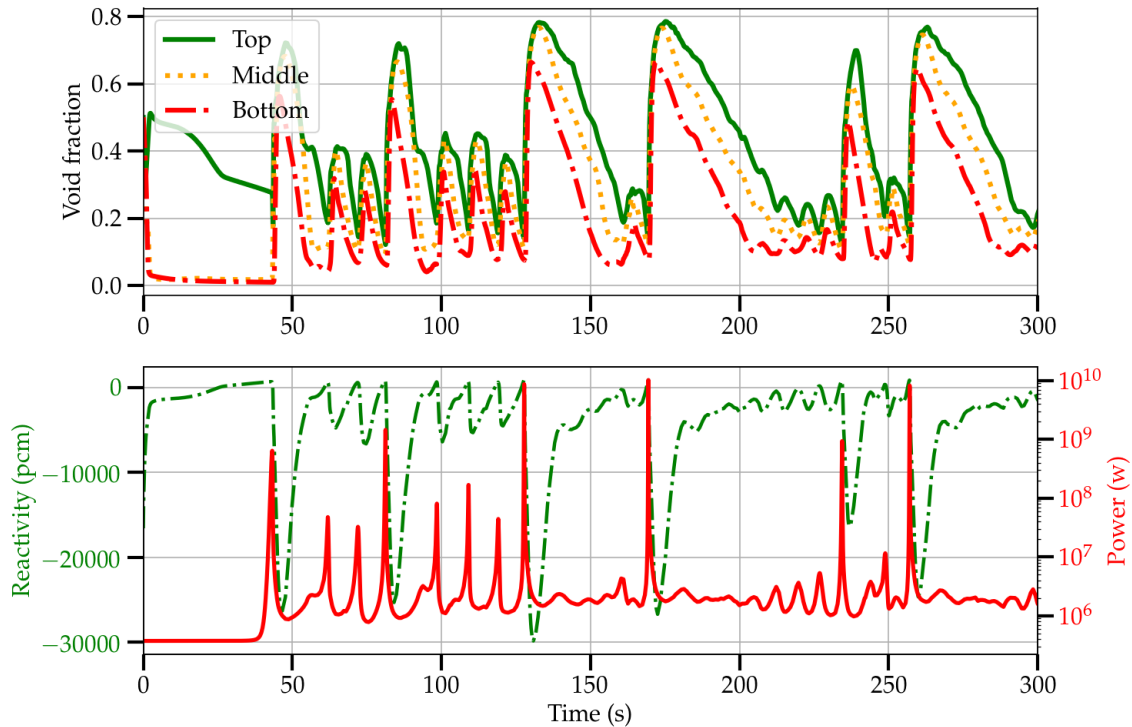


Figure V.7: Reflooding at 0.3 MPa of a 75 t debris bed.

pulses is not constant and the period between the strong power pulses is not constant either. On the simulated time window, the behaviour of the debris bed can be described as chaotic: indeed the system shows some patterns but none of them is reproduced regularly.

The simulation of reflooding performed at 0.4 MPa shows a different behaviour. In figure V.8, the void fraction in all layers decreases until it reaches the critical value. At this moment, nuclear power is generated, which leads to the generation of steam inside the debris bed. The void fraction insertion decreases the reactivity, then the dry debris bed is reflooded. The reactivity insertion by the reflooding is slow enough to allow the nuclear power to increase fast enough to halt the reflooding and prevent a prompt critical event. A higher concentration of precursors than at the beginning is required to see this effect. Then, the void fraction, the power and the reactivity start to oscillate (as shown in figure V.8). In fact, the oscillations (void fraction and power) seem to be self-sustained. Mathematical analyses and much longer simulations are required to obtain reliable conclusions.

The simulation performed with a mass set at 65 t shows also a complex behaviour, although the *reserve of reactivity* is lower. The number of the weaker power pulses between the strong power pulses is not constant and the period between the strong power pulses is not constant either. On the simulated time window the behaviour of the debris bed can be described again as chaotic.

The time of reflooding depends on the previously deposited energy. The drying of the bed increases with the deposited energy of the power transient.

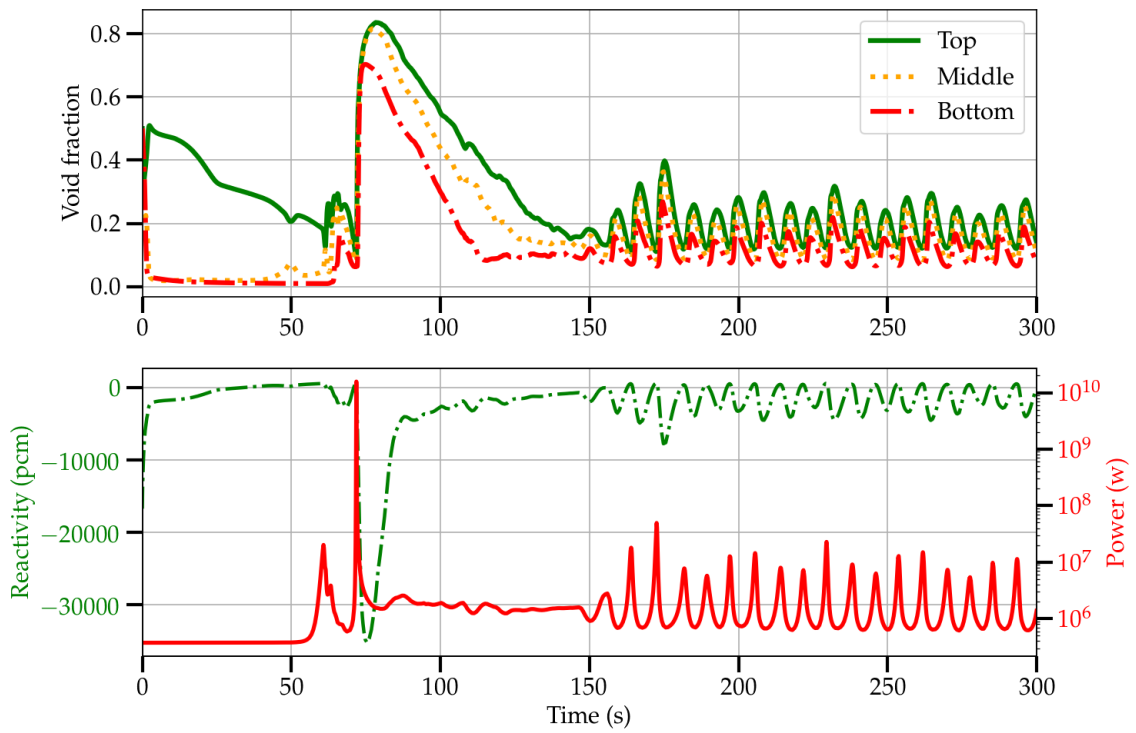


Figure V.8: Reflooding at 0.4 MPa of a 75 t debris bed.

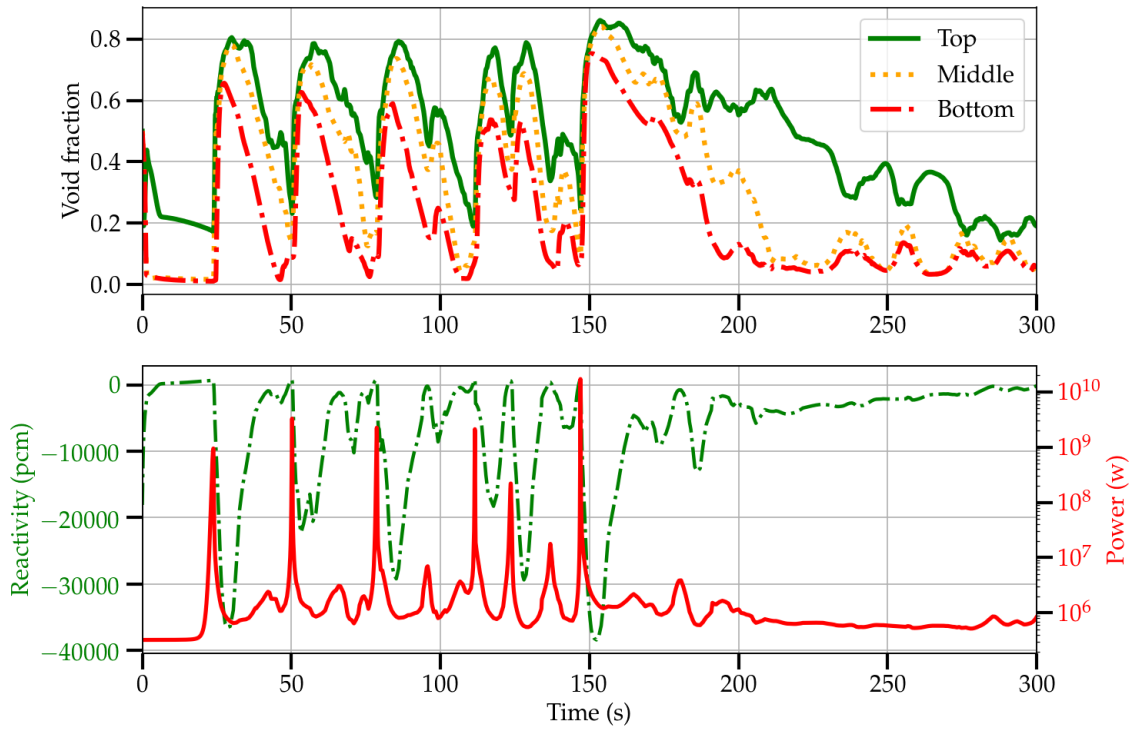


Figure V.9: Reflooding at 0.1 MPa of a 65 t debris bed.

## V.2.2 Discussion on the behaviour of the simulated systems

On all transients previously illustrated in figures V.5 V.6 V.7 V.8, the reactivity exceeded the critical value many times. Even after power transients, the reactivity increases until reaching the super-critical values. The rate of injection of liquid water is set high enough to reflood the debris bed, which explains the observed trends. However, each return to criticality appears to be different from the others (the void fraction map is always different). Thus, as long as the debris bed (made of the academic composition defined in chapter III) is cooled by the injection of liquid water (and assuming that the power density is low enough and the debris bed height is sufficient) the debris bed will reach criticality sooner or later.

A special attention was paid to the behaviours of the transients at 0.1 and 0.4 MPa. The simulated configuration is a non-linear dynamical system possibly leading to complex patterns: a preliminary investigation was first performed illustrating the power transients in the phase space in figure V.10 and in figure V.11, where the first 140 s were discarded.

In figure V.10 we illustrate the fact that both systems are evolving under different conditions leading to difference on the phase space region covered by the system evolution. The phase space covered is larger with the system at 0.1 MPa than the system at 0.4 MPa. The critical events are situated on the right part of the figure (where the criticality is positive): the system at 0.1 MPa has undergone multiple critical events, but none with the same average void fraction. The case at 0.4 MPa shows that the critical events occurred with features that are close to each other. The points are all clustered and in the figure V.11 the system seems to evolve towards a limit cycle, ie, a periodic behaviour.

The phase spaces were normalized, as illustrated in figure V.11. The behaviour of the system at 0.1 MPa looks to be less organized and no patterns can be distinguished. In the time window, this system can be characterized as a chaotic system, although the asymptotic existence of a strange attractor (ie, a chaotic behaviour) would require a careful mathematical analysis of the underlying equations. The behaviour of the system at 0.4 MPa shows that loops occur in the space phase indicating that a pattern is repeated indefinitely. This system may correspond to an *attractor*, but the identification of the kind of attractor would require additional mathematical analysis. The figure V.12 shows on an adapted time window the transient at 0.4 MPa in a three dimensional space. A three dimensional pattern can indeed be noticed. This pattern keeps approximately the same shape but its size and position seems to vary. A similar behaviour has been observed in boiling water reactors [2], where strange attractors have been both experimentally detected and numerically simulated.

Peculiar features were detected with high pressure ( $> 0.3$  MPa), where oscillations of void fraction and nuclear power are observed during simulation. The pressure increase leads to the increase of the steam density thus less water is ejected from the debris beds at a power pulse. The lack of quick water ejection made it possible to keep nuclear power and the precursors concentrations high enough to prevent a quick reflooding and so a next powerful transient.

These simulations show a complex behaviour where the slight change of a parameter (i.e. the mass of debris and the pressure) might induce strong differences, so that the systems appear to be inherently unpredictable. The case at high pressure shows nevertheless a stable boiling-reflooding pattern, so that these cases may be the only ones where it is possible to draw some conclusions concerning the *source term*.

This uncertainty stemming from the chaotic behaviours prevents from drawing conclusions about the maximum power pulse. However, it can be expected under precise conditions (pressure, total debris mass, power density) that the behaviour will be reproducible.

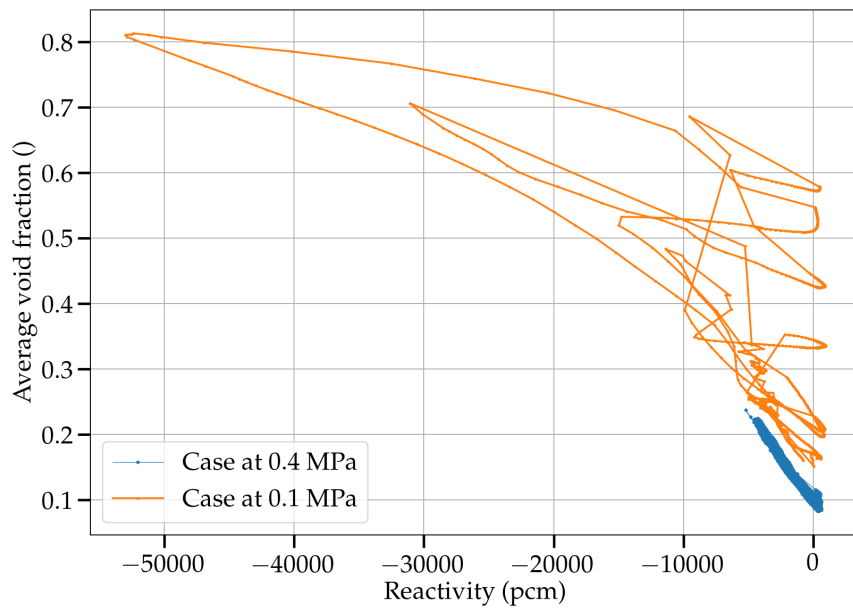


Figure V.10: Reflooding at 0.1 and 0.4 MPa of a 75 t debris bed from 140 to 300 s.

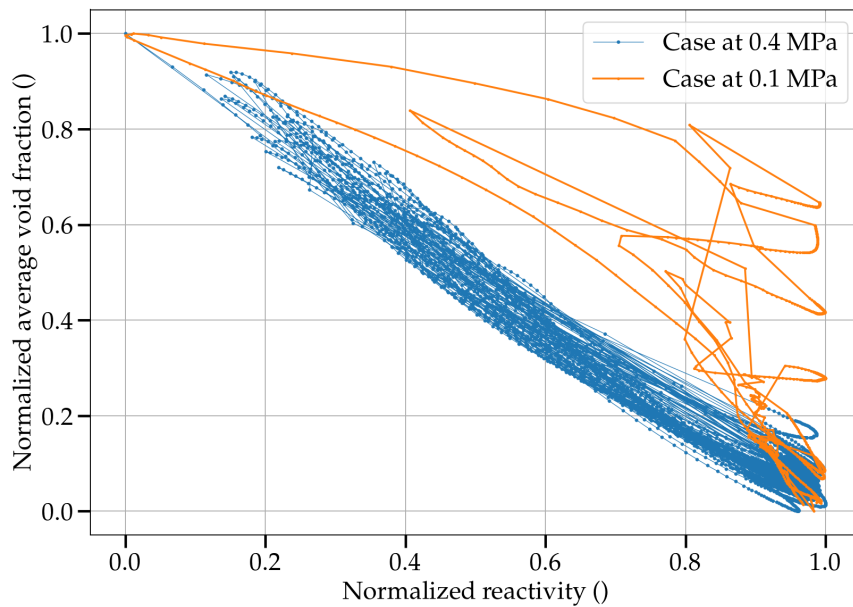


Figure V.11: Reflooding at 0.1 and 0.4 MPa of a 75 t debris bed, normalized from 140 to 300 s.

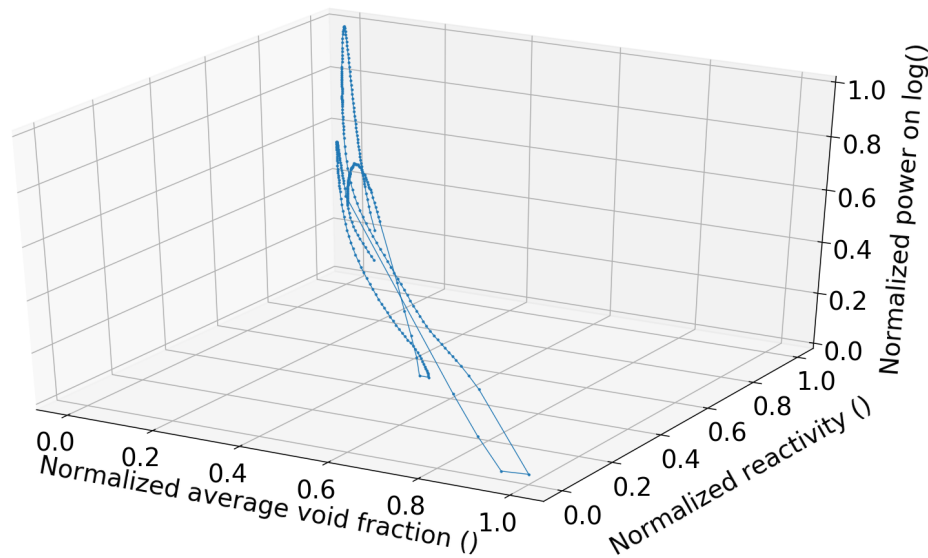


Figure V.12: Sample of the reflooding at 0.4 MPa of a 75 t debris bed, the time ranges from 170 s to 190 s.

### V.2.3 Investigation of "ad hoc" cases to identify a reliable maximum source term

Regarding the uncertainties on the maximum energy released, the choice was made to create *artificial* conditions to try to maximize the power and the source term. In order to have maximal power pulse, the transient simulations starts with a fully dry debris bed at saturation temperature with very low power density ( $10 \text{ KW/m}^3$ ) and  $30 \text{ m}^3$  of liquid water upon the debris bed. A scheme of these artificial initial conditions is illustrated in figure V.13.

At the beginning of the simulation the liquid water goes down immediately into the debris bed, reflooding it quickly. The fast reflooding of the debris bed at low power density may insert the maximum reactivity while delaying feedbacks effects and generating a strong power pulse.

As the total mass of debris can have an impact on the reflooding time and on the reactivity, a parametric study was done on different masses from 55 to 100 t. The deposited energy by unit mass of debris and the maximum temperature reached is assessed. This couple of values tells us which power transient can have the strongest mechanical consequences. The value of deposited energy by unit mass of debris can be used to estimate the maximum temperature reached under adiabatic conditions. The results of the parametric study are summarized in the table V.3.

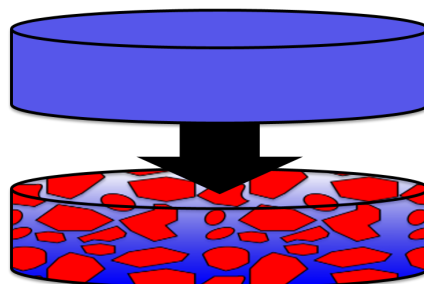


Figure V.13: Schematic of the artificial quick reflooding.

Mass of debris (t)	Maximum reactivity ( $\rho$ )	Maximum temperature (K)	Total deposited energy (GJ)	Maximum of deposited energy density (J/kg)
55	0.26	374	$\approx 0$	$\approx 0$
60	1.92	655	6.09	$1.86 \times 10^5$
70	1.38	514	3.51	$1.22 \times 10^5$
80	2.51	947	11.82	$3.41 \times 10^5$
90	2.24	872	11.04	$3.11 \times 10^5$
100	2.06	794	9.66	$2.71 \times 10^5$

Table V.3: Physical values of interest recorded during simulations.

For example the power transient simulated with 80 t of debris is presented in figure V.14 and V.15. The reactivity computed by the ANN and by Apollo-2 can be remarked in the figure. The Apollo-2 calculations are performed only when the reactivity of the system is close to criticality.

The power transient is fast and the value of the  $\beta_{eff}$  is exceeded during a period of 86 ms. The obtained void fractions show that the quick reflooding of the debris bed leads to the prompt transient. The reactivity starts to decrease when the debris temperature goes up thanks to the Doppler effect. The reactivity becomes stable after the power peak (at 3.10 s) and the reflooding was stopped, whereas the moderator effect is not yet present.

In figure V.14, some milliseconds after the power peak (at 3.125 s in this figure), the heat began to be transferred significantly from the debris to the liquid water. This effect induces the fast generation of steam which will decrease significantly the reactivity. However, at the occurrence of boiling, around 97 % of the total energy is already deposited, which reflects the significant delay of the moderator feedback in the case of prompt transients.

During the power transient, the debris temperature reaches high temperatures ( $\approx 950$  K), which even impact the power distribution, as illustrated in the figure V.17 and the figure V.18. These effects lead to a decrease of the power distribution peak from 2.6 to 2.2. Hence, the Doppler effect contributes to decrease the maximum deposited energy density.



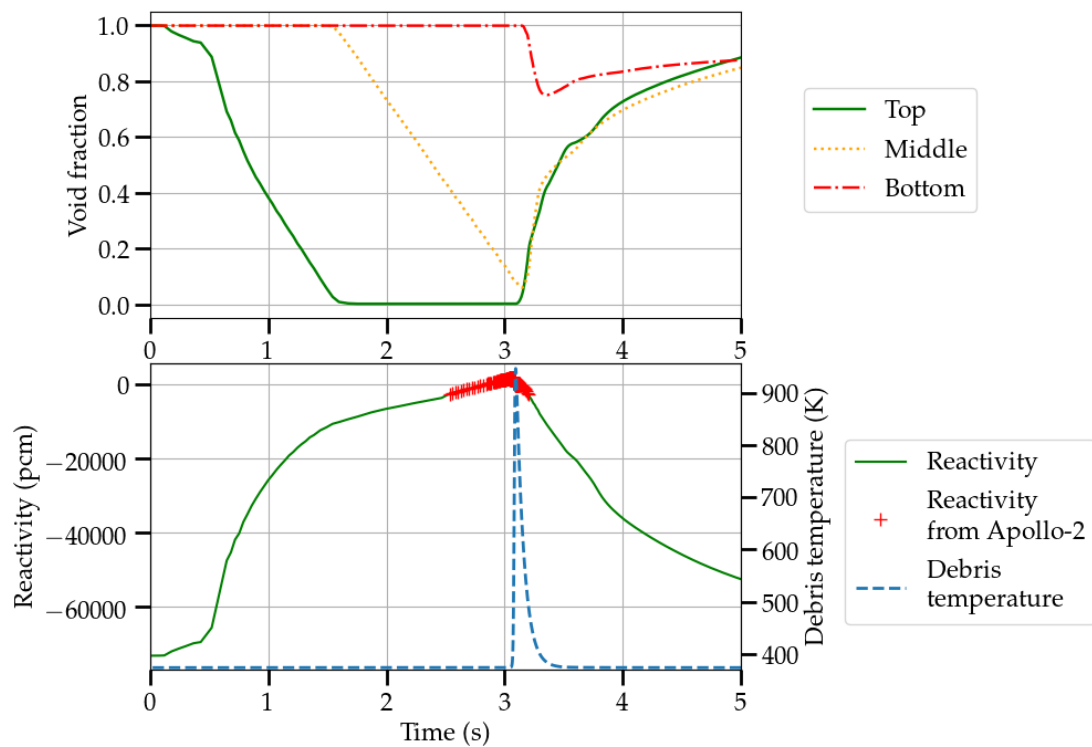


Figure V.14: Large visualisation of the void fraction, reactivity and maximum debris temperature during the artificial reflooding of the 80 t case.

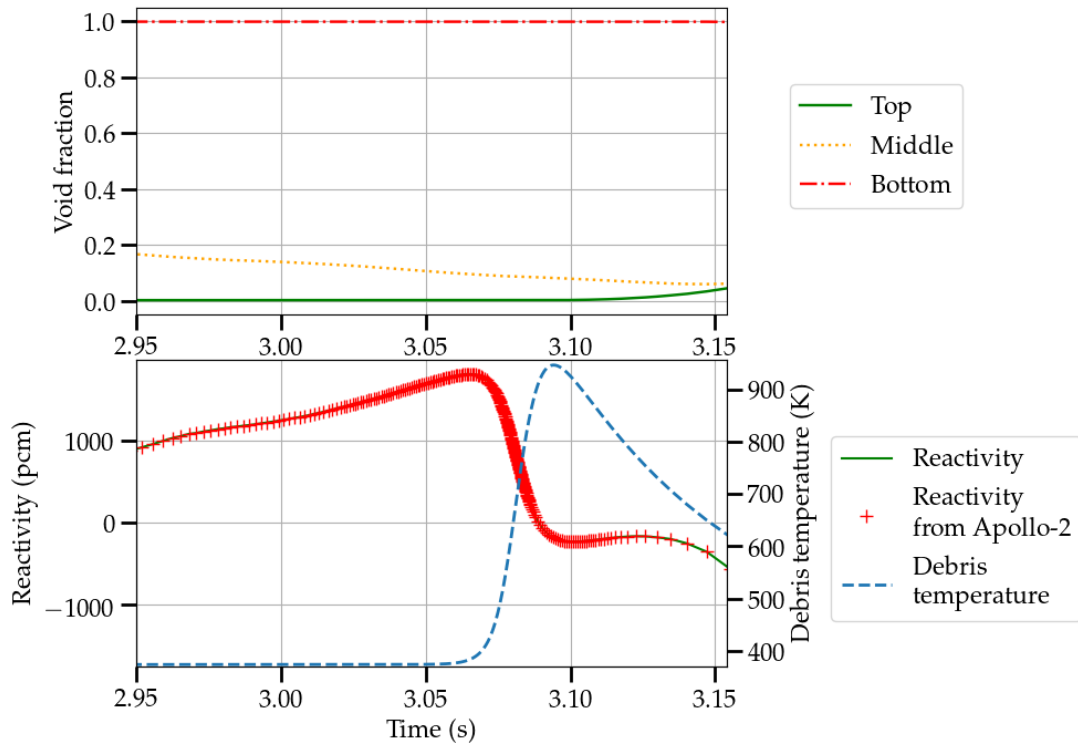


Figure V.15: Focus on the prompt transient of the void fraction, reactivity and maximum debris temperature during the artificial reflooding of the 80 t case.



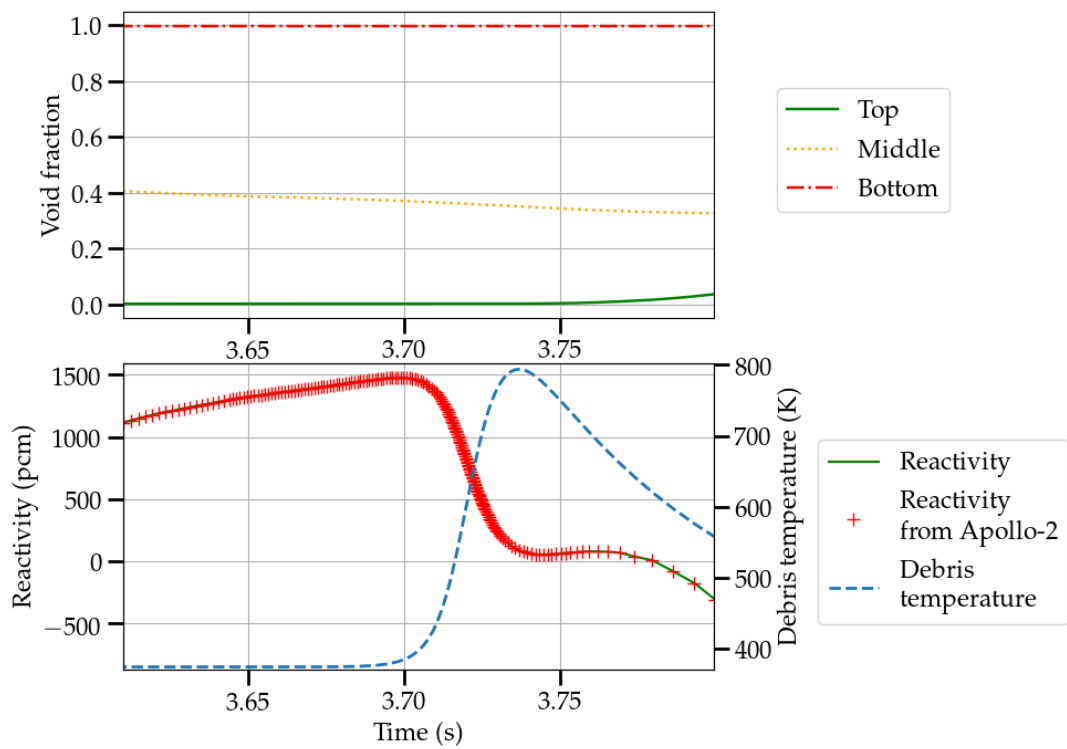


Figure V.16: Focus on the prompt transient of the void fraction, reactivity and maximum debris temperature during the artificial reflooding of the 100 t case.

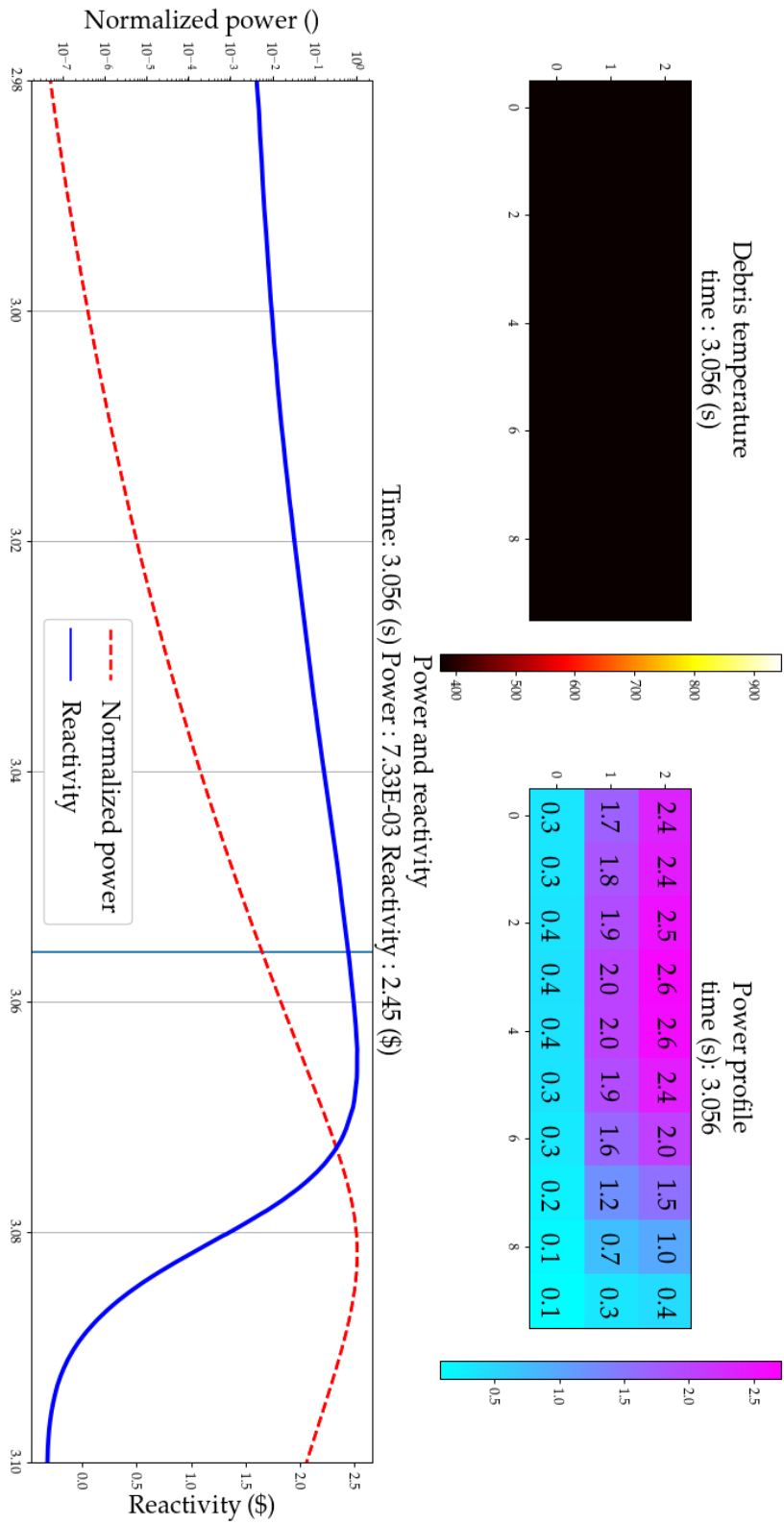


Figure V17: State of the debris bed before the power peak (the vertical line indicates the time in the graphic).

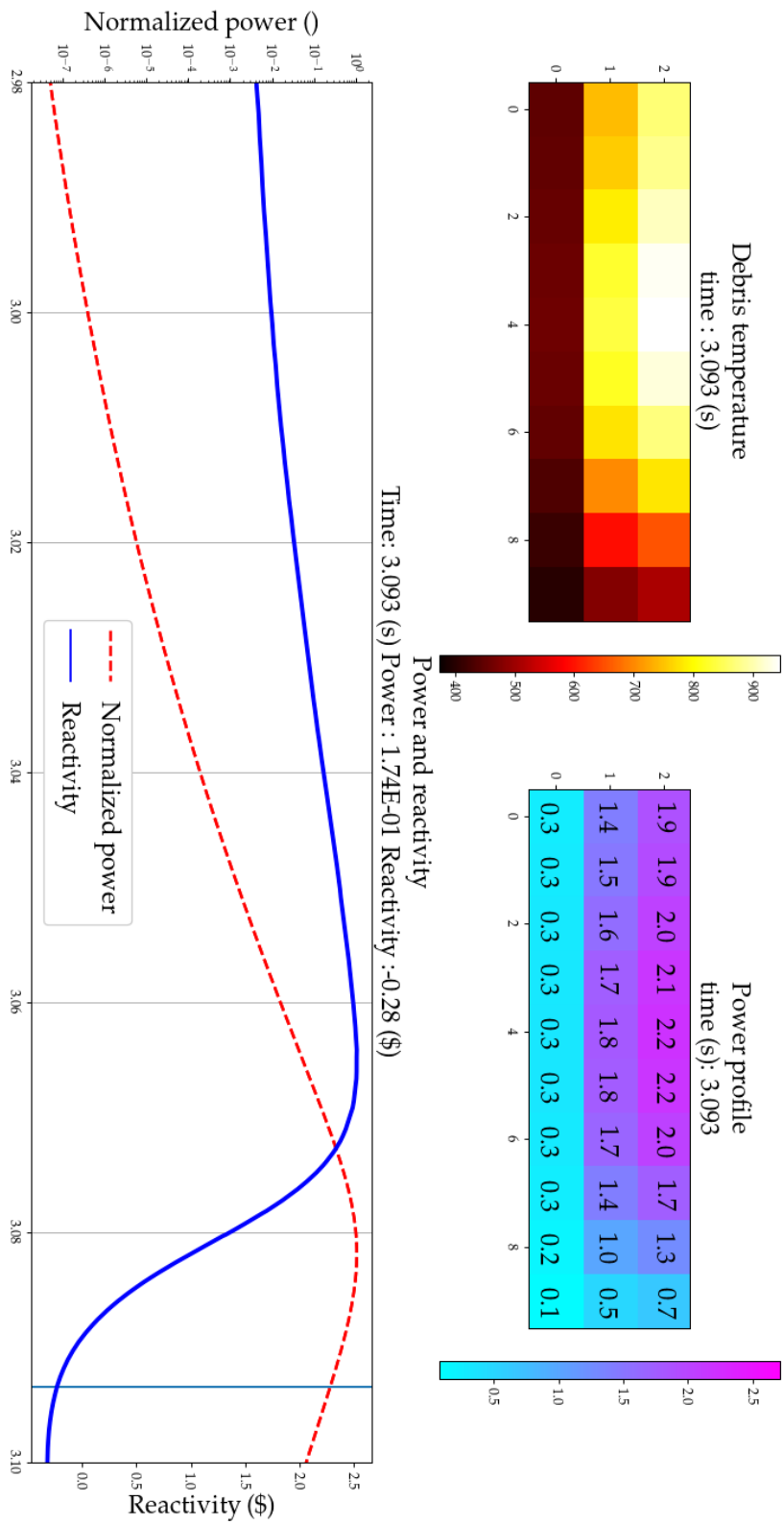


Figure V18: State of the debris bed after the power peak (the vertical line indicates the time on the graphic).

The transient simulation with 100 t of debris is illustrated in figure V.16. The 100 t case might be expected to present the maximum reactivity, as the neutron leakage is minimal as compared to other cases when fully flooded. However, the reflooding speed (relatively to the thickness of the debris bed) is lower. Thus, the reactivity slope during the reflooding is about 8300 pcm/s for the 80 t and only 4400 pcm/s for the 100 t. A slower reactivity insertion leads to feedback effects happening sooner (based on the reactivity insertion) and can preclude the maximum reactivity possible. The maximum reactivity was reached with the case at 80 t.

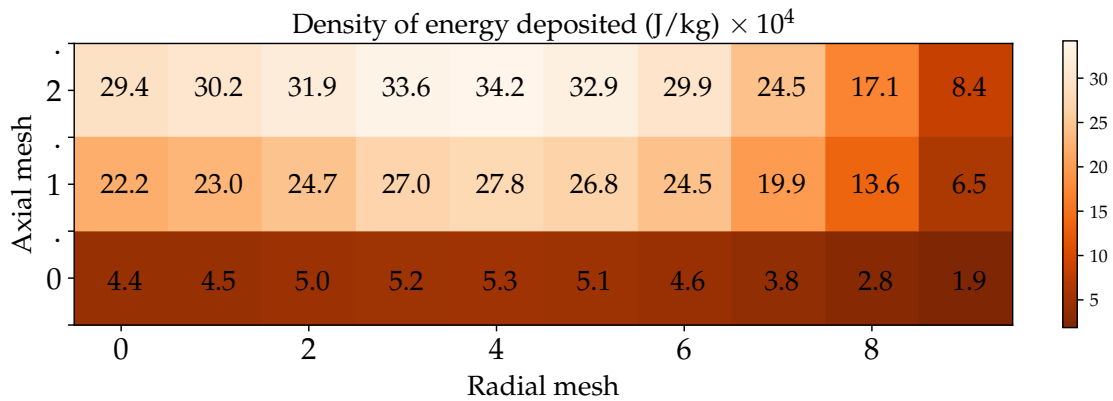


Figure V.19: Map of the density of deposited energy during the most powerful artificial reflooding transient.

The source is discretized on the coupling mesh. It takes the shape of an energy distribution per kilogram. The maximum recorded source term is shown in figure V.19. The cell which received the highest energy is the cell located at top at the middle of the radius of debris bed. During the transient, the reflooding front is not perfectly flat in the horizontal direction. The reflooding front is shifted by some *cm* in the centre of the geometry, which leads to a energy peak in the middle of the radius. All transients show this small heterogeneity in the reflooding front. Investigation about MC3D boundaries are required.

### V.3 Synthesis

In this chapter, additional physical models were implemented and coupled together to have a methodology capable of simulating power transients. Special attention was paid to the time-step adaptation and the required precision. A first assessment of power excursions has shown that the behaviour of a critical debris bed can be chaotic at low pressure or more stable at high pressure (maximum 0.4 MPa). These observed behaviours show that it can be difficult to assess the maximum *source term*, as the behaviour is relatively unpredictable. We have made the choice to apply "ad-hoc" conditions in order to favour the creation of the maximum *source term*. A parametric study was done to identify the conditions that can generate the maximum *source term*. These results stress the necessity of having a method to estimate the mechanical consequences of a power transient after obtaining the spatial distribution of the

deposited energy.

## Bibliography

- [1] C. Patricot, A.-M. Baudron, and O. Fandeur, “The multi-physics improved quasi-static method - application to a neutronics-thermomechanics coupling,” *Progress in Nuclear Energy*, vol. 101, pp. 352 – 359, 2017. Special Issue on the Physics of Reactors International Conference PHYSOR 2016: Unifying Theory and Experiments in the 21st Century.
- [2] J. March-Leuba, “Nonlinear dynamics and chaos in boiling water reactors,” Jan 1988.

# Chapter VI

## Preliminary assessment of the consequences of a critical event in a generic debris bed

### Contents

---

<b>VI.1 Qualitative assessment based on debris temperature</b> . . . . .	<b>127</b>
<b>VI.2 A first attempt of mechanical consequences evaluation</b> . . . . .	<b>129</b>
VI.2.1 Model and assumptions . . . . .	129
VI.2.2 Description of the simulated transient . . . . .	131
VI.2.3 Assessment of the mechanical impulsion . . . . .	134
VI.2.4 Sensitivity calculations . . . . .	135
<b>VI.3 Synthesis</b> . . . . .	<b>136</b>
<b>Bibliography</b> . . . . .	<b>137</b>

---

## Introduction

The multi-physics coupling detailed in chapter V is essential to obtain the fission power distribution of a critical event transient within a generic debris bed. However, more effort are necessary to estimate the mechanical consequences around the debris bed. The structural damage may come from the steam bubble created within the debris bed after the power transient, which can be generated very quickly and lead to the spread of an overpressure wave. In order estimate the consequences of this event, the mechanical impulsion must be therefore calculated. In the first section, preliminary analyses are discussed, and the following section is devoted to the simulation of the mechanical consequences, using the MC3D code. Finally, the obtained impulsions are compared to reference values and their significance is discussed.

### VI.1 Qualitative assessment based on debris temperature

The fission energy release source term is an input for mechanical consequences calculations. However, a preliminary assessment is done regarding the required conditions to trigger a steam explosion (described in chapter I), considered in this section as a reference for mechanical damage.

Actually, based on the previous simulations presented in chapter V, the spatial distribution of deposited energy by kilogram was obtained. This information is considered as the *source term*. During the transient simulation a very small fraction of the deposited energy is transferred to the water, through thermal diffusion within debris and thermal convection at debris-water interface. The choice was made to ignore this energy leakage in order to maximize the temperature distribution profile. A maximum temperature of 1133 K is obtained (a maximal temperature of about 950 K was recorded during the power transient in the chapter V, considering the thermal transfer between debris and water). The obtained temperature distribution with adiabatic conditions is illustrated in figure VI.1.

The debris temperature increase (760 K) is high as the debris starting temperature is around 373 K. Nevertheless, this temperature does not reach the debris solidus temperature, which is around 2800 K. No melting can happen even in the hottest point of the debris bed. The phenomenon of steam explosion would be triggered by the interaction of two liquid materials (water and debris) with a very high temperature difference [1]. Without debris melting, the phenomenon of steam explosion cannot be generated. A steam bubble can still be created when the heat from the debris is transferred to the liquid water, although the pressure wave amplitude is expected to be lower than a steam explosion. Indeed, if the fuel material does not reach the melting temperature, the heat transfer even with the largest temperature difference will not be high enough. Taking into account the boiling regime as described in Nukiyama's boiling curve described in figure VI.2, the phenomena of film boiling will appear around the hot debris, decreasing significantly the heat transfer between the liquid water and the debris [2]. Hence, we can expect to have limited or negligible mechanical consequences.

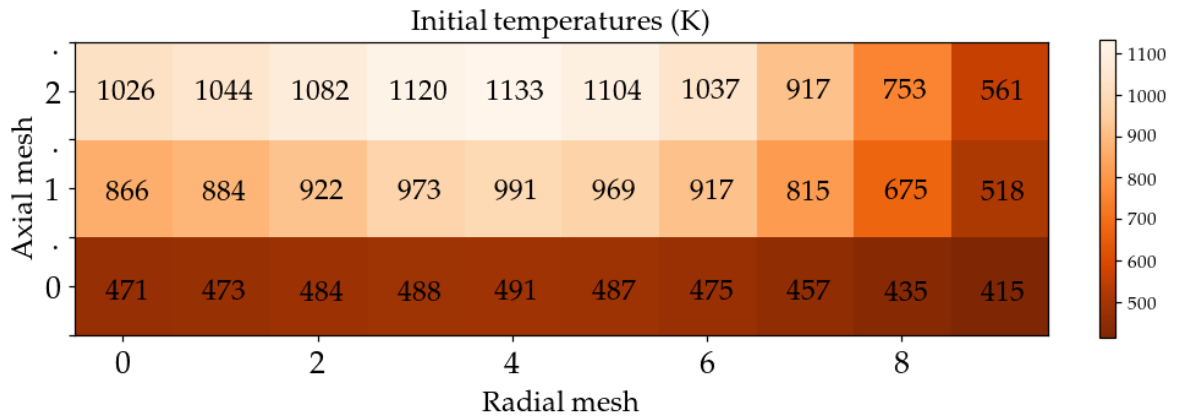


Figure VI.1: Initial temperature field inserted for MC3D. This is the source term, the debris temperature difference with water temperature will generate rapidly a steam bubble.

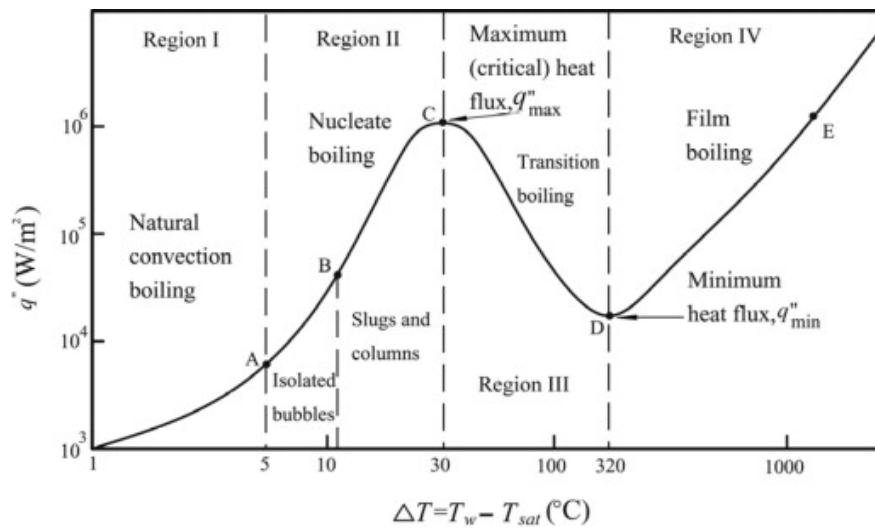


Figure VI.2: Heat transfer regime in boiling conditions depending on the wall temperature [3].



## VI.2 A first attempt of mechanical consequences evaluation

Previous section suggests that the mechanical consequences should be limited thanks to the favourable conditions in the debris beds, the maximal debris temperature being lower than the solidus temperature. However, a simulation is still required using the fission energy source term generated so as to enhance the reliability of the obtained estimates for the potential mechanical consequences. In this section, the mechanical simulation is done with MC3D, the pressure and the recorded impulsions are discussed and compared to steam explosion simulations values, considered as a reference.

### VI.2.1 Model and assumptions

The simulation of the energy generated during power excursions is not enough to estimate the mechanical consequences. The energy transferred to the liquid water may vaporize it quickly. The work in papers [4] [5] shows that MC3D is also able to simulate fast hydrodynamic flows in conditions of high temperature difference (higher than 760 K). However, the approximation of static debris should be avoided in order to accurately assess the mechanical consequences. Thus, the MC3D simulation is done with loose debris, and the debris temperature distribution estimated in adiabatic condition is used as an input instead of the thermal power. The use of temperature instead of power is the only way we found to transfer the whole fission energy to loose debris in the MC3D simulation. Since loose debris might be dragged by the steam flows, the geometry will be broken, so a power density mesh cannot be apply during the transient.

The MC3D input temperature distribution to simulate mechanical loading corresponds to the total energy release during criticality transient, and this energy is converted in debris temperature increase. The code MC3D is used to simulate fast pressurisation (as a steam explosion). The system geometry chosen for this application is a simplified mock-up configuration. In order to compute the mechanical impulsion, a single structure (representing the reactor pressure vessel) is added upon the debris bed. The resulting geometry is described in the figure VI.3. All the solid boundaries are adiabatic. The debris are totally free of movement like the other phases. The domain of calculation is extended to capture the effect of pressurisation of the volume. The system modelled in MC3D is described in figure VI.4, the mesh far from debris bed and the lower part of the vessel is coarser. For the purpose of estimating the mechanical impulsion, the pressure is carefully estimated at points marked in orange in figure VI.5. These points were chosen in accordance with reference simulations [6]. The pressures are recorded on 7 points in the system: one at the vessel bottom, one on the floor in the centre, one on the floor at mid-radius, 4 on the wall at constant space steps from 0.0 to 1.7 m.

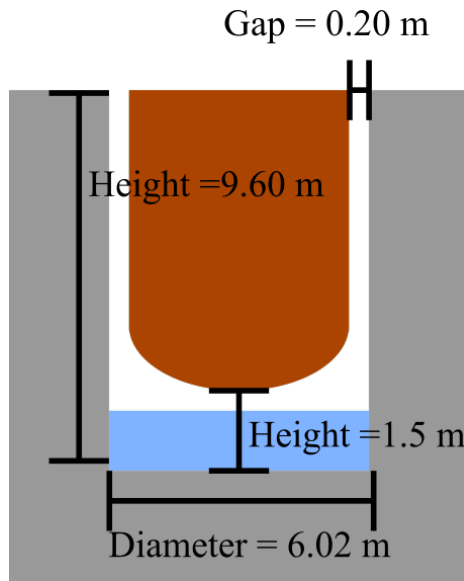


Figure VI.3: Scheme of the geometry modelled in MC3D.

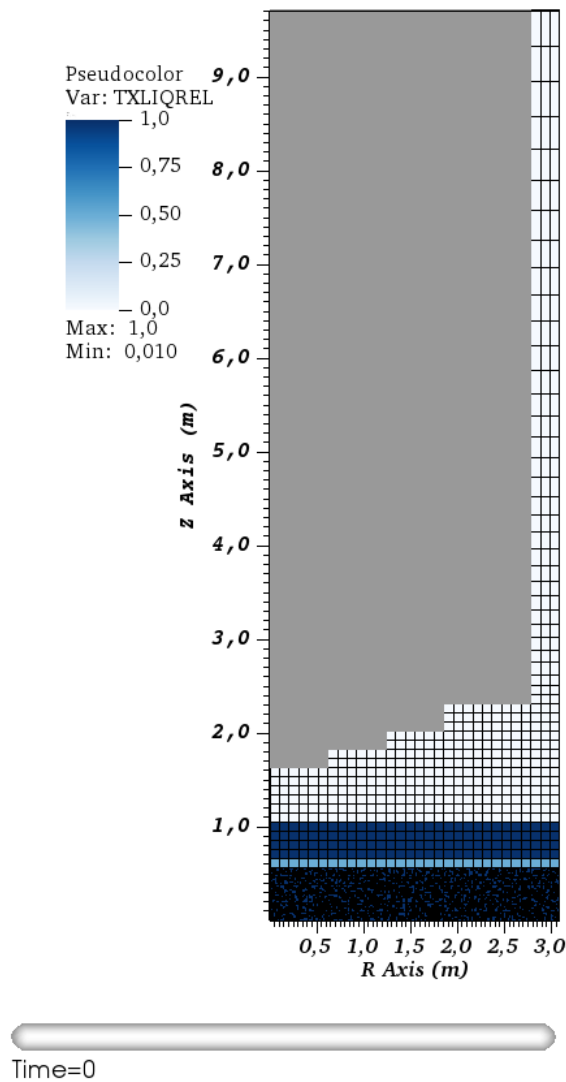


Figure VI.4: Scheme of the entire geometry at the initial time (liquid water in blue).

The simulation was performed with a relatively small minimal time-step of  $10^{-8}$  s. The simulation starts with the debris bed fully flooded and the debris at the initial temperature (provided by the maximum temperature map). The pressure was set at  $10^5$  Pa and the water temperature is near saturation. There are 13 t of water upon the debris bed, 7 t of water within the debris bed, and the debris bed mass is set to 80 t in accordance with the selected power transient in chapter V.

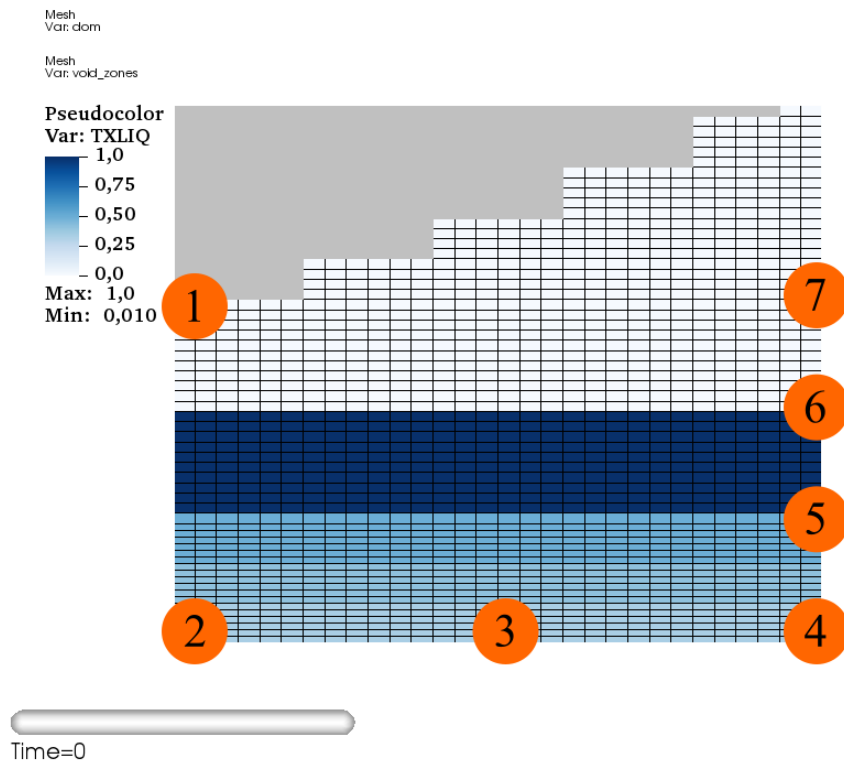


Figure VI.5: Scheme of the geometry at the initial time (liquid water in blue), orange disks indicate where the pressures are recorded.

## VI.2.2 Description of the simulated transient

The course of events is described in the figures VI.6 VI.7 VI.8. At 0.04 s a steam bubble can be remarked in the hottest part of the debris bed i.e. in the top centre. Then figure VI.6 shows that the bubble expansion. The liquid water and the debris are propelled together by the steam bubble.

In figure VI.7, at the time 0.06, the steam bubble is pushing the liquid water to the vessel bottom. The steam is also dragging the debris to the top. At 0.08 s the liquid water has struck the vessel, and in the mean time the steam bubble kept expanding in the vessel pit. At 0.4 s a fraction of the liquid water is pushed into the gap between the vessel and the concrete wall. Debris dragged by the steam and the liquid water are following the same path. At 1.0 s there is still a strong flow in the gap directed to the top. In figure VI.9, at 5.5 s all the liquid water was either expelled or boiled into steam: the system is stable, and the remaining debris lies on the concrete floor. The debris bed takes approximately the shape of a flat cylinder.

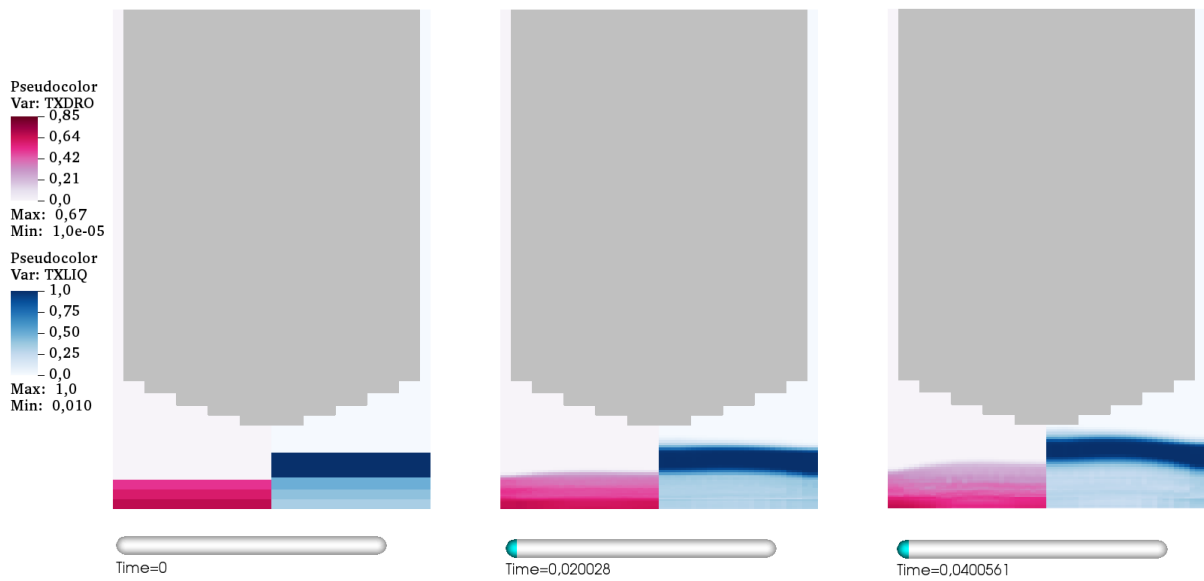


Figure VI.6: Evolution of the debris presence and the liquid water. There is an axial symmetry in the centre, the debris fraction is on the left and the liquid water fraction is on the right.

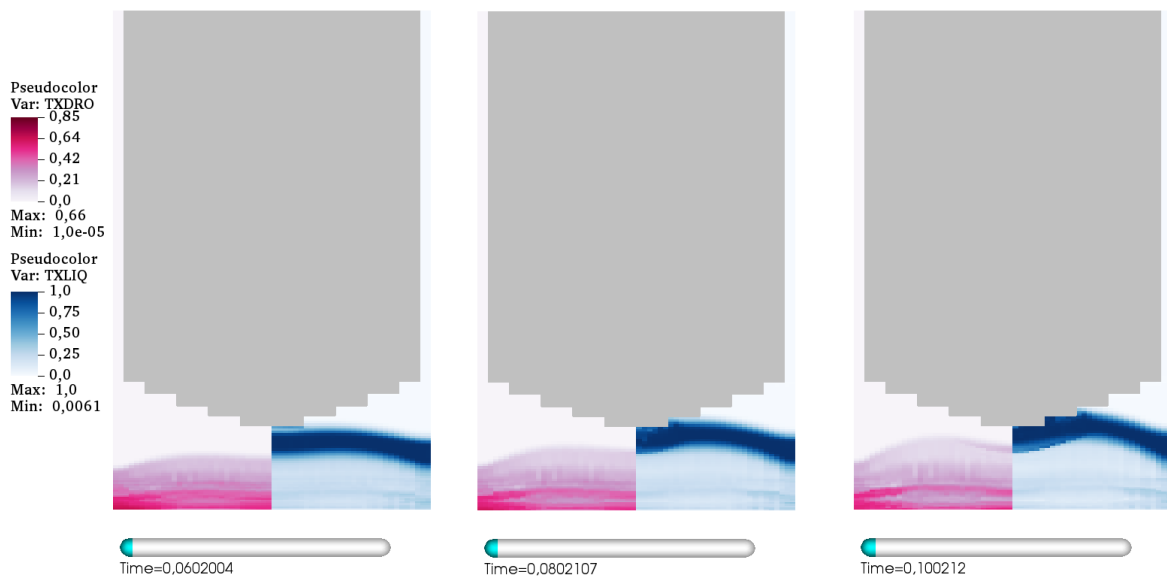


Figure VI.7: Evolution of the debris presence and the liquid water. Axial symmetry in the centre, the debris fraction is on the left and the liquid water fraction is on the right.

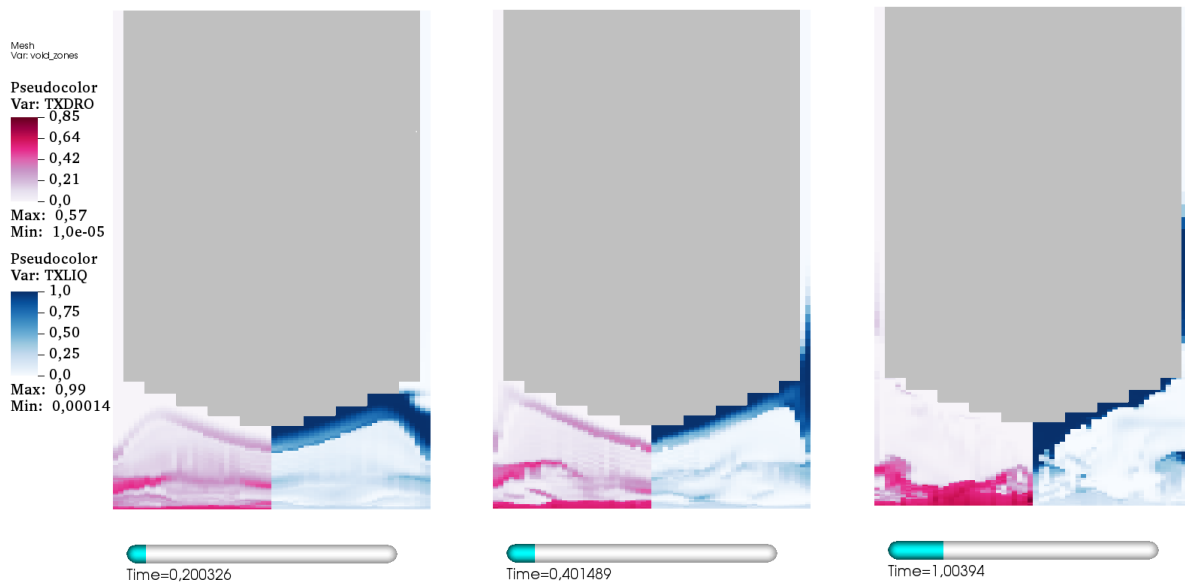


Figure VI.8: Evolution of the debris presence and the liquid water. Axial symmetry in the centre, the debris fraction is on the left and the liquid water fraction is on the right.

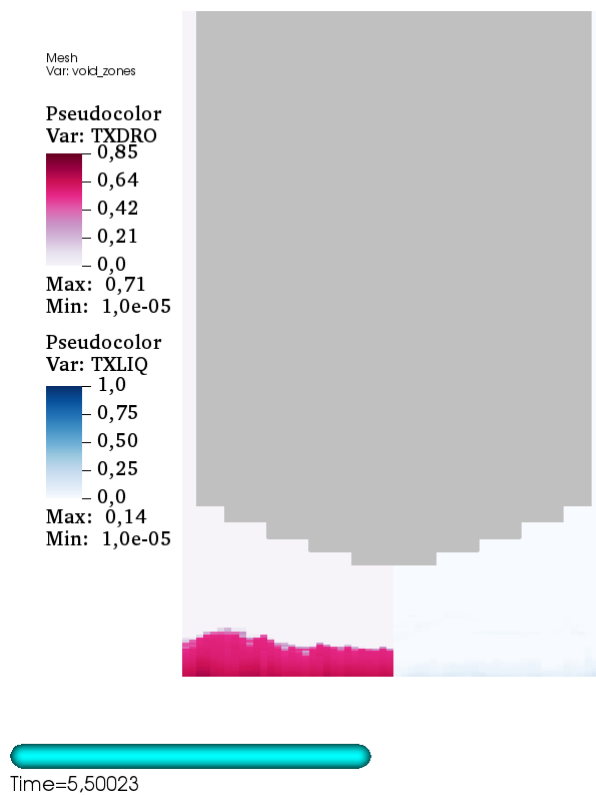


Figure VI.9: Final state of the debris presence and the liquid water. Axial symmetry in the centre, the debris fraction is on the left and the liquid water fraction is on the right.

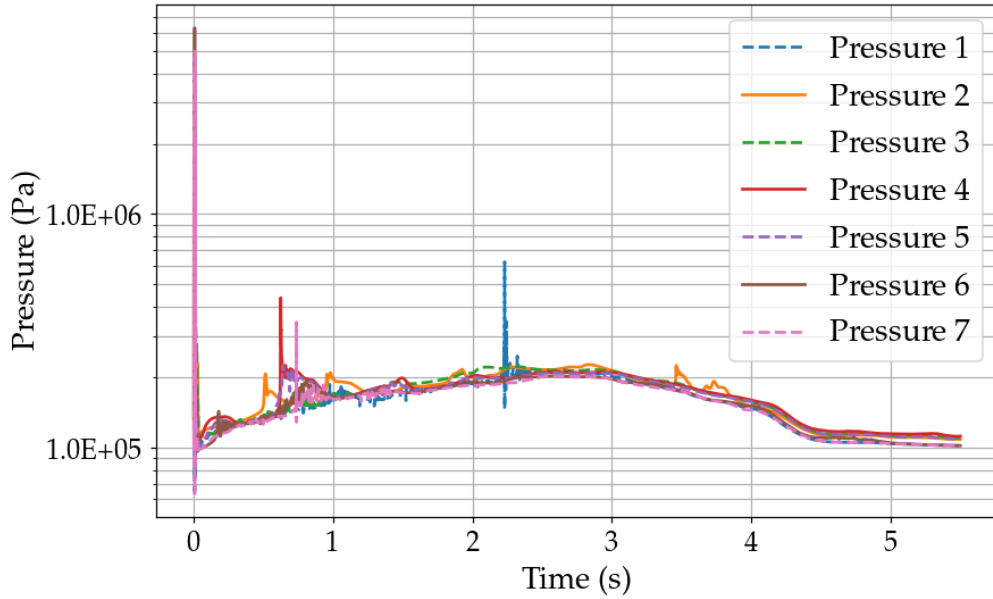


Figure VI.10: Recorded pressure during the simulation.

In figure VI.10 we display the pressure recorded during the simulation. The pressure on the floor and on the wall shows some relatively strong pulses during the steam bubble formation. After this event, the pressure recorded at the vessel bottom shows a pressure peak which corresponds to the impact of the liquid water on the vessel. The recorded impact pressure (at 0.8 s) are weaker than the steam bubble generation pressure (at 0.0025 s). Then, the pressure goes slowly up until it reaches a plateau at 2.2 s and finally begins to drop at 3 s.

An unforeseen phenomenon highlighted by the simulation is the ejection of debris mass upon the pressure-vessel. Indeed, the debris were dragged by the liquid water (which was itself pushed by the steam bubble) to the gap between the vessel and the wall. The pressure in the debris bed zone was kept higher by the constant generation of steam: this pressure gradient has pushed the liquid water and some debris to the top beyond the system boundaries. At the end of the simulation, a mass of 3.0 t of debris has been ejected from the system. We will present sensitivity calculations in the subsection VI.2.4.

### VI.2.3 Assessment of the mechanical impulsion

Mechanical consequences can be assessed in terms of the mechanical impulsion [7]. To characterize the shock wave force, the integral of the pressure load on a point is computed. The impulsion equation reads:

$$I = \int_t^{t+t_{wave}} \Delta P dt \tag{VI.1}$$

$\Delta P$  is the recorded pressure gradient at the time  $t$  during the duration  $t \rightarrow t + t_{wave}$  corresponding to the positive phase of normally reflected waves [7]. The impulsion is a *source term* for structural damage calculation. The impulsions generated by a criticality event could be compared with reference impulsions to classify mechanical consequences.

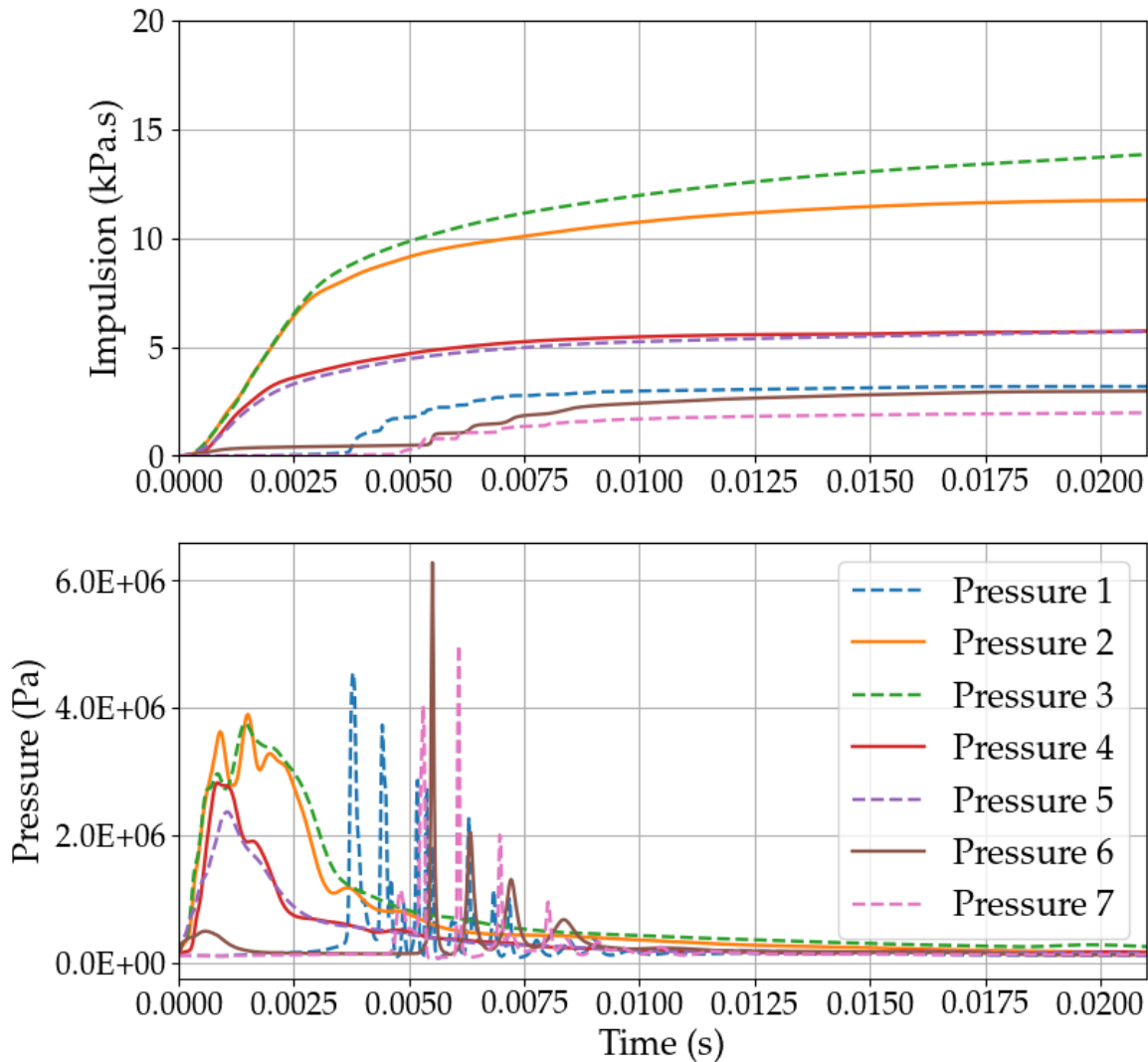


Figure VI.11: Pressures and impulsions at the pressure peak.

The figure VI.11 shows that, at the pressure peak, the impulsions increased quickly until  $t = 0.020$  s. Then the impulsions were increasing relatively slowly. The strongest impulsions were obtained on the pressure points 2, 3 and 4, and correspond to the concrete floor. The recorded impulsions range from 3 kPa.s to 14 kPa.s. The pressure points 1, 5, 6, and 7 have undergone strong peaks after the steam bubble generation, but the resulting impulses are relatively weaker than the other points. The simulations of steam explosion performed on a test case (the OECD project SERENA [6] consisting of an experimental and an analytical investigation about steam exposition in nuclear reactor) show a maximum impulsion of about 178 kPa.s [6]. The impulsion simulated for our configuration is 92 % less powerful, this leads to the conclusion that the mechanical consequences may be negligible. Although the water displacements in the previous figures seem abrupt, the strongest impulsions come from the generation of the steam bubble at the beginning of the simulation.

#### VI.2.4 Sensitivity calculations

Several approximations were done to estimate the mechanical impulsion, included the modelling in MC3D. To evaluate the contributions of the proposed method and the impact of these approximations, sensitivity calculations were performed. The table VI.1 gives the mod-

ifications done in the the model and the resulting maximum impulsion recorded during the first and strongest pressure peaks of the simulation. First the pressure effect was investigated, then the modelling details (like the impact of a fully flooded vessel pit). A calculation was performed using a homogenous distribution of energy resulting in a flat temperature profile: as a reminder, 11.8 GJ were released in 80 t of debris (which corresponds to an homogenous temperature of 702 K).

Modelling difference with the standard case	Maximum impulsion (kPa.s)	Time at the maximum impulsion (s)	Mass of debris expelled (t)
Standard case	14	0.020	3.00
Pressure set at 0.2 Mpa	12	0.020	0.13
Pressure set at 0.4 Mpa	9	0.008	≈ 0
Fully flooded vessel pit	15	0.018	1.40
Absence of upper water layer	13	0.020	2.70
Homogenous debris temperature (702 K)	14	0.015	6.90

Table VI.1: Maximum impulsions recorded corresponding to modified configurations.

In table VI.1, the maximum impulsion decreases when the pressure increases. The fully flooded case shows a slightly higher value of maximum impulsion. The simulation performed without the upper layer of water shows the same maximum impulsion than the standard case. The simulation with an homogenous distribution of the energy shows a maximum impulsion equal to the standard case.

The removal of the upper water layer is another simplification that would not impact the impulsion recorded in the studied case. In the table VI.1 we report the mass of debris expelled from the system during the transient. The increase of pressure leads to a decrease in the mass of debris expelled during the transient. The absence of an upper layer of water decreases slightly (0.7 t) the mass expelled from the system. The use of the flat energy distribution (homogenous temperature at 702 K) to simulate the transient shows an increase of 117 % of the expelled mass.

The absence of impulsion difference between the standard case and the homogenous distribution case highlights that simplifications could be done to model the mechanical consequences. Based on these findings, the energy distribution seems to be unnecessary to accurately estimate the impulsion. This conclusion might be true only in the case of weak impulsions as measured here.

### VI.3 Synthesis

The obtained deposited energy distribution from the multi-physics simulations is a crucial information which was used as an input in the calculation of mechanical consequences. These preliminary analyses suggest a very low probability of extensive damage, because the melting debris temperature was not reached. If this criterion is not met, the creation of steam explosion might be prevented and the structural damages should be limited. Finally, we performed a calculation with realistic conditions using a relevant geometry of the pressure vessel pit. The calculation shows that the steam bubble is created quickly but generates low impulsion. The maximum impact was recorded on the concrete floor. The maximum mechanical impulsion is 14 kPa.s. This value compared to steam explosion impulsions simulated in the SERENA project is 92 % lower [6]. Thanks to the simulation with MC3D, the expulsion



of 3.00 t (out of 80 t initially present) of debris in the upper boundaries was observed. The source term generated in the chapter V brought enough information to successfully simulate the mechanical consequences of a relevant critical debris bed.

## Bibliography

- [1] B. R. Sehgal, ed., *Nuclear Safety in Light Water Reactors Severe Accident Phenomenology*. Boston: Academic Press, 2012.
- [2] D. P. Incropera, Frank P.; DeWitt, *Fundamentals of Heat and Mass Transfer (5th ed.)*. Wiley India Pvt. Limited, 2002.
- [3] A. Faghri and Y. Zhang, “10 - boiling,” in *Transport Phenomena in Multiphase Systems* (A. Faghri and Y. Zhang, eds.), pp. 765 – 852, Boston: Academic Press, 2006.
- [4] R. Meignen, B. Raverdy, M. Buck, G. Pohlner, P. Kudinov, W. Ma, C. Brayer, P. Piluso, S.-W. Hong, M. Leskovar, M. Uršič, G. Albrecht, I. Lindholm, and I. Ivanov, “Status of steam explosion understanding and modelling,” *Annals of Nuclear Energy*, vol. 74, pp. 125–133, 2014.
- [5] R. Meignen, S. Picchi, J. Lamome, B. Raverdy, S. C. Escobar, and G. Nicaise, “The challenge of modeling fuel–coolant interaction: Part i – premixing,” *Nuclear Engineering and Design*, vol. 280, pp. 511 – 527, 2014.
- [6] M. Leskovar and M. Uršič, “Analysis of PWR ex-vessel steam explosion for axial and side melt release,” *Nuclear Engineering and Design*, vol. 283, pp. 40–50, 2015.
- [7] W. Baker, P. Cox, J. Kulesz, R. Strehlow, and P. Westine, *Explosion Hazards and Evaluation*. ISSN, Elsevier Science, 2012.

# Conclusions

The main objective of this thesis was the development of a methodology to assess the risk of criticality of debris beds and to estimate the potential consequences. The first part of this work concerned the context of the criticality of debris beds and the simulations codes and tools that should be used in order to provide reliable estimates for the physical quantities of interest. The second part was devoted to the analysis of the main hypotheses that we have introduced and to the development of a generic debris bed model. Based on these considerations, we have assessed the impact of decay heat on the criticality risk, then we have examined the time evolution of a criticality event, and finally we have provided a preliminary attempt at estimating the mechanical consequences of such accidents.

## Context and state of art related to debris beds

The first two chapters were devoted to the state of art of the knowledge about critical debris beds and the theory to model this kind of systems.

In the chapter I, the state-of-art about debris beds formation and criticality was provided. A particular attention was paid to the severe accidents leading to the creation of fuel debris beds in the past. The phenomena that can generate debris beds such as molten material-water interaction or the concrete ablation by the corium were detailed and explained. The definition of criticality was presented, including the phenomena that can prevent or enhance the criticality occurrence. The cooling of debris beds in diphasic conditions was shown to be complex: the sensitivity of the maximum heat flux was analysed and the trends regarding the pressure, the debris size and the porosity were provided.

In the chapter II we discussed the models and the calculation codes required to simulate critical debris beds. The modelling of flow in porous media, and of diphasic flows into heated debris beds were presented. Some thermal-hydraulics codes were listed, and a particular attention was paid to the code MC3D. Then, the physics of neutron transport was detailed. Two numerical methods to model the neutron transport were illustrated. The quasi-static theory, useful for transient simulation, was presented. The simulation of neutron transport in random geometry was explained. Finally, the basics of statistical machine learning were presented. Regression models and their resolution were explained, followed by the training of the artificial neural networks.

## Discussion of the methodology development

Based on the considerations presented in these two chapters, preliminary steps towards the development of a methodology for the assessment of the criticality risk were taken. This methodology was deployed as follows:

- building a generic model of debris bed;

- developing a basic multi-physics coupling to investigate the critical risk of debris beds;
- developing a refined multi-physics coupling to simulate super-critical transients within debris beds;
- simulating the mechanical consequences resulting from the super-critical transients.

In the following, these challenges and the numerical tools implemented to meet them are detailed.

### Preliminary investigations

In the chapter III assumptions related to the generic debris bed established for this work were detailed, in addition to model description, approximations were also discussed. Several analyses were done to find an equivalent debris diameter [1], the equivalent surface diameter or volume diameter were assessed in the past [2]. But, the novel methods developed in [3] to model Poisson random geometries were extensively used in this work. This analysis has helped to select a proper equivalent diameter to represent the debris size distribution for the neutron transport model. Concerning the thermal-hydraulics, the debris size distribution impact is not perfectly documented: solutions were proposed such as the use of Sauter diameter, surface equivalent diameter, or volume equivalent diameter [4] [1]. According to [4], the surface equivalent diameter has shown the best agreement to fit experimental results on cooling capabilities. The preliminary step to investigate criticality debris beds is illustrated in VI.12.

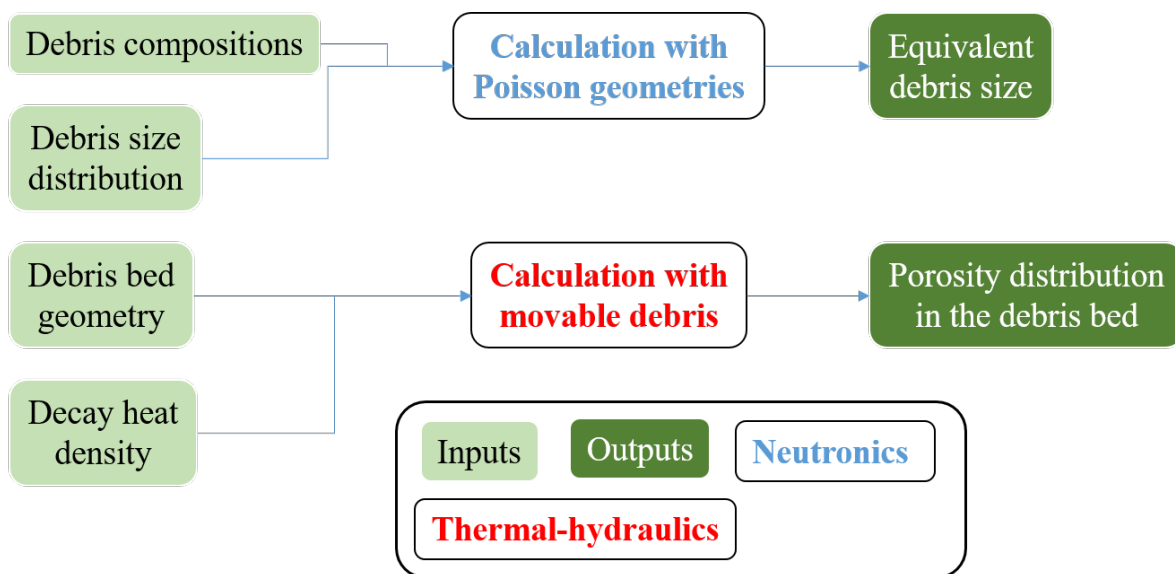


Figure VI.12: Preliminary requirement to model critical debris bed.

However, some limitations should be noted. The equivalent diameter was obtained in fully flooded case, but additional investigations are required to ascertain whether the same equivalent diameter is obtained when taking into account void fraction in the water of the random geometry. The equivalent diameter (in FCC lattice) was chosen to be as close as possible (or conservative) with respect to the multiplication factor obtained when simulating the random geometries. Nevertheless, the equivalent diameter was selected for the lowest porosity, but for the cells with higher porosity the same diameter was used. This induces a bias of about 1000 pcm, and additional efforts would be required to evaluate this bias precisely. To improve the modelling, an equivalent diameter should be chosen for each porosity

value used in the debris beds modelling. In addition the equivalent debris diameter was defined for FCC lattice, the use of Apollo-2 double heterogeneity model may have induced a slightly different equivalent diameter.

In the thermal-hydraulics modelling, the equivalent surface diameter was used. The thermal-hydraulics code was used in this work in diphasic conditions and also in mono-phasic conditions when the debris beds were artificially reflooded by a large mass of water without power density. These conditions did not exactly meet the physical conditions where the equivalent diameter results were assessed.

The mesh used for MC3D and Apollo-2 were selected to have a good balance between accuracy and calculation time. The coupling mesh was selected early in the work to avoid large flows of data. However, regarding the performance of the coupling methodology, it was unfortunate that the coupling mesh was less refined than the other meshes (in neutron transport and thermal-hydraulics). A preliminary study has shown that the coupling mesh was fine enough to have a very low error (0.5 %) on the deposited energy as opposed to a more refined mesh. However, this investigation should be revisited in view of the improvements achieved in the methodology later in the thesis.

The use of a coarser mesh on the coupling mesh leads to a loss of information from the neutronics and the thermal-hydraulics calculation. On one hand, the information transmitted to each code corresponds to the physical data of each coupling cells. On the other hand the results of calculations obtained on refined mesh are averaged to fit in the coupling mesh. A large effort should be done to refine the coupling mesh and create a dynamic condensation to avoid as much as possible the loss of information.

## Critical assessment of debris beds

Critical assessment was addressed in the chapter IV. It took the form of a data exchange between codes and especially between the thermal-hydraulics and neutron transport simulation code. This section is devoted to the discussion about the methodology to assess the criticality in debris beds.

A particular attention was paid to model the debris beds, so to avoid any numerical instabilities. The Apollo-2 model proves to be accurate and the calculation scheme to be time-effective.

The reactivity assessment required several neutronics calculations. The number of calculations was actually too high to have a reasonable simulation time. To accelerate the simulation, the use of artificial neural networks was investigated. This kind of surrogate model has met the accuracy criteria and its computing time was relatively fast ( $\approx 10^{-3}$  s). An optimisation work was done to improve the model accuracy. The steps to build the database and train the ANN are described in VI.13.

Thanks to the trained ANN, the acceleration of the reactivity estimation was very effective: it went from 30 s with Apollo-2 to less than 1 s with the ANN. This improvement has allowed us to explore the different simulation scenarii in a shorter time.

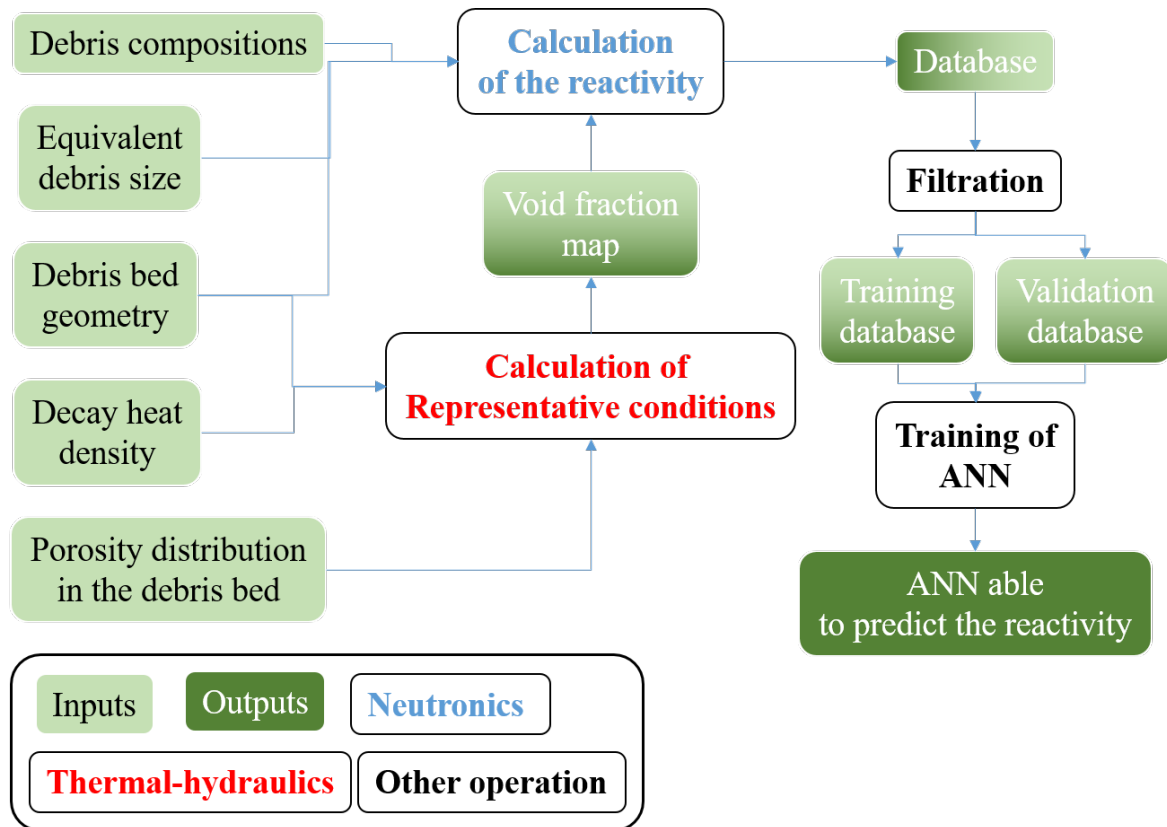


Figure VI.13: Procedure to build the database and train the ANN.

One flaw of the surrogate model is that even when it shows good performance its accuracy can not be ensured. Some cases were validated using Apollo-2 calculations done on regular time-step, and the results showed slight discrepancies ( $\approx 250$  pcm). Moreover, despite the errors, the ANN reproduced properly physical conditions (pressure, power density) impact on reactivity variation. The utilisation of ANN could be described as a less accurate, and time-effective exploration method.

Different approximations were done to establish an efficient multi-physics coupling methodology. The Doppler effect and the moderator temperature effect were neglected, which can induce a bias in the reactivity assessment. This choice was justified by the temperature variations (from 373 K to 420 K) in the domain, which were considered to be relatively small. The moderator temperature effect comes from the displacement of the neutron thermal flux peak. As the calculations with Apollo-2 were done at a pre-set temperature of 373 K (whereas the saturation temperature varies from 373 K to 420 K depending on the pressure), the criticality may be slightly overestimated. The Doppler effect can induce a negative reactivity of about 250 pcm and the moderator temperature effect a negative reactivity of about 130 pcm. These approximations were based on the low effect on criticality and the complexity of implementing properly the water temperature map and the debris temperature map in the database (with the debris temperature and moderator temperature, the dimensions of inputs would amount to 91, asking larger training and validation database to train surrogate model).

### Thermal-hydraulics development and hypotheses

MC3D was successfully used to simulate the thermal-hydraulics state of the debris beds. An investigation was done to implement realistic boundary conditions and to avoid numerical

instabilities.

One assumption required by the limitations of the coupling code is that the debris are totally static into the debris beds, which is not realistic in transient simulation. During the critical assessment, the debris displacements are small, as shown by the study on the porosity profile in subsection III.1.4. However, even small changes in the debris beds porosity due to debris movements might induce an impact on the reactivity of the system. Simulations taking into account the debris movements even in critical assessment might be necessary to improve the reliability of the models.

The spatial porosity distribution was static and did not depend on the thickness of the debris beds. When there is more mass in the top layer, a stronger force will be applied on the lower layer, leading to a decrease of the porosity. The modelling of the debris beds at different heights was done by an homography application, which means that the debris beds structure keeps its relative distribution but it can vary in size. However, the porosity profile might actually change depending of the debris beds height. More work is required to assess the porosity profile depending on the total mass of free debris. The simulation of criticality with debris free of movement would eliminate this approximation from the spatial distribution of porosity, as the porosity map would become an inputs parameter just like the void fraction map.

### **Trends highlighted on the test cases**

Two investigations were performed in the domain presented in the chapter III. The trends stemming from the simulation show that the reactivity of a debris bed strongly depends on the physical conditions. The power density is a limiting factor for the returns to criticality, whereas the pressure favours it. The simulations show that the contribution to thermal-hydraulics to criticality calculation leads to the counter-intuitive effect where the maximum fissile mass does not always bring the highest value of reactivity.

Although these conclusions should be taken with care in view of the approximations described before and the case assessed was based on a simplified debris bed model, we have shown that the coupling of different disciplines (neutron transport and thermal-hydraulics) was essential.

### **Development of the multi-physics coupling**

The critical assessment highlights important trends regarding the criticality of debris beds in accident conditions. The aim of the chapter V was to develop a multi-physics coupling, to estimate the deposited energy map. In this section, is discussed the coupling methodology and the results.

In this thesis we have estimated the multi-physics behaviour of a critical debris bed. The use of a code devoted to debris bed cooling (MC3D) has allowed the calculation of complex diphasic flow inside debris beds. The validation of this code on transient experiments such as PEARL [5] enhances the reliability of the obtained results. The coupling with the neutronics, (reactivity assessment, nuclear power evolution and power profile estimation) has allowed us to calculate transient power surges. The module of double-heterogeneity in the code Apollo-2 has been useful. Indeed, the neutron transport calculations have shown low discrepancies compared to reference calculations (with TRIPOLI-4<sup>®</sup>) on a large system (see chapter III). An approximation done in the methodology comes from the value of the  $\beta_{eff}$ . The pre-calculations have shown that its value is relatively stable with respect to the temperature or the void fraction in the debris beds. However, its calculation at each time-step

when the reactivity is close to criticality would surely increase the reliability of the prompt transients.

### Estimation of mechanical consequences

In the chapter VI we presented a first attempt at modelling mechanical consequences. A simulation was done with MC3D, and the pressure were recorded to estimate the impulsion. These criteria were not met with the most powerful transients simulated. A preliminary qualitative analysis excluded strong mechanical consequences.

Thanks to the generation of the source term, mechanical consequences were estimated with the MC3D code. This simulation was done with an approximative modelling of the structures of the reactor vessel pit and using only 2 dimensions (R,Z). The precise description of the building would be required to improve the reliability of the obtained results. The pressure was recorded (the locations were set according to the literature) and the mechanical impulsion was obtained. The results have shown that the impulsion resulting from the expansion of the steam bubble is about 14 kPa.s, and that around 4% of the debris are expelled above the pressure vessel. The maximum impulsion was relatively low, indeed, it corresponds to 8 % of the impulsion recorded in steam explosion simulations on the wall [6]. This estimation has shown that the damages from a prompt critical generic debris bed reflooded in non-realistic conditions (to obtain a powerful source term) were limited and can be even considered negligible.

### Summary

A methodology adapted to the consequences analysis of a debris beds critical event was successfully developed. The methodology has been tested on a generic model. The trends highlighted concerning the criticality are:

- the higher is the decay heat, the lower will be the reactivity, thanks to the generated steam;
- the higher is the pressure, the higher will be the reactivity, thanks to the steam density variation;
- the critical mass depends on the decay heat, and smaller debris beds can be more reactive.

The coupling of the thermal-hydraulics and neutronics leads to the conclusions:

- at high pressure (>0.3 MPa), the debris beds behaviour can stabilize itself;
- at low pressure, the power of the returns of criticality is difficult to predict.

The decision was made to generate a conservative fission energy source term by applying an artificial reflooding condition in order to obtain a conservative evaluation of mechanical consequences.

It has been demonstrated that the methodology is capable of assessing the risk of criticality. Finally the obtained source term from the multi-physics simulations can be used as an input to calculate the mechanical impulsion. Now, the methodology is ready to be deployed for real cases, the procedure is illustrated in the figure VI.14.



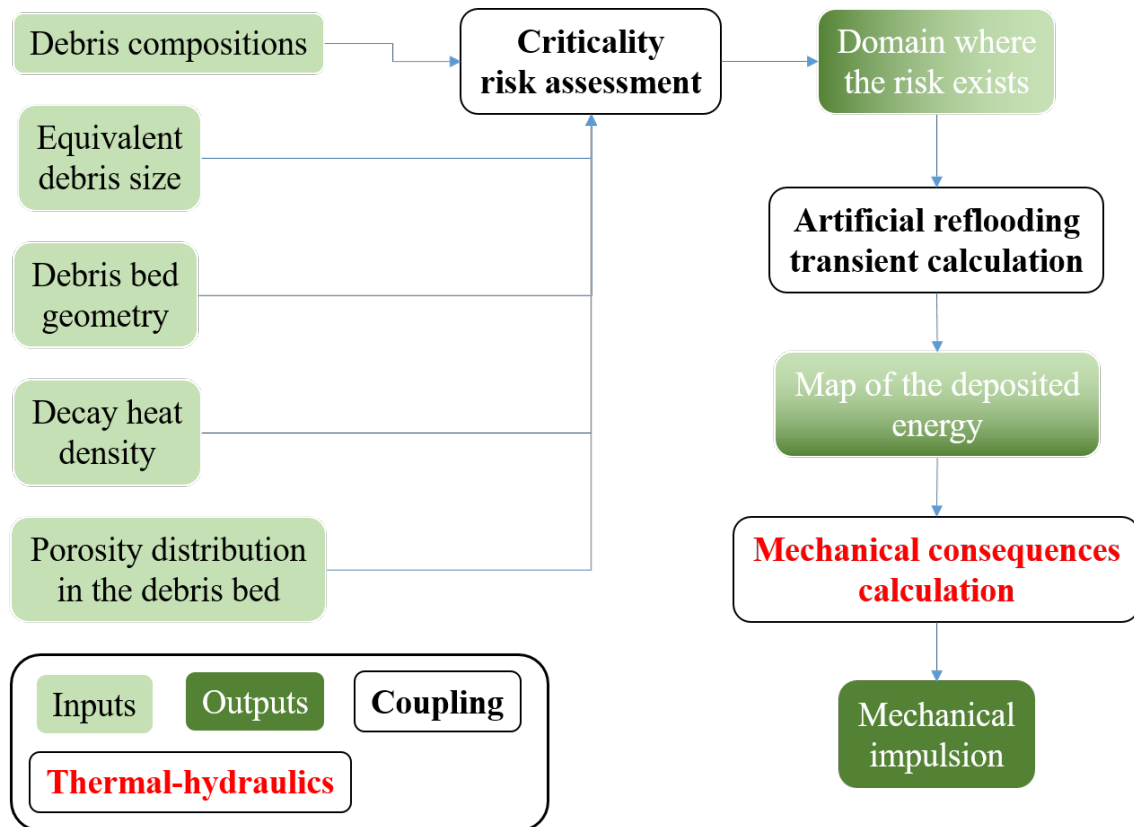


Figure VI.14: The procedure to estimate the risk of criticality and the potential mechanical consequences.

## Perspectives

Concerning the assumptions of the generic debris bed model, no scenario was favoured. However, the simulation of a debris bed created by interaction of concrete and corium would demand to treat differently the decay heat (as a fraction would come from the floor). More work is needed to explore this feature.

The thermal-hydraulics code MC3D was used, however, in the long term, CFD simulations in porous media may help to capture the thermal state of debris beds with a stronger reliability. Moreover, regarding the strong impact of the thermal-hydraulics on the simulation the coupling with other codes (like COCOMO [7] or DECOSIM [8]) would help to confirm or refute the conclusions reached in this thesis, enhancing the confidence in the obtained results.

In the chapter V, the quasi-static method was applied to simulate super-critical prompt transients. This approximation was not assessed. 3 dimensional kinetics with novel neutron transport codes as Apollo-3® [9] would help to estimate the error inserted by the application of the quasi-static method. A reference calculation with the TRIPOLI-4® kinetics simulation capabilities [10] can further expand the reliability of the methodology developed in this thesis.

In the chapter V, the artificial reflooding has highlighted the need of more refined mesh to represent properly the reflooding front. However, the coupling mesh was not refined due to time and numerical constraints. A new study should be done to readapt the coupling mesh which was set early in the development.

In the chapter V, we have illustrated the complex behaviour of critical debris bed. These



behaviours seems to be unpredictable. At high pressure it was shown that the system looks chaotic. Mathematical investigations should be done to demonstrate the chaotic characteristic of these systems.

In the chapter IV, the machine learning method was effective to speed up calculations. One asset of this method is the very high compression rate of data. Indeed, in this work, the best ANN trained, has learnt  $2800 \times 32$  values on approximately 1400 weights and has captured the behaviour to properly extrapolate or interpolate the points in the validation dataset. Further investigation would concern the use of ANN (and especially the use convolutional neural network to learn the geometry impact on simulation [11]) to learn the solution of iterative process (for example: the core calculation of the neutron transport in Apollo-3® [9]). By proposing a first guess close to the solution, any iterative process can be significantly sped-up. This acceleration might be particularly useful for industrial calculations where the dataset can be constantly enlarged, the calculations inputs dimension are similar, and the inputs values are always in the same domain.

## Bibliography

- [1] N. Chikhi, O. Coindreau, L. X. Li, W. M. Ma, V. Taivassalo, E. Takasuo, S. Leininger, R. Kulenovic, and E. Laurien, "Evaluation of an effective diameter to study quenching and dry-out of complex debris bed," *Annals of Nuclear Energy*, vol. 74, pp. 24–41, 2014.
- [2] M. F. López, M. Buck, and J. Starflinger, "Neutronic modeling of debris beds for a criticality evaluation," *Annals of Nuclear Energy*, vol. 130, pp. 164 – 172, 2019.
- [3] C. Larmier, *Stochastic particle transport in disordered media : beyond the Boltzmann equation*. PhD thesis, (Paris Saclay), 2018.
- [4] J. H. Park, H. S. Park, , and M. Lee, "A new two-phase pressure drop model for porous media in boiling conditions for dryout heat flux prediction," *ERMSAR proceedings*, 2019.
- [5] N. Chikhi and F. Fichot, "Experimental and theoretical study of large scale debris bed reflood in the pearl facility," *Nuclear Engineering and Design*, vol. 312, pp. 48 – 58, 2017.
- [6] M. Leskovar and M. Uršič, "Analysis of PWR ex-vessel steam explosion for axial and side melt release," *Nuclear Engineering and Design*, vol. 283, pp. 40–50, 2015.
- [7] M. Buck and G. Pohlner, "Ex-vessel debris bed formation and coolability – challenges and chances for severe accident mitigation," *Proceedings of ICAPP*, vol. 2, pp. 1217–1226, 2016.
- [8] S. Yakush, P. Kudinov, and T.-N. Dinh, "Modeling of two-phase natural convection flows in a water pool with a decay-heated debris bed," *Proceedings of ICAPP*, vol. 2, pp. 1141–1150, 2008.
- [9] D. Schneider, F. Dolci, F. Gabriel, J.-M. Palau, M. Guillo, and B. Pothet, "APOLLO3® CEA/-DEN deterministic multi-purpose code for reactor physics analysis," in *PHYSOR 2016 – Unifying Theory and Experiments in the 21st Century*, (Sun Valley, United States), May 2016.

- [10] M. Faucher, *Coupling between Monte Carlo neutron transport and thermal-hydraulics for the simulation of transients due to reactivity insertions*. PhD thesis, Paris-Saclay, 2019.
- [11] T. Hastie, R. Tibshirani, and J. Friedman, *The elements of statistical Learning*. Springer, 2008.

# Appendix A

## Nomenclature and back-propagation example

### A.1 Nomenclature

#### A.1.1 Thermal-hydraulics nomenclature

$i$  : index of the phase

$\alpha_i$  : volume ratio of the phase  $i$  ()

$P$  : pressure (Pa)

$d$  : debris diameter (m)

$T$  : temperature (K)

$\epsilon$  : porosity of the porous media ()

$\rho_i$  : density of the phase  $i$  (kg/m<sup>3</sup>)

$\alpha$  : steam volume ratio ()

$s$  : liquid water volume ratio ()

$s_i$  : volume ratio of the phase  $i$  ()

$V_i$  : velocity of the phase  $i$  (m/s<sup>2</sup>)

$v_{si}$  : superficial velocity of the phase  $i$  (m/s<sup>2</sup>)

$\mu_i$  : dynamic viscosity of the phase  $i$  (Pa.s)

$k$  : permeability (m<sup>2</sup>)

$\eta$  : passability (m)

$k_{ri}$  : relative permeability of the phase  $i$  ()

$\eta_{ri}$  : relative passability of the phase  $i$  ()

$g$  : gravity acceleration (m/s<sup>2</sup>)

**A.1.2 Thermal diffusion nomenclature**

$T$  : temperature (K)

$F_{heat}$  : the heat flux (W)

$T_{\infty}$  : the fluid temperature (K)

$T_s$  : the solid surface temperature (K)

$\lambda$  : thermal diffusion coefficient ( $m^2/s$ )

$\rho$  : mass density ( $kg/m^3$ )

$C_p$  : specific heat capacity (J/kg/K)

$\beta$  : thermal dilatation coefficient ( $m^3/K$ )

$D$  : diameter (m)

$h$  : thermal convection coefficient ( $W/m^2$ )

$\gamma$  : thermal diffusivity coefficient  $\gamma = \frac{\lambda}{\rho C_p}$  ( $m^2/s$ )

$\mu$  : dynamic viscosity (Pa.s)

$g$  : gravity acceleration ( $m/s^2$ )

**A.1.3 Neutron transport nomenclature**

$n$  : neutron density (neutron/ $m^3$ )

$m$  : neutron mass (kg)

$E$  : neutron energy (J)

$\Sigma_s$  : macroscopic cross-section of diffusion ( $m^2$ )

$\Sigma_t$  : macroscopic cross-section of transport ( $m^2$ )

$\Sigma_a$  : macroscopic cross-section of absorption ( $m^2$ )

$\Sigma_f$  : macroscopic cross-section of fission ( $m^2$ )

$\nu$  : average number of neutrons produced per fission ( )

$v$  : neutron velocity (m/s)

$J$  : neutron current density (neutron/ $m^2/s$ )

$S$  : neutron source (neutron/s)

$D$  : neutron diffusion coefficient (m)

$\Phi$  : neutron flux (neutron/ $m^2/s$ )

$k$  : neutron multiplication coefficient ( )

$k_{\infty}$  : neutron multiplication coefficient in an infinite space ( )

$\rho$  : reactivity ()

$w_i$  : neutronics weight of the cell  $i$  ()

$P_i$  : power profile in cell  $i$  ()

$V_i$  : volume in cell  $i$  (m<sup>3</sup>)

## A.2 Example of back propagation computation

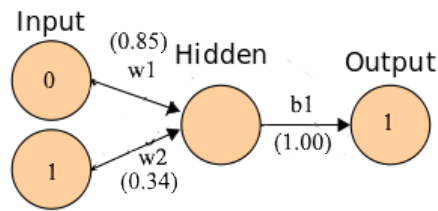


Figure A.1: Small artificial neural network to do an example of backpropagation.

The target is 1 and the inputs are 0 and 1 as described in figure A.1. The network is detailed below:

$$network = w1 \times input_1 + w2 \times input_2 = 0.850 \times 0.000 + 0.340 \times 1.000 = 0.340$$

$$output = b1 \times \frac{1}{1 + e^{-network}} = 1.000 \times \frac{1}{1 + e^{-0.340}} = 0.584$$

First is calculated the impact of the weight  $w1$  on the error (E). Then the chain rule is applied:

$$\frac{\partial E}{\partial w1} = \frac{\partial E}{\partial output} \times \frac{\partial output}{\partial network} \times \frac{\partial network}{\partial w1}$$

The partial derivative of the logistic function is:

$$\frac{\partial output}{\partial network} = output \times b1 \times (1 - output) = 0.584 \times 1.000 \times (1 - 0.584) = 0.249$$

Here the total error with respect to the output is:

$$\frac{\partial E}{\partial output} = -(target - output) = -(1 - 0.584) = -0.416$$

$$\frac{\partial network}{\partial w1} = 1 \times output \times w1^{1-1} = 1 \times 0.584 \times 0.850^{1-1} = 0.497$$

$$\frac{\partial E}{\partial w1} = -(target - output) \times output(1 - output) \times output \times w1^{1-1}$$

$$\frac{\partial E}{\partial w1} = -(1.000 - 0.584) \times 0.584(1 - 0.584) \times 0.584 \times 0.85 = -0.050$$

One constant is introduced here; it is the learning rate written  $\eta$  (taken to 15 here). Now the weight  $w1$  can be corrected to get a better fit of the target.

$$\Delta w1 = -\eta \times \frac{\partial E}{\partial w1}$$

$$w1^+ = w1 - \Delta w1 = 0.850 - 15.0 \times 0.050 = 0.098$$

The same calculation is done on the weight  $w2$  and the bias  $b1$ . After one learning the results are compared: The output goes from 0.584 to 0.961 and the error goes from  $-4.16 \times 10^{-1}$  to  $-3.9 \times 10^{-2}$ . The method successfully diminished the error of the prediction.

# Appendix B

## Résumé détaillé en français

### B.1 Introduction

La survenue d'un accident grave dans une installation nucléaire, comme celui de Three-Miles-Island-2 (TMI-2), de Tchernobyl ou de Fukushima, pourrait avoir des conséquences importantes [1]. Alors qu'un accident grave représente déjà une préoccupation majeure, un retour en criticité pourrait aggraver l'état de l'installation nucléaire. Un retour en criticité peut se produire si la réaction en chaîne des neutrons est entretenue par des conditions physiques favorables, sans aucun moyen de contrôle en raison de l'accident initial. Les fissions créeront des nucléides radioactifs et seront une source immédiate d'irradiation. Un accident de criticité peut entraîner des conséquences non négligeables. En effet, la densité de neutrons augmentera et la chaleur produite pourrait, dans certaines circonstances, mener à des conséquences mécaniques sur les structures du bâtiment réacteur.

Cependant, le retour en criticité nécessite des conditions physiques locales spécifiques. Cet événement potentiel doit être étudié pour évaluer ses conséquences potentielles, en tenant compte du fait des conditions particulières de l'accident grave.

L'objectif de cette thèse de doctorat est d'estimer le risque de retour en criticité et ses conséquences lors d'un accident grave, en prenant en compte les aspects multi-physiques et le couplage entre la physique des neutrons et la thermo-hydraulique. Un accent particulier a été mis sur la simulation cinétique afin de prédire l'évolution de la population de neutrons en fonction de l'évolution des conditions dans le réacteur endommagé.

### B.2 État de l'art concernant la criticité des lits de débris

Nous avons présenté trois accidents graves historiques (classés 5 ou plus sur l'échelle INES [2]). Ces événements ont déclenché un fort accroissement des efforts pour améliorer les connaissances liées aux accidents graves et pour étudier le risque de criticité en cas d'accident grave. La phénoménologie d'un accident grave a été expliquée, en particulier la création d'un lit de débris à partir du corium. Dans ce cas, le cœur a atteint un état très dégradé et ce cœur fondu s'est écoulé hors de la cuve. C'est lorsque le lit de débris est inondé par l'eau nécessaire à son refroidissement que la question de la criticité doit être abordée. De plus, lors des accidents graves survenus dans le passé, la criticité était déjà une préoccupation [3] [4] qui a été traitée grâce à l'injection de bore à TMI-2 [5] et avec grâce à actions identiques à Tchernobyl lorsque la criticité a été détectée [6]. Des ressources importantes sont déployées au Japon pour analyser les problèmes de criticité de l'installation nucléaire de Fukushima et pour s'assurer que les opérations de démantèlement, de récupération et de nettoyage du combustible nucléaire ne créeront pas de risque de criticité [7].

Les études réalisées dans les conditions d'accident grave rencontrées à Fukushima ont montré qu'un lit de débris peut être sur-critique [8] lorsqu'il est renoyé. Cependant, les contre-réactions thermo-hydrauliques n'ont pas été prises en compte. Les lits de débris ont une géométrie non structurée, qui peut être complexe à modéliser pour simuler le transport des neutrons. Des efforts ont été apportés pour modéliser ce type de milieu [9] avec des méthodes simples (comme l'utilisation d'une taille unique de débris). Des recherches récentes ont également envisagé l'utilisation de géométries stochastiques afin de prendre en compte la dispersion aléatoire des lits de débris [10] [11], améliorant la confiance dans les analyses neutroniques. Il a été démontré qu'un accident de criticité peut avoir des conséquences mécaniques ou radiologiques [7], d'où la nécessité d'étudier la criticité des lits de débris. Toutefois, il convient de noter que si l'état thermo-hydraulique du lit de débris a un impact sur la criticité, les écoulements complexes au sein du lit de débris n'ont pas été pris en compte jusqu'à présent [7] [8]. Les analyses de criticité des lits de débris demandent de prendre en compte l'effet de la puissance résiduelle sur les écoulements. Les conséquences seront évaluées si le risque de criticité est possible.

### **B.3 Modèles et codes de simulation**

Des modèles appropriés de transport de neutrons et de thermo-hydraulique d'un lit de débris nécessitent des outils de simulation spécifiques, qui seront abordés dans ce chapitre. Depuis l'accident de TMI-2, des efforts importants ont été faits pour améliorer les connaissances et les modèles qui décrivent le comportement des lits de débris. Ce domaine a connu un regain d'intérêt après l'accident de Fukushima, ce qui a conduit à une intensification des activités de recherche sur la manière de modéliser correctement les milieux poreux [12]. En effet, les milieux poreux sont supposés être le prototype de description des lits de débris [13]. Dans ce chapitre, les modèles et les outils de simulation pour la description des milieux poreux sont présentés, avec un accent particulier sur le transport des neutrons et la thermo-hydraulique.

La simulation du transport des neutrons et de la thermo-hydraulique dans les lits de débris nécessite des modèles sophistiqués. Dans le domaine de la thermo-hydraulique, le développement de codes comme MC3D [14] ou COCOMO [15] nous a permis de disposer d'outils appropriés pour prendre en compte les mécanismes de refroidissement des lits de débris. La discipline du transport de neutrons a également besoin d'un traitement particulier pour pouvoir calculer le transport des neutrons dans des lits de débris. Des modèles comme la double hétérogénéité [16] ou les tessellations de Poisson [10], ouvrent la voie à la simulation en milieu désordonné. Les codes disponibles résolvent l'équation du transport de neutrons en utilisant des méthodes déterministes (comme Apollo-2 [17]) ou la méthode de Monte Carlo (comme TRIPOLI-4<sup>®</sup> [18]) et sont nécessaires pour évaluer la criticité des lits de débris. La simulation de transitoires implique de faire de nombreux calculs qui peuvent être coûteux en temps. L'utilisation de méta-modèles peut nous permettre d'effectuer des estimations rapides de certaines quantités physiques et donc d'accélérer la simulation de transitoire de puissance.

### **B.4 Simulation de lits de débris : une étude préliminaire**

Dans ce chapitre, les outils nécessaires à la construction de la simulation de lit de débris sont abordés. L'aspect numérique des domaines de la neutronique et de la thermo-hydraulique a été abordé. Finalement, un diamètre de débris équivalent a été recherché pour simplifier et accélérer les calculs dans les domaines du transport de neutrons et de la thermo-hydraulique. Le générateur de géométries aléatoires de Poisson est utilisé pour créer un modèle de référence [10]. Il sera ensuite comparé aux calculs simplifiés de lattice [19]. Le



diamètre équivalent en thermo-hydraulique est obtenu grâce à la littérature traitant de ce sujet [20] [21] [22].

## B.5 Évaluation de la criticité des lits de débris

Ce chapitre traite de l'élaboration d'une méthodologie d'évaluation de la criticité.

Nous avons introduit une méthodologie pour estimer la criticité des lits de débris. Une attention particulière a été accordée à la modélisation hydraulique (comme la question des boucles de convection dans la thermo-hydraulique). Un réseau de neurones artificiels a été formé et optimisé pour accélérer les simulations. Les résultats de cette accélération sont substantiels : en effet, sans l'utilisation de modèles de substitution, la simulation aurait été beaucoup plus longue et la méthodologie employée inexploitable. Un code en C++ a été développé dans le but de stocker les données et de les transmettre au code MC3D.

Un domaine de paramètres composé de la puissance résiduelle, de la pression et de la masse du lit de débris a été exploré. Bien que l'étude préliminaire n'ait pas été réalisée avec un diamètre équivalent (publié dans [23]), il convient de noter que la réactivité maximale estimée lors des simulations diminue lorsque la densité de puissance augmente et la pression diminue.

Une analyse complémentaire a été faite avec un diamètre de débris pertinent pour une distribution réaliste de la taille des débris. Cette étude montre des comportements contre-intuitifs : pour une puissance résiduelle constante, la réactivité maximale n'a pas été observée avec la masse de débris la plus élevée. Le résultat de la deuxième étude est significatif car il montre que la masse optimale pour avoir un lit critique dépend fortement de la puissance résiduelle : il peut exister une masse optimale différente de la masse maximale. Enfin, la principale conclusion de l'application de la méthodologie est que la puissance résiduelle empêche le retour à la criticité.

Ces recherches ont apporté des connaissances importantes sur la criticité des lits de débris. Néanmoins, pour estimer les conséquences mécaniques potentielles en cas de criticité, il est nécessaire de disposer d'un *terme source*. Ce terme source est l'énergie libérée par les fissions dans le lit de débris en cas de transitoire de puissance. Par conséquent, l'étape suivante consiste à adapter la méthodologie afin de calculer l'énergie déposée pendant le transitoire, et de mettre en œuvre un calcul de cinétique pour obtenir l'évolution temporelle de la puissance nucléaire.

## B.6 Estimation de l'énergie déposée lors d'un événement critique dans un lit de débris

Ce chapitre traite du développement du couplage multi-physique, nécessaire pour estimer la distribution de l'énergie de fission libérée, appelé ici le *terme source*. Le terme source est nécessaire pour évaluer les conséquences mécaniques. Dans ce chapitre, des modèles physiques additionnels (cinétique point) couplés ensemble pour disposer d'une méthodologie capable de simuler le transitoire de puissance. Une attention particulière a été accordée à l'adaptation du pas de temps et à la précision requise lors d'une simulation de transitoire. Une première évaluation des transitoires de puissance a montré que le comportement d'un lit de débris critique peut être chaotique à basse pression ou plus stable à haute pression (> 0,3 MPa). Ces comportements observés montrent qu'il peut être difficile d'évaluer le *terme source* maximum car le comportement des lits de débris critiques est relativement imprévisible. Nous avons fait le choix d'appliquer des conditions "ad-hoc" afin de favoriser la création

d'un *terme source* maximale digne de confiance. Une étude paramétrique a été réalisée afin d'identifier les conditions qui peuvent générer le *terme source* maximale. Ces résultats ont amené à la nécessité de disposer d'une méthode pour estimer les conséquences mécaniques d'un transitoire de puissance après avoir obtenu la distribution spatiale de l'énergie déposée.

## B.7 Évaluation préliminaire des conséquences d'un événement critique dans un lit de débris

Le couplage multi-physique détaillé au chapitre V est essentiel pour obtenir la distribution de la puissance de fission d'un événement critique transitoire dans un lit de débris générique. Cependant, des efforts supplémentaires sont nécessaires pour estimer les conséquences mécaniques dans le puits de cuve. Les dommages structurels peuvent provenir de la bulle de vapeur créée à l'intérieur du lit de débris après le transitoire de puissance, qui peut être générée très rapidement et entraîner la propagation d'une onde de surpression. Une première estimation des conséquences mécaniques de cet événement, ce qui nécessite de calculer la valeur de l'impulsion mécanique.

La distribution de l'énergie déposée obtenue par la simulation multi-physique est une information cruciale qui a été utilisée comme entrée dans le calcul des conséquences mécaniques. L'analyse préliminaire met en évidence une très faible probabilité de voir des dommages importants car la température de fusion des débris n'a pas été atteinte. Si ce critère n'est pas rempli, la création d'une explosion de vapeur pourrait être évitée et les dommages structurels devraient être très limités voir inexistants. Enfin, nous avons réalisé un calcul avec des conditions appropriées en utilisant une géométrie de puits de cuve. Le calcul montre que la bulle de vapeur est créée rapidement mais génère une faible impulsion. L'impact maximum a été enregistré sur le fond du puits de cuve. L'impulsion mécanique maximale est de 14 kPa.s. Cette valeur comparée aux impulsions d'explosion de vapeur obtenues par simulation (178 kPa.s) est relativement faible [24]. Grâce à la simulation avec MC3D, l'expulsion de 3.0 t (sur 80 t initialement) de débris au delà des limites supérieures du système modélisé a été observée. Le terme source généré dans le chapitre V a apporté suffisamment d'informations pour simuler avec succès les conséquences mécaniques d'un lit de débris critique.

## B.8 Conclusions

Une méthodologie consacré à l'analyse des conséquences d'un transitoire de criticité dans un lit de débris a été développée avec succès. La méthodologie a été testée sur un cas générique. Les tendances mises en évidence concernant la criticité sont les suivantes:

- plus la puissance résiduelle est élevée, plus la réactivité sera faible, grâce à la vapeur générée ;
- plus la pression est élevée, plus la réactivité sera élevée, grâce à la variation de la densité de la vapeur ;
- la masse critique dépend de la puissance résiduelle, ainsi les petits lits de débris peuvent être plus réactifs.

La simulation de transitoires s'appuyant sur le couplage de la thermo-hydraulique et du transport de neutrons permet de tirer ces conclusions:

- à haute pression ( $> 0,3$  MPa), le comportement des lits de débris peut se stabiliser ;

- à basse pression, la puissance des retours de criticité est difficile à prévoir.

Des conditions "ad-hoc" consistant en un renoyage rapide ont été employées pour obtenir un terme source d'énergie de fission dans l'étude des conséquences mécaniques. Il a été démontré que la méthodologie est capable d'analyser rapidement le risque de criticité, et d'évaluer le transitoire de puissance généré par un retour en criticité. Enfin, le terme source obtenu à partir de la simulation multi-physique peut être utilisé comme entrée pour calculer l'impulsion mécanique. La méthodologie est prête à être déployée sur des cas réels.

## Bibliography

- [1] B. R. Sehgal, ed., *Nuclear Safety in Light Water Reactors Severe Accident Phenomenology*. Boston: Academic Press, 2012.
- [2] *INES: The International Nuclear and Radiological Event Scale User's Manual*. Non-serial Publications, Vienna: International Atomic Energy Agency, 2013.
- [3] "Three Mile Island Accident of 1979 Knowledge Management Digest Recovery and Cleanup," tech. rep., USNRC, 2016.
- [4] R. Stone, "Chernobyl: The Explosions That Shook the World," *Science*, vol. 272, no. 5260, pp. 352–354, 1996.
- [5] R. Westfall, J. West, G. Whitesides, and J. T. Thomas, "Criticality analyses of disrupted core models of Three Mile Island unit 2," tech. rep., ORNL, december 1979.
- [6] V. M. Pavlovych, "Nuclear Fuel in the Destroyed 4th Unit of Chernobyl NPP," *Recent Research Activities about the Chernobyl NPP Accident in Belarus, Ukraine and Russia*, 2002.
- [7] R. Kimura and T. Yutaka, "Development of analysis code PORCAS-f for dynamic behavior of re-critical fuel debris," *ICAPP Proceedings*, 2017.
- [8] P. Darnowski, K. Potapczyk, and K. Świrski, "Investigation of the recriticality potential during reflooding phase of Fukushima Daiichi unit-3 accident," *Annals of Nuclear Energy*, vol. 99, pp. 495–509, 2017.
- [9] M. F. López, M. Buck, and J. Starflinger, "Neutronic modeling of debris beds for a criticality evaluation," *Annals of Nuclear Energy*, vol. 130, pp. 164 – 172, 2019.
- [10] C. Larmier, *Stochastic particle transport in disordered media : beyond the Boltzmann equation*. PhD thesis, (Paris Saclay), 2018.
- [11] C. Larmier, A. Zoia, F. Malvagi, E. Dumonteil, and A. Mazzolo, "Neutron multiplication in random media: Reactivity and kinetics parameters," *Annals of Nuclear Energy*, vol. 111, pp. 391–406, 2018.
- [12] E. Takasuo, "An experimental study of the coolability of debris beds with geometry variations," *Annals of Nuclear Energy*, vol. 92, pp. 251–261, 2016.

- [13] A. E. Scheidegger, *The physics of flow through porous media*. University of Toronto Press, 1957.
- [14] B. Raverdy, R. Meignen, L. Piar, S. Picchi, and T. Janin, “Capabilities of mc3d to investigate the coolability of corium debris beds,” *Nuclear Engineering and Design*, vol. 319, pp. 48–60, 2017.
- [15] M. Buck and G. Pohlner, “Ex-vessel debris bed formation and coolability – challenges and chances for severe accident mitigation,” *Proceedings of ICAPP*, vol. 2, pp. 1217–1226, 2016.
- [16] A. Hébert, “A collision probability analysis of the double-heterogeneity problem,” *Nuclear Science and Engineering*, vol. 115, no. 2, pp. 177–184, 1993.
- [17] R. Sanchez, I. Zmijarevic, M. Coste-Delclaux, E. Masiello, S. Santandrea, E. Martinolli, L. Villate, N. Schwartz, and N. Guler, “Apollo2 year 2010,” *Nuclear Engineering and Technology*, vol. 42, no. 5, pp. 474–499, 2010.
- [18] E. Brun, A. Zoia, and al., “Tripoli-4®, cea, edf and areva reference monte carlo code,” *Annals of Nuclear Energy*, vol. 82, pp. 151–160, 2015.
- [19] P. Boulard, C. Larmier, J.-C. Jaboulay, A. Zoia, and J.-M. Martinez, “Neutron multiplication in fuel-water random media,” *ICNC proceedings*, 2019.
- [20] J. H. Park, H. S. Park, , and M. Lee, “A new two-phase pressure drop model for porous media in boiling conditions for dryout heat flux prediction,” *ERMSAR proceedings*, 2019.
- [21] L. Li and W. Ma, “Experimental characterization of the effective particle diameter of a particulate bed packed with multi-diameter spheres,” *Nuclear Engineering and Design*, vol. 241, no. 5, pp. 1736–1745, 2011.
- [22] N. Chikhi, O. Coindreau, L. X. Li, W. M. Ma, V. Taivassalo, E. Takasuo, S. Leininger, R. Kulenovic, and E. Laurien, “Evaluation of an effective diameter to study quenching and dry-out of complex debris bed,” *Annals of Nuclear Energy*, vol. 74, pp. 24–41, 2014.
- [23] P. Boulard, J.-C. Jaboulay, J.-M. Martinez, and A. Zoia, “Contribution of thermal-hydraulics simulation to criticality analysis of a debris bed numerical mock-up,” *PHYSOR proceedings*, 2020.
- [24] M. Leskovar and M. Uršič, “Analysis of PWR ex-vessel steam explosion for axial and side melt release,” *Nuclear Engineering and Design*, vol. 283, pp. 40–50, 2015.

**Titre :** Contribution à l'évaluation multi-physique du risque de retour en criticité du corium en cas d'accident grave dans un réacteur de type REP.

**Mots clés :** Multi-physique, lit de débris, criticité, accident grave, corium

**Résumé :** Suite à l'accident de Fukushima, le sujet d'un éventuel risque de criticité du corium a connu un regain d'intérêt. Lors d'un accident grave, le combustible – s'il n'est pas refroidi à temps – va finir par fondre et former un mélange appelé corium. Celui-ci peut percer la cuve et se déverser dans le puit de cuve. En cas d'aspersion d'eau, le corium va se fragmenter en débris de petite taille (taille médiane observée lors des expériences FARO  $\approx 3$  mm). Sous certaines conditions (de porosité, de taux de présence en eau liquide) le lit de débris constitué peut atteindre la criticité. L'évaluation de l'énergie relâchée lors d'un transitoire de réactivité doit être estimée afin d'évaluer les conséquences d'un tel événement. L'objectif de cette thèse est d'élargir les connaissances sur la criticité des lits de débris et de proposer une méthodologie permettant l'évaluation de l'énergie déposée en cas de retour en criticité. L'évaluation de l'énergie déposée demande à ce que tous les aspects physiques (neutroniques et thermo-hydrauliques) soient simulés en régime transitoire, ce qui implique des simulations numériques très gourmandes en temps de calcul. Un des objectifs de ce travail a donc été la recherche de l'optimisation du temps de calcul (dans cette thèse via l'utilisation de méta-modèles).

Concernant le comportement neutronique, simulé à l'aide des codes APOLLO2 ou TRIPOLI-4 ou encore via des descriptions condensées de type « cinétique point », les travaux de thèse ont porté également sur l'utilisation des géométries aléatoires et la possibilité de modéliser la distribution de la taille des débris par une taille « représentative » de débris. L'utilisation d'un maillage 2D (R, Z) pour décrire le lit de débris permet une évaluation plus fine des contre-réactions (effets Doppler et modérateur) et donc de l'énergie déposée lors de la simulation de transitoire. Au sujet de la thermo-hydraulique, un modèle de diffusion thermique a été développé pour obtenir la température au sein même des débris et un code de simulation multiphasique (eau liquide, eau vapeur, débris) MC3D a été sélectionné pour simuler l'état thermo-hydraulique du lit de débris (les champs de température et de taux de vide). La mise en œuvre d'un couplage des disciplines évoquées précédemment a permis l'étude du risque de criticité en fonction de la puissance résiduelle produite par le corium, ou encore l'évaluation de l'énergie déposée dans une configuration représentative d'un lit de débris.

**Title :** Contribution to the multi-physical analysis of the risk of recriticality of corium during severe accident in a PWR reactor.

**Keywords :** Mutliphysics, debris bed, criticality, severe accident, corium

**Abstract :** Following the accident in Fukushima, the subject of a possible risk of criticality of the corium has been the subject of renewed interest. In a severe accident, the fuel - if not cooled in time - will eventually melt and form a mixture called corium. This can pierce the vessel and spill into the vessel shaft. If water is sprayed on, the corium will fragment into small debris (median size observed during the FARO experiments  $\approx 3$  mm). Under certain conditions (porosity, liquid water presence rate) the debris bed can reach criticality. The energy released during a reactivity transient must be estimated in order to evaluate the consequences of such an event. The objective of this thesis is to widen the knowledge on the criticality of debris beds and to propose a methodology allowing the evaluation of the energy deposited in case of a return to criticality. The evaluation of the deposited energy requires that all the physical aspects (neutronics and thermo-hydraulic) be simulated in transient regime, which implies very time-consuming numerical simulations. One of the objectives of this work has therefore been the search for the optimization of the calculation time (in this thesis through the use of meta-models).

Concerning the neutron behaviour, simulated using the APOLLO2 or TRIPOLI-4 codes or via condensed descriptions of the "kinetic point" type, the thesis work also focused on the use of random geometries and the possibility of modelling the size distribution of debris by a "representative" debris size. The use of a 2D mesh (R, Z) to describe the debris bed allows a more precise evaluation of the counter-reactions (Doppler and moderator effects) and thus of the energy deposited during the transient simulation. Concerning thermo-hydraulics, a thermal diffusion model has been developed to obtain the temperature within the debris itself and a multiphase simulation code (liquid water, steam water, debris) MC3D has been selected to simulate the thermo-hydraulic state of the debris bed (temperature and void rate fields). The implementation of a coupling of the above-mentioned disciplines allowed the study of the criticality risk as a function of the residual power produced by the corium, or the evaluation of the energy deposited in a representative configuration of a debris bed.